Experimental Determination of Solar and Infrared Aerosol Radiative Forcing

Krzysztof Markowicz

Warsaw University
Faculty of Physics

Doctoral dissertation performed under advise of prof. dr hab. Krzysztof Haman at the Institute of Geophysics at Warsaw University with assistance of dr Piotr Flatau (Scripps Institution of Oceanography, UCSD, USA)

-Warsaw 2003-

Wpływ aerozolu na zmiany transferu promieniowania krótko- i długofalowego w atmosferze – badania eksperymentalne.

Krzysztof Markowicz

Uniwersytet Warszawski
Wydział Fizyki

Praca doktorska wykonana pod kierunkiem prof. dr hab. Krzysztofa Hamana w Instytucie Geofizyki Uniwersytetu Warszawskiego przy współpracy z Piotrem Flatau (Instytut Oceanografii im Scripps UCSD, USA)

-Warszawa 2003-

moim rodzicom

Abstract

Direct radiometric observations and radiative modeling studies of aerosol radiative forcing in the Earth's infrared and solar spectrum obtained during the ACE-Asia and the INDOEX experiments on board of the research cruises of the R/V Ronald H. Brown and during the MINOS experiment (Crete, Greece) are presented. On the basis of these experiments similarities and differences between the global and regional aerosol effects on Earth's radiative budget are discussed. The analysis shows the great role of absorbing aerosols in large parts of the industrialized world. The negative surface forcing and large positive atmospheric forcing values observed for the Mediterranean aerosols are nearly identical to that of the highly absorbing south Asian haze observed over the Arabian Sea found during the Indian Ocean Experiment. A strong aerosol effect on the radiation budget over the Mediterranean Sea is associated with the biomass burning in the eastern and south-eastern part of Europe. A strong correlation between single scattering albedo and relative humidity, as well as, mean aerosol forcing efficiency and relative humidity is observed in the Sea of Japan. It is shown that relative humidity has a large influence on the global aerosol forcing efficiency. The aerosol radiative forcing in the mid-infrared "atmospheric window" is determined both experimentally (using data obtained from the NOAA Ship Ronald H. Brown cruise during ACE-Asia) and theoretically with use of models. The presented data permit investigation of aerosol infrared forcing caused by a variety of aerosol types and column loadings encountered during the cruise. It is shown that both anthropogenic and natural aerosols can give significant surface infrared forcing and the mechanism of this effect is explained by means of detailed modeling analysis.

Contents

1 Introduction

1.1 Problem statement

Atmospheric aerosols play an important role in many atmospheric processes. They modify the radiation balance and energetics of the earth-atmosphere system (see e.g. [*Houghton et al.*, 1995]), provide the base for heterogeneous chemical reactions [*Aitken,* 1923; *Coulier,* 1875] and also act as condensation nuclei in the formation of clouds [*Twomey*, 1959]. Major components of aerosols are: sulfates due to fossil fuel burning, oxidation of sulphure compounds and volcanic emission; carbonaceous particles which include black and organic carbon; mineral dust from soils.

Fig. 1.1 SeaWIFS pictures of the dust over the Mediterranean Sea on 24 July 2000

Atmospheric aerosols arise from a variety of sources which include both natural (Fig. 1.1) and anthropogenic processes. Their sources can be divided into two major categories: widespread surface and spatial sources. In the first case, aerosol is produced by sources localized at the Earth's surface (e.g. oceans, deserts, and anthropogenic sources). In the second case

sources are localized in the atmosphere and are associated with cloud processes and gas-to-particle conversion [*Warneck,* 1988]. An additional source of aerosols are volcanoes, which can influence even the stratosphere. Inhomogeneous geographic distribution of the aerosols sources and their varying chemical composition makes them difficult to study. Pollution derived from many sources are distributed in the atmosphere trough turbulence and long-distance atmospheric transport of the air masses [*Hobbs et al.,* 1971]. Aerosols are removed from the atmosphere by sedimentation, precipitation, and coagulation processes. Residence time of the aerosols in the atmosphere depends on several factors such as particles size, atmospheric circulation and precipitation and undergoes large variations.

Fig. 1.2 Dense haze over the Sea of Japan observed during ACE-Asia cruise in April 2001

Aerosols produced by both natural and anthropogenic processes can affect the radiation balance of earth-atmosphere system directly [*Charlson et al.,* 1987] by reflecting sunlight back to space, by absorbing solar radiation [*Grassl* 1975*, Hansen at al.* 1997*, Ackerman* 2000], and by absorbing and emitting infrared (IR) radiation [*Lubin et al.*, 1996; *Vogelmann et al.*, 2003]. Impact of the aerosol on the solar radiation is referred to as direct effect (Fig. 1.2) [*Coakley and Cess,* 1985]. Indirect effect is related to cloudy conditions, during which the aerosols and the clouds may interact in a number of ways: the aerosol may increase the cloud droplet concentration [*Twomey*, 1977], thereby, influencing the cloud albedo; the aerosol may influence

cloud persistence; or it may affect precipitation efficiency. A second indirect effect is associated with enhanced cloud life time due to the aerosols modifying cloud microphysical properties [*Albrecht*, 1989; *Rosenfeld*, 2000]. Additional atmospheric heating caused by absorption of solar radiation by the aerosol enhances cloud droplets evaporation. This effect is known as the semidirect effect [*Ackerman et al.*, 2000; *Hansen et al.*, 1997; *Kiehl et al.*, 1999]. At present, quantification of the indirect forcing is difficult.

One of the main aims of this study is the improvement of our understanding of the direct impact of aerosols on the clear sky solar and infrared radiation budget.

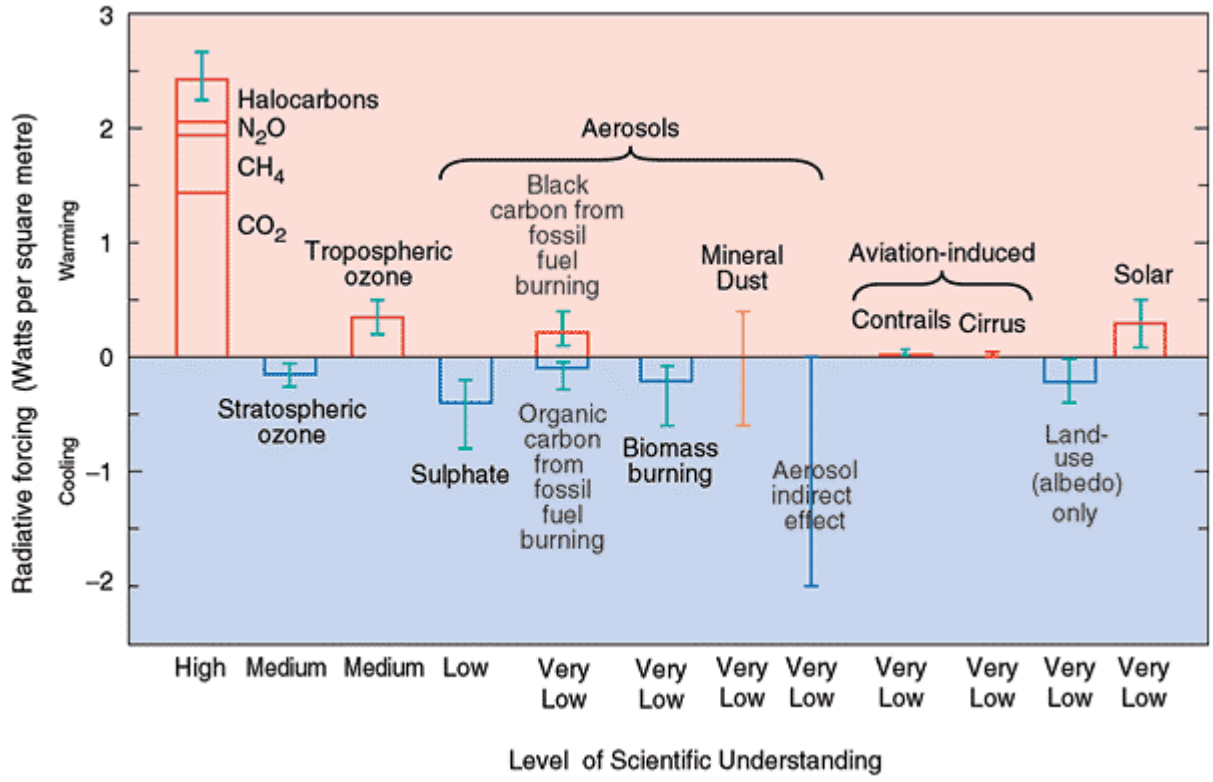

Fig.1.3 The global mean radiative forcing of the climate system for the year 2000, relative to 1750, IPCC 2001

According to IPCC (Intergovernmental Panel of Climate Change) report the effect of radiative forcing[1] by anthropogenic aerosol is one of the most important sources of uncertainties in predicting climate changes. The global direct aerosol forcing ranges between –0.5 and –2.5 Wm^{-2} [*Houghton*, 2001]. Estimates of the indirect effect are very uncertain (-2 to 0 Wm^{-2}) and significant research efforts are directed toward its quantification (Fig 1.3). Direct global aerosol forcing by the sulfates is about $0.5Wm^{-2}$ but uncertainties of this estimation is about 0.7 Wm^{-2}.

[1] For definition of radiative forcing see Chapter 2.1

Similarly, aerosols from biomass burning lead to negative forcing of about -0.2 Wm^{-2}. Aerosol forcing of black carbon is positive (0.2 Wm^{-2}), but the organic carbon cools the system by about 0.1 Wm^{-2}. Large uncertainties are associated with mineral dust because dust has a significant effect on the IR radiation. Direct dust aerosol forcing range between –0.6 and 0.5 Wm^{-2}. The reports of the Intergovernmental Panel of Climate Change [*Houghton*, 2001; *Houghton et al.*, 1995] show that at the global scale magnitude aerosol forcing can be comparable with radiative forcing of the greenhouse gasses. Therefore, intensive study and field observations are important for a better understanding of the role of aerosol in global atmospheric system forcing.

Much of the recent work has been devoted to reducing aerosol forcing uncertainties by using global circulation models [*Chin et al.*, 2002; *Takemura et al.*, 2002] and transport models [*Collins et al.*, 2001]. Establishment of observational networks such as the aerosol robotic network (AERONET) [*Holben et al.*, 2001], a European aerosol research lidar network (EARLINET), and the micro-pulse lidar network (MPLNET), dedicated to monitoring aerosol properties and its vertical distribution supported by satellite observations [*Wielicki*, 1996] yields fast progress in this field. An important part of these research projects are major observational campaigns (SCAR-B [*Kaufman et al.*, 1998], TARFOX [*Hobbs*, 1999], ACE1 [*Bates et al.*, 1998], ACE2 [*Raes et al.*, 2000], INDOEX [*Ramanathan et al.*, 2001], MINOS [*Lelieveld et al.*, 2002], SAFARI2002 [*Swamp et al.,* 2002], and SHADE [*Tandre et al*., 2003]).

Direct observations of aerosol IR forcing at both the surface (e.g.,[*Lubin and Simpson*, 1994; *Spänkuch et al*., 2000] and the top of the atmosphere [*Ackerman and Chung*, 1992; *Hsu et al.,* 2000]) are rare. The IR radiative effect of aerosol involves many uncertainties and is usually neglected. However recent field programs have provided new observations of aerosol IR effects. During the Saharan Dust Experiment (SHADE) in the Cape Verde region, the Airborne Research Interferometer Evaluation System (ARIES) measured 8-12 μm signal of a large Saharan dust storm [*Highwood et al.,* 2002], clearly showing the direct radiative effect of dust in the atmospheric IR window. *Vogelmann et al.* (2003) observationally surveyed a range of surface aerosol IR radiative forcings encountered during the Aerosol Characterization Experiment in Asia (ACE-Asia). They found that the aerosol IR surface forcing can be significant, with values that can exceed 9 Wm^{-2} (instantaneous value). Modeling studies indicate that the mineral aerosols have a highly varying optical properties that can modify the surface IR flux by 7 to 25 Wm^{-2} [*Sokolik et al.,* 1998]. Also, global modeling radiative forcing studies showed large differences due to mineral aerosol [*Myhre and Stordal,* 2001; *Tegen at al.,* 1996]. The modeling study by *Lubin et al* [2002] showed that during the Indian Ocean Experiment (INDOEX)

experiment the aerosol IR radiative forcing over the Arabian Sea could be as much as 15% of the large, anthropogenic short-wave forcing.

In the last 4 years we participated in three international experiments; Indian Ocean Experiment (INDOEX), Aerosol Characterization Experiment (ACE-Asia), and Mediterranean Intensive Oxidant Study (MINOS). This dissertation is based on the results from these campaigns and focused on aerosol solar and infrared (IR) radiative effect on the climate system. We examine the role of atmospheric aerosols on regulation of the amount of solar radiation absorbed in the atmosphere and that which reaches the surface.

Main objectives of this dissertation; (1) establish the role of relative humidity on the aerosol optical properties and aerosol radiative forcing; (2) estimate the IR radiative forcing and IR aerosol optical properties; (3) establish the role of large absorbing aerosols in the climate system; (4) compare aerosol optical properties and the aerosol radiative forcing from three different world sides (the Indian Ocean, Central and Western Pacific Ocean, and Eastern Mediterranean Sea); (5) construct the aerosol-optical database which makes possible determining optical properties of aerosols mixtures.

This study accomplishes these goals using experimental data consisting of instantaneous solar and IR radiative fluxes observations taken at the surface and from satellite platforms. Simultaneous measurements of the physical, chemical, and optical properties of the aerosols are used to build an aerosol-optical model. This model is used to link the variations in the radiative fluxes with variations of the physical properties of the atmosphere and is used to calculate radiative fluxes at the top of the atmosphere and at the surface.

Furthermore, we report a combined modeling and observational study of the IR aerosol optical properties and the direct IR radiative forcing from the ACE-Asia project. We discuss and compare model results with direct observations of the IR aerosol forcing. The model is validated on the basis of multifaceted observations including surface chemical and optical aerosol properties, columnar and vertical profiles of aerosol optical properties, and surface longwave and solar radiation fluxes.

The role of relative humidity on aerosol radiative properties has been investigated in transport models by assuming humidity growth factors for various aerosols [*Chin et al.*, 2002; *Takemura et al.*, 2002] and the role of hygroscopic growth on direct radiative forcing at the surface was shown recently to be significant [*Im et al.*, 2001; *Kotchenruther et al.*, 1999]. However, these studies are based on simple aerosol forcing models while we used a more accurate radiative transfer model to estimate this effect. In retrospect, the meteorological setting of several recent field projects was such that large relative humidity gradients were observed

either between the land and ocean, or between the regions of descending and ascending branches of Hadley circulation. It is shown in this work that these conditions are important when estimating aerosol radiative effects in terms of the aerosol forcing efficiency, a commonly used tool for quantifying aerosol radiative effects on the Earth's energy balance[2].

At first, we planned to use in this study the spectral observations of aerosol optical thickness to determine columnar aerosol size distribution and aerosol single scattering properties, but first results from 5-channels sunphotmoeter were not satisfactory. In our instrument, two channels in UV appeared defective, and, therefore, we decided to omit this retrieval calculations.

1.2 Dissertation plan

This dissertation is partially based on subset of 7 publications written with participation of the author and listed below as M1 to M7. Chapter 2 reviews the basic concepts such as aerosol radiative forcing, definition of the aerosol optical properties and a simple aerosol model. In chapter 3 we will discuss methods of the aerosol forcing determination and type of data used in this study. In chapter 4 (based partly on the paper M3), results from the Indian Ocean Experiment are presented. Main results of this dissertation are included in chapter 5, 6 and 7. Chapter 5 (based on M4, M5, M6, M7) discusses the influence of relative humidity on the aerosol optical properties and solar aerosol forcing. We present unique results concerning the infrared forcing based on the ACE-Asia experiment. Chapter 6 (M1, M2) presents results from the MINOS experiment and demonstrates large role of the absorbing aerosols on Earth's radiative budget. Chapter 7 presents conclusions based on all 3 experiments. In appendices A and B we discuss instrumentation setup, scattering correction, and radiometers calibrations which were performed during campaigns. Appendix C presents description of the aerosol optical database used in this study. This database was constructed by the author because previous ones had a lot of limitations. Appendix D lists the acronyms and appendix E the symbols used in the text.

[2]Aerosol forcing is defined as the radiative flux when aerosols are present minus when they are absent, and the aerosol forcing efficiency is the aerosol forcing per unit aerosol optical depth [*Satheesh and Ramanathan,* 2000]

[M1] *Markowicz, K. M., Flatau, P. J., Ramana, M. V., Crutzen, P. J., Ramanathan, V.* Absorbing Mediterranean aerosols lead to a large reduction in the solar radiation at the surface, *Geophysical Research Letters*, doi:10.1029/2002GL015767, 2002.

[M2] *Lelieveld, J., H. Berresheim, S. Borrmann, P.J. Crutzen, F.J. Dentener, H. Fischer, J. Feichter, P.J. Flatau, J. Heland, R. Holzinger, R. Korrmann, M.G. Lawrence, Z. Levin, K. Markowicz, N. Mihalopoulos, A. Minikin, V. Ramanathan, M. de Reus, G.J. Roelofs, H.A. Scheeren, J. Sciare, H. Schlager, M. Schultz, P. Siegmund, B. Steil, E.G. Stephanou, P. Stier, M. Traub, C. Warneke, J. Williams, H. Ziereis,* Global air pollution crossroads over the Mediterranean, *Science*, Vol. 298, No. 5594, Issue of 25 Oct 2002, pp. 794-799, 2002.

[M3] *Welton, E. J., K. J. Voss, P. K. Quinn, P. J. Flatau, K. Markowicz, J. R. Campbell, J. D. Spinhirne, H.R. Gordon, and James E. Johnson,* Measurements of aerosol vertical profiles and optical properties during INDOEX 1999 using micropulse lidars, *Journal of Geophysical Research*, 107 (D19), 8019, doi:10.1029/2000JD000038, 2002.

[M4] *Vogelmann, A. M., P. J. Flatau, M. Szczodrak, K. M. Markowicz and P. J. Minnett*, Observations of large greenhouse effects for anthropogenic aerosols, G*eophysical Research Letters, 30,* No. 12, 1654, doi:10.1029/2003GL017229, 2003

[M5] *Markowicz, K. M., P. J. Flatau, P. K. Quinn, C. M. Carrico, M. K. Flatau, A. M. Vogelmann, M. Liu*, Influence of Relative Humidity on Aerosol Radiative Forcing, *Journal of Geophysical Research.* 108 (D23), 8662, doi:10.1029/2002JD003066, 2003

[M6] *Markowicz, K. M., P. J. Flatau, A. M. Vogelmann, P. K. Quinn, D. Bates*, Modeling and observations of infrared radiative forcing during ACE-Asia, in press in *Quarterly Journal of the Royal Meteorological Society*, 2003

[M7] *Conant, W. C., J. H. Seinfeld, and J. Wang, G. R. Carmichael, Y. Tang, I. Uno, P. J. Flatau, K. M. Markowicz, P. K. Quinn*, A model for the radiative forcing during ACE-Asia derived from CIRPAS Twin Otter and R/V Ronald H. Brown data and comparison with observations, *Journal of Geophysical Research*, 108 (D23), 8661, doi:10.1029/2002JD003260, 2003.

2 Aerosol Forcing Concept

This chapter presents a brief overview of how the radiation budget in the atmosphere leads to radiative-convective equilibrium of the Earth-Atmosphere system. Based on the planetary equilibrium we define the aerosol radiative forcing. Some general aerosol optical properties are defined and used to describe the aerosol effect on the climate system. We introduce a conceptual model of the solar aerosol radiative forcing, which shows the influence of the aerosol optical properties on the solar radiation at the surface and at the top of the atmosphere.

2.1 Radiation and climate

Climate is usually defined as the average state of the atmosphere observed as weather and described in terms of statistical parameters that measure the variability of weather over a suitably

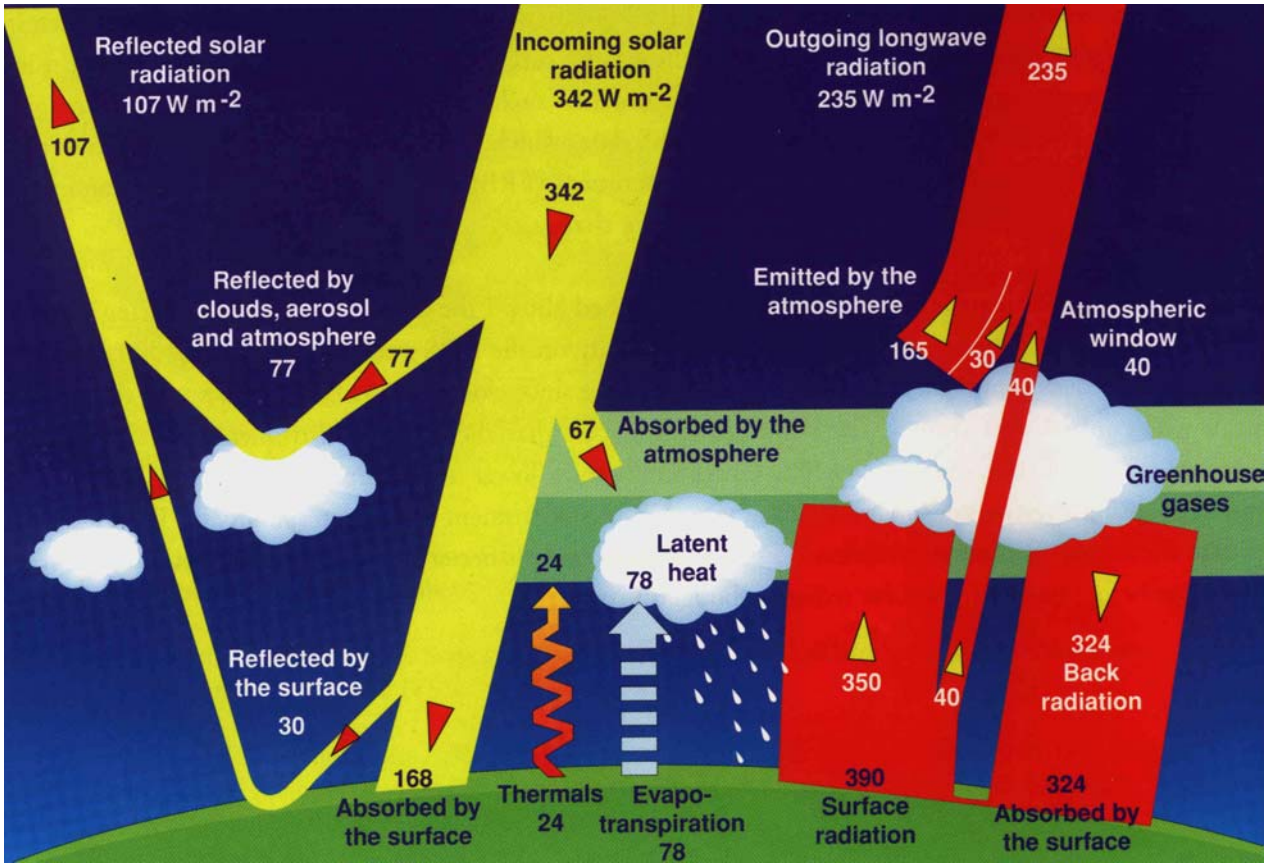

Fig. 2.1 Earth's energy budget

long period of time. Changes in climate involve interactions of the atmosphere with other parts of the climate system, including the oceans, ice, snow, and land, associated with natural and variability and anthropogenic perturbations. Natural variability includes changes in the solar insolation associated with sunspots activity, changes in the solar insolation distribution caused by the earth's orbit around the sun, changes in atmosphere composition due to volcanic eruptions. These are referred to as external forcing, which may also occur as a result of human activities, such as increase in greenhouse gases and anthropogenic aerosols.

Planetary radiative equilibrium (Fig. 2.1) at the top of the atmosphere (TOA[3]) represents the fundamental mode of the climate system. The incoming solar radiation that is absorbed by the earth-atmosphere system must by balanced by an equal amount of emitted thermal infrared energy so as to achieve climate equilibrium. Climatic records show that Earth's climate has been remarkably stable over geologic periods of time but rapid variations also took place. Our present concern is about possible fluctuations, which, due to their magnitude and suddenness, may present a hazard to the mankind.

The atmosphere plays a key role in the energy balance of our planet. Earth is heated by the absorption of solar radiation and cooled by emission of thermal infrared radiation (Fig. 2.1). Because the atmosphere is nearly transparent in the visible part of the solar radiation about 50% of solar radiation reaches the surface. The rest of the solar energy is absorbed (mainly by water vapor, CO_2, and aerosols) and scattered (clouds and aerosols). In contrast to solar radiation, the atmosphere absorbs significant part of the surface thermal radiation. Only in a relatively narrow

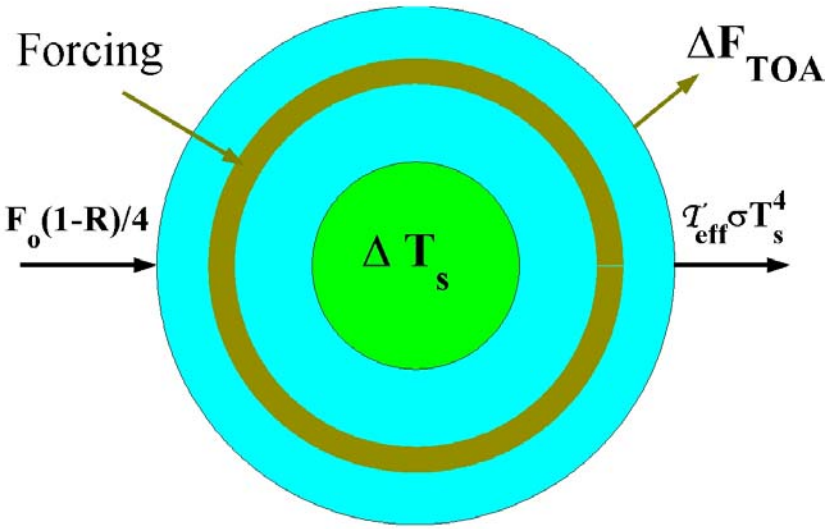

Fig. 2.2 Global climate system forcing

[3] For acronyms see appendix D

spectrum band in IR (the so called atmospheric window) is the atmosphere relatively transparent.

Let's consider the energetic balance at the top of the atmosphere (TOA). If $(1-R)F_o$ [4] is the total incoming solar radiation absorbed in an Earth-Atmosphere system and F_{TOA} is the outgoing longwave radiation then the balance of the energy (Fig. 2.2) can by written as

$$N = (1-R)F_o - F_{TOA}, \tag{2.1}$$

where N is called mean radiative forcing and is equal to the net flux at the TOA and R is the planetary albedo. Time (over a climatologic time scale) and space-averaged radiative forcing is very close to zero ($\langle N \rangle \cong 0$) because of the planetary radiative quasi-equilibrium. The second term in Eq. 2.1 includes the surface and atmosphere contribution. In a first order approximation outgoing longwave radiation can be written as a function of the surface temperature T_s

$$F_{TOA}(T_s) = \tau_{eff}\,\sigma T_s^4, \tag{2.2}$$

where τ_{eff} is an effective thermal flux transmittance in the atmosphere, and σ is the Stefan-Boltzmann constant. The thermal flux transmittance is mostly a function of the total water vapor and CO_2 content.

Consider a small perturbation to the radiative forcing (Fig. 2.2), such that $N(T_s)$, is changed to $N(T_s)+\Delta N$. We assume that the Earth-Atmosphere climate system reaches a new quasi-equilibrium. With respect to N this new state can be written as a sum of the radiative forcing (ΔN) and the atmosphere response [*Thomas and Stamnes,* 1999]:

$$\Delta N + \frac{\partial N}{\partial T_s}\Delta T_s = 0. \tag{2.3}$$

The second term in Eq. 2.3 describes the effect of the radiative forcing due to the change of the surface temperature. Fig. 2.2 shows that radiative forcing in the solar spectrum (e.g. associated with change of the planetary albedo) leads to change in the outgoing longwave radiation (ΔF_{TOA}). Based on Eq. 2.3, the change of the surface temperature is described by

$$\Delta T_s = \alpha \Delta N, \tag{2.4}$$

where α is called the climate sensitivity and can be written as

$$\alpha = -\left(\frac{\partial N}{\partial T_s}\right)^{-1}. \tag{2.5}$$

Using the Eq. 2.1 we can write climate sensitivity in the following form

[4] For symbols see appendix E

$$\alpha = \left(\frac{\partial F_{TOA}}{\partial T_s} - \frac{\partial F_o (1-R)}{\partial T_s} \right)^{-1} . \tag{2.6}$$

Notice, that the surface temperature change defined in the Eq. 2.4 is associated with the direct temperature response (the change in surface temperature due to change ΔN in the radiative forcing). The indirect effect is associated with temperature-dependent processes leading to a positive or a negative feedback (for example increase of the surface temperature tends to increase evaporation and thus raise the humidity enhancing the greenhouse effect).

In more realistic models of climate systems incoming and outgoing radiation (N) at the TOA depend on several parameters q_1, q_2,..., where each depends upon the surface temperature. Then the total change in the radiative forcing becomes

$$\Delta N + \left(\frac{\partial N}{\partial q_1} \frac{\partial q_1}{\partial T_s} + \frac{\partial N}{\partial q_2} \frac{\partial q_2}{\partial T_s} + ... \right) \Delta T_s . \tag{2.7}$$

Change of the surface temperature can by written in a similar form as in Eq. 2.4

$$\Delta T_s = \alpha \Delta N , \tag{2.8}$$

where climate sensitivity is defined as

$$\alpha = \left(\frac{\partial F_{TOA}}{\partial T_s} - \sum_i \frac{\partial N}{\partial q_i} \frac{\partial q_i}{\partial T_s} \right)^{-1} . \tag{2.9}$$

2.2 Aerosol radiative forcing definitions

Aerosol forcing is the perturbation of the Earth-Atmosphere system radiative heat budget caused by the aerosols. Direct aerosol forcing (for clear-sky) is defined as the difference between the net (down minus up) radiative flux for a clear-sky atmosphere with aerosol and net clear-sky radiative flux without aerosol

$$A = Net_a - Net_c . \tag{2.10}$$

Similar definition can be adopted for the TOA (A_{TOA}) and for the surface (A_s)

$$A_{TOA} = F_c^{TOA} - F_a^{TOA} \text{ and} \tag{2.11}$$

$$A_s = (1 - R_s)(F_a^s - F_c^s) \tag{2.12}$$

where F_c^{TOA} and F_a^{TOA} are the upward aerosol-free and aerosol modified solar fluxes at the TOA, R_s is the surface albedo. The F_c^s and F_a^s are downward fluxes at the surface with and without

aerosols in the atmosphere. The TOA and the surface aerosol forcings are functions of the surface albedo but in this study only aerosol effects over the sea is being considered. The aerosol atmosphere forcing (A_a) in this study is defined as the difference between the TOA and the surface forcing, and, therefore, describes columnar effect. Notice that local atmospheric heating is associated with divergence of the net radiative fluxes.

The aerosol forcing is usually defined as the mean diurnal value, however, instantaneous forcing is sometimes used. Aerosols change the planetary albedo (R) and outgoing longwave radiation (OLR). Influence of aerosols on albedo is due to solar radiation absorption and backscatter. Absorption of solar radiation decreases the system albedo but backscatter increases it. It is possible to have positive or negative aerosol forcing at the TOA [*Chylek and Coakley,* 1974; *Haywood et al.* 1995] depending on the optical properties of aerosol such as single scattering albedo or phase function. In the other hand the presence of aerosol always reduces the solar radiation at the surface. Atmospheric forcing in the solar spectral range is positive as a consequence of the aerosol absorption. Also reduction of the solar radiation which reaches the surface modifies infrared aerosol forcing at the TOA. In other words, negative solar forcing at the surface decreases the OLR. Additionally, aerosols interact with infrared radiation (absorption and scattering of thermal radiation). This will be discussed in more detail in chapter 4.

To the first approximation aerosol forcing is a linear function of the aerosol optical thickness (AOT) (see chapter 2.4). Thus, it is convenient to describe the aerosol forcing at the TOA, at the surface, and in the atmosphere by an aerosol forcing efficiency [*Satheesh and Ramanathan,* 2000]. This parameter is defined as

$$F_{eff} = \frac{A}{\tau_{500}}, \tag{2.13}$$

where τ_{500} is the AOT at 500 nm wavelength (see definition in chapter 2.3). Aerosol forcing efficiency is independent of the total aerosol content but is a function of the aerosol optical properties e. g. single scattering albedo or phase function. The mean daily aerosol forcing efficiency and mean aerosol forcing depend on the latitude and the day of year.

2.3 Aerosol optical properties

Inherent optical properties specify the optical properties of aerosols in a form suited to the needs of the radiative transfer theory. The inherent properties include scattering, absorption

and extinction coefficients, and phase function. The scattering (σ_{sca}) and absorption (σ_{abs}) monochromatic coefficients for aerosol particles, are defined as

$$\sigma_{sca}(\lambda) = \int \pi r^2 n(r) Q_{sca}(2\pi r/\lambda, m + ik) dr , \tag{2.14}$$

$$\sigma_{abs}(\lambda) = \int \pi r^2 n(r) Q_{abs}(2\pi r/\lambda, m + ik) dr , \tag{2.15}$$

where Q_{sca} and Q_{abs} are scattering and absorption efficiencies which are functions of wavelength (λ), the particles radius (r), and real (m) and imaginary (k) part of refractive index; n(r) is a aerosol size distribution. For wavelengths significantly smaller than particles radius the scattering and absorption coefficients are given by the Rayleigh theory [*Bohren and Huffman,* 1983]. For aerosol particles for which this assumption is not valid, aerosol optical properties are described by Lohrentz-Mie regime of the scattering [*Bohren and Huffman,* 1983; *Hulst*, 1957]. Extinction coefficient (σ_e) is defined by the sum of the scattering and absorption coefficients. The ratio of the scattering coefficient to the extinction coefficient is called a single scattering albedo (SSA)

$$\omega = \frac{\sigma_{sca}}{\sigma_{ext}} . \tag{2.16}$$

Because $\omega \le 1$ we interpret SSA as the probability that a photon will be scattered, given an extinction event. The quantity (1-ω) is also called the co-albedo or emittance for the thermal radiation respectively.

In order to describe the angular distribution of scattered energy in conjunction with multiple scattering and radiative transfer analyses, we define a nondimensional parameter called the phase function, P(Θ), such that

$$\int_0^{2\pi}\int_0^{\pi} \frac{P(\Theta)}{4\pi} \sin\Theta d\Theta d\varphi = 1 , \tag{2.17}$$

where Θ is a scattering angle which can by obtain from cosine law of spherical geometry

$$\cos\Theta = \cos\theta_o \cos\theta + \sin\theta_o \sin\theta \cos(\varphi_o - \varphi) , \tag{2.18}$$

where θ_o and φ_o are zenith and azimuth angle for incident radiation and θ, φ are zenith and azimuth angle of the scattered radiation. For spherically symmetric (or the averaged properties of randomly oriented) particles, the phase function P(Θ), has only one degree of freedom Θ, the scattering angle. Otherwise, phase function depends on the aerosol particle orientation relative to the incident radiation. Since P(Θ)/4π varies between 0 and 1 this suggests a probability interpretation. Given that a scattering event has occurred, the probability "p" of scattering in the direction Ω(θ,φ) into the solid angle dΩ centered around Ω(θ,φ) is

$$\frac{p(\theta_o,\varphi_o;\theta,\varphi)}{4\pi}d\Omega = \frac{P(\Theta)}{4\pi}d\Omega \ . \tag{2.19}$$

The first moment of the phase function (average cosine of the scattering angle) is referred to as the asymmetry parameter

$$g = \int_0^{2\pi}\int_0^{\pi} \frac{P(\Theta)}{4\pi}\cos\Theta\sin\Theta d\Theta d\varphi \, . \tag{2.20}$$

Asymmetry parameter is important in radiative transfer equation. For isotropic scattering, the asymmetry parameter is zero, as it for Rayleigh scattering. For Lohrenz-Mie type particles whose phase function has a generally sharp peak at the 0° scattering angle the asymmetry parameter denotes the relative strength of forward scattering. Another useful parameter is a backscatter ratio, which corresponds to the fraction of radiation scattered backward. The backscatter ratio can be obtain from the phase function in the following

$$\beta = \int_0^{2\pi}\int_{\pi/2}^{\pi} P(\Theta)\sin\Theta d\Theta d\varphi \, . \tag{2.21}$$

In addition, in lidar observations a backscatter coefficient is used (see Appendix A2). This parameter is defined as

$$\beta_A = P(\Theta=\pi)\sigma_s \, . \tag{2.22}$$

The total aerosol content in the atmosphere above the level z is characterized by the aerosol optical thickness (AOT)

$$\tau = \int_z^{\infty} \sigma_{ext} dz' \, . \tag{2.23}$$

The AOT is the most important parameter which determines aerosol effect on radiative budget at the surface and at the TOA. The AOT is a function that is strongly dependent upon the aerosol column concentration. Spectral dependence of the AOT is described by the Ångstrom exponent which can be written as

$$\alpha = -\frac{d\ln\tau}{d\ln\lambda} \, . \tag{2.24}$$

Notice that for small particles (Rayleigh regime) the Ångstrom exponent is 4. In the case where aerosols size distribution may be described by Junge function ($n(r) = cr^{-\gamma-1}$) the Ångstrom exponent is $\alpha = \gamma - 3$, where γ represents the so called shaping constant. Unfortunately aerosol size distribution in most cases is much better described by the lognormal size distribution [*Aitchison and Brown,* 1957] and the Ångstrom exponent as a function of the wavelength. If

aerosol size distribution is given by superposition of the log-normal size distributions then the Ångstrom exponent may be written [*Shifrin*, 1995]

$$\alpha = \sum_i \alpha_i \frac{\tau_i}{\tau}, \tag{2.25}$$

where α_i and τ_i are the Ångstrom exponent and the AOT for "ith" mode size distribution respectively. The Ångstrom exponent in visible range for the aerosol accumulation mode[5] varies between 1 and 1.6 while for coarse mode[6] is usually close to zero. If we assume aerosol size distribution as a sum of two log-normal size distributions and constant modes radiuses then the Ångstrom exponent is a function of the ratio of particles number in accumulation mode to the particles number of particles in coarse mode. Thus, spectral measurements of the AOT provide useful information about aerosol size distribution.

The methodology of measurements of aerosol optical properties is described in Appendix A. Notice that the above defined aerosol optical properties are a function of the wavelength. These properties depend on the chemical composition of the aerosol particles, relative humidity, size distribution, and shape of the particles.

2.4 Simple model of the aerosol direct forcing

For many atmospheric radiative transfer applications, it is physically appropriate to consider that the atmosphere is locally plane-parallel so that variations of the radiation intensity (radiance) and atmospheric parameters (temperature, pressure, and trace gasses vertical profiles) are permitted only in the vertical direction. Solar and infrared radiation monochromatic intensity I for the plane-parallel atmosphere is described by the radiative transfer equation [*Schwarzschild,* 1914; *Chandrasekhar*, 1950; *Thomas and Stamnes,* 1999].

$$\mu \frac{dI(\tau;\mu,\phi)}{d\tau} = I(\tau;\mu,\phi) - J(\tau;\mu,\phi), \tag{2.26}$$

where μ is a cosine of upward normal (cosine of the zenith angle, $\mu>0$ for upward radiation), J is a source function given by

[5] Accumulation mode, extending from 0.1 to about 2.5 μm diameter. The source of particles in accumulation mode is the coagulation of smaller particles (from nuclei mode) and from condensation of vapors onto existing particles, causing them to grow into this size range.

[6] Coarse mode, from >2.5 μm diameter, is formed by mechanical processes and usually consists of man-made and natural dust particles.

$$J(\tau;\mu,\phi)=\frac{\omega}{4\pi}\int_0^{2\pi}d\phi'\int_{-1}^{1}d\mu' I(\tau;\mu',\phi)P(\mu,\phi;\mu',\phi')+\frac{\omega}{4\pi}F_o P(\mu,\phi;-\mu_o,\phi_o)\exp\left(-\frac{\tau}{\mu_o}\right)+(1-\omega)B(T(\tau)) \tag{2.27}$$

where, μ_o is the cosine of the solar zenith angle, φ_o is the solar azimuth angle, F_o is the downward solar flux at the TOA, and B is the Planck function depending on the temperature T. The first term of the source function associates with multiple scattering, the second with first-order scattering, and the last one with thermal emission. In several atmospheric conditions, the plane-parallel assumption may not be valid. These include the transfer of radiation in the atmosphere where spherical geometry must be accounted for, in clouds of finite size, and inhomogeneity in the horizontal direction. For the solar zenith angle greater than 80° and twilight situations, we have to take the curvature of the Earth into account and solve the radiative transfer equation appropriate for a spherical shell atmosphere.

The aerosol forcing is defined for the radiative fluxes, which can be obtained from the normal component of the intensity integrated over the entire hemispheric solid angle. Thus downward flux (irradiance) may be written as

$$F^{\downarrow}=\int_0^{2\pi}\int_{-1}^{0} I(\mu,\varphi)\mu d\mu d\varphi \tag{2.28}$$

Although precise determination of the radiation budget requires solving the radiation transfer equation, satisfactory results can be obtained also by means of a simple conceptual radiation model, presented in the following. Consider a simple one-layer aerosol model (Fig. 2.3) [*Seinfeld and Pandis*, 1998; *Charslon et al.,* 1991]. We assume, that the solar radiation interacts only with the aerosol, the sun is directly overhead, and the molecular scattering can by negligible.

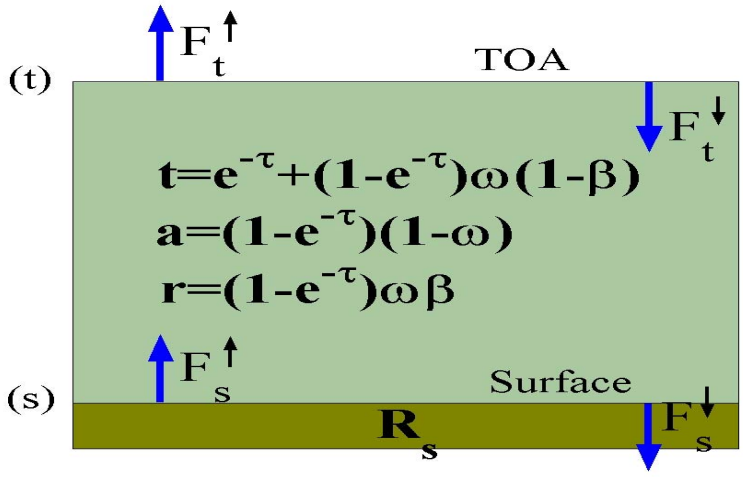

Fig. 2.3 Solar radiative budget in the aerosol layer

If "t" is the aerosol transmission and "r" is the aerosol reflection then downward radiation at the surface $F_s^{\downarrow}$ can by written as

$$F_s^{\downarrow} = tF_t^{\downarrow} + rF_s^{\uparrow}, \tag{2.29}$$

and upward radiation at the top of the aerosol layer $F_t^{\uparrow}$

$$F_t^{\uparrow} = tF_s^{\uparrow} + rF_t^{\downarrow}, \tag{2.30}$$

where,

$F_t^{\downarrow}$ and $F_s^{\uparrow}$ are the downward radiation at the top of the aerosol layer and upward radiation at the surface respectively. Boundary conditions at the surface can be written as

$$F_s^{\uparrow} = R_s F_s^{\downarrow} \ . \tag{2.31}$$

After simple rearrangement of Eq. 2.29-2.31 we obtain formulas for downward radiation at the surface and upward radiation at the top of the aerosol layer

$$F_s^{\downarrow} = F_t^{\downarrow}\left(t + \frac{rtR_s}{1 - rR_s}\right) \tag{2.32}$$

$$F_t^{\uparrow} = F_t^{\downarrow}\left(r + \frac{R_s t^2}{1 - rR_s}\right) \tag{2.33}$$

The first term in the bracket of Eq. 2.32 corresponds to the part of total flux transmitted trough the atmosphere without reflection from the surface (R_s=0) and the second one to the fraction of radiation scattered downward. Similarly in Eq. 2.33 the first term in the bracket is associated with the part of radiation reflected upward by the atmosphere and the second part of the radiation which was multiple scattered between the surface and the aerosol layer.

The total part of the incident radiation transmitted downward through the layer is

$$t = e^{-\tau} + (1 - e^{-\tau})\omega(1 - \beta), \tag{2.34}$$

where, β is the backscatter ratio. The first term of this equation shows direct part of radiation transmitted by the aerosol layer and second the diffuse part. The reflected part of the radiation is defined as

$$r = (1 - e^{-\tau})\omega\beta . \tag{2.35}$$

The part of radiation absorbed by the aerosol is

$$a = (1 - e^{-\tau})(1 - \omega) . \tag{2.36}$$

If we apply the definition of the radiative aerosol forcing for the top of the aerosol layer we can express aerosol forcing as

$$A_t = (F_t^{\uparrow})_{clear} - (F_t^{\uparrow})_{aerosol}, \tag{2.37}$$

$$A_t = F_t^{\downarrow}\left(R_s - r - \frac{R_s t^2}{1 - rR_s}\right), \tag{2.38}$$

Similarly we can write the aerosol radiative forcing at the surface as

$$A_s = (F_s^{\downarrow} - F_s^{\uparrow})_{aerosol} - (F_s^{\downarrow} - F_s^{\uparrow})_{clear}, \tag{2.39}$$

$$A_s = F_t^{\downarrow}(1 - R_s)\left(t + \frac{rtR_s}{1 - rR_s} - 1\right). \tag{2.40}$$

For typical atmospheric conditions the AOT is about 0.1-0.2 therefore mathematical approximation $\tau << 1$ is reasonable. Thus the transmission "t" and the reflection "r" may be written as

$$t = 1 - \tau + \omega\tau(1 - \beta), \tag{2.41}$$

$$r = \omega\tau\beta. \tag{2.42}$$

Substitution of these parameters to Eq. 2.38 and Eq. 2.40 leads to simple expressions for the TOA and the surface aerosol forcing.

$$A_t = -F_t^{\downarrow}\tau[\omega\beta(1 - R_s)^2 - 2R_s(1 - \omega)], \tag{2.43}$$

$$A_s = -F_t^{\downarrow}\tau(1 - R_s)[1 - \omega(1 - \beta(1 - R_s))]. \tag{2.44}$$

This simple model shows that in the first approximation both TOA and surface aerosol forcing are linear functions of AOT. Notice that the term in the square bracket of the Eq. 2.44 is positive because backscatter fraction β fulfils inequality $\beta \le 0.5$. Therefore, the surface forcing is always negative as a result of the absorption and backward scattering by the aerosol layer. The sign of the TOA forcing depends on the SSA and the backscatter fraction. The critical value of SSA that defines the boundary between negative and positive forcing is [*Chylek and Coakley,* 1974]

$$\omega_c = \frac{2R_s}{2R_s + \beta(1 - R_s)^2}, \tag{2.45}$$

Thus, for SSA lager than the critical value, the aerosol layer increases the planetary albedo (cooling) and for smaller values albedo decreases (heating). The critical value of SSA is practically independent of the actual value of the AOT.

Fig 2.4 shows the critical value of the SSA as a function of the surface albedo for five different asymmetry parameters. We used the *Wiscombe* and *Grams* [1976] approximation

$$\beta = 0.5[1 - g] \tag{2.46}$$

to calculate the backscatter fraction from the asymmetry parameter. For large surface albedo (over the snow or above the low clouds layer) aerosol decreases the planetary albedo as a result

the of the multiple surface reflection, and, as a consequence significant photon absorption probability. Over the sea ($R_s \approx 0.05$) the TOA forcing for typical SSA is negative. However, mean global surface albedo is about 0.15. Thus the sign of the forcing depends strongly on the aerosol optical properties. For small particles (small asymmetry parameter) the boundary between cooling and heating shifts toward the high absorbing aerosols. Notice that the typical range of the aerosol SSA variation is between 0.85 and 1 and that of asymmetry parameter is between 0.6 and 0.8.

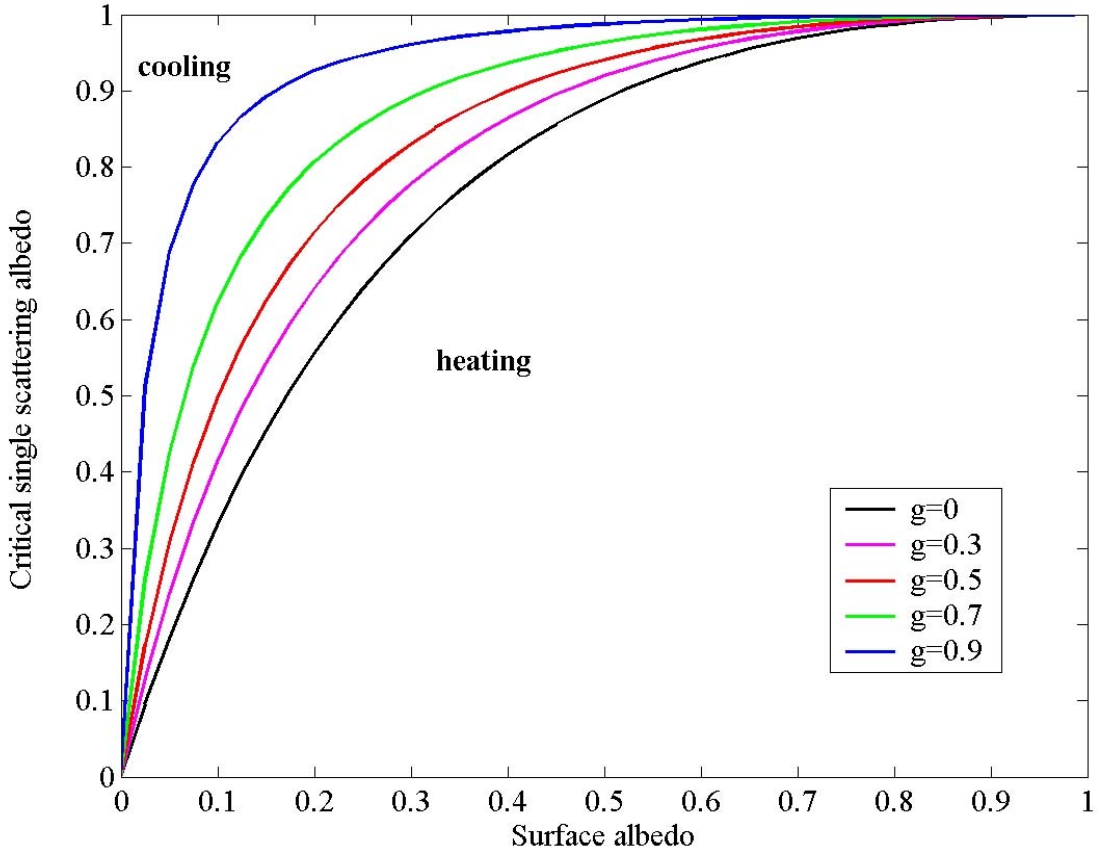

Fig. 2.4 Critical single scattering albedo as a function of the surface albedo for five different asymmetry parameters.

Notice that for derivation of the simple formula (Eq. 2.45) which defines the critical SSA that we made a few assumptions. One of the most important limitations was neglecting the molecular scattering. Although Rayleigh scattering strongly decreases with wavelength, this effect is important in UV and visible part of solar radiation. For example, the molecular optical thickness at 500 nm is 0.14 and is usually comparable with aerosol optical thickness. If we include the molecular scattering the aerosol forcing at the TOA and at the surface may be written as:

$$A_t = F_t^{\downarrow}\left(r_m + \frac{R_s t_m^2}{1 - r_m R_s} - r - \frac{R_s t^2}{1 - r R_s} \right), \tag{2.47}$$

$$A_s = F_t^{\downarrow}(1 - R_s)\left(t + \frac{r t R_s}{1 - r R_s} - t_m - \frac{r_m t_m R_s}{1 - r_m R_s} \right), \tag{2.48}$$

where t_m and r_m are molecular transmission and reflection respectively, t and r are total (aerosol plus molecular) transmission and reflection. The TOA (a) and the surface (b) forcing based on these equations are shown in Fig. 2.5. The calculations of the aerosol forcing was performed for the constant asymmetry parameter (g=0.65) and AOT (0.2) but for different surface albedo and SSA. Negative aerosol forcing at the TOA appears only for non- (or little) absorbing aerosols or for small surface albedo (over water). For larger surface albedo TOA forcing is positive and its

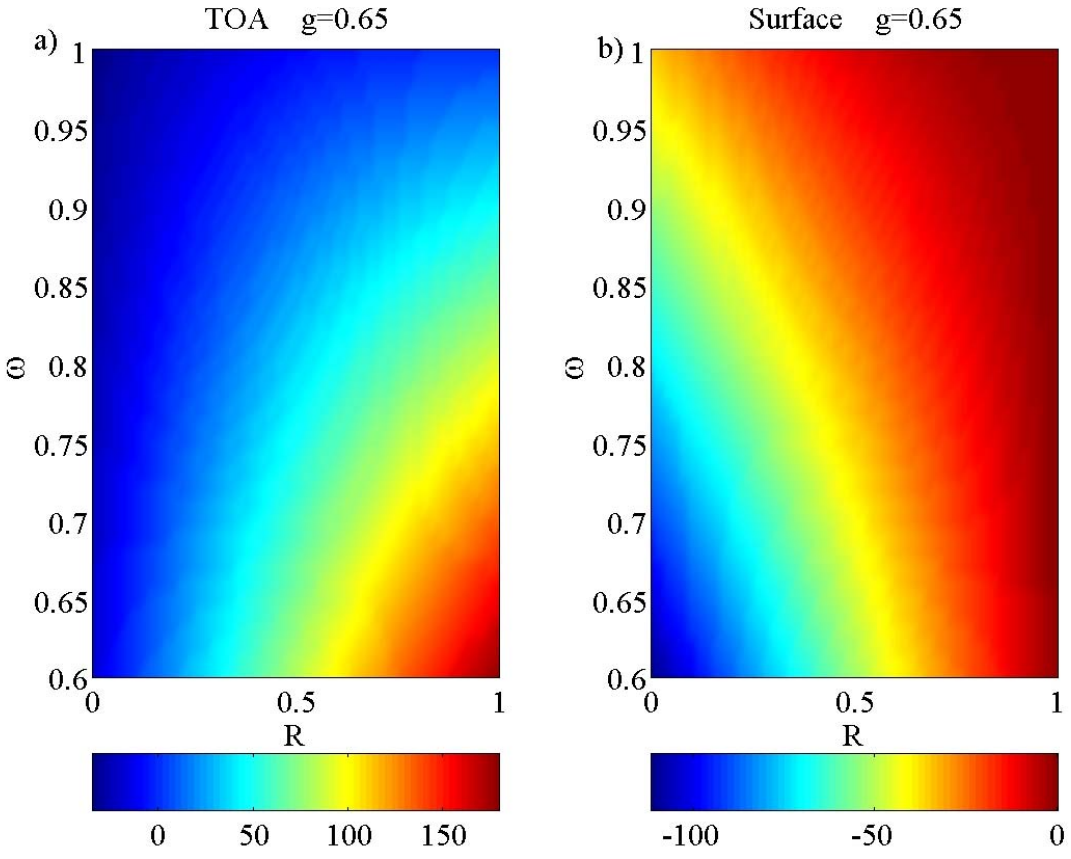

Fig. 2.5 The TOA (a) and the surface (b) aerosol forcing (in Wm^{-2}) as a function of the SSA and the surface albedo. Asymmetry parameter in both cases is 0.65 and AOT is 0.2.

magnitude increases with the increase of aerosols absorption. The surface aerosol forcing is always negative. Its magnitude reaches maximum for black surface and non-absorbing aerosols. In this case a significant part of solar radiation is absorbed in the atmosphere. The aerosol forcing may

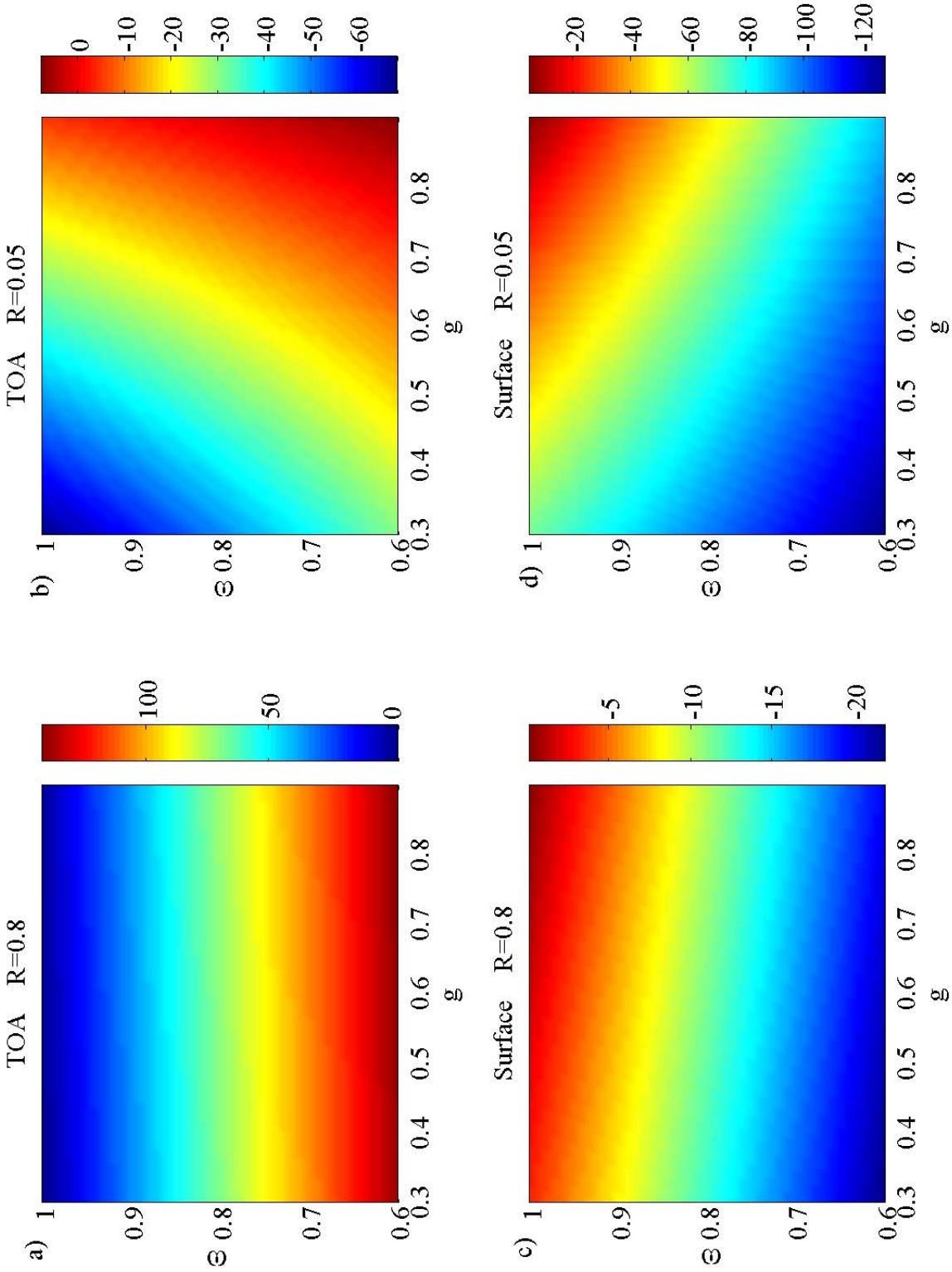

Fig. 2.6 The TOA (upper panel, a, b) and the surface (bottom panel c, d) aerosol forcing (in Wm^{-2}) as a function of the SSA and asymmetry parameter for two surface albedo. Figures (a) and (c) show aerosol forcing for R=0.8 and (b) and (c) for R=0.05. AOT in all cases is 0.2.

reach –100 Wm^{-2} during noon time. Increase of both the surface albedo and the SSA lead to the decrease of the aerosol impact on the solar radiation at the surface. For large surface albedo the surface aerosol forcing is small because a significant part of solar radiation is reflected from the ground. Thus surface albedo has different effects on the TOA and the surface aerosol forcing.

Fig. 2.6 shows aerosol radiative forcing as a function of the asymmetry parameter and the SSA for the surface albedo equal 0.05 (a, c) and 0.8 (b, d). The AOT in all cases is 0.2. For larger surface albedo (e.g. snow) the TOA (Fig. 2.6a) and the surface (Fig. 2.6c) aerosol forcing is nearly independent on the asymmetry parameter (size of the aerosol). Thus "white" surface aerosol forcing is determined by the absorption of the aerosol layer. For example, outgoing solar radiation at the TOA in not sensitive to the fraction of radiation scattered upward, because radiation scattered forward is mostly reflected by the ground and leaves the atmosphere.

In the case of small surface albedo (e.g. water, chernozem) the size of the aerosol particles is an important parameter for aerosol forcing. Large particles with strong forward pick of the phase function (high asymmetry parameter) have a small effect on the TOA aerosol radiative forcing, because only a residual fraction of the scattered solar radiation is scattered upward. Thus small particles have significantly larger effect on the TOA aerosol forcing. These calculations show that for large particles and the small SSA, aerosol forcing at the TOA can be positive. Similarly, the magnitude of the aerosol forcing at the surface is large for small particles while for large non-absorbing particles (e.g. mineral dust) is close to zero.

Consider the influence of the change of planetary albedo on the surface temperature. For this purpose we assume that the aerosols reduce planetary albedo by 1%. This value corresponds to the aerosol forcing at TOA equal to –3.4 Wm^{-2}. Direct change of the surface temperature is given by Eq. 2.4, where climate sensitivity (Eq. 2.6) may by written as

$$\alpha = \frac{T_s}{4F_{TOA}} \approx 0.3 \text{ K W}^{-1} \text{ m}^2 . \qquad (2.49)$$

Thus direct change of the surface temperature which is defined as a product of the climate sensitivity and radiative forcing is about –1 K. Notice that similar calculations of the surface temperature corresponding to the change of CO_2 over the period 1900-2000, yield its increase of about 0.4 K [*Thomas and Stamnes,* 1999]. These results need two comments. First, we omit in this simple analysis the feedbacks and response time lag; second, aerosol forcing taken into account is larger than the global mean. However as will be shown in this study, the magnitude of the aerosol radiative forcing in local scale can be significantly larger than that assumed above.

3 Outlook of Observations and Modeling of Aerosol Forcing

In this chapter, we describe methods used in this study in order to determine the aerosol radiative forcing. We briefly discuss a radiative transfer model which was used to calculate radiative fluxes with and without aerosol in the atmosphere. The content of this chapter includes information about the kind of data applied to the radiative transfer model such as atmospheric soundings, aerosol optical properties and surface albedo. Also we discuss satellite data used for determination of the solar and infrared radiative fluxes at the top of the atmosphere.

Determination of aerosol forcing is not a straightforward task because there always are aerosols present in the atmosphere and the aerosol-free fluxes can not be directly measured. Therefore, aerosol-free flux must be either calculated using the radiative transfer model or determined empirically with a relatively high degree of uncertainty. One of such empirical method of deriving aerosol forcing [*Conant*, 2000] is based on a difference between a very clean day and a polluted day (a clean day is defined as a day without clouds and little or no pollution). However, during the experiments considered in this dissertation, the AOT was relatively large, which makes it difficult to find a convenient base state. Therefore, the hybrid technique [*Satheesh and Ramanathan*, 2000] was used in this study. In this method, aerosol-free fluxes are obtained from a radiative transfer model. Unfortunately, the calculated aerosol forcing is not zero for zero optical depth (as it should) due to an offset error. This offset depends on the uncertainties of the radiative fluxes observations, errors of the radiative transfer model, parameterizations of the molecular gases absorption, specification of the total ozone and water vapor content. *Satheesh* and *Ramanathan* [2000] used the "slope" method to minimize these errors. The slope of the linear fit to the aerosol forcing versus the AOT is independent of the offset error. This slope defines aerosol forcing efficiency (Eq. 2.13). Notice that the "slope" method is limited to days with similar optical properties, because the aerosol forcing efficiency is a function of the single scattering albedo and scattering phase function. During the MINOS experiment we used two aerosol forcing efficiencies to deal with dissimilar cases.

Our dataset during the ACE-Asia is limited to a few days with small cloud fraction and we used the radiative transfer model together with the aerosol-optical model to calculate radiative fluxes. Subsequently, the aerosol forcing was obtained, which was compared with the results from observational (hybrid) method.

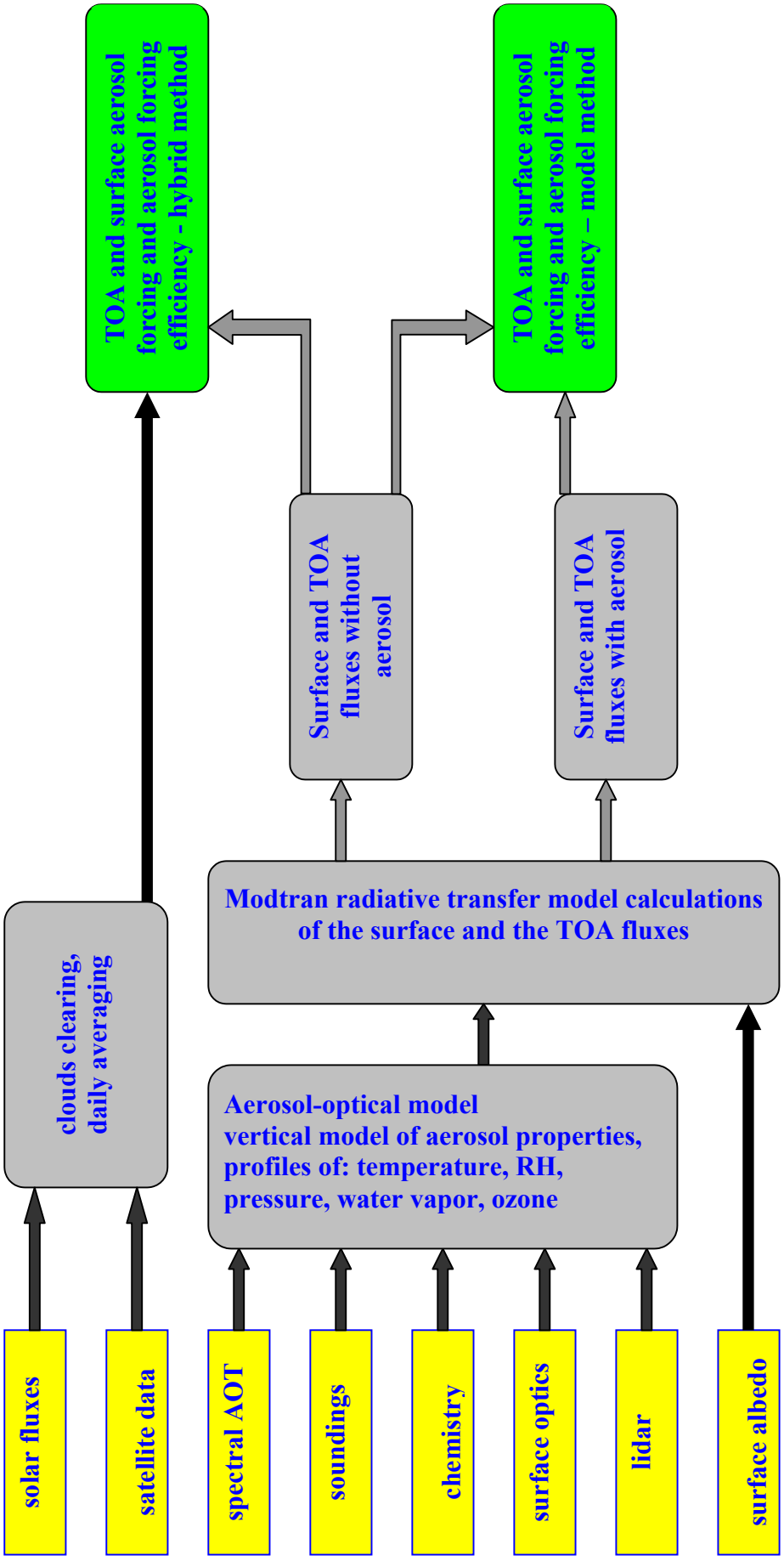

Fig. 3.1 Structure of available data and logic flow for determination of the aerosol forcing.

Fig 3.1 shows the algorithm used for determination the aerosol forcing based on observations and radiative transfer model calculation. Observations include measurements of the downward solar and infrared radiative fluxes at the surface, the spectral aerosol optical thickness, the top of the atmosphere outgoing solar and infrared radiative fluxes from CERES, the atmospheric vertical soundings, the surface aerosol chemistry, the surface aerosol optical properties, the aerosol vertical profiles of the extinction coefficient from lidar and the surface albedo. The aerosol optical properties are calculated by aerosol chemistry. From these data, radiative fluxes necessary to obtain the aerosol forcing are calculated. Aerosol-free fluxes are computed with the aerosol model module switched off.

3.1 Radiative transfer model

Solar and infrared fluxes at the surface and at the TOA were calculated using the MODTRAN (Moderate Resolution Transmittance Code) version 4.1 [*Berk et al.*, 1998]. The MODTRAN calculates atmospheric transmittance and radiance for wave numbers from 0 to 50,000 cm^{-1} at moderate spectral resolutions, primarily 2 cm^{-1} (20 cm^{-1} in the UV). MODTRAN capabilities include spherical refractive geometry, solar and lunar source functions, scattering (Rayleigh, Mie single and multiple) and default profiles (gases, aerosols, clouds, fogs, and rain). The MODTRAN model is a two-parameter equivalent width band model (proportional to temperature and pressure) that employs large pre-stored spectral databases. The databases are derived directly from the spectral line parameters of the HITRAN 2000 [*Rothman et al.*, 1998] database for each of 13 molecular species, and cross sections for the heavy molecules (e.g. CFC's) based on the HITRAN 2000 database. The 4.1 version of MODTRAN has implemented the so called correlated-k algorithm [*Bernstein et al.*, 1996] which facilitates accurate calculation of multiple scattering. This method is used because band model of transmittance (T) do not follow Beer's law and the transmittance for a given layer must be expressed as a weighted (Δg) sum of n exponential terms:

$$T = \sum_{i=1}^{n} \Delta g_i e^{-K_i u} , \tag{3.1}$$

where K_i are monochromatic absorption coefficients and u is the path length (gcm^{-2}) of the absorber. The path length can be written as

$$u = \int_{o}^{s} \rho ds' \tag{3.2}$$

where s is a distance and ρ is the density of the absorber.

The radiative transfer equation in MODTRAN is solved by the discrete ordinate method (DISORT) [*Stamnes et al.*, 1988]. DISORT considers the transfer of monochromatic unpolarized radiation in a scattering and emitting plane-parallel medium, with a specified bidirectional reflectivity (BRDF) at the lower boundary. The medium can be forced by a parallel beam and/or diffuse incidence and/or Planck emission at either boundary. Intensities at user-selected angles and levels are the normal output. These levels need not be subsets of the computational levels necessary to resolve the medium, nor need the angles be subsets of the quadrature angles necessary to perform the integrals over angle.

In this study the MODTRAN was run in the following configuration: for solar and thermal fluxes calculations, bandwidth of 15 cm^{-1} and 1 cm^{-1} was used. The DISORT solver was used with 8 streams, user-specified atmosphere and surface albedo, and user defined aerosol properties including spectral extinction, absorption coefficient, and asymmetry parameter. The scattering phase function was based on the *Henyey-Greenste*in approximation [*Henyey* and *Greenstein,* 1941].

3.2 Atmospheric soundings

Vertical profiles of pressure, temperature, and specific humidity, which are necessary for running the radiative transfer model were taken from atmospheric soundings. During the ACE-Asia soundings from ship were available approximately every 3 hours. During the MINOS campaign only one sounding a day (00 UTC) was available. Vertical profiles of the specific humidity were taken from nighttime soundings, but the total water content was scaled by the water vapor measured by the MICROTOPS (see Appendix A2). Because vertical profiles from soundings were available, usually only up to 15 km, the standard summer mid-latitude profiles were used above this altitude. In addition, the vertical profiles of relative humidity were used to define vertical profiles of the aerosol optical model.

3.3 Surface albedo

Aerosol forcing is sensitive to the surface albedo. During the ACE-Asia experiment the radiative observations were performed on the R/V Ronald H. Brown ship. The sea albedo includes contributions from the Fresnel reflection and small background correction due to phytoplankton contribution. These models are taken from the 6S code (Second Simulation of the Satellite Signal in the Solar Spectrum) and coupled with the MODTRAN program. The white caps contribution as well as that of air bubbles were not modeled. In reality, the white caps could have been modeled, but during the ACE-Asia cruise days with small fraction of clouds were correlated with fairly calm sea and only these days are analyzed.

During the MINOS experiment (see chapter 6) radiation fluxes were observed over the land. However, the aerosol radiative forcing was determined above the sea. Therefore, we used the radiative transfer model to obtain a small correction in observed surface downward fluxes due to the change of the albedo from land to sea. This correction is associated with multiple scattering and is important for estimate of the upward radiative fluxes. For this purpose albedo over the land must be determined. This parameter close to Finokalia station was measured from the King Air plane by two Kipp and Zonen pyranometers. One of them measured downward and another upward broadband fluxes. Basing on flights close to the station we estimated the broadband (0.28-2.8 μm) albedo as 0.15.

3.4 Cloud clearing and daily averaging

Influence of the clouds contamination on the solar fluxes observation was minimized by considering only days with small cloud cover fraction (less then 25%). More than 50% of days during MINOS satisfied this limitation but only 6 days from 5 weeks of the ACE-Asia cruise were that clear. The daily mean aerosol forcing was determined. For this purpose modeled fluxes were calculated from sunrise to sunset for every 30 min.

3.5 Surface chemistry observations

The surface aerosol chemical observations were made during the ACE-Asia. These data which together with vertical profiles of relative humidity and extinction coefficient (from the lidar) define the aerosol-optical model. Details of the chemical measurements will be discussed in chapter 5. Notice that surface chemical composition is extended as height-independent to the whole boundary layer while in the free atmosphere the pollution is treated as mineral dust.

3.6 Aerosol-optical model

Although this dissertation emphasizes observational analyses, the aerosol-optical model and radiative transfer calculations are used to support the data interpretation. The aerosol-optical model is used to determine these aerosol properties, which were not directly measured particularly spectral extinction and absorption coefficients and asymmetry parameters. These parameters are defined for two vertical layers: the first up to 2 km and the second from 2 km up to 10 km. Since in MODTRAM only extinction coefficients are defined as continuous functions of the altitude. The aerosol single scattering albedo and asymmetry parameter are assumed constant in the first and second layer.

3.7 Surface optics

Aerosol optical model was validated by the surface optical observations such as aerosol scattering at 450, 550, and 700 nm and absorption coefficients at 565 nm (see instrumentations setup during the ACE-Asia and the MINOS experiment in chapter 5 and 6). The aerosol forcing is most sensitive to variations of the single scattering albedo which is determined by absorption and scattering.

3.8 Satellite data

The top of the atmospheric radiative fluxes were obtained from the CERES instrument onboard the TERRA satellite. The resolution of the CERES instrument is about 20 km at nadir

position. CERES measures radiances in solar spectrum ($0.3<\lambda<5$ μm), atmospheric window ($8<\lambda<12$ μm), and infrared range ($\lambda>5$ μm) which are converted to fluxes. Radiative fluxes are calculated using the angular distribution models [*Loeb and Kato*, 2002]. For ACE-Asia the Beta 2 SSF CERES data is used. This type of data was not available for the MINOS period and Edition 1 ES-8 of CERES data were used. In ES-8 the radiance is converted to fluxes by ERBE-like angular distribution model [*Loeb et al.*, 2000], which is significantly worse than the SSF product. For example, a dispersion parameter which is defined as the ratio of the albedo standard deviation to the average albedo is about 2.2% for the angular distribution model [*Loeb and Kato*, 2002] and 8.8% for ERBE like product which uses simple relationship between radiance and flux. Except for the angular distribution model, cloud contamination has a large influence on the uncertainties of the CERES retrievals. In this study, only days without clouds (as observed from the ground) were used. In addition, SSF product includes cloud contamination in footprints obtained from a higher-resolution imager such as Moderate-Resolution Imaging Spectroradiometer (MODIS) on the TERRA satellite.

During the ACE-Asia CERES, the footprint and ship position were collocated with maximum deviation of 25 km. In case of the MINOS experiment, the footprint of the CERES instrument was collocated about 30-50 km northwards from Finokalia to minimize influence of island albedo on the observational TOA fluxes. The view angle was limited to less than 60° because for larger angles the angular distribution model includes significant errors.

The instantaneous solar fluxes were converted to diurnal mean values using the MODTRAN radiative transfer model.

4 Indian Ocean Experiment

In this chapter we discuss main results based on the Indian Ocean Experiment (INDOEX). Data presented here come from published papers and our observations performed [*Welton et al.,* 2002] on the NOAA ship Ronald H. Brown. Although our observations during INDOEX were limited to only three instruments (two sunphotometers and the lidar) we found their results interesting enough to justify including item into these dissertation. Observations made during this campaign discovered a dense haze in northern part of Indian Ocean which has significant impact on the solar radiation budget in the atmosphere, at the surface, and at the TOA. In addition we found strong pollution gradient between southern and northern hemispheres as result of the winter monsoon circulation. This makes these data particularly interesting with respect to the main aims of this study.

4.1 Experimental setup

Indian Ocean Experiment (INDOEX) was a large climate experiment involving researchers from many countries including US, India, France, Germany, and Poland. The main goal of the experiment was to study how air pollution affects climate processes over the tropical Indian Ocean. The Indian subcontinent and other parts of Asia, which together have a population of over 2 billion people, and emit a great amount of pollutants that are carried to the Indian Ocean during the northern hemisphere winter by the monsoon winds from the northeast. The INDOEX experiment took place in February and March 1999. This time is ideal to study the role of anthropogenic aerosols in climate change, because during the winter monsoon mineral dust contribution to the total pollution is small. Large pollution in the northern part of the Indian Ocean is caused by growing economic developments in recent decades. Air pollution from Indian subcontinent is advected by the northeast monsoon flow into the Intertropical Convergence Zone (ITCZ) which is located between equator and about 12°S. Because southern air mass is considerably cleaner, one of the most important goals of INDOEX was to exploit the north-south gradients of aerosol optical depth over the Indian Ocean and Arabian Sea, surface solar radiative fluxes and boundary layer aerosol chemical properties. Another important goal of INDOEX was to assess the significance of sulfates and other continental aerosols for the global

radiative forcing and for magnitude of the solar absorption at the surface and in the troposphere including the clouds systems.

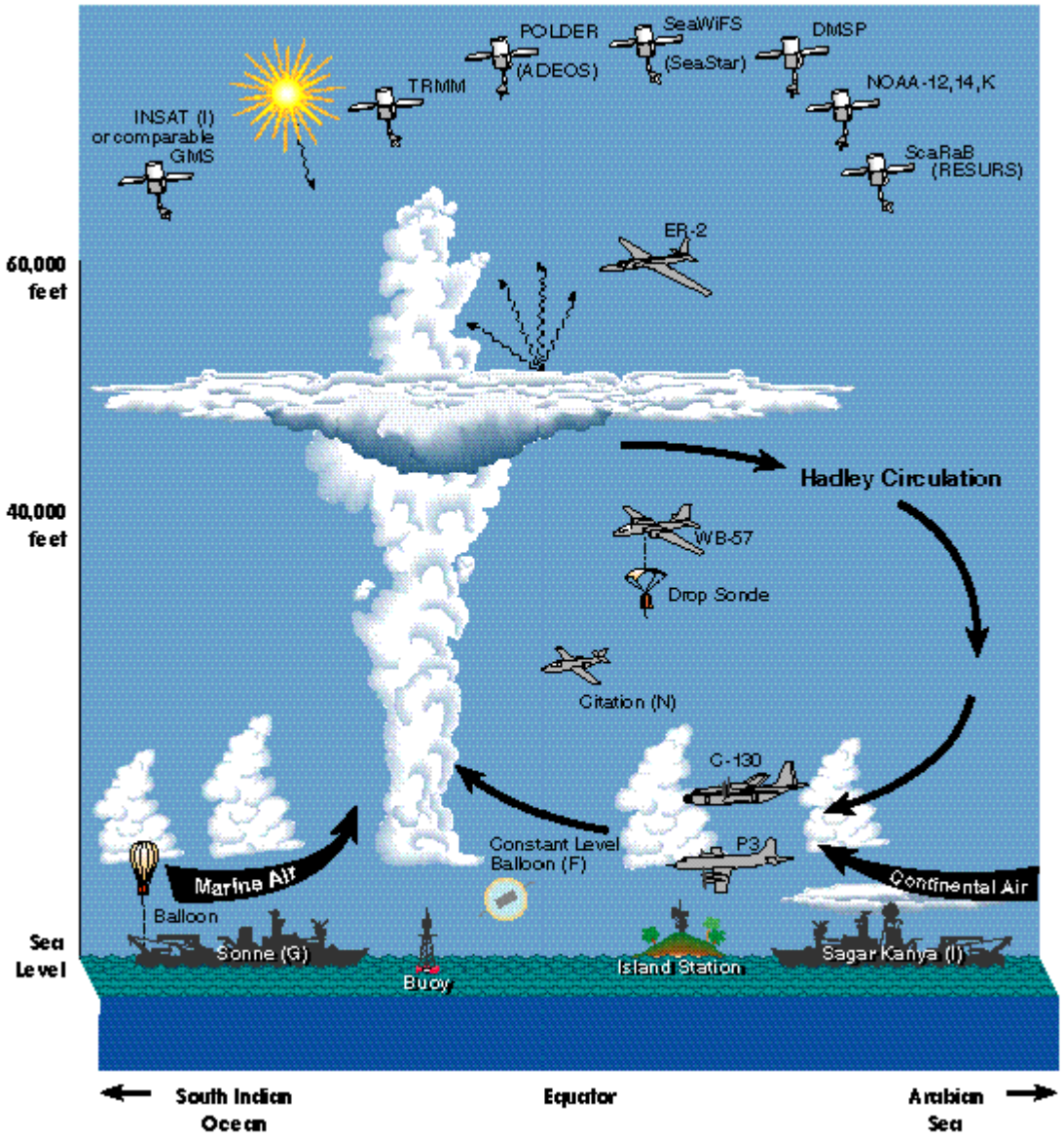

Fig. 4.1 Proposed observing platforms during INDOEX

The INDOEX experiment involved various observational platforms (Fig. 4.1), such as satellites (METEOSAT-5, INSAT, NOAA 14,15 with AVHRR, and TRMM with CERES instrument), two ships (Ronald H. Brown and Sagar Kanya), aircrafts (C-130, Falcon, Citation, and Geophysica), balloons, dropsondes and the surface station at Maldives Kaashidhoo Climate Observatory. Measurements performed during INDOEX comprehended solar radiation fluxes, aerosol optical and chemical properties, aerosol distribution, clouds microphysics, chemical species, vertical profiles of ozone, water vapor and aerosol extinction coefficient, and

meteorological conditions. The author participated in the R/V Ronald H. Brown cruise and deployed (see [*Welton et al.,* 2002]) MICROTOPS (Appendix A3), Lidar (Appendix A2) and SIMBAD instruments which measured the spectral aerosol optical thickness, total columnar water vapor and ozone, vertical profile of aerosol extinction and backscatter coefficient, and water leaving radiance respectively.

4.2 Results

INDOEX findings are documented in two special issues of the Journal Geophysical Research. The results show that air pollutants dramatically impact that region. It was found that a dense brownish pollution haze extended from the ocean surface up to 1 to 3 km altitude. The haze layer covered a lot of the research area almost constantly during the 6-week experiment. The affected area covers most of the northern Indian Ocean including the Arabian Sea, a large part of the Bay of Bengal, and the equatorial Indian Ocean to about 5 degrees south of the Equator. The haze was caused by high concentrations of small particles, with sizes mostly less than one micrometers in diameter. The haze particles were primarily composed of soot (14% of the total aerosol mass), sulfates (32%), organic particles (26%), fly ash (5%) and mineral dust (10%) [*Ramanathan et al.*, 2001b]. Because of this pollution, visibility over the open ocean was often less then 10 km, a range that is typically found near polluted source regions of the United States and Europe. The haze layer contains also relatively high concentrations of gases including carbon monoxide, various organic compounds, and sulfur dioxide. This evidence supports that the haze layer is caused by pollution.

The airborne particles over the northern Indian Ocean are unusually dark because they contain large amounts of soot and other materials from incompletely burned fuels and wastes. Large contribution of black carbon (14%) is typical for INDOEX type of aerosol and causes large solar absorption. The mean single scattering albedo at Kaashidhoo Climate Observatory varied between 0.85 and 0.9 [*Ramanathan et al.*, 2001b]. Airborne particles over the Indian Ocean appear fundamentally different from those over North America and Europe, where advanced pollution control technologies remove much of the dark material and yield particles that are relatively “white”, and have a different effect on radiative processes.

One of the most important results from INDOEX campaign was the finding of significant reductions in the solar radiation, reaching the surface and up to 50% increase in solar heating of the lower atmosphere. The mean daily direct aerosol forcing for clear sky is: -7 Wm^{-2} at the

TOA, -23 Wm^{-2} at the surface, and 16 Wm^{-2} in the atmosphere [*Ramanathan et al.*, 2001b]. For comparison, the mean global value of aerosol forcing at TOA presented in the IPCC report [*Houghton et al.*, 1995] ranges from –0.5 to –2 Wm^{-2}. Aerosol forcing efficiency is also used to estimate the solar radiation budget. This parameter, at the Kaashidhoo Climate Observatory station, was –25 Wm^{-2} at the TOA and –75 Wm^{-2} at the surface [*Satheesh and Ramanathan*, 2000]. Notice that these values include natural and anthropogenic types of aerosol, because they are based on measured (not modeled) solar fluxes. At the TOA direct aerosol forcing under mean conditions (including clouds) is much smaller (-2 Wm^{-2}). At the surface the aerosol forcing was –20 Wm^{-2} and in the atmosphere was 18 Wm^{-2}. Thus, the surface aerosol forcing is about 10 times larger than that at the TOA. Smaller value of the TOA forcing in the case when clouds are present is associated with the aerosol absorption above the tops of the clouds. Because clouds have high albedo a significant part of solar radiation passes by the aerosol layer twice and, therefore, the probability of the photon absorption is larger under cloudy conditions.

INDOEX observations indicated that the dense pollution haze layer was derived from sources at least a thousand or more kilometers away. In contrast to the situation over the northern Indian Ocean, the lower atmosphere over the southern Indian Ocean remained remarkably clean. A narrow zone of deep and towering thunderstorms forming over the warmest part of the equatorial ocean the ITCZ, intercepts polluted air masses and removes much of the pollution in rainfall. But the deep convective ITCZ clouds move substantial amounts of pollutants into the upper atmosphere where they can be spread over large areas. A large gradient of pollution between the clear southern hemisphere and the hazy condition over the Arabian Sea was observed during the R/V Ronald H. Brown ship cruise (Fig. 4.2). On the southern side of the ITCZ the aerosol optical thickness (at 500 nm) ranged from 0.05 to 0.1. A significant increase of the AOT was measured north of about 5°S (maximum strength of the ITCZ), but the maximum of AOT was observed about 5°N and exceeded 0.4 at 500 nm. A strong gradient of the AOT in the northern hemisphere is associated with the stable northeast trades in the boundary layer, which transport pollution from the Indian subcontinent. Thus, atmospheric circulation strongly affects aerosol distribution over the Indian Ocean.

Observations during the first field phase of INDOEX (Feb, Mar 1998) show that aerosol concentration has daily and annual variability. In winter of 1998 the AOT at 500 nm was about two times smaller than during the INDOEX experiment [*Satheesh and Ramanathan*, 2000; *Satheesh et al.*, 1999]. However this change was not correlated with the strength of winter monsoon. Thus, the significant increase of pollution during INDOEX seems not associated with

the transport of aerosols from main sources (Indian Subcontinent) towards the southern hemisphere.

In summary, the INDOEX measurements show that the impact of Asian pollution on climate processes appear to be fundamentally different from that of North American or East Asian pollution. It appears that the large absorption by the haze layer has a significant impact on the regional radiation balance with potential indirect consequences of haze involving regional and global climate and the water cycle [*Ramanathan et al.*, 2001a]. Another indirect effect of this "Asian Brown Cloud" such as cooling of the land surface may increase frequency and strength of thermal inversions that traps more pollution, evaporation reduction, and causes disruption of the monsoon rainfall patterns.

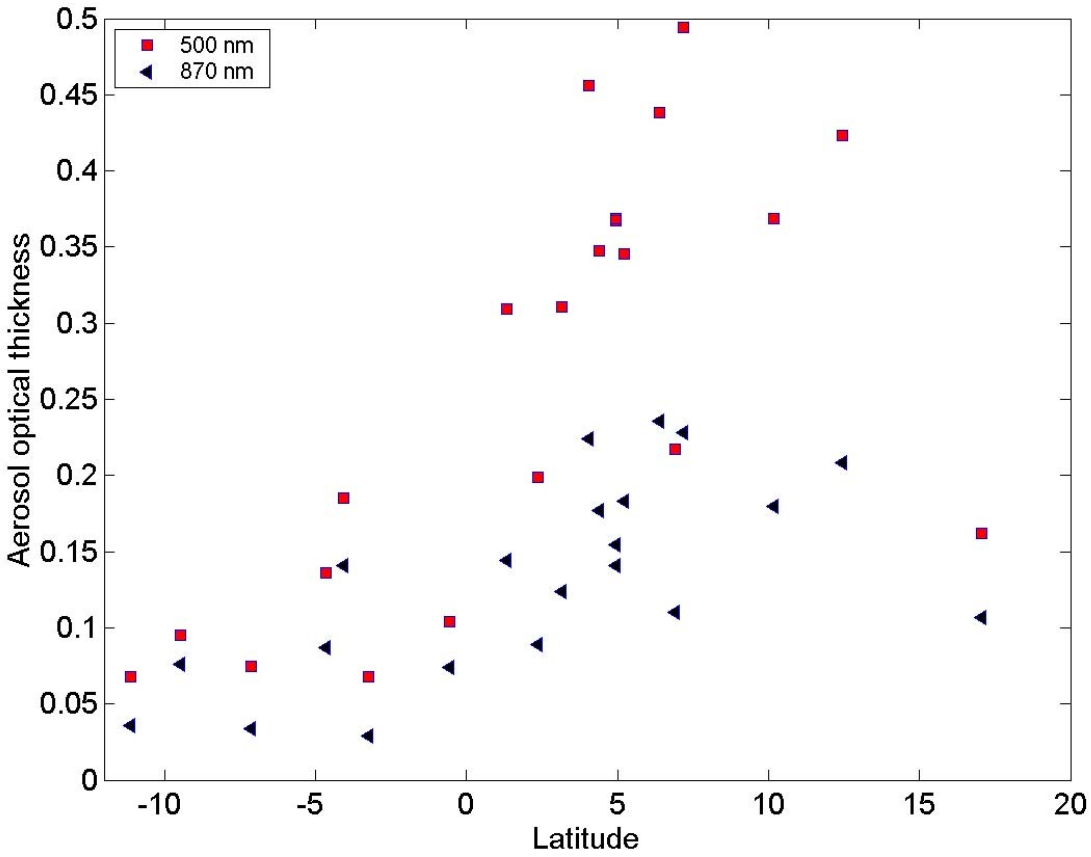

Fig. 4.2 Aerosol optical thickness at 500 nm (squares) and 870 nm (triangles) as a function of the latitude during R/V Brown ship cruise during INDOEX (Feb, Mar 1999).

5 Solar and Infrared Aerosol Forcing During ACE-Asia Experiment[7].

This chapter presents a brief overview of the ACE-Asia objectives, instrumentations and sources of data used in this study. We present direct radiometric observations of the aerosol forcing taken from the NOAA ship, Ronald H. Brown, as well as, the aerosol optical properties measured in the solar spectrum and modeled in the infrared (atmospheric window) range.
One of important results of this study is the analysis of the influence of the relative humidity on the aerosol forcing efficiency. We show that decreasing the relative humidity to 55% enhances the aerosol forcing efficiency by as much as 6 to 10 Wm^{-2}. This dependency on relative humidity has implications for comparisons of aerosol forcing efficiencies between different geographical locations.

In this chapter we also present infrared radiative forcing related to the aerosol optical properties in infrared. These results are based on aerosol optical properties measurements in the visible spectrum combined with chemical observations and mathematical modeling. Such studies are rare in recent research. Our results are new and provide interesting results, particularly at the TOA. For example, mean infrared aerosol optical thickness at 10 μm during ACE-Asia cruise was 0.08 and the single scattering albedo was 0.55. It was shown that because of the relatively large single scattering albedo (in the atmospheric window) aerosol scattering in infrared is important and cannot be neglected contrary to what some recent studies are suggesting. We define a new parameter called “infrared aerosol forcing efficiency” which provides a useful tool for describing the infrared aerosol impact on climate systems. This study shows the infrared aerosol forcing is a considerable component of both the surface and the TOA radiative forcing.

[7] Text of this chapter comes from two papers:
K.M, Markowicz, P.J. Flatau, P.K. Quinn, C.M. Carrico, M.K. Flatau, A.M. Vogelmann, D. Bates, M. Liu, and M.J. Rood, Influence of Relative Humidity on Aerosol Radiative Forcing: An ACE-Asia Experiment Perspective, *J. Geophys. Res.*, 2003 (in press).

K.M., Markowicz, P.J. Flatau, A.M. Vogelmann, P.K. Quinn, and E.J. Welton, Infrared aerosol radiative forcing at the surface and the top of the atmosphere., *Quarterly Journal of the Royal Meteorological Society*, 2003 (in press).

For example, the infrared aerosol forcing at the TOA can go up to 19% of the solar aerosol forcing.

5.1 Objectives

The Aerosol Characterization Experiment (ACE-Asia, Fig. 5.1.) took place in March and April of 2001 and was designed to study the complex outflow of mineral dust and air pollution from Asia at mid-latitudes. The East Asian coastal region is characterized by anthropogenic emissions that are already high in many localities and are rapidly growing throughout much of the region. The Asia/Western Pacific region has a unique mixture of aerosols and trace gases because of these distinctive patterns of emissions in combination with particular meteorological conditions affecting this region.

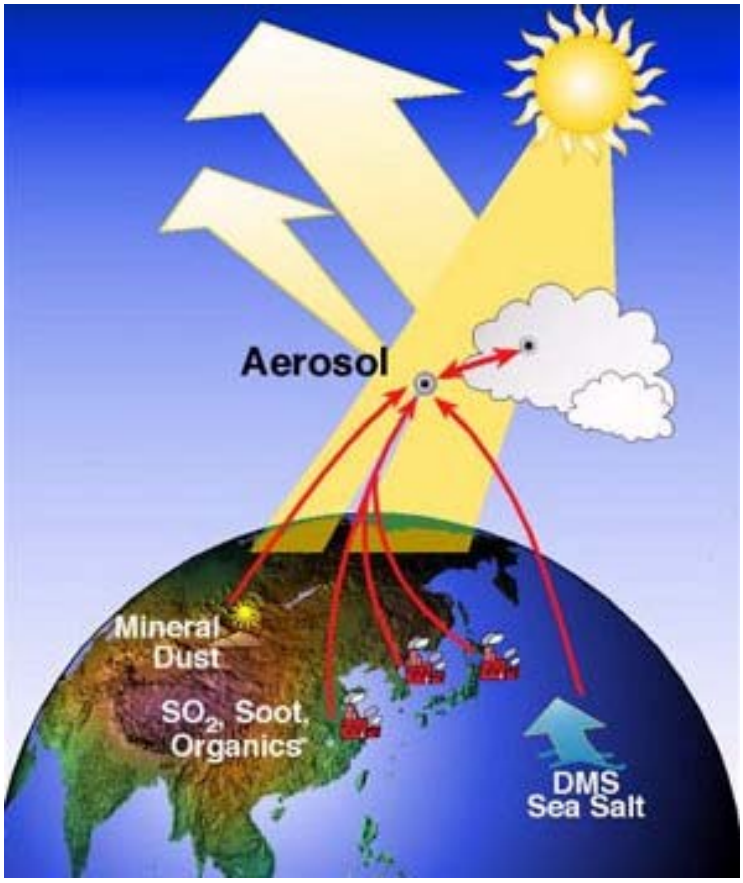

Fig. 5.1 ACE-Asia experiment logo. The experiment took place in March and April of 2001.

Mineral dust, gaseous, and particulate pollutants from the Asian continent are transported eastward over the Pacific, especially in the spring, and the effects of these materials are widespread. Similarly, recent modeling studies indicate that increasing emission from fossil fuel

combustion in Asia will affect surface ozone concentrations in the United States [*Jacob et al.,* 1999]. The ACE-Asia project focused on outflow from Asia with the goals of (1) determining the physical, chemical, and radiative properties of the major aerosol types in the Eastern Asia and Northwest Pacific region and investigating the relationships among these properties, (2) quantifying the interactions between aerosols and radiation in the Eastern Asia and Northwest Pacific region, (3) quantifying the physical and chemical processes controlling the evolution of the major aerosol types and in particular of their physical, chemical, and radiative properties.

The ACE-Asia project includes observations from different platforms. In-situ and column integrated measurements at a network of ground stations quantified the chemical, physical and radiative properties of aerosols in the ACE-Asia study area and assessed their spatial and temporal (seasonal and intra-annual) variability. In addition, during the ACE-Asia, research was performed from ships (NOAA R/V Ronald H. Brown and two Japanese ships Hakuho and Mirai) and airplanes (Twin Otter, C-130, and King Air). Observations were correlated with satellites such as TERRA, SeaWIFS, and NOAA with AVHRR.

Spring time in the South Eastern part of Asia and in the Western Pacific Ocean is dominated by extra tropical cyclonic activity which leads to long distance transport of pollution over the Pacific Ocean. Notice that climatologically, over the south part of Japan, there is a jet stream maximum where wind speed exceed 70 m/s. The cyclonic activity limited clear days suitable for radiometric work to only 6 days.

The author participated in the ACE-Asia project on board of the NOAA research vessel R/V Ronald H. Brown and the content of this Chapter refers mostly to his research prepared during this cruise.

5.2 Instrumentations on the NOAA Ship R/V Ronald H. Brown

During the ACE-Asia field project on board of the NOAA research ship Ronald H. Brown (Fig. 5.2) a number of radiation measurements were performed. Total broadband (280-2800 nm) radiative fluxes were obtained using CM21 Kipp and Zonen pyranometers (see Appendix A1). To minimize the ship's pitch and roll the pyranometers were mounted on gimbaled (moving) suspension. The total infrared radiative fluxes (3.5-50 μm) were obtained using the broadband, hemispheric view, precision IR radiometer pyrgeometer (PIR, Eppley). According to the technical specifications provided by the manufacturer this instrument has an absolute accuracy of ±2 %.

The Fourier Transform Infrared (FTIR) radiometer [*Minnett et al.*, 2001] measured the sky radiance during the cruise; its design is based on the Atmospheric Emitted Radiance Interferometer (AERI) [*Revercomb et al.*, 1988]. The Marine-AERI (M-AERI) measured the sky radiance from 520 to 3020 cm^{-1} (about 18 to 3 μm) at ~0.5 cm^{-1} resolution. *Vogelmann et al* [2003] developed a methodology that determined the IR aerosol forcing in the 10 μm window from the M-AERI measurements. These observations were used here to test aerosol IR model.

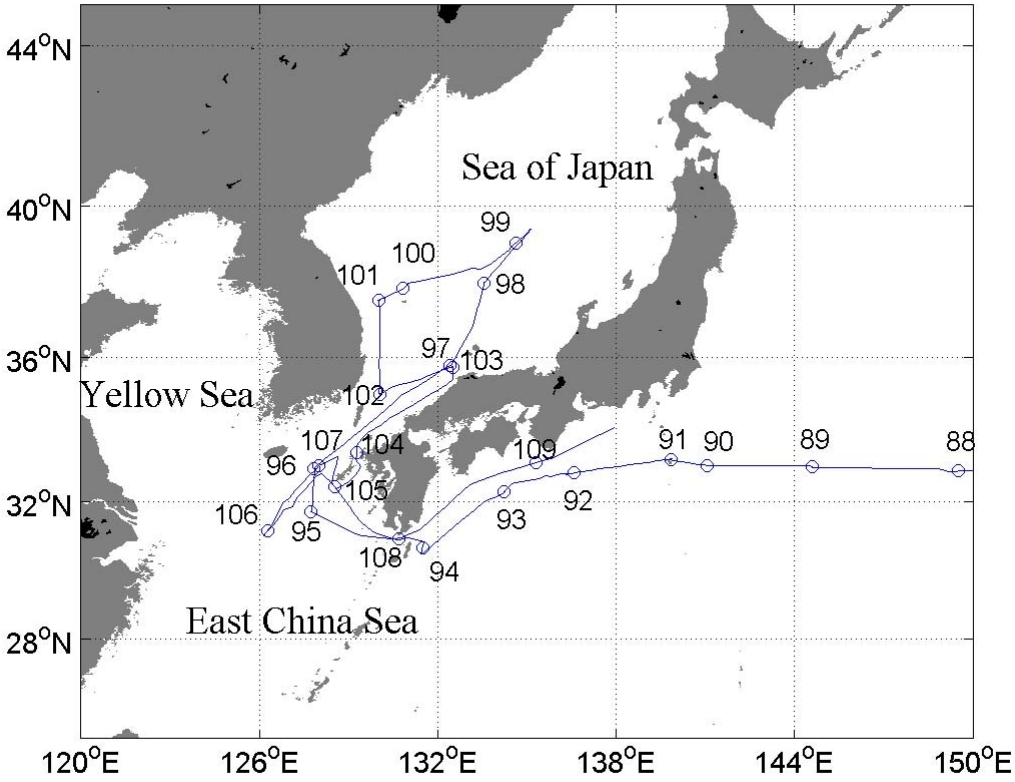

Fig. 5.2 NOAA Ship Ronald H. Brown track during the ACE-Asia cruise between Honolulu and Yokosuka in March and April 2001.

Two handheld Microtops II (Sunphotometer and Ozonometer) [*Morys et al.*, 2001] with spectral filters for visible and near-infrared (NIR) wavelengths were used to retrieve aerosol optical thickness, columnar water vapor, and columnar ozone. The AOT was measured at 380, 440, 500, 675, 870 nm by the Sunphotometer (see Appendix A3) and at 1020 nm by the Ozonometer. The total water column was obtained from the sun radiance measured at 936 nm and 1020 nm.

Vertical profiles of the aerosol extinction coefficient at 523 nm were measured by a micropulse lidar (MPL) [*Welton et al.*, 2000]. The vertical resolution of this instrument is 75m.

The aerosol extinction coefficient was obtained from the calibrated lidar signal and the Microtops observations of the AOT.

Concentrations of chemical components in the sub- and supermicron[8] size ranges were determined by NOAA's Pacific Marine Environmental Laboratory (PMEL). The analyzed components include sea salt, sulfate, nitrate, total organic carbon, elemental carbon, and dust. The last 1.5 m of the mast on which the samples were collected was heated to establish a stable reference RH for the sample air equal to 55 ± 5%. A stable reference RH allows for constant instrumental size segregation in spite of variations in ambient RH, and results in chemical, physical, and optical measurements that are directly comparable. In addition, measurement at a constant reference RH enables the end users of the dataset (process, chemical transport, and radiative transfer models) to adjust the measured parameters to desired relative humidity, provided the appropriate growth factor are known. A reference RH 55% was chosen because it has been shown to reduce the impactor bounce (since there is enough water associated with the hygroscopic aerosol species at this RH to make the aerosol "sticky"). In addition, for the atmospheric conditions encountered during Ace Asia, it was possible to maintain 55% RH without excessive heating of the aerosol.

The methodology of the chemical analysis is described elsewhere [*c.f. Quinn et al.*, 2001; *Quinn et al.*, 2002a, *Quinn et al.,*2002b]. Chemical species were divided into several groups according to their physical properties: sulfate and nitrate aerosol mass, sea-salt mass, total organic carbon, elemental carbon, and dust. The concentration of dust was derived assuming that all elements were in their common oxide form [*Malm et al.*, 1994]. The particulate organic matter (POM) was determined from the measured organic carbon concentration and the expression POM=2.1xOC (μg m^{-3}) [*Turpin and Lim*, 2001]. On the basis of these mass concentrations, the optical properties of aerosols were deducted accounting for its chemical composition.

The aerosol absorption coefficient at the surface was obtained from the Particle Soot Absorption Photometer (PSAP) produced by Radiance Research [*Bond et al.*, 1999]. Measured values were corrected for the scattering artifact, the deposit spot size, the PSAP flow rate, and the manufacturer's calibration. Values are reported at 550 nm. Sources of uncertainty in the PSAP measurement include noise, drift, correction for the manufacturer's calibration and correction for the scattering artifact [*Bond et al.*, 1999]. A rms follows from these errors yields absolute uncertainties of 0.38×10^{-6} m^{-1} and 0.68×10^{-6} m^{-1} for an absorption coefficient equal to

[8] Submicron and supermicron refer to all particles with aerodynamic diameters less than 1 μm and between 1 and 10 μm, respectively, at 55% relative humidity (RH).

$2.8x10^{-6}$ m^{-1} and $13x10^{-6}$ m^{-1}, respectively, for a 30 minute averaging time. Measurements of aerosol scattering and hemispheric backscattering coefficients were made with an integrating nephelometer (Model 3563, TSI Inc.) at wavelengths of 450, 550, and 700 nm at 55 ± 10% RH and sub-10 micron (particles with diameter less than 10 μm) data were used. The RH was measured inside the nephelometer sensing volume. Values measured directly by the nephelometer are corrected for an offset determined by measuring filtered air over a period of several hours [*Anderson and Ogren*, 1998]. In addition, they were corrected for the angular non-idealities, including truncation errors and non-lambertian response of the nephelometer as per *Anderson and Ogren* [1998].

The PMEL PSAP and nephelometer were also kept at 55 ± 10% relative humidity. In addition, the aerosol light scattering as a function of relative humidity, was measured using controlled relative humidity nephelometry (humidograph) [*Carrico et al.*, 1998]. The aerosol sample was scanned from an RH of 35 to 85% over an hourly cycle time while continually measuring the aerosol light scattering at 450, 550, and 700 nm. To investigate hysteresis effects from meta-stable droplet formation, RH scans were performed with increasing RH beginning with a "dry" aerosol and with decreasing RH beginning with a hydrated aerosol [*Carrico et al.*, 2000]. Data from both increasing and decreasing RH regimes were used in this study.

The top-of-atmosphere fluxes were obtained from the CERES instrument onboard the TERRA satellite (the resolution of CERES is 20 km at nadir). The data from CERES instrument was available about 10:30 local time.

5.3 Aerosol-optical model

Although the solar aerosol forcing in this study is in principle determined from analysis of observational data, aerosol-optical model and radiative transfer calculations (MODTRAN version 4.1) were used to support the data interpretation. After its validation, the aerosol model is used to determine properties that could not be measured directly. For example, the aerosol model was used to derive the top of the atmosphere forcing for days when CERES data were not available. Also, because observational dataset is limited, the radiative transfer model results were used to help determine the effects of relative humidity on the aerosol forcing results.

Aerosols were divided into seven types: water-soluble, soot, sea salt accumulation and coarse modes, mineral dust accumulation and coarse modes, and sulfate. The "soluble" categories are: (a) nitrate and POM, and (b) sulfates (they differ because different humidity

growth factors are assumed). The "soot" category includes elemental carbon. The mass of the "dust" category is defined as Mass=2.2Al+2.49Si+1.63Ca+2.42Fe+1.94Ti with numerical factors adjusted such that the major elements in dust are converted to their common oxide form [*Malm et al.*, 1994].

Aerosol optical properties as a function of the relative humidity and wavelength (from 0.25 to 200 μm) were obtained from aerosol-optical database (see Appendix C for more details). The soluble, soot, and sulfate types of aerosols (which are generally small) are defined by only one single lognormal size distribution (Table C.2). The sea salt and dust particles are described by two lognormal size distributions (accumulation and coarse mode).

This aerosol optical model is based on OPAC/GADS [*Hess et al.*, 1998] and HAWKS 2000 [*Rothman et al.*, 1998] but offers more flexibility. In this study, all calculations of the aerosol optical properties were performed for an external mixture based on Mie code [*Bohren and Huffman*, 1983].

The aerosol chemical composition is assumed to be altitude independent up to 3 km but the vertical optical properties change with height because of the humidity variability. In the upper layer (above 3 km), the aerosol optical model includes only dust particles, which is consistent with the numerical simulations performed by the COAMPS/Navy Transport Model and MPL lidar observations, which show layered dust structure for YD99 onwards. The optical thickness and vertical structure of these two layers were obtained from the MPL lidar measurements at wavelength 523 nm.

The optical properties determined in the way described above and in Appendix C are used in radiative transfer calculations to compute the radiative fluxes at the surface and TOA. For these calculations, we need the vertical distributions of the aerosol extinction coefficient, absorption coefficient, and asymmetry parameter as functions of wavelength. The averages of these scattering properties are determined from our model for two layers (0-3 km, 3-10 km) as

$$\left\langle \tilde{\sigma}_{ext}(\lambda) \right\rangle = \frac{\int \sigma^{550}{}_{ext}(z)\tilde{\sigma}_{ext}(\lambda, RH(z))dz}{\int \sigma^{550}{}_{ext}(z)dz} \tag{5.1}$$

$$\left\langle \tilde{\sigma}_{abs}(\lambda) \right\rangle = \frac{\int \sigma^{550}{}_{ext}(z)\tilde{\sigma}_{abs}(\lambda, RH(z))dz}{\int \sigma^{550}{}_{ext}(z)dz} \tag{5.2}$$

$$\left\langle g(\lambda) \right\rangle = \frac{\int \sigma^{550}{}_{\mathrm{ext}}(z)g(\lambda, RH(z))\omega(\lambda, RH(z))dz}{\int \sigma^{550}{}_{\mathrm{ext}}(z)\omega(\lambda, RH(z))dz} \tag{5.3}$$

where $\sigma^{550}{}_{ext}(z)$ is the lidar vertical profile of aerosol extinction coefficient scaled by aerosol optical thickness, $\tilde{\sigma}_{ext}(\lambda, RH(z))$ and $\tilde{\sigma}_{abs}(\lambda, RH(z))$ are the spectral and relative humidity functions of the extinction and absorption coefficients normalized to extinction at 550 nm, $\omega(\lambda, RH(z))$ is the single-scattering albedo, and $g(\lambda, RH(z))$ is the asymmetry parameter. The aerosol-optical model has both advantages and limitations. The next section shows that the predictions of this model, based on the aerosol-optical database (Appendix C) and measured chemistry, agree with some of the inherent and derived optical properties that are observed independently of the model.

5.4 Solar aerosol forcing

5.4.1 Aerosol optical thickness and single scattering albedo

The aerosol optical thickness and single scattering albedo are important parameters for determining the aerosol forcing at the surface, in the atmosphere, and at the top of the

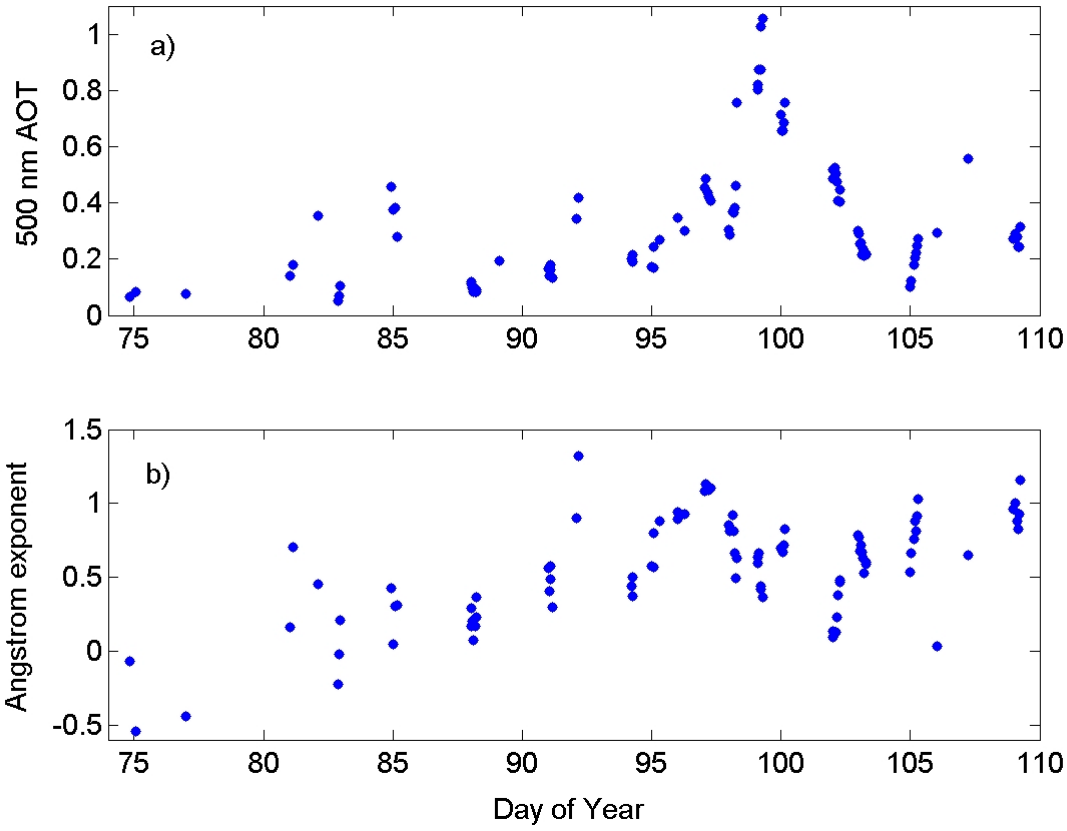

Fig. 5.3 Temporal variation of (a) aerosol optical thickness (AOT) at 500 nm and (b) Ångstrom exponent

atmosphere over the low-albedo surface of the ocean. Fig. 5.3a shows the variation in AOT at 500 nm during the cruise (March and April of 2001). The AOT ranges from 0.05 to 1 and has significant daily variability. The lower value of AOT, observed during the first part of the cruise, is associated with clear marine air masses of the central Pacific Ocean. Only during YD85, after the frontal passage, we measured large AOT in the marine air mass, with values reaching about 0.45 in the morning and 0.3 later in the afternoon. Independently, we also observed a large aerosol infrared forcing ($4.5\pm0.7\ Wm^{-2}$) using a Fourier Transform Interferometer (FTIR) [*Vogelmann et al.*, 2003]. This is reported here only to stress that the YD85 large optical depth was indeed present. Sea salt and non-sea salt sulfates were important components of the aerosol during that day, as confirmed by the chemical composition analysis [*Quinn et al.*, 2002a] but their abundance values at the surface was not large enough to justify such a high AOT.

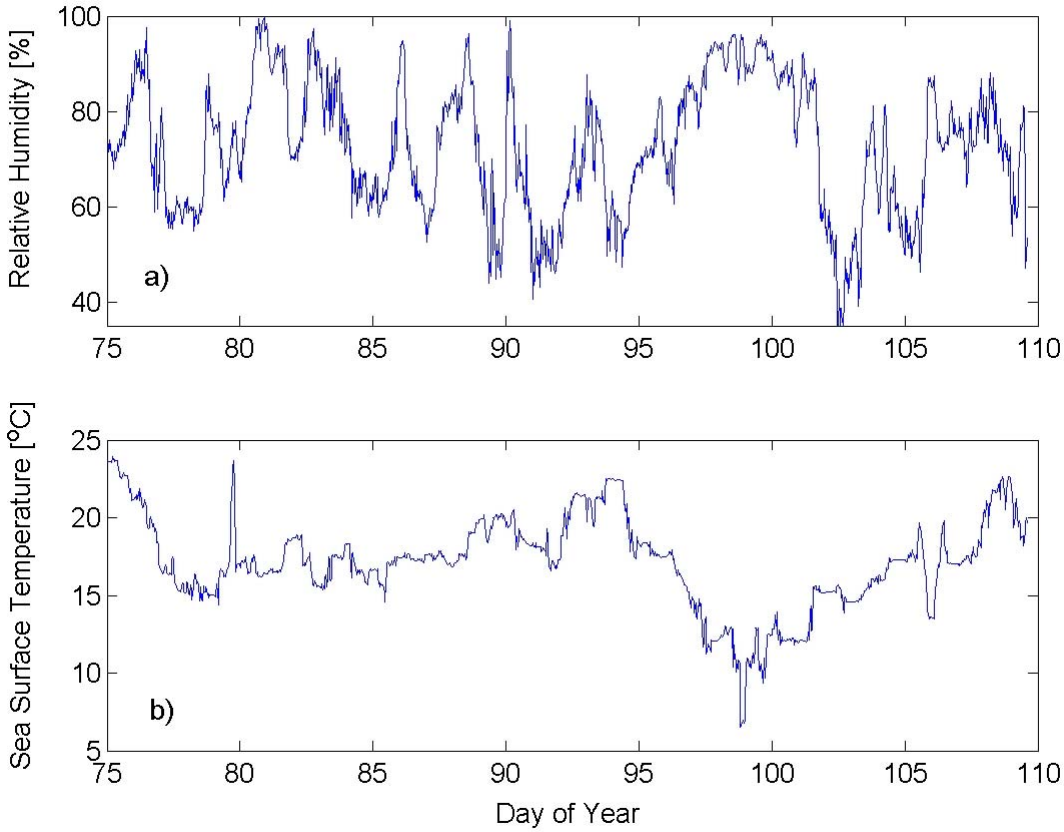

Fig. 5.4 (a) Surface relative humidity and (b) sea surface temperature during the ACE-Asia cruise.

A numerical simulation based on the GOCART model (Mian Chin, private communication) indicates that there was dust at the top of the boundary layer for that day and approximately half of the AOT is attributed to dust. This is interesting, but not unexpected, to see dust transported so

far from Asia. Thus, we interpret an increase of the AOT above the background (by about 0.2-0.3) as being associated with dust at the top of the boundary layer. The largest AOT (close to 1) was measured in the Sea of Japan during YD99 and was associated with high relative humidity of about 95% at the surface (Fig. 5.4a). However, the middle atmosphere was dry and the total columnar water vapor was only about 1.4 g/cm^2. During that day the visibility at the surface was poor, which made it difficult to detect thin clouds covering the sun.

The Ångstrom exponent (α in $\tau = \beta\lambda^{-\alpha}$, evaluated for wavelengths between 500-1020 nm) is shown in Fig. 5.3b for the ACE-Asia cruise. Large α are associated with small particles. Its negative values over the central Pacific Ocean correspond to clean marine air masses with a small fraction of submicron particles. Between YD97 and YD103, mineral dust aloft had significant influence on the optical properties of aerosol as follows from the small Ångstrom exponent. However, this is not directly observed in the surface chemistry until YD101 because the dust gradually descended towards the surface. The upper layer dust event between YD99 and YD101 is seen on the US Navy's (COAMPS) transport model (Fig. 5.5).

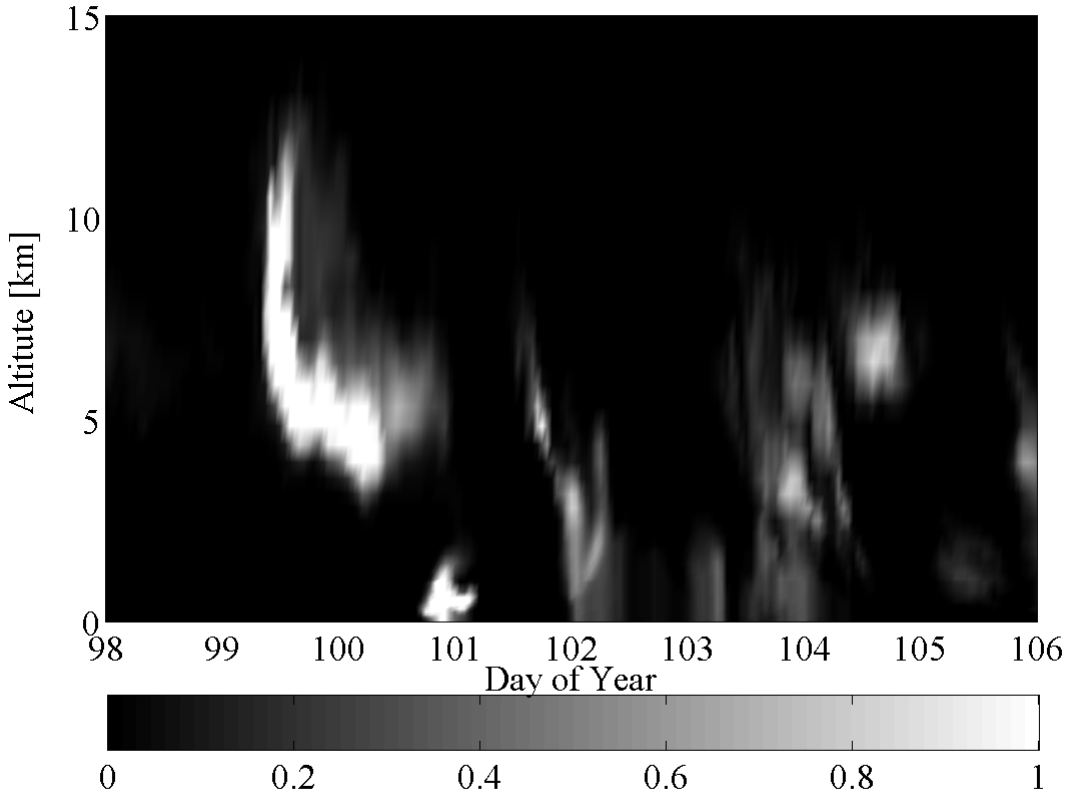

Fig. 5.5 Extinction coefficient in arbitrary units obtained from US Navy's (COAMPS) transport model. The model results were interpolated to NOAA Ship *R. H. Brown* position.

The dust layer spread from 4 to 13 km with the maximum of extinction coefficient about 5 km. YD102 was dominated by dust in boundary layer; in the morning the mass fraction of dust for particles less then 10 μm in diameter was about 85% and in the afternoon about 55%. The decrease of dust concentrations at the surface correlated with decrease of the AOT and increase of the Ångstrom exponent (Fig. 5.3a and Fig. 5.3b).

Fig. 5.6 shows the single-scattering albedo (SSA) obtained by three independent methods. The solid blue line represents the SSA for ambient RH, based on the total scattering determined by the humidograph nephelometer method, and absorption determined by the PSAP instrument. Note that the absorption coefficient was measured at RH 55% and the SSA for ambient RH was calculated assuming that RH has a negligible influence on the absorption

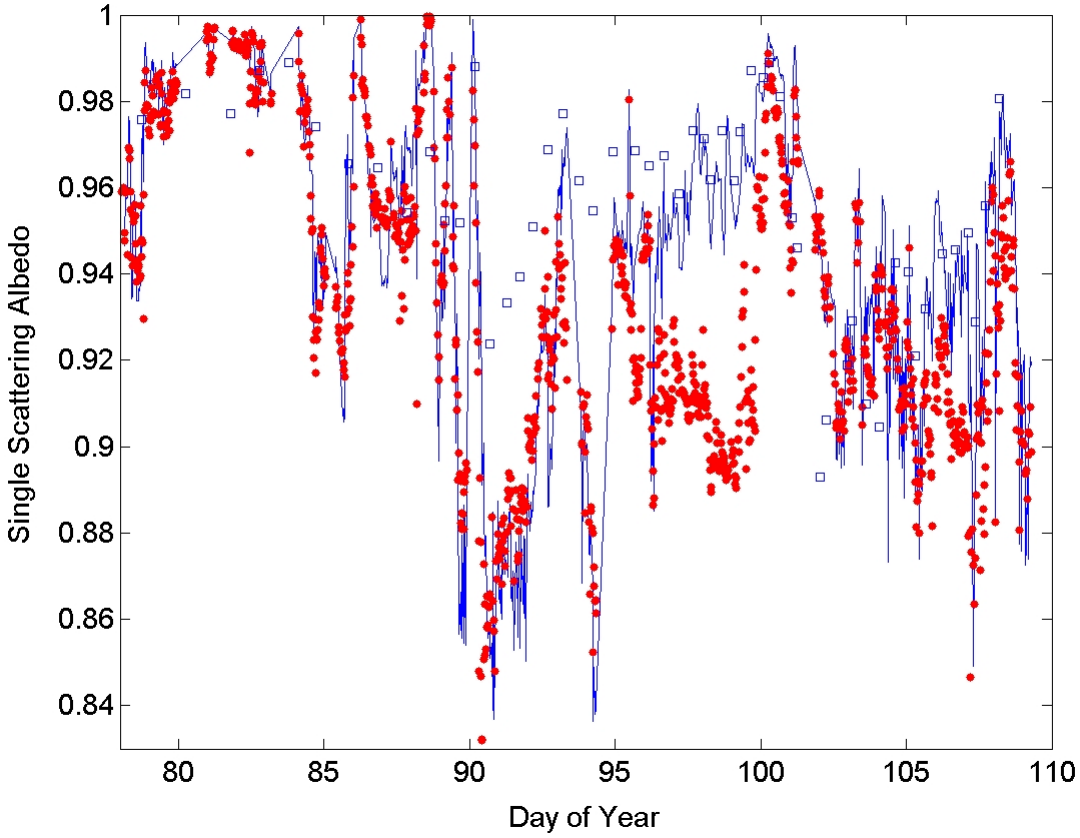

Fig. 5.6 Single scattering albedo (SSA) obtained from three independent methods: The solid blue line represents the SSA for ambient RH, based on the total scattering determined by the humidograph nephelometer method and absorption determined by the PSAP instrument (the PSAP absorption data were not corrected for changes in RH=55%); solid red circles are the PMEL nephelometer and PSAP-based SSA at 55% relative humidity; and blue squares give the SSA calculated from our aerosol-chemical model at ambient RH.

coefficient. The solid red circles are the PMEL nephelometer and PSAP-based SSA at 55% relative humidity, and the blue squares are the SSA calculated with our aerosol-chemical model

at ambient RH. During the first part of the cruise, the SSA was conservative (close to 1) because the aerosol was dominated by non-absorbing sea-salt and sulfates. SSA decreased from 0.98 to 0.87 on YD90 due to an increase in absorption, decrease in scattering, and low ambient RH. The low RH was associated with the passage of the cold front and a cooler and drier air mass (relative humidity decreased to 50% and temperature decreased by 10ºC). During that event, the decrease in RH (Fig. 5.4a) correlated with an almost four-fold decrease in the sea-salt mass concentration, which dominated the decrease in soot concentration and yielded lower SSA.

Another example, showing the correlation between the SSA and RH, can be seen between YD96 and YD99. The SSA observed at ambient conditions (solid line) and calculated from the model (squares) increased due to increasing relative humidity, but the SSA observed at a constant relative humidity of 55% decreased. This leads to a large SSA difference of 0.06 on YD99 between the constant 55% and ambient RH cases. This large increase of relative humidity was measured only in the first several hundred meters above the sea surface, and was associated with decreasing sea surface temperature (Fig. 5.4b) as we were sailing North (Fig. 5.2).

For days YD100 toYD102, all three methods show good agreement despite the large range of relative humidity values. The Navy transport model Fig. 5.5 indicates for YD100-YD101 dust aloft, which descended and increased concentrations at the surface, and YD102 was governed by a transition to low humidity with dust at the surface. This indicates a smaller effect of humidity on SSA for dust-influenced aerosols when the presence of dust is accompanied by relatively dry air.

Fig. 5.7 shows the SSA as function of relative humidity based on the humidograph measurements of scattering at ambient RH and PSAP measurements of absorption at constant RH=55% for the section of cruise in the Sea of Japan. Squares on Fig. 5.7 show SSA as a function of the RH for particles with diameters $D \leq 10$ μm. Triangles show the same relationship but only for particles with diameters $D \leq 1$ μm. There is a significant correlation between the SSA and relative humidity ($r^2=0.69$), and the observations clearly show an increase of SSA with relative humidity. This effect is important for the aerosol forcing efficiency, which will be discussed later. Influence of the RH on the SSA is larger for smaller particles, because a significant part of the supermicron particles are non-hygroscopic dust.

Because the aerosol light scattering was measured as a function of relative humidity [*Carrico et al.*, 1998], we can plot single-scattering albedo with increasing RH beginning with a "dry" aerosol, and with decreasing RH beginning with a hydrated aerosol [*Carrico et al.*, 2000]. This is on the same figure, where single-scattering albedo is plotted for almost simultaneous times (separated by approximately ½ hour) but for "up" (open points) and "down" (dotted point)

relative humidity changes, while assuming that absorption does not change with RH. For small RH the SSA, and, consequently, aerosol forcing efficiency, depends not only on its absolute value, but also on its time change, which may be governed by the air mass transformation. Such transformations may be related to large scale subsidence, frontal passages, or advection over a colder surface. However, in the following, we do not differentiate between the "up" and "down" RH changes because we are focusing on the first-order effects of the relative humidity changes.

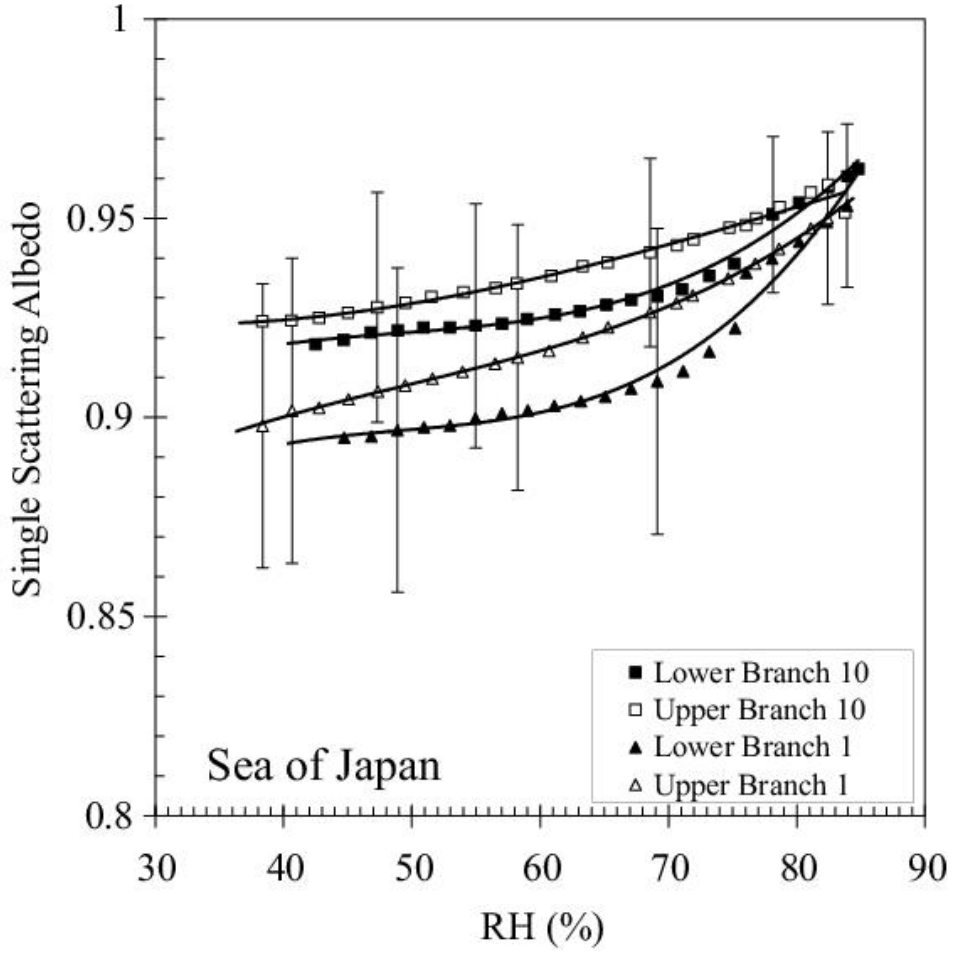

Fig. 5.7 The single scattering albedo from the humidograph as a function of relative humidity in the Sea of Japan. The squares points correspond to particles with diameter D≤10 μm and triangles correspond to submicron particles (D≤1 μm). Open points mark the single- scattering albedo measured by humidograph during "up" and dotted points during "down" relative humidity changes.

The mean value of SSA over the Sea of Japan is 0.95 at ambient condition and 0.92 at 55 % of RH. These values are consistent with SSA derived from recent global model estimates [*Takemura et al.*, 2002], and are larger (smaller absorption) than those observed over the Arabian

Sea (SSA=0.89) [*Ramanathan et al.*, 2001b] and the Mediterranean Sea (SSA=0.87) [*Markowicz et al.*, 2002].

5.4.2 Direct estimate of surface and top of the atmosphere aerosol forcing

Fig. 5.8a shows the daily mean aerosol forcing at the surface as a function of the AOT at 500 nm. Circles represent the aerosol forcing based on observations, and the solid line is a linear fit to these points. Notice that aerosol forcing is not zero for zero optical depth (as it should) due to offset errors in the observations and in the modeling.

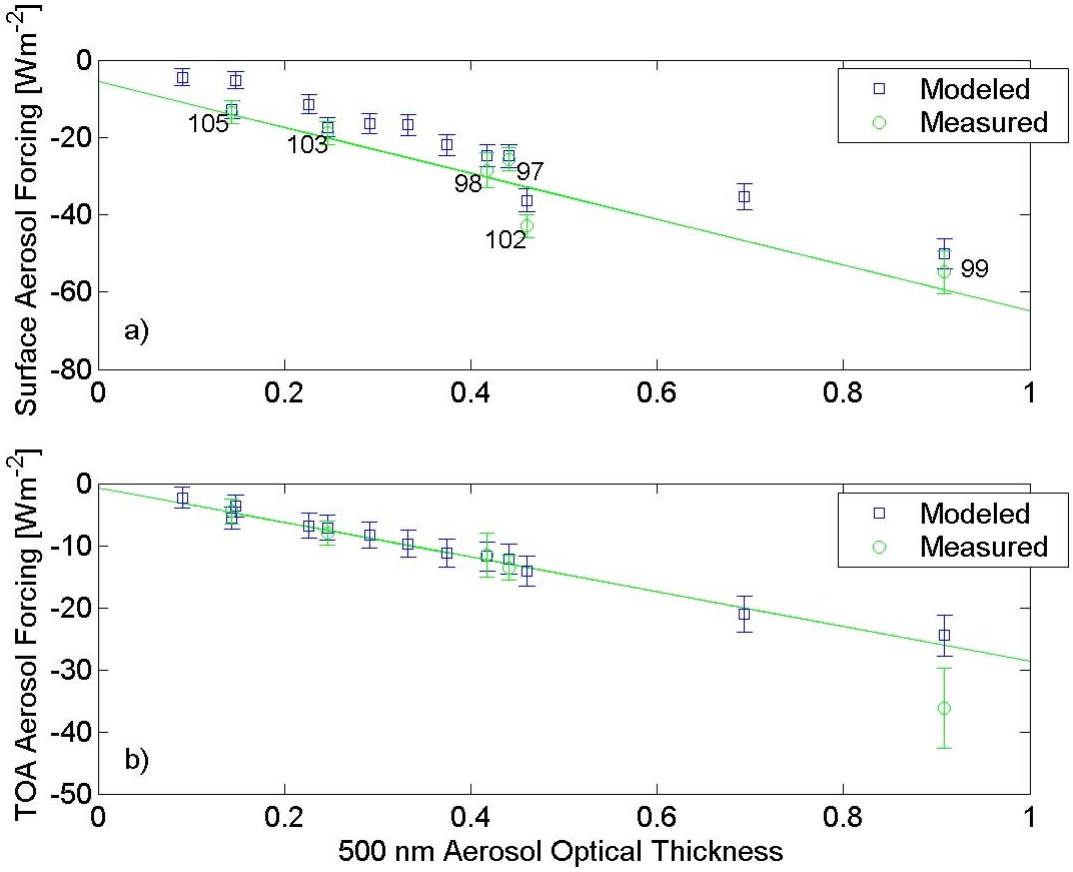

Fig. 5.8 (a) The solar aerosol forcing at the Earth's surface (broadband and diurnal averaged) as a function of aerosol optical thickness (AOT); (b) the solar aerosol forcing at the TOA (broadband and diurnal averaged). The open circles in both cases represent the aerosol forcing obtained from observations, square points represent the aerosol forcing obtained from radiative transfer model, and the solid line is a linear fit to the observations.

However the slope, obtained from the linear fit of the forcing, is independent of this bias and is used here; this slope is identical with the aerosol forcing efficiency (aerosol forcing per unit of

AOT). This estimate of the efficiency provides the average radiative effect of regional aerosols. Between YD97 and YD105, the regional aerosol varied between polluted (composed primarily of sulfate, organic carbon, and elementary carbon) and pollution mixed with dust (composed primarily of sulfate, organic carbon, elementary carbon, and dust) [*Quinn et al.*, 2002a]. Hence, the SSA varied between 0.92 and 0.98 due to RH effects and differences in the uptake of water by the dominant chemical components.

The mean daily aerosol forcing efficiency between YD97 and YD105 is –59.9 ± 7.3 Wm^{-2}. In comparison, the mean aerosol forcing efficiency during MINOS is –85 Wm^{-2} [*Markowicz et al.*, 2002] and during INDOEX it is –75 Wm^{-2} [*Satheesh and Ramanathan*, 2000]. The variation in single-scattering albedo, as well as, particle sizes may play significant roles in these differences. During the ACE-Asia measurement period, the aerosol over the Sea of Japan was more conservative (SSA closer to 1) compared to these other two campaigns, which leads to a smaller aerosol forcing efficiency at the surface.

The aerosol forcing efficiency (Fig. 5.8a) for YD102 is substantially larger than that found for the other days. This behavior is consistent with a lower value of SSA (in comparison to other days, c.f. Fig. 5.6) that occurs during the dust event with lower RH. This decrease of SSA during the YD102 leads to a –10 to -15 Wm^{-2} enhancement in surface forcing. Such change is consistent with a forcing efficiency in the range of –80 to –93 Wm^{-2}, rather than -60 Wm^{-2}.

The aerosol forcing at the TOA as a function of AOT is shown on Fig. 5.8b. The open circles represent the aerosol forcing determined from the CERES observations (TERRA satellite). We collocated the satellite observing footprint and ship position (maximum deviation of 25 km) when the viewing angle was less then 60 degrees. YD99 was classified by the satellite algorithm as cloudy, probably because of the hazy conditions with a large AOT close to 1. Therefore, we did not include this (misclassified) point when deriving the slope. The TOA aerosol forcing efficiency is -27.5±3.9 Wm^{-2}. This result is comparable to the –25 Wm^{-2} TOA aerosol forcing efficiency observed during the INDOEX [*Satheesh and Ramanathan*, 2000].

5.4.3 Modeled surface and TOA aerosol forcing

A comparison of the downward flux for YD103 (Fig. 5.9a) at the surface between measured (solid line) and modeled flux (open circles) shows excellent agreement. The model agreement is better quantified on Fig. 5.9b where the data for all days are presented. The model total flux underestimates the observations by 4.4 Wm^{-2}, and the small deviation (rms 12.9 Wm^{-2})

is within the range of pyranometer uncertainty. This good agreement is somewhat surprising given that we assumed constant aerosol composition with height. For example, YD99 is where the transport model indicates an elevated dust layer aloft between 4 and 13 km (Fig. 5.5). A plausible explanation for this agreement is that the optical properties, at the surface and aloft, were not radically different.

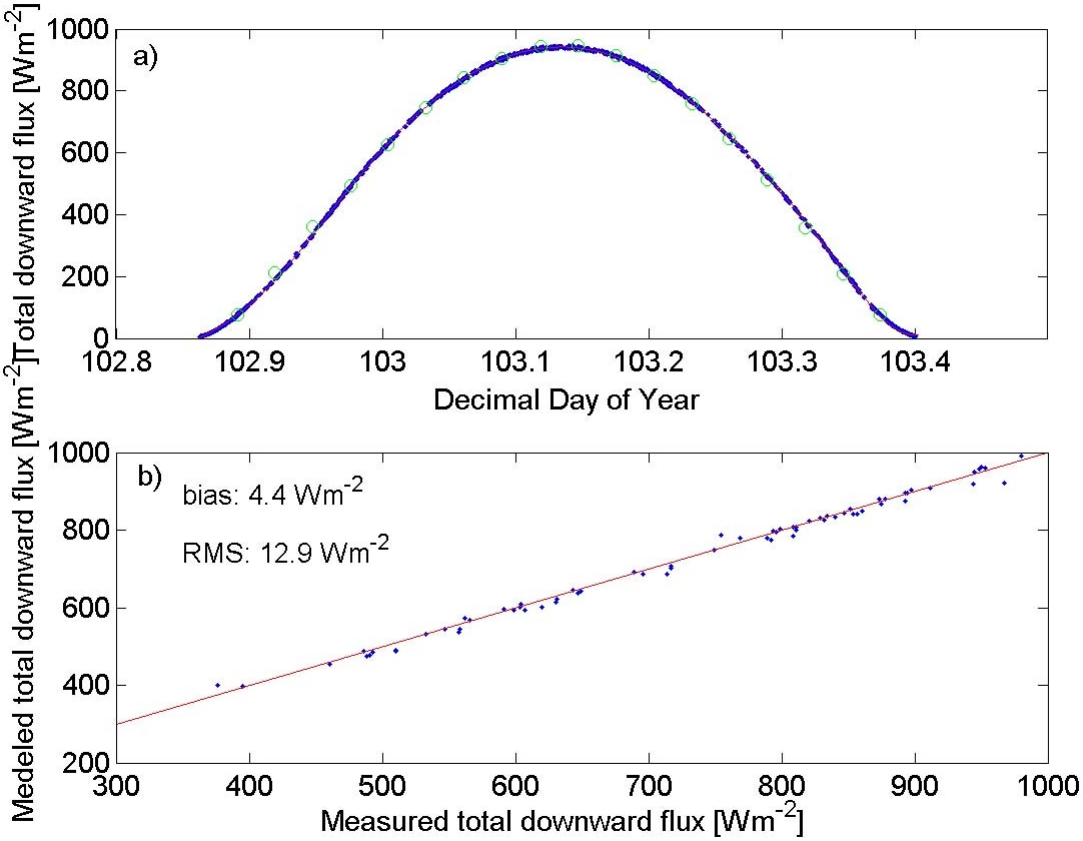

Fig. 5.9 (a) YD103 daily cycle of total broadband fluxes at the surfaces. The solid line represents the pyranometer observations and the open points are from the radiative transfer model, (b) comparison of the measured and estimated surface broadband total fluxes for all days. The solid line corresponds to perfect agreement.

The square points in Fig. 5.8a represent the aerosol forcing at the surface obtained from the model, with the slope (aerosol forcing efficiency) of –57.0±3.9 Wm^{-2}. This agrees with the observations for which forcing efficiency is –59.9±7.3 Wm^{-2}. Similarly, the aerosol forcing at the TOA as function of AOT is shown in Fig. 5.8b. Again, the agreement between the model (open squares) and measurements (open circles) is excellent. The TOA aerosol forcing efficiency derived from the model is -28.0±3.1 Wm^{-2}, compared to the observed -27.5±3.9 Wm^{-2}.

Fig. 5.10a shows the aerosol forcing as a function of Year Day (YD). The modeled aerosol forcing is given by open squares and open circles indicate the observations. Values for

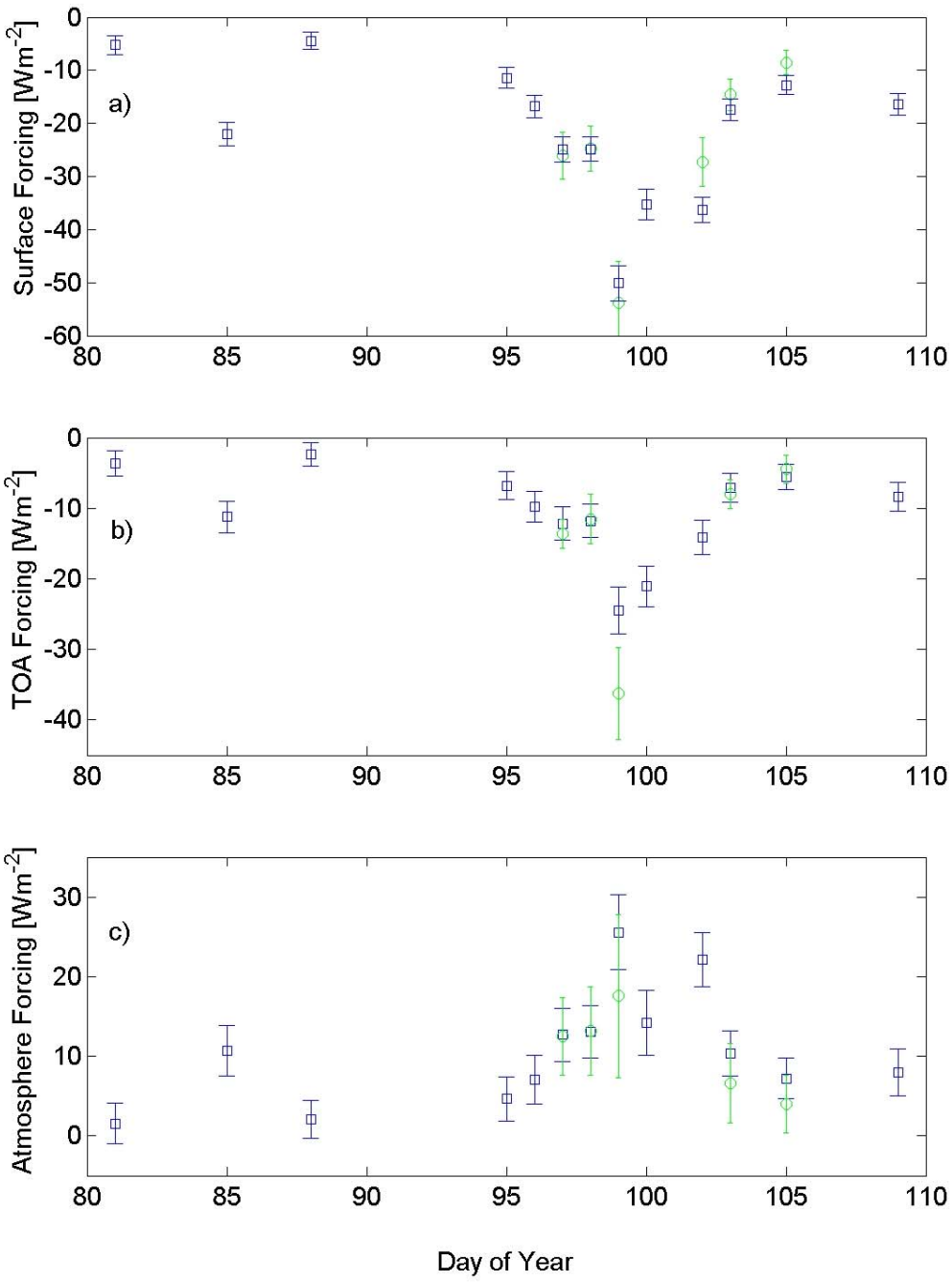

Fig. 5.10 Temporal variation of aerosol forcing at the (a) surface, (b) TOA, and (c) atmosphere. The open points correspond to observations and square points represent model results.

the observational aerosol forcing were determined by the mean aerosol forcing efficiency (by averaging all data) multiplied by the daily averaged AOT. The background aerosol forcing observed during the Pacific transect was smaller than -10 Wm^{-2}, with the exception of YD85 when the forcing increased to –22 Wm^{-2}, presumably, due to the sea-salt generated by strong

winds. The Pacific transect section in Fig. 5.10a requires further explanation. Within that three week period, we observed extra-tropical cyclones passing by every three to four days with associated cloud systems. Not surprisingly, we were able to measure the optical depth somewhat sporadically during that time. Before it was hypothesized (e.g., [*Jacobson*, 2001; *Winter and Chylek*, 1997]) that strengthening of storm tracks may lead to increased sea-salt radiative forcing. Indeed, the YD85 measurements show strong sea-salt radiative forcing dependence on wind speed, but more work remains to be done in this respect.

The TOA aerosol forcing is shown in Fig. 5.10b. The Pacific transect values are small. The Sea of Japan exhibits gradually increasing values with a maximum of –24.5 Wm^{-2} for YD99 and YD100, which are caused by relatively conservative scattering. The average value for the cruise is -10.6 Wm^{-2}.

The aerosol atmospheric forcing is shown in Fig. 5.10c. The Pacific transect was characterized by a small forcing (2 to 3 Wm^{-2}) with the exception of YD85 already discussed. In the Sea of Japan, atmospheric forcing increased on average to 10 to 15 Wm^{-2}. However, during two days it reached larger values of 25 Wm^{-2} (YD99) and 22 Wm^{-2} (YD102), which were associated with the aerosol absorption (c.f. Fig. 5.6) and large optical thickness.

5.4.4 Relative humidity influence on aerosol forcing efficiency

Fig. 5.11 shows the monthly averaged surface relative humidity (NCEP Reanalysis) for April 2001. There is a significant gradient of relative humidity caused by the sea surface temperature gradient in the Sea of Japan. In April 2001 the oceanic polar front was positioned at 38-40°N and the ship was in that region on YD98 and YD99 where the SST gradient was close to 6.5°C (Fig. 5.4b). The warmer air-mass-flow from Asia leads to increased RH in the shallow layer close to the surface. For example, on YD99 the relative humidity was 95% (Fig. 5.4a) but dry, subsidence driven conditions existed above 500m. This resulted in shallow and extended haze conditions in the lower boundary layer for which the AOT was above one and the SSA was 0.98. The increase in relative humidity leads to particle growth, increase in scattering, and the associated increases in AOT, SSA and asymmetry parameter. The AOT increase causes an increase of aerosol forcing at the surface as well as at the TOA. The SSA increase causes an aerosol forcing decrease at the surface and an increase at the TOA. The asymmetry parameter increase causes a forcing decrease at the surface as well as at the top of the atmosphere. These are opposite trends therefore we performed a numerical sensitivity study to determine the net

effect on the forcing efficiency (which is, to the first approximation, independent of the optical depth).

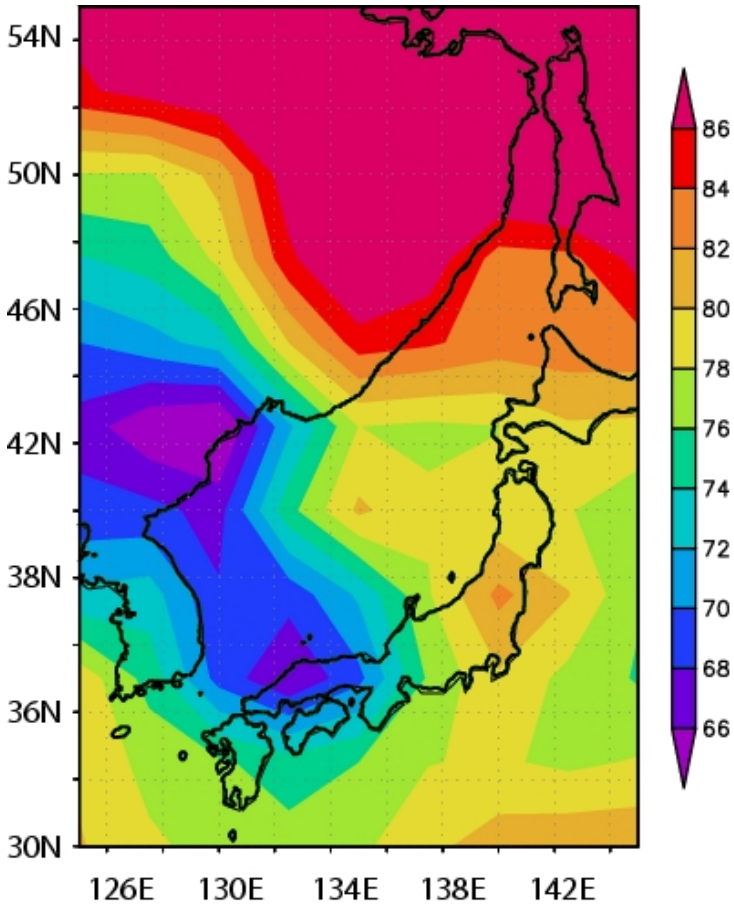

Fig. 5.11 Mean monthly surface relative humidity over the Sea of Japan in April 2001.

The optical properties were modified for a shallow, but humid lower layer by assuming a constant 55% relative humidity. Between YD95 and YD99 when the humidity effects were large, radiative transfer calculations showed that the aerosol forcing efficiency was enhanced by -5 to -10 Wm^{-2} (Fig. 5.12a) at the surface and decreased up to 2 Wm^{-2} (Fig. 5.12b) at the TOA. In other words, large values of relative humidity caused a decrease in the aerosol forcing efficiency over the Sea of Japan, despite of the significant transport from anthropogenic sources in Asia (including soot).

Fig. 5.13a and Fig. 5.13b show the surface and TOA aerosol forcing efficiency as a function of relative humidity for modeled YD99, which assumes constant relative humidity in the boundary layer up to 2 km. Only the optical properties of the aerosol were modified by RH changes. In this case the change in the surface aerosol forcing efficiency is about 20 Wm^{-2} between RH=55% and RH=95%. This is significantly larger than that presented in Fig. 5.12a because, in that case we modified the relative humidity in the lower boundary layer only.

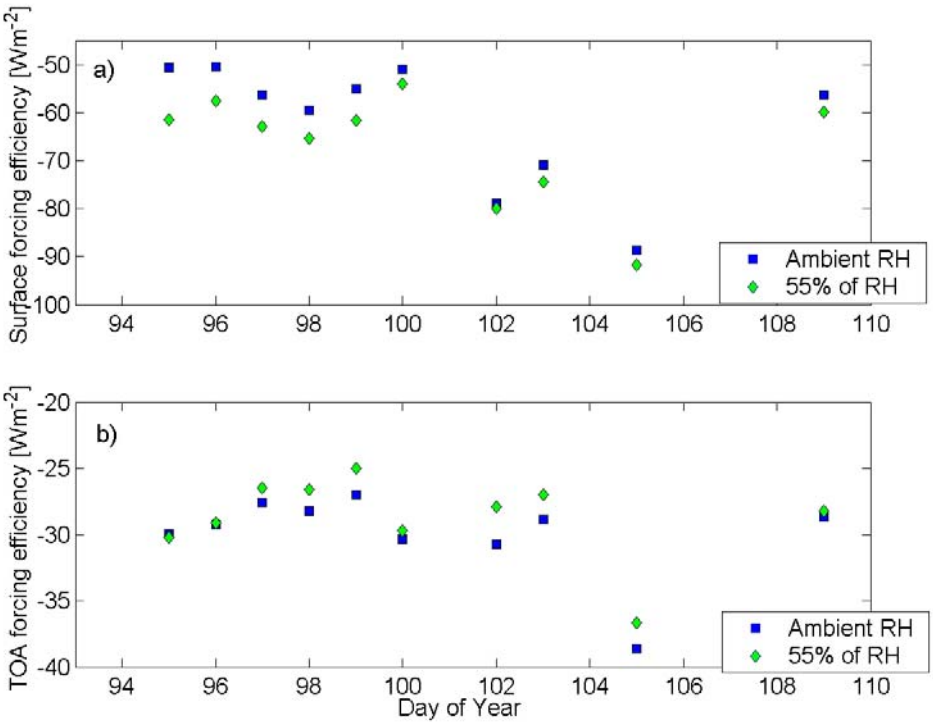

Fig. 5.12 Aerosol forcing efficiency as a function of Day of Year determined from the radiative transfer model. The square points mark aerosol forcing efficiency obtained at ambient relative humidity and the diamond points corresponds to calculations with maximum 55% of relative humidity in first 1 km of the atmosphere.

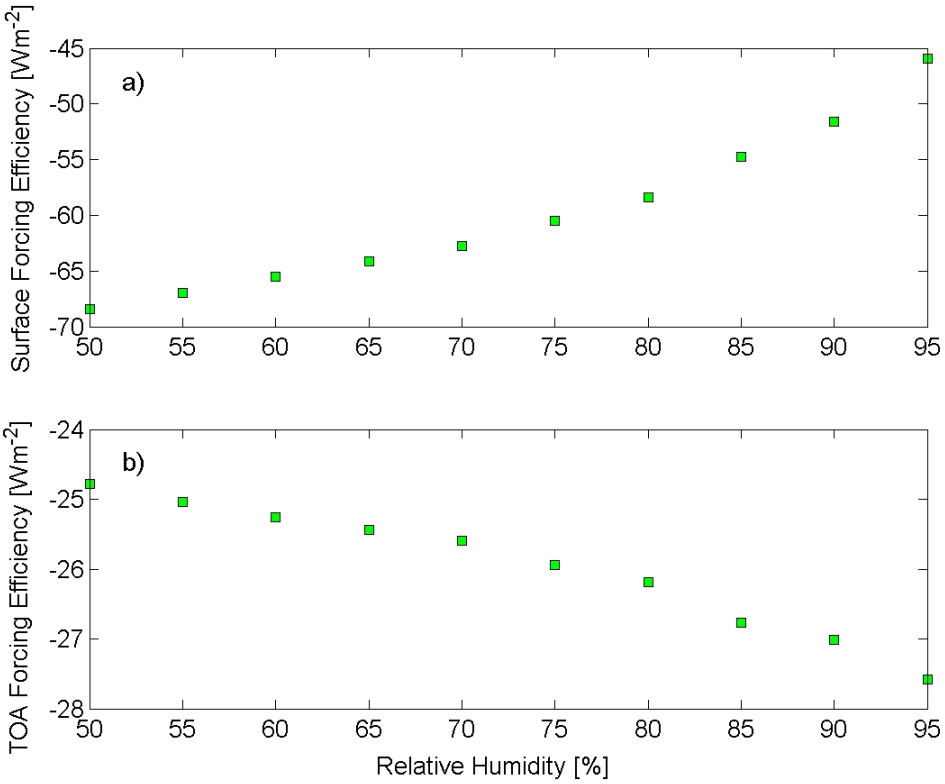

Fig. 5.13 Diurnal averaged surface (a) and TOA (b) aerosol forcing efficiencies determined from the radiative transfer model as a function of relative humidity for YD99.

(approximately 200-300 m). The change of the TOA aerosol forcing efficiency due to relative humidity changes is about 2.5 Wm^{-2}. These changes depend on the aerosol growth factors and thus have a similar functional dependence.

5.5 Infrared aerosol forcing

5.5.1 Infrared broadband fluxes

Fig. 5.14 shows the downward longwave radiation (3.5-50 μm) at the surface during the cruise. The solid line corresponds to pyrgeometer observations and open circles mark radiative transfer model results. High values of fluxes are correlated with the cloudy conditions and large relative humidity. Notice that the model results define the minimal envelope of the pyrgeometer observations associated with the clear sky conditions. For example, after the stormy night on YD85, we measured visible AOT as high as 0.45 which correlates with a small longwave flux (275-285 Wm^{-2}), which indicates non-cloudy conditions.

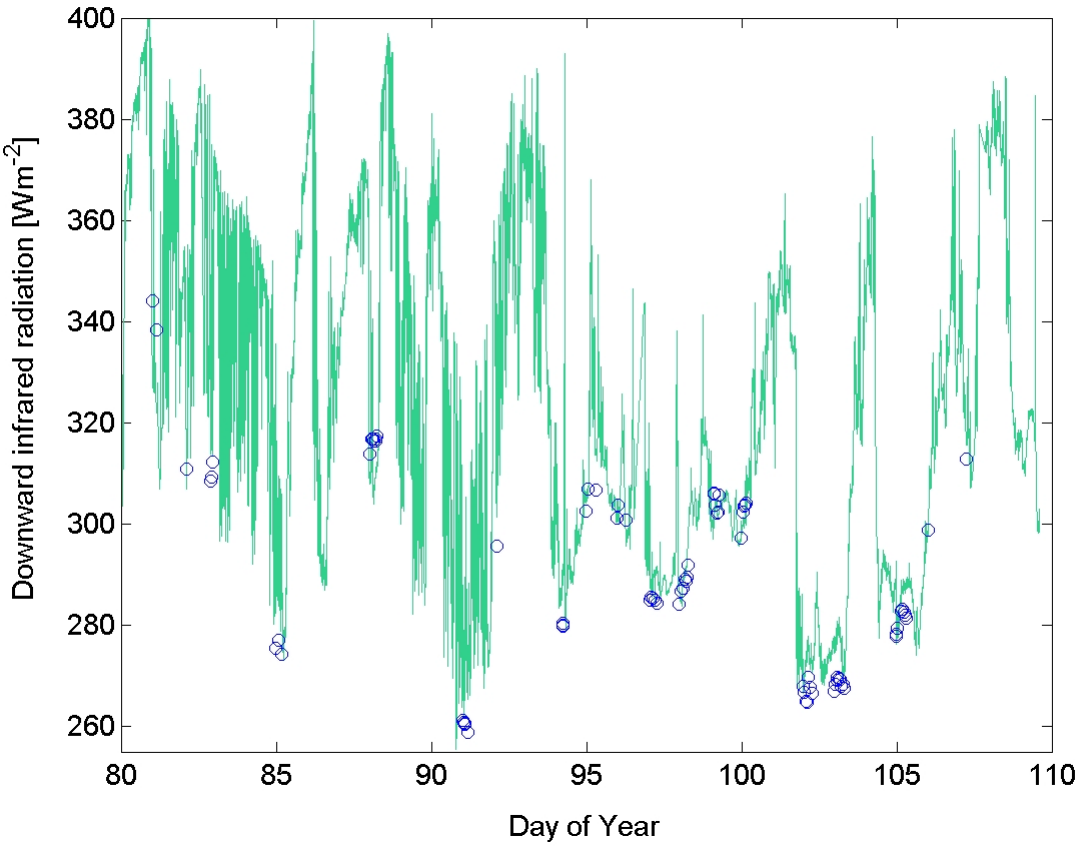

Fig. 5.14 Downward longwave flux (3.5 - 50 μm) at the surface as a function of Year Day. The solid line represents pyrgeometer observation and the open circles mark model results.

The agreement between the model and the pyrgeometer is better quantified on Fig. 5.15a. The radiative transfer model underestimates the total downward fluxes by 2.9 Wm^{-2} (Fig. 5.15a). In spite of a relatively large rms (7.3 Wm^{-2}) the modeled fluxes can be considered in good agreement with the measurements. The difference between observations and model results is significantly influenced by the total columnar water partially, because soundings were available, at best only, every 3 hours (no attempt was made to use FTIR retrieved soundings in this work). Because of these issues and potential cloud presence, we do not use the pyrgeometer to derive IR forcing.

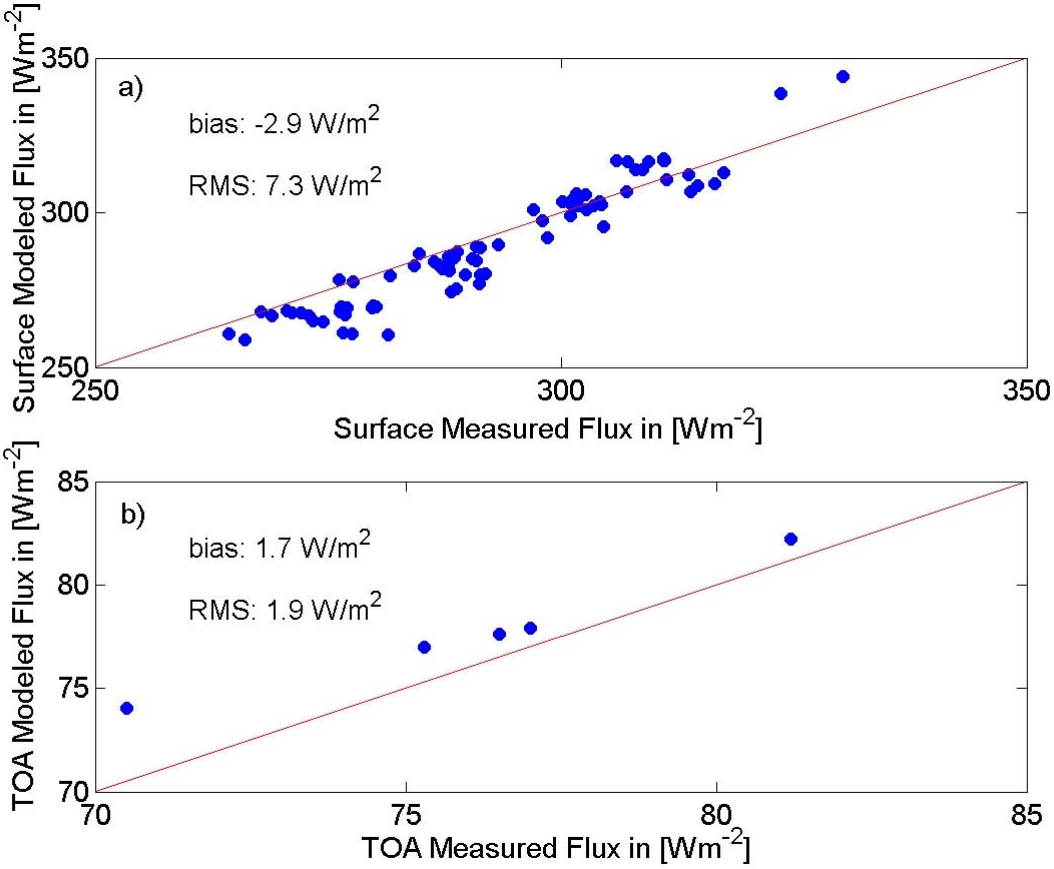

Fig. 5.15 Comparison of measured and modeled (a) downward fluxes at the surface between 3.5 and 50 μm, and (b) outgoing fluxes at the TOA in the atmospheric window (8-12 μm).

The CERES observations (on the TERRA satellite) were used to compare fluxes at the TOA. Fig. 5.15b shows a comparison of modeled and CERES outgoing longwave radiance in the atmospheric window (8-12 μm) at the TOA. We have only 5 days with the cloud free conditions. For TOA the model overestimated the satellite data by 1.7 Wm^{-2}. The difference between model and observations is positive and has a smaller rms (1.9 Wm^{-2}). Possible error sources are the angular distribution model (ADM) specifications [*Loeb and Kato*, 2002], which are used to convert radiances to fluxes in the SSF CERES data and uncertainties in the aerosol optical model

specifications. Model calculations of fluxes in the atmospheric window at the TOA show that the outgoing longwave flux is largely independent of the total column water vapor and, therefore, the TOA flux from CERES can be used to estimate the IR aerosol forcing.

5.5.2 Infrared aerosol-optical properties

In this section the infrared radiation in the atmospheric window between 8-12 μm is discussed. As usual, aerosol properties depend on the refraction index and the aerosol size distribution. The coarse mode particles ($r > 0.5$ μm) can effectively scatter or absorb longwave radiation. For these particles their single scattering properties are determined by the transition between the Rayleigh and Mie regimes (size parameter $x > 0.3$, where $x=2\pi r/\lambda$). Because the extinction efficiency is small for $x \approx 0.3$, and because there are not many large aerosol particles, the infrared extinction is small

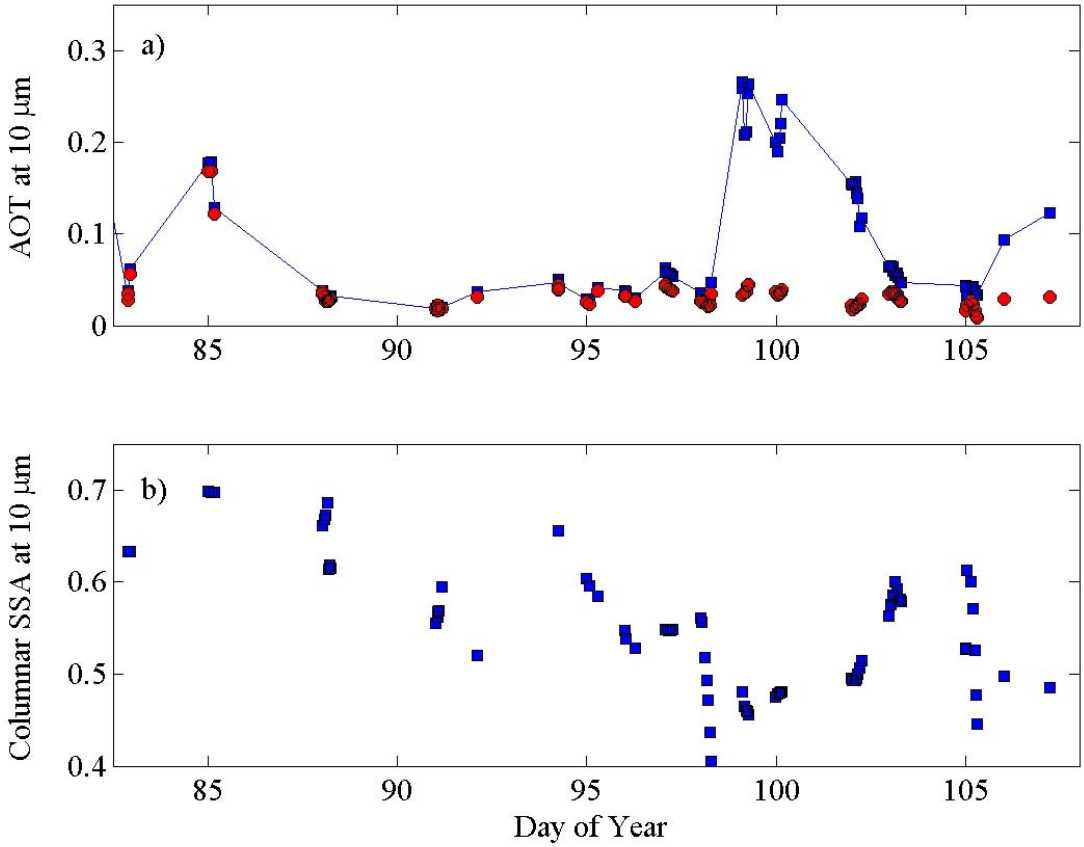

Fig 5.16 Temporal variation of (a) total (solid blue squares and solid line) and no-dust (solid red circles) aerosol optical thickness (AOT) at 10 μm, and (b) vertically averaged infrared single scattering albedo (SSA) at 10 μm during the ACE-Asia cruise.

in comparison to the visible extinction. During the ACE-Asia the number of particles in the sea salt coarse mode varied between 0.005 to 0.38 in cm^{-3} and number of dust particles in coarse mode varied between 0.01-0.63 cm^{-3} (remember that these are derived concentrations and that they can possibly contain contributions from various errors).

Using the aerosol optical model, the vertical profile of extinction coefficient from MPL lidar observations and the aerosol optical thickness at 500 nm, we obtained the aerosol optical properties in the infrared atmospheric window. Fig. 5.16a shows a high temporal variation of the infrared aerosol optical thickness during the cruise. The blue line and solid squares on Fig. 5.16a correspond to total IR aerosol optical thickness and solid red circles mark IR no-dust optical thickness. The mean value of the infrared AOT is 0.08 (±0.07) and it is five times smaller than the AOT observed at 500 nm [*Markowicz et al.*, 2003a]. Lower values (between 0.03 and 0.05) of the infrared AOT in the first part of the cruise were associated with the clean marine air masses of the central and western Pacific Ocean. Only during YD85, after the frontal passage, infrared AOT increased to about 0.18 in the morning, and 0.13 later that afternoon. The visible to the infrared AOT ratio was approximately 2.5, which is relatively small and due to the increase in large particle concentration. For that case we observed a flat spectral AOT (small Ångstrom exponent) in the visible and near infrared.

Between YD98 and YD99 the infrared AOT increased strongly which correlates with the dust layers in the middle troposphere. Throughout YD99 the infrared AOT is 0.25 while the visible AOT is about 1. From YD99 onwards the layer of dust was descending and on YD102 the situation was dominated by dust in the boundary layer. The number of dust particles in the coarse mode inferred from chemical measurements at the surface is about 0.6 cm^{-3}. The infrared AOT was 0.15 in the morning and decreased to 0.1 later that afternoon. These results correlate with the visible AOT and the dust concentration at the surface. During the last days of the cruise the infrared AOT was small with the exception of YD107 when it increased to 0.13.

The IR optical thickness with dust effect removed (red circles in Fig. 5.16a) was much smaller in comparison with the case when they were accounted for. The no-dust IR optical thickness was usually smaller than 0.05 with exception YD85. During days with dust composition of this component to the total IR optical thickness was about 20%.

The correlation coefficient between the infrared AOT and visible (500 nm) AOT computed for all available data is 0.82 (Fig. 5.17). In spite of the significant correlation, we cannot estimate the infrared AOT basing only on one measurement in the visible range. However, the multi-spectral observations by the sunphotometer yield information about columnar size distribution. For example, the Ångstrom exponent defined for two wavelengths is

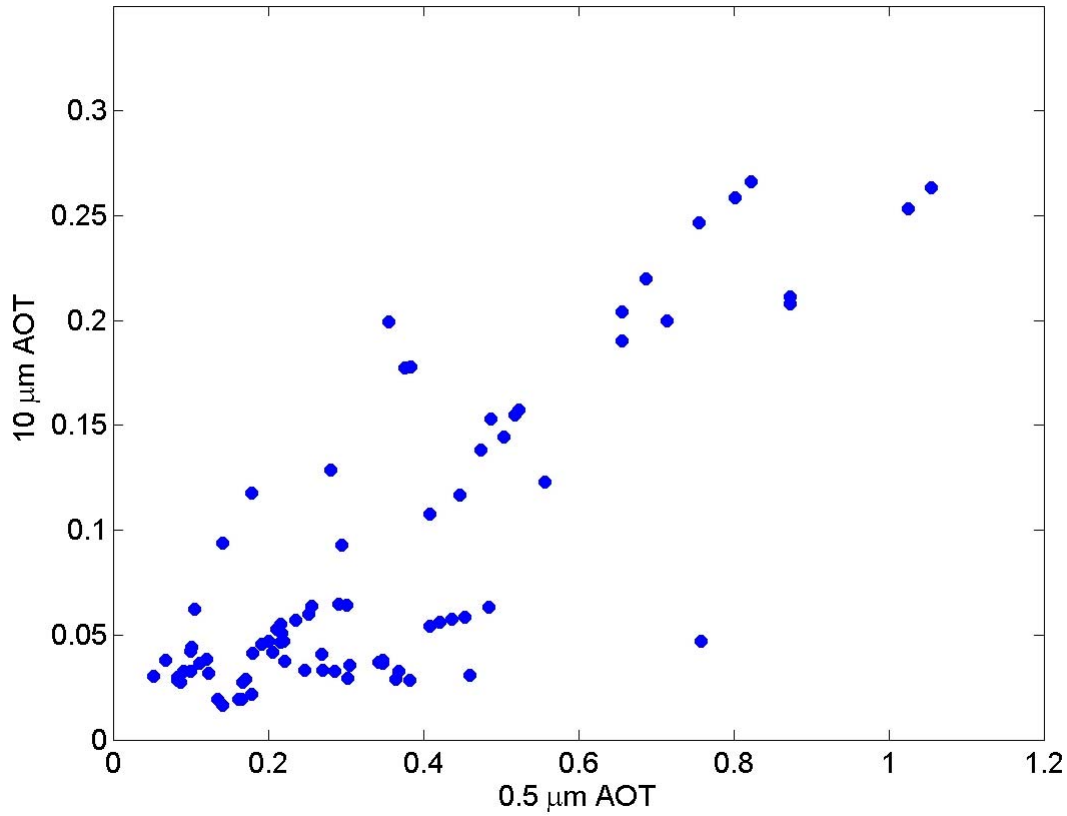

Fig. 5.17 Infrared (at 10 μm) aerosol optical thickness as a function of the visible (at 0.5 μm) aerosol optical thickness.

a function of the ratio of particle concentration in the accumulation and the coarse modes. Therefore, during days with high infrared AOT we measured low value of Ångtrom exponent. Moreover, during these days correlation of the infrared AOT and visible AOT was much better (Fig. 5.17).

The columnar infrared single scattering albedo (SSA) at 10 μm, is defined as

$$< \omega >= \frac{\int_0^{10km} \omega(z)\sigma_{ext}(z)dz}{\int_0^{10km} \sigma_{ext}(z)dz}. \qquad (5.4)$$

Fig. 5.16b shows the columnar infrared SSA during ACE-Asia cruise. The SSA varies from 0.4 to 0.7, thus the scattering of radiation in the atmospheric window is appreciable. The highest values of the SSA (0.65-0.7) were observed in the first part of the cruise and correspond to almost conservative SSA in the visible. The correlation between visible and infrared SSA is poor, (r^2=0.66) although the general trend of these two quantities (not presented) is similar. One important reason for such a small correlation is the presence of water vapor. In the visible range,

the increase of RH leads to an increase of SSA, while in the infrared atmospheric window the imaginary part of the refractive index of water is large and the increase of RH correlates with an increase of absorption (smaller SSA). Over the Sea of Japan, the infrared SSA is smaller in comparison to the Pacific transect and during the dust events the infrared SSA is between 0.45 to 0.5.

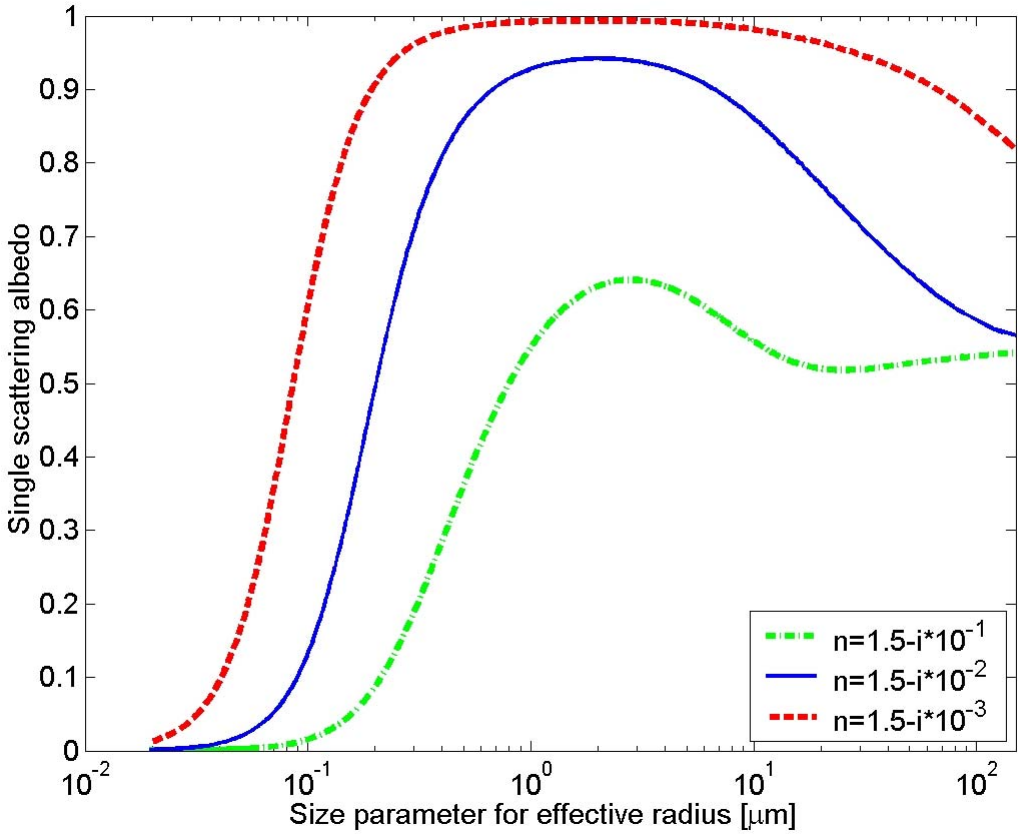

Fig. 5.18 Single scattering albedo (SSA) as function of size parameter based on size distribution effective radius. The dashed (red) line corresponds to (constant with wavelength) refractive index $n=1.5-i10^{-3}$, the solid line is for $n=1.5-i10^{-2}$, and the dash-dotted (green) line is for $n=1.5-i10^{-1}$. The SSA was obtained for spherical particles based on MIE theory.

There were no direct measurements of the SSA in the infrared. However, the measured surface SSA at 550 nm compares well with the modeling results [*Markowicz et al.*, 2003a] in the visible, which provides a certain degree of confidence about the validity of our optical model. The aerosol refractive index and size distribution of particles are the source of uncertainties in derivation of the infrared SSA. This is particularly true about mineral dust. The mineral dust refractive index changes significantly with its composition [*Sokolik et al.*, 1998]. However, in this study we used the refractive index of dust available in the OPAC/GADS database. We validate our optical model against available measurements, such as, radiation fluxes and

absorption and scattering coefficients. Also, the size distribution changes lead to large changes of the infrared SSA.

The Fig. 5.18 shows results of the MIE calculations performed for spherical particles. In this figure the SSA is shown as a function of a size parameter ($x=2\pi r/\lambda$) based on the effective radius. The three lines on this figure correspond to different imaginary parts of the refraction index (k). The dotted line corresponds to $k=10^{-3}$, the solid line to $k=10^{-2}$, and the dash-dotted line corresponds to $k=10^{-1}$. In the infrared (8-12 μm) part of the spectrum the size parameter is usually less than $x_{eff} < 1$ and the SSA is, therefore, a fast changing function of the effective radius. The decrease of particle radius leads to a decrease of the SSA and a change of the surface and TOA infrared aerosol forcing. The fact that small particles (fine mode) are black in the infrared indicates that only large particles can effectively scatter radiation.

5.5.3 Infrared aerosol forcing

In this section we derive the longwave radiative aerosol forcing at the surface and at the top of the atmosphere (TOA). At the surface, the forcing is defined as the difference between downward longwave flux with the aerosol and without the aerosol in the atmosphere. In contrast to the aerosol forcing in solar spectrum (where the Sun is the source of energy and even small backscatter can cause a negative aerosol forcing) the infrared aerosol forcing at the surface is always positive. This is caused by the additional downward flux from the aerosol layers. At the top of the atmosphere the outgoing longwave radiation (OLR) is, in most cases, reduced by the aerosols except for strong inversion cases when the temperature of the aerosol is higher than the surface temperature. To determine the aerosol forcing we perform two radiative transfer calculations with and without aerosols in the atmosphere.

The effect of aerosols on longwave radiation is significant only in the atmospheric window range (8-12 μm), where the absorption by greenhouse gases (mostly water vapor and carbon dioxide) is small. Therefore, we present model results in this range. We compare these model results with the aerosol forcing obtained from more detailed observations based on M-AERI. The observational IR aerosol radiative forcing was described by *Vogelmann* and the author of this dissertation [2003]. The M-AERI measured spectra contain the combined downward emissions by aerosols and greenhouse gases (e.g., H_2O, CO_2). The aerosol's radiative effect was obtained by removing the contribution of gaseous emission using a modeled, clean-sky (no aerosol) spectrum. The aerosol radiance effect was converted to an aerosol IR radiative

forcing using a radiance-to-flux conversion. The clean-sky spectra were computed using the Line-By-Line Radiative Transfer Model LBLRTM. In *Vogelman et al.* [2003] the water vapor and

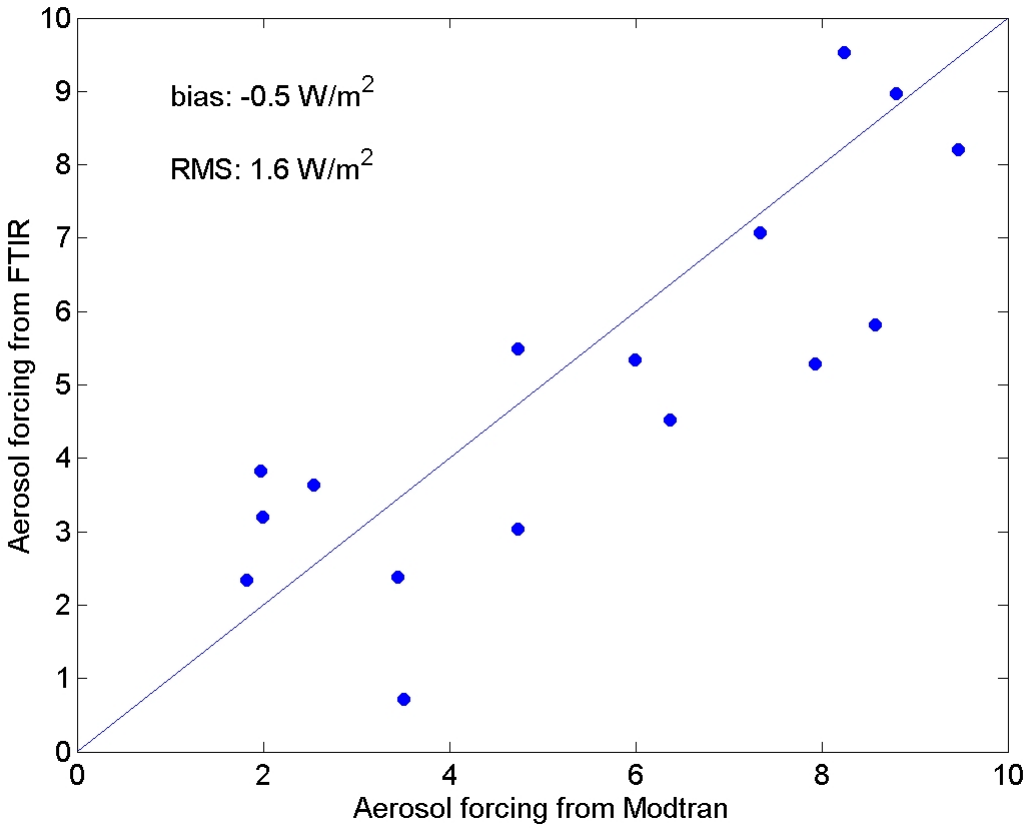

Fig. 5.19 Comparison of longwave aerosol forcing at the surface obtained from radiative transfer model and FTIR observations. Solid line corresponds to perfect agreement.

temperature profiles are specified every 10 min using M-AERI retrievals for the lowest 3 km and, above that, the nearest radiosonde launched from the ship whereas. Whereas in spite of this, the modeled study of the IR aerosol forcing (described in this paragraph) used only the radiosonde data.

The general comparison of the surface infrared aerosol forcing obtained from M-AERI and from our radiative transfer model is shown in Fig. 5.19. Although the mean difference between model and observations is small (0.5 Wm^{-2}) the rms is relatively large 1.6 Wm^{-2}. Let us recall that the model calculations are based on surface optical properties derived from the chemical characterization of the aerosol and the vertical extinction profile derived from lidar and visible AOT at 500 nm. Possible discrepancies between the M-AERI and the model results reported here may be related to the fact that the surface chemistry is not representative for

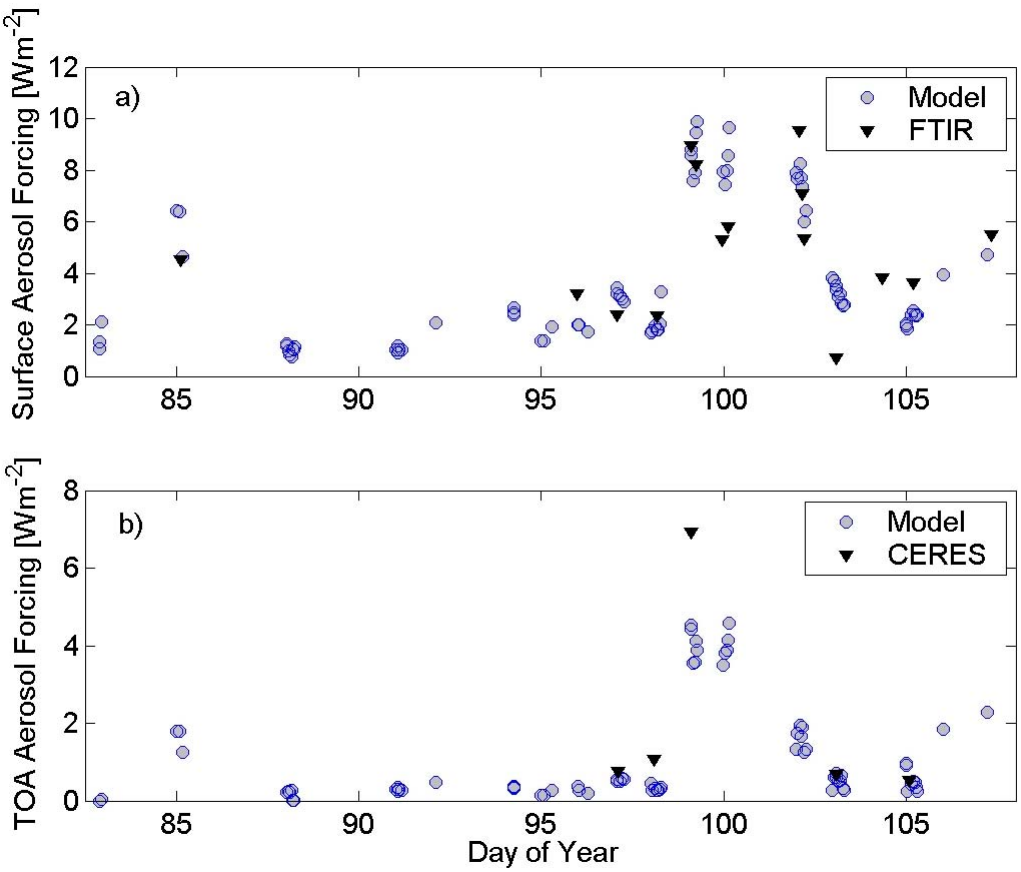

Fig. 5.20 (a) Surface and (b) the TOA infrared aerosol forcing as a function of Year Day. The open circles represent radiative transfer model results and the solid triangles define the surface (a) and the TOA (b) forcing obtained from the FTIR and TERRA satellite CERES data respectively.

the lower troposphere and that dust properties are not modeled properly. Also, the lidar extinction algorithm is source of error. However, the overall comparison is good and many features are resolved by our model, as is, illustrated in Fig. 5.20. This provides additional validation for the aerosol-optical properties choice. In the central part of the Pacific Ocean the longwave surface forcing is small and equal to about 1 Wm^{-2} with the exception of YD85. For comparison, the solar aerosol forcing in this region is –5 Wm^{-2} [*Markowicz et al.*, 2003a]. During YD85, the longwave aerosol forcing increased and in the morning was about 6 Wm^{-2} decreasing to about 4.5 Wm^{-2} in the late afternoon. The mean daily solar aerosol forcing on YD85 was –22 Wm^{-2}. The GOCART transport model (private comunication Mian Chin) shows dust in the boundary layer. This indicates that combined effect of the sea salt close to surface and dust in the boundary layer has an important effect on radiation in both solar and infrared and leads to a strong cooling at the surface. Between YD86 and YD99 the infrared forcing slowly increased to over 2 Wm^{-2}. The maximum aerosol forcing observed on YD99 and YD100 (8-10 Wm^{-2}) is associated with the dust layer in the middle troposphere (Fig. 5.5). For these days the surface

aerosol forcing in the solar region is about 5 times larger (absolute value) than in the infrared forcing. The infrared forcing for YD99 and YD102 are similar but their AOTs (both in solar and IR) are different. This is because on YD99 the dust was between 5-10 km, and on YD102 it was closer to surface, thus, the temperature effect of the warmer dust compensated for its smaller optical depth.

The longwave TOA aerosol forcing is obtained from the radiative transfer model and CERES data (only 5 clear days). The TOA forcing is estimated by subtracting the clear air (without aerosol) outgoing flux in the atmospheric window obtained from the radiative transfer model and the flux measured by the CERES instrument. After plotting the infrared forcing as a function of the infrared AOT, we noticed a bias for small AOTs, of approximately 0.9 Wm^{-2}. However, on physical grounds, one would not expect any forcing for small AOT. Such a bias may be due to several factors related to clear-sky model imperfections. Guided by the slope technique derived for the solar spectrum forcing calculations [*Satheesh and Ramanathan*, 2000], we applied the same methodology to remove the bias. Fig. 5.20b shows the temporal variation of the TOA infrared aerosol forcing. The solid triangles on Fig. 5.20b show the aerosol forcing at the TOA between YD97 and YD105 obtained from satellite. The blue circles are model results. The results are in good agreement with radiative transfer calculations with the exception of YD99. During this day, the aerosol forcing from satellite observations is about 2.5 Wm^{-2} larger than obtained from the model. However, YD99 was misclassified by the satellite algorithm as cloudy probably due to hazy conditions. The largest forcing is about 4.5 Wm^{-2} during YD99 and YD100 and is about two times less than at the surface. Much smaller TOA forcing was observed on YD102 which is due to the previously discussed temperature effect. The TOA aerosol forcing without dust is small and did not exceed 0.5 Wm^{-2}. However, for sea-salt dominated YD85 the TOA longwave forcing is between 1.2 and 1.8 Wm^{-2}. For comparison, the TOA aerosol forcing in the solar spectrum is about 4 to 6 times smaller than the infrared aerosol forcing.

The strong correlation between infrared aerosol forcing and infrared (10 μm) AOT is shown on Fig. 5.21. The red squares represent cases with upper aerosol layers present and blue circles mark all other data. This division is based on the following criterion $(T_a/T_s)^4<1.2$, where T_s is the surface temperature and T_a is the mean aerosol temperature which is defined as

$$T_a = \frac{\int_0^{10km} T(z)\sigma_{ext}(z)dz}{\int_0^{10km} \sigma_{ext}(z)dz} \tag{5.5}$$

It can be seen that, in the first approximation, the infrared aerosol forcing is a linear function of the infrared AOT. Let us now define the infrared aerosol forcing efficiency as the ratio of aerosol forcing to infrared AOT. The infrared forcing efficiency is 55 Wm^{-2} (per IR optical depth unit) for the boundary layer aerosol and 37 Wm^{-2} (per IR optical depth unit) in the case of elevated

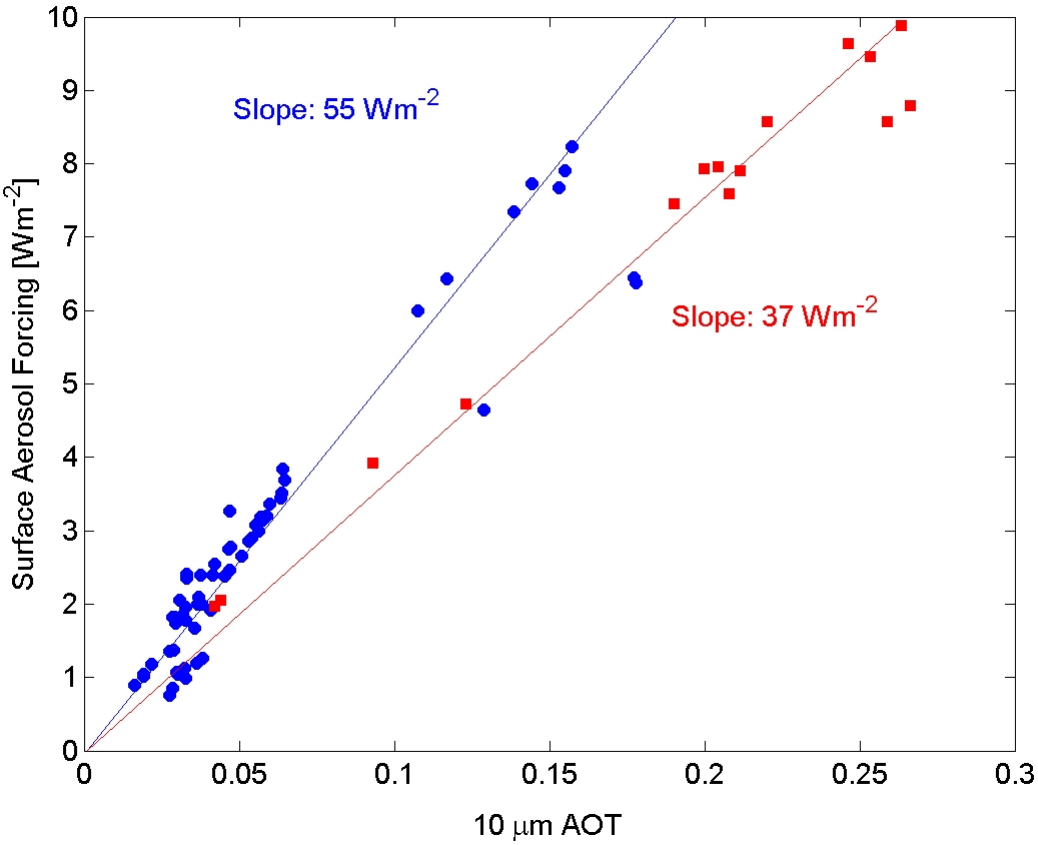

Fig. 5.21 The longwave aerosol forcing as function of infrared AOT. Square (red) points represent aerosol forcing during the upper layer event and circles (blue) are for all other days. The upper layer dust events was classified on the basis of surface and aerosol temperatures $(T_s/T_a)^4>1.2$.

dust. If the aerosols are close to the surface, they cause an increase of the surface forcing but a decrease of the TOA forcing. The TOA aerosol forcing as a function of the infrared AOT is shown on Fig. 5.22; the forcing efficiencies is about 18 Wm^{-2} (per IR optical depth unit) in the case of elevated dust and 10 Wm^{-2} (per IR optical depth unit) when the aerosol is mostly in the boundary layer. This difference of forcing efficiency is due to the emission temperature differences.

We attempted to derive the radiative forcing using the Eppley broadband, hemispheric field of view pyrgeometer, but the results were unpromising. This is most probably due to

following effects: (a) a too broad spectral range (3.5-50μm), (b) the hemispheric field of view (cloud contamination), (c) uncertainty in the water vapor profiles.

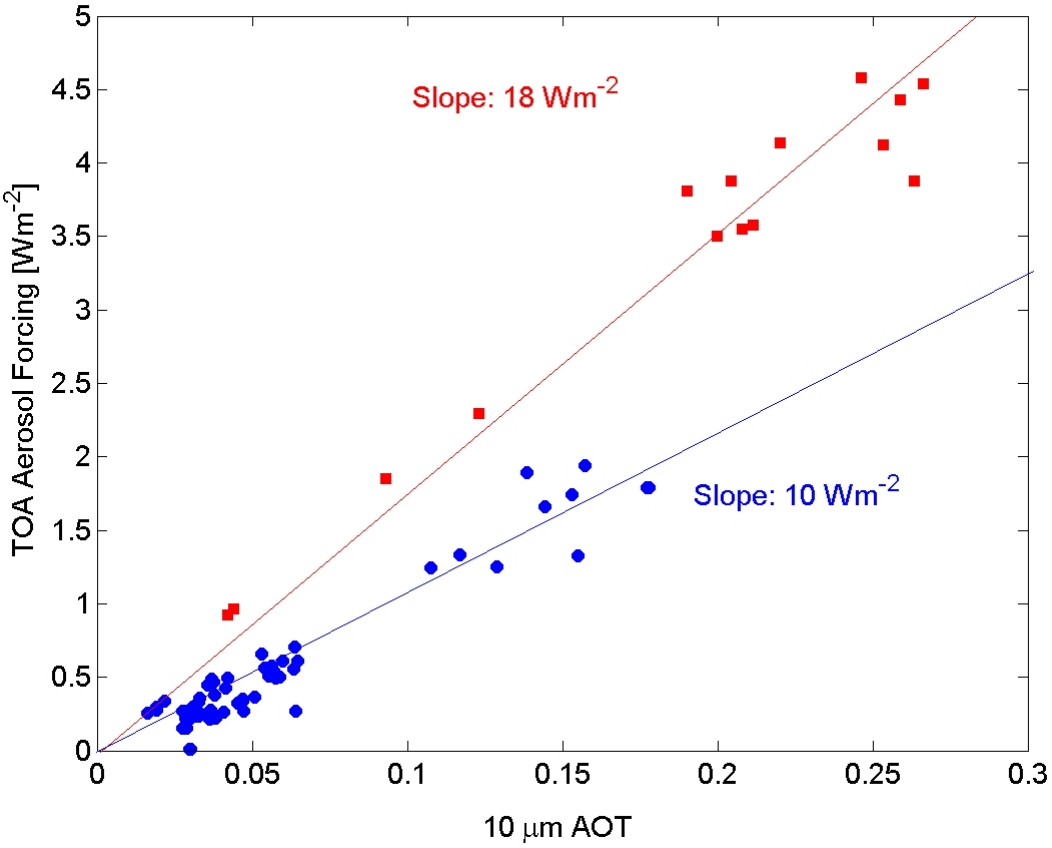

Fig. 5.22 Same as Fig. 5.21 but for the TOA aerosol forcing

5.5.4 A simple model of infrared forcing

In this section a simple 2-stream model is developed aimed at gaining insight into the physics of dust forcing. We assume that the aerosol layer is isothermal and that there is no gaseous absorption in the atmospheric window. Neglecting multiple scattering we can write the flux at the top ($F_t^{\uparrow}$) and at the bottom ($F_s^{\downarrow}$) of the aerosol layer as:

$$F_t^{\uparrow} = tF_s^{\uparrow} + F_s^{\uparrow} r^{\uparrow} + \pi a B_a , \tag{5.6}$$

$$F_s^{\downarrow} = r^{\downarrow} F_s^{\uparrow} + \pi a B_a , \tag{5.7}$$

where, B_a is the black body irradiance at the temperature of the aerosol layer. Parameters a and t are the aerosol absorption and transmittance, $r^{\uparrow}$ and $r^{\downarrow}$ are up and down reflection coefficients, respectively, subscript “s” stands for “surface” and “a” for “aerosol". In the case of small optical thickness τ, the parameters in equations (5.6) and (5.7) can be written as:

$$t = 1 - \tau, \tag{5.8}$$

$$a = \tau(1 - \omega), \tag{5.9}$$

$$r^{\uparrow} = \tau\omega(1 - \beta), \tag{5.10}$$

$$r^{\downarrow} = \tau\omega\beta \tag{5.11}$$

where ω is a single scattering albedo and β is the backscatter fraction (ratio). The radiative forcing above and below the aerosol layer can be written as

$$\Delta F_t = (F_t^{\uparrow})_{clear} - (F_t^{\uparrow})_{aerosol} = F_s^{\uparrow} - (tF_s^{\uparrow} + r^{\uparrow}F_s^{\uparrow} + \pi a B_a), \tag{5.12}$$

$$\Delta F_s = (F_s^{\downarrow})_{aerosol} - (F_s^{\downarrow})_{clear} = r^{\downarrow}F_s^{\uparrow} + \pi a B_a - 0. \tag{5.13}$$

Substituting parameters from Eq. 5.8-5.11 leads to solutions

$$\Delta F_t = \tau\pi B_s\left[\left(1 - \frac{B_a}{B_s}\right)(1 - \omega) + \omega\beta\right], \tag{5.14}$$

$$\Delta F_s = \tau\pi B_s\left[\frac{B_a}{B_s}(1 - \omega) + \omega\beta\right] \tag{5.15}$$

where, B_s is the black body irradiance at the surface temperature. In this simple model the aerosol forcing at the TOA and at the surface is a linear function of the infrared AOT. The first terms in Equations 5.14 and 5.15 are associated with the thermal emission by the aerosol layer relative to the surface emission and the second terms are associated with the downward scattered fraction of radiance. For typical values, the terms at the TOA (Eq. 514) are comparable, while at the surface (Eq. 5.15) the contribution by the relative emission is about 2-3 times larger than the scattering term. Thus, the TOA infrared aerosol forcing in contrast to the surface aerosol forcing is more sensitive to the aerosol scattering.

The thermal effects at the TOA and at the surface are opposite and are consistent with detailed radiative transfer model calculations (Fig. 5.21 and Fig. 5.22). The backscatter ratio can be written approximately as $\beta=1/2(1-g)$ [*Wiscombe and Grams*, 1976]). The influence of the backscatter on the infrared aerosol forcing is similar at the TOA and at the surface. In both cases the increase of the backscatter leads to an increase of the aerosol forcing. Thus, smaller particles (small asymmetry parameter) have a larger influence on the aerosol forcing in the infrared due to the scattering effect, which is similar to the solar aerosol forcing. The infrared SSA influences the infrared aerosol forcing in two opposite ways. Decrease of SSA leads to an increase of thermal emission by the aerosol layer, and decreases the scattered part of radiation. It follows from Eq. (5.15) that for

$$\beta < \frac{B_a}{B_s} \tag{5.16}$$

the decrease of SSA leads to an increase of the infrared aerosol forcing at the surface. This condition is always satisfied, because the backscatter coefficient is less than 0.5 and B_a/B_s ratio is usually between 0.8 and 1. The SSA influence on the TOA aerosol forcing is more complicated. For

$$\frac{B_a}{B_s} < 1 - \beta \tag{5.17}$$

the decrease of SSA leads to an increase of the infrared aerosol forcing at the TOA. Thus, for a constant backscatter coefficient one can always find a temperature at which the TOA aerosol forcing is increasing with increased absorption. For typical atmospheric conditions Eq. 5.17 may or may not be satisfied. Therefore, the relationship between the infrared TOA forcing and SSA changes depends on relative black body temperatures and the backscatter coefficient. On the other hand, the shortwave TOA forcing always increases with increasing absorption (but can be positive or negative).

5.5.5 The role of scattering on TOA and surface infrared forcing

By keeping the total aerosol absorption and extinction constant and performing two calculations with asymmetry parameter equal one (a), and asymmetry parameter determined from the aerosol optical model, (b), we can investigate the role of scattering on the infrared aerosol forcing. Upper plots on Fig. 5.23 correspond to the surface aerosol forcing and bottom plots correspond to the TOA forcing. Solid lines are for the asymmetry parameter (g) determined from the aerosol optical model and the dotted lines are for g=1. In the last case only forward scattering is possible and is what corresponds to the "non-backscattering" instance. Neglect of aerosol scattering leads to an underestimate of the surface and TOA IR forcing. Scattering has larger effect on the TOA forcing and this results is consistent with the simple aerosol forcing model. Neglecting scattering causes mean error of 20-30% but sometimes increases it to 50%. The surface aerosol forcing decreases about 10-15 % as result of zero backscattering. These results are consistent with model results presented by *Dufresne et al*. [2002].

To estimate the water vapor effect on IR aerosol forcing, we performed additional calculations varying the total water vapor content. We scaled the RH vertical profile by the total

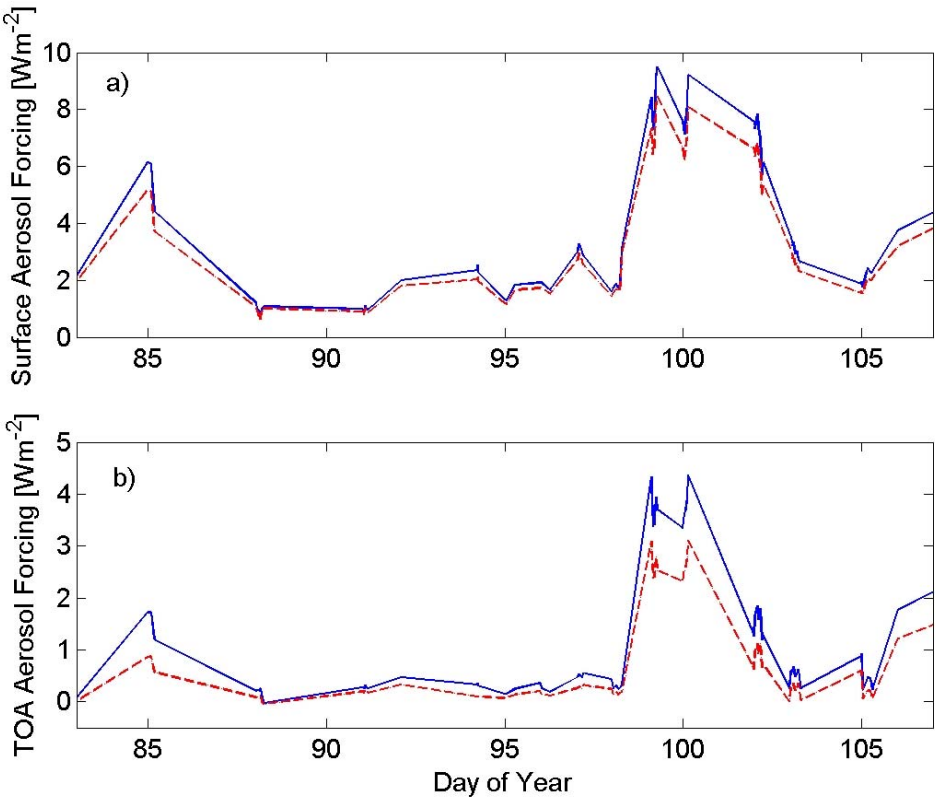

Fig. 5.23 The surface (a) and the TOA aerosol IR forcing as a function of the Year Day. Computation is either exact (solid blue line) or neglects scattering (dotted red line).

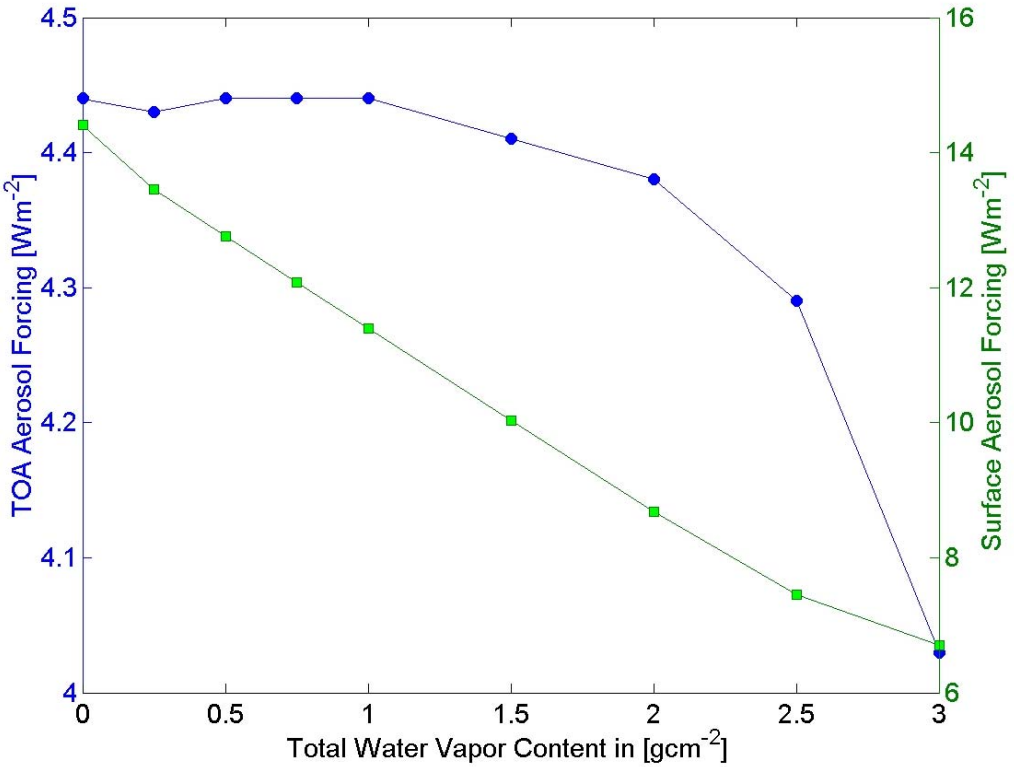

Fig. 5.24 The TOA (solid blue circles) and the surface (solid green squares) aerosol forcing as a function of the total water vapor content.

water vapor content, which varied from 0 g/cm^2 to 3 g/cm^2. Fig. 5.24 shows the TOA (blue circles) and the surface (green squares) aerosol forcing computed on YD99. Increase of total water vapor from 0 g/cm^2 to 3 g/cm^2 leads to large decrease of the surface aerosol forcing by about 50% while it is only 9% at the TOA. Relationship of the total water vapor content on the TOA and the surface IR aerosol forcing is complicated and depends on vertical profiles of water vapor and the extinction coefficient. In the case presented in this paper, the TOA IR aerosol forcing is in first approximation independent on total water vapor content between 0 and 2 g/cm^2 although the surface forcing changes significantly. This small influence of water vapor on the infrared TOA indicates that one can retrieve infrared aerosol effects from satellite observations. On the other hand the set of all the cruises' data do not show a significant correlation between the longwave surface aerosol forcing and the total water vapor in a column because optical depth and temperature provide the dominant effect.

5.6 Conclusions

The transect from Honolulu to Japan aboard the NOAA Ship *Ronald H. Brown* during ACE-Asia provided the opportunity for detailed measurements of aerosol properties and their radiative effects. Conditions ranged from "clean" regions of the central Pacific, to highly polluted and dusty conditions in the proximity of Asia and Japan. The large gradient in optical depth observed while passing from the open Pacific Ocean to near the Asian continent is similar to observations during INDOEX (Fig. 5.2), where the transition between the clean Southern Hemisphere to the polluted Northern Hemisphere was observed.

Close to Asia, the ship crossed the oceanic polar front at 38°N in the Sea of Japan, which determined sea surface temperature and relative humidity. We observed hazy conditions when the water was cool and the relative humidity approached 95%. In retrospect, other recent field campaigns devoted to aerosol radiative effects (e.g. MINOS and INDOEX) were conducted in the regions with large relative humidity gradients and reported widespread haze.

We show from the direct observations that water uptake changes radiative solar aerosol efficiency. This efficiency is approximately -60 Wm^{-2} as follows from estimation based on the data from our cruise in the Sea of Japan and Twin Otter flights [*Conant et al.*, 2003]. Numerical calculations provides evidence that a 25% decrease in relative humidity enhances the surface forcing efficiency by 6 to 10 Wm^{-2}. RH influence on forcing itself was not modeled, but recent studies show that the role of hygroscopic growth on direct radiative forcing at the surface is

significant [*Im et al.*, 2001; *Kotchenruther et al.*, 1999]. Though some certain recent study suggests that aerosol efficiency is largely invariant in space and time, and is approximately equal to –80 Wm^{-2} [*Kaufman et al.*, 2002]. However, our results point out that there may be important synoptic scale regional differences caused by relative humidity variations.

Additionally, the aerosol infrared radiative forcing is studied in detail. On the basis of chemical measurements and optical properties in the visible band (MPL lidar and sunphotometer observations) the infrared aerosol optical thickness, the single scattering albedo, and the asymmetry parameter were estimated. The surface model results were compared to more detailed FTIR based observations of *Vogelmann et al.* [2003]. The uncertainty of their method is about $\pm 1 Wm^{-2}$. The rms of the difference between the FTIR and our model calculations is about 1.6 Wm^{-2}. Possible discrepancies may be related to uncertainties in the vertical representations of the chemistry, uncertainties in dust properties, errors in lidar extinction retrievals, and errors in the visible AOT estimate. Despite these errors, many features are properly resolved by the present model. This combined approach augments the FTIR observational study, validates the optical

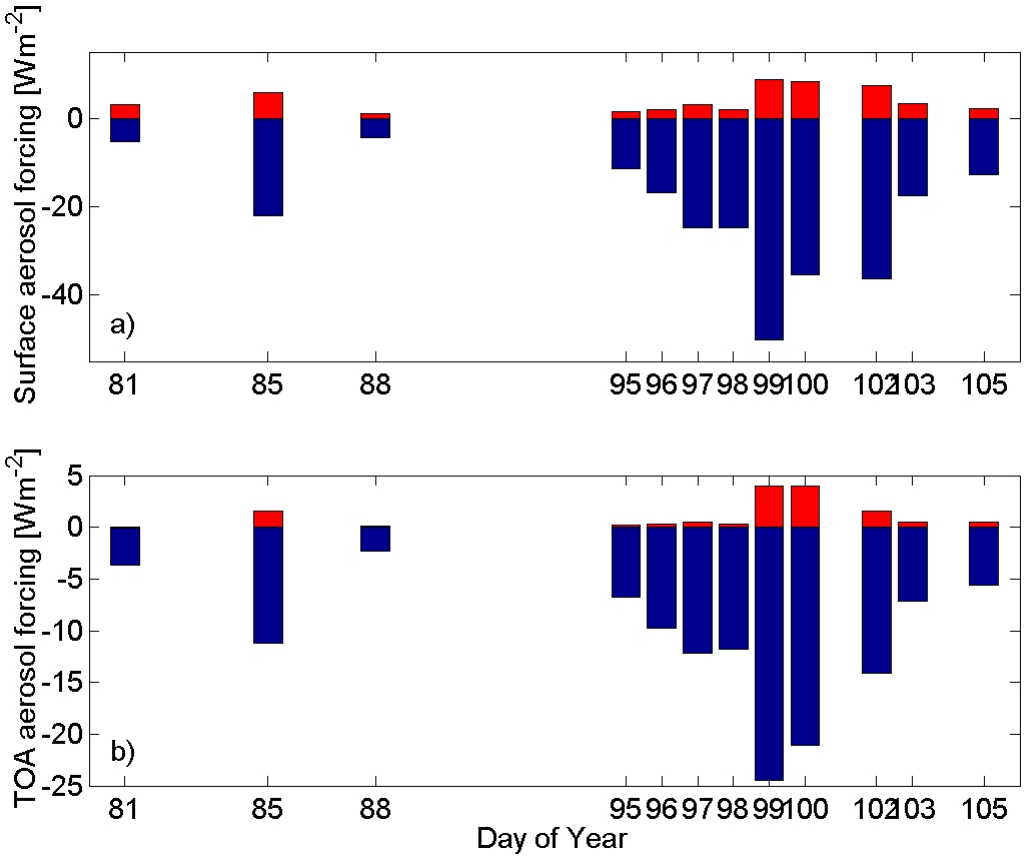

Fig. 5.25 Comparison between (a) the surface and (b) the TOA shortwave and IR aerosol forcing. The positive values correspond with the IR forcing and negative values are for the solar aerosol forcing.

model, and thus provides a technique of deriving infrared forcing at the TOA, as well as, estimating infrared single scattering properties of aerosols. The mean infrared AOT at 10 μm was 0.08 (±0.07) and SSA was 0.55. The infrared aerosol forcing reaches up to 10 Wm^{-2} during the ACE-Asia cruise which is a significant contribution to the total direct aerosol effect. Fig. 5.25 shows the mean daily solar and longwave aerosol forcing at (a) the surface and (b) the TOA. The surface IR aerosol radiative forcing (Fig. 5.25a) is between 10 to 25% of the solar aerosol forcing. The infrared TOA aerosol forcing is between 1% to 19% of the solar aerosol forcing (Fig. 5.25b). Results show that the effect of negative solar aerosol forcing during days with large AOT (YD99, YD100, YD102) is reduced by the IR forcing by about 20%. Over the Sea of Japan, the mean solar forcing during the ACE-Asia was -26.1 Wm^{-2} [*Markowicz et al.*, 2003a] and the total solar-IR radiative forcing was –21.5 Wm^{-2} at the surface. At the TOA the mean shortwave forcing was –12.7 Wm^{-2} and the total was -11.2 Wm^{-2}. It was found that the infrared AOT is strongly correlated with the infrared aerosol forcing at the TOA and at the surface, following from Fig. 5.25. We shown that for a constant aerosol temperature, the TOA and the surface forcing are linear functions of the infrared AOT. This means that the infrared forcing efficiency is a useful parameter for describing the aerosol effects at the TOA and at the Earth's surface. The TOA forcing efficiency is a fast varying function of the aerosol layer temperature and changes between 10 to 18 Wm^{-2} (per unit of infrared optical depth) while the surface forcing efficiency varied between 37 and 55 Wm^{-2} (per unit of infrared optical depth). For comparison, the solar aerosol forcing efficiency over the Sea of Japan was –27 Wm^{-2} (per unit of infrared optical depth) and -58 Wm^{-2} (per unit of infrared optical depth), respectively, at the TOA and at the surface.

6 A Large Reduction of the Solar Radiation Over Mediterranean Sea[9]

This chapter presents a study of the direct aerosol effect on the solar radiation budget over the Mediterranean Sea. We briefly discuss circulation above this region which leads to convergence of pollution during the summer time. In particular the patterns flow supplemented with vertical profiles of the aerosol properties show that strongly absorbing pollution from southern part of Asia can be found in upper troposphere over the Mediterranean Sea. In the lower troposphere (mostly in the boundary layer) aerosol produced by biomass burning plays particularly important role.

Our studies presented in this chapter are based on the observational data. We developed two independent methods to determine the aerosol forcing. The first one uses the broadband instruments (solar spectrum) while the second one uses BSI instruments which measure solar radiation only in the visible range. In the second case, solar radiation is not affected by water vapor, which is the largest source of aerosol forcing uncertainties.

One of the important results of this study was a finding that the aerosol forcing efficiency in periods of biomass burning increases (absolute value) as much as 20 Wm^{-2} (per unit of aerosol optical thickness). This enhancement of the surface aerosol forcing for air masses influenced by the soot from biomass burning is caused by strong solar absorption in the atmosphere.

6.1 MINOS experiment overview

The Mediterranean Intensive Oxidant Study (MINOS) took place in July and August 2001 on the Greek island of Crete. MINOS was a comprehensive field project aimed at investigation of anthropogenic contributions to the environment of the central Mediterranean, and provided measurements of the aerosol chemistry, microphysics, and radiation [*Lelieveld et al.*, 2002]. The objective of the MINOS project was to quantify the main processes involved in

[9]Text of this chapter comes mostly from published paper:
K. M. Markowicz, P. J. Flatau, M.V. Ramana, P. J. Crutzen, and V. Ramanathan., Absorbing Mediterranean aerosols leads to a large reduction of the solar radiation at the surface, Geophysical Research Letter, 29(DX), 10.1029/2002GL015767, 20022002

the Mediterranean pollution build-up; transport of pollution from Europe and from remote sources, chemical mechanisms that contribute to the build-up of oxidants and aerosols, and export of pollutants to the global environment, e.g. towards southeast Asia.

The coastal measurement station Finokalia in the north-eastern part of Crete at 35.34 N, 25.67 E about 265 m above sea level was used to measure aerosol optical, physical, and chemical properties, trace gases and meteorological parameters. Falcon and King Air aircraft were operated from the Heraklion airport, performing measurement flights across the Mediterranean.

6.2 Meteorological overview

The typical pressure distribution in July and August in the Mediterranean Sea region presents a shallow low, located in the proximity of Rhodos Island (south west coast of Turkey) and a high pressure area localized in the Tyrrhenian Sea. The pressure gradient around Crete is very stable (about 1hPa/100 km) and has a north-east direction. This causes a north and northwest gradient wind of 10-13 m/s which is fairly strong for this season. In July and August this flow (bottom panel on Fig 6.1) carries polluted air masses from Eastern and Central Europe.

In the mid-troposphere, weak westerlies cause advection of air masses from the West Europe and the Atlantic Ocean (middle panel on Fig. 6.1). In addition, dust events in Northern Africa are triggered by synoptic disturbances in that region and are advected towards Eastern Mediterranean. In the upper troposphere (upper panel on Fig. 6.1), air masses originate over the Atlantic Ocean or southern Asia depending on the strength of the upper level anticyclone over northern Africa. The circulation from southern Asia at 8-12 km is influenced by Tibetan plateau low pressure system. Low troposphere air masses from this region are transported by deep convection associated with the summer monsoon to the upper troposphere and subsequently transported by the eastern jet stream over Africa and the Mediterranean Sea. During summer, the eastern part of the Mediterranean Sea is a convergence region of pollution from Central Europe, north west Africa and south Asia. Central Mediterranean Sea in summer is under the influence of the subsiding branch of the Hadley circulation. This is responsible for the mostly clear sky conditions. Therefore, this region provides an excellent environment for studying the radiative effects of anthropogenic aerosols.

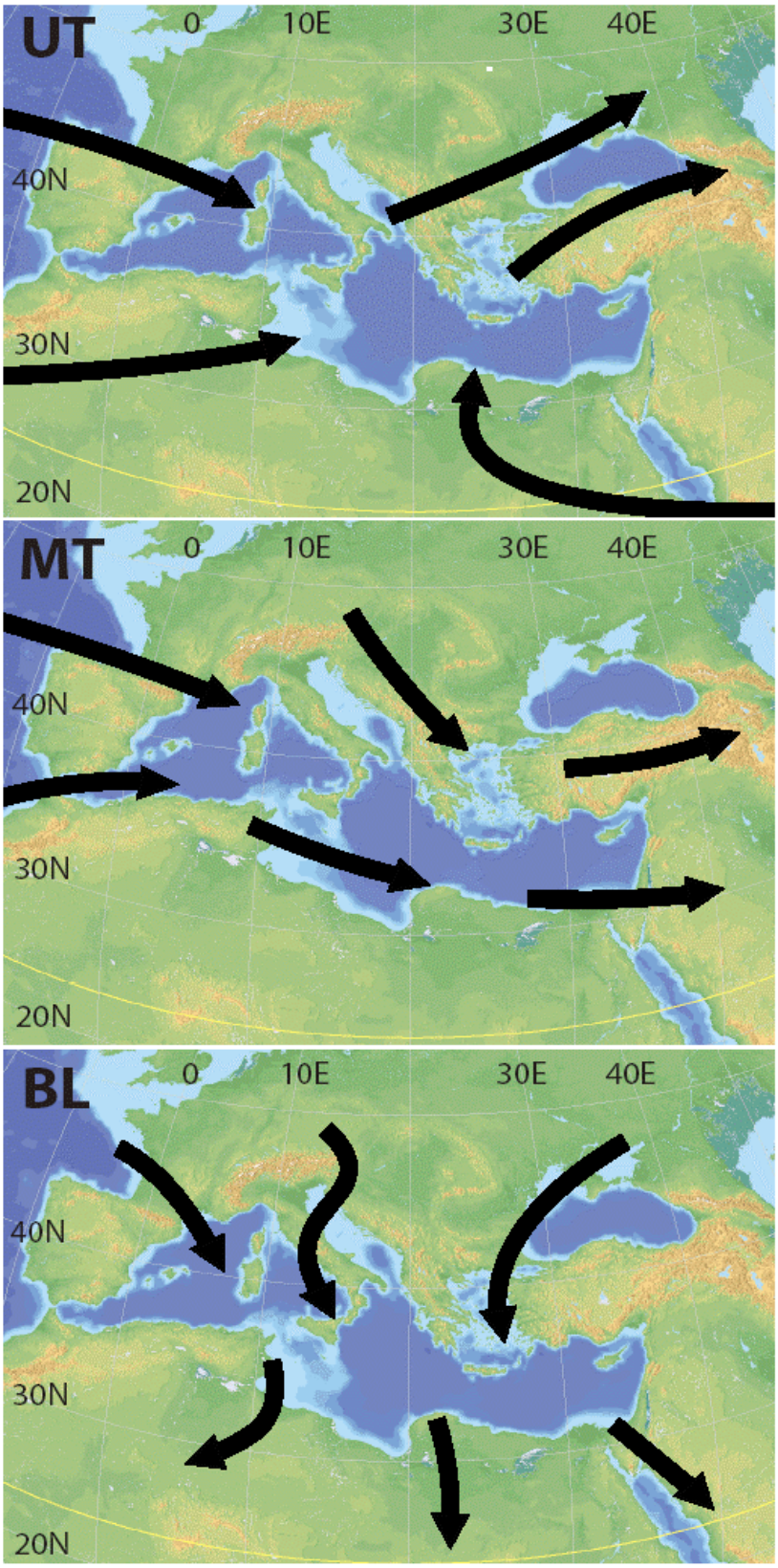

Fig. 6.4 Atmosphere circulation during summer over Mediterranean Sea. Upper, middle, and bottom panel show mean flow in upper, middle troposphere, and in the boundary layer respectively.

6.3 Instrumentation setup

During the MINOS experiment radiation flux measurements were performed at the Finokalia Sampling Station, where the average wind speed was about 8 m/s, and grassy terrain prevented local dust mobilization [*Mihalopoulos et al.*, 1997]. Total and diffuse broadband radiative (280-2800 nm) fluxes were obtained using CM21 Kipp and Zonen pyranometers (see more detail in Appendix A1). The direct flux was measured by a CH1 Kipp and Zonen pyrheliometer (Appendix A1) mounted on a sun tracker. In order to minimize the water vapor impact on radiative forcing uncertainty determination, we used two GUV-511 Biospherical Instruments radiometers (Appendix A1); one of them was shadowed and another was non-shadowed. Together, they measure diffuse and total (sum of direct and diffuse fluxes) radiation fluxes in the visible band (400-700 nm). Aerosol optical thickness in the visible and near infrared (at 380, 440, 500, 675, 870, and 1020 nm), total columnar water vapor and ozone were obtained using the MICROTOPS instrument [*Morys et al.*, 2001] (see Appendix A3) and the Analytical Spectral Device (FS Dual VNIR) (see Appendix A4).

The aerosol absorption coefficient at the surface was obtained from the Particle Soot Absorption Photometer (PSAP) produced by Radiance Research [*Bond et al.*, 1999]. Measured values were corrected for a scattering artifact, the deposit spot size, the PSAP flow rate, and the manufacturer's calibration. Measurements of aerosol scattering and hemispheric backscattering coefficients were made with an integrating nephelometer (Model 3563, TSI Inc.) at wavelengths of 450, 550, and 700 nm at ambient relative humidity.

The top of the atmosphere fluxes were obtained from the Clouds and Earth Radiant Energy System (CERES) instrument onboard NASA's TERRA satellite [*Wielicki*, 1996].

6.4 Aerosol optical depth and single scattering albedo

Fig. 6.2 shows variation of the aerosol optical thickness (AOT) during July and August of 2001. AOT at 500 nm (open squares) ranges from 0.08 to 0.5 and has significant daily and monthly variability. The average clear sky AOT values during MINOS experiment was 0.21 (and 0.25 for all days), which is characteristic for polluted areas (e.g., the mean value for the Arabian

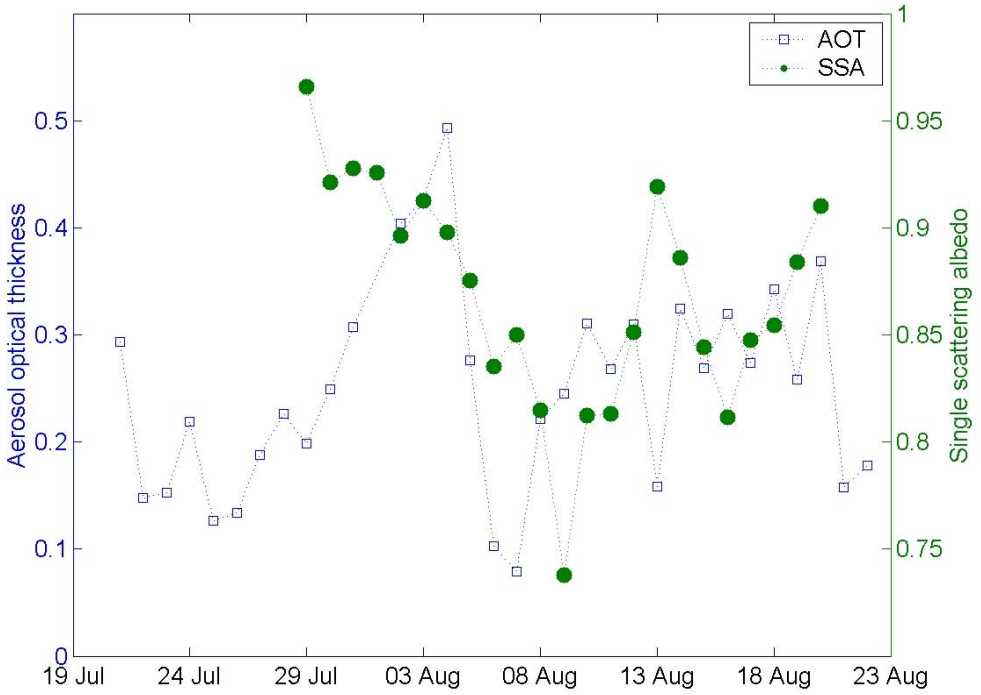

Fig. 6.2. Temporal variation of mean daily aerosol optical thickness (open squares) at 500 nm and single scattering albedo (solid circles) at 550 nm during July and August 2001.

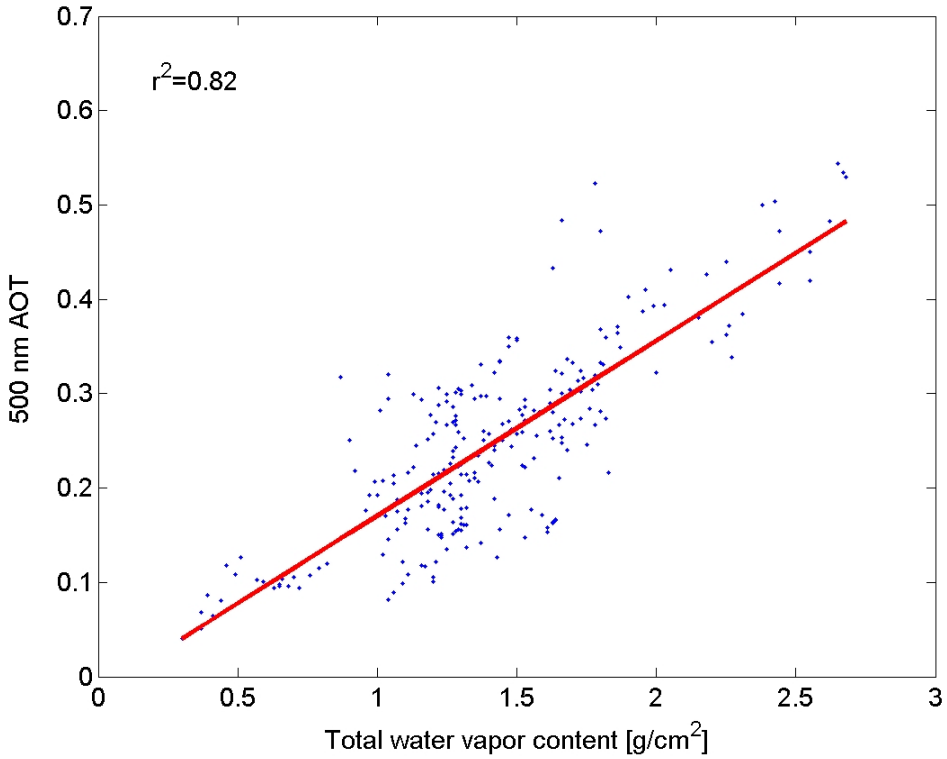

Fig. 6.3 Aerosol optical thickness at 550 nm as a function of the total water vapor content based on the MICROTOPS observations. Solid line corresponds to linear fit.

sea during the INDOEX experiment was about 0.25 [*Eck et al.*, 2001]). For example, the large value around August 4th is associated with increased humidity due to local orographic forcing.

On the basis of all the data collected, it was found that a strong correlation between AOT and total water vapor content (Fig. 6.3) exists, which indicates that water vapor may have a strong impact on aerosol optical properties at Finokalia sampling station and further indicates that soluble species, such as sulfates, nitrates and oxidants organics, may be components of pollution over that part of the Mediterranean Sea. This agrees with conclusions of chapter 5 with respect to relation between water vapor and optical properties of aerosol.

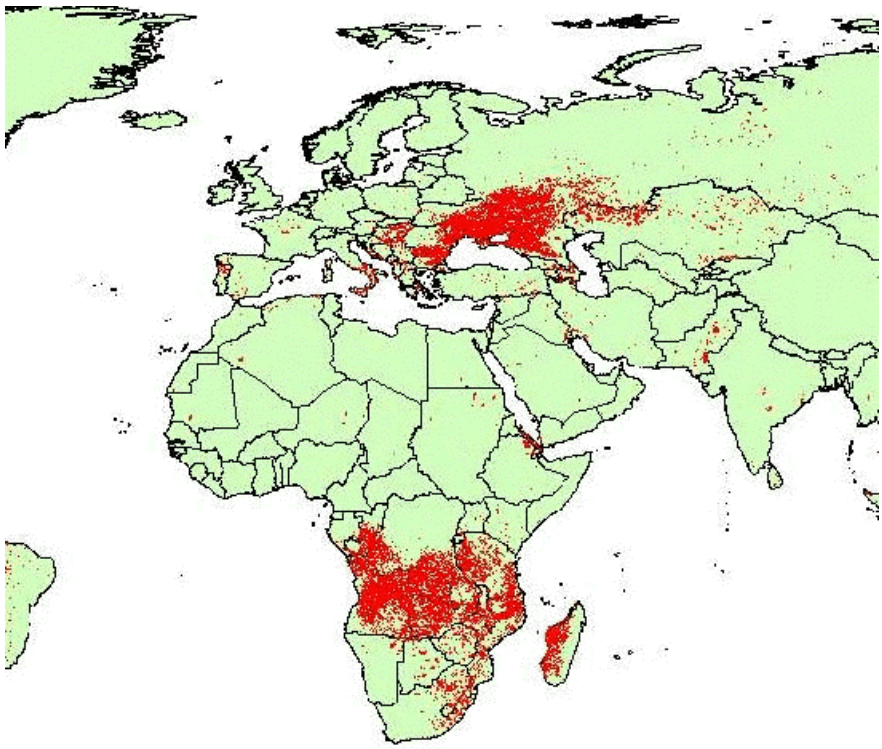

Fig. 6.4 MODIS- Land Fire Detection shows distribution of fires for the month of August 2001. Each detection represents the center of a 1 km pixel flagged by the algorithm as containing a fire within that pixes (University of Maryland prototype fire product).

Several days during MINOS campaign (e.g. from 6 of August to 12 of August, see solid circles on Fig. 6.2) biomass burning in Greece, Turkey and Ukraine (Fig. 6.4) had a strong influence on aerosol properties over Finokalia station. The absorption coefficient during this period was about three times larger (about 30×10^{-6} m^{-1}) than its typical value at the Finokalia station. This change of absorption coefficient was not observed at the Psiloritis station (1700 m above sea level and 70 km from the Finokalia station) what suggests that only the boundary layer aerosol was affected by biomass burning. Single scattering albedo (SSA) at 550 nm during biomass burning was only about 0.8 (solid circles on Fig. 6.2). For comparison, SSA before the

time of fires was larger than 0.9. Variability of the AOT and SSA during the MINOS experiment was correlated with mesoscale disturbances passing over Central Europe. During August 12th and 13th an active cold front crossed Central Europe and brought clear arctic air masses. Because of that, the decrease of AOT to 0.15 and the increase of the single scattering albedo to 0.92 were observed. A similar situation occurred between the 6th and 7th of August.

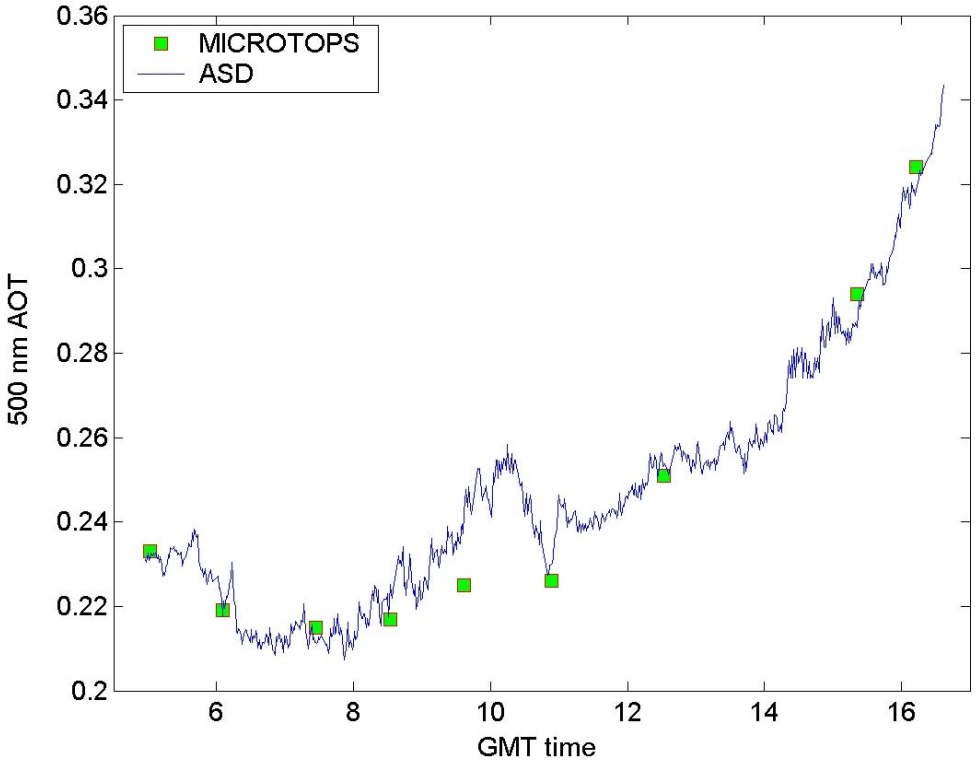

Fig. 6.5 Comparison of 500 nm AOT measured by the MICROTOPS and the ASD on Aug 9th.

Large daily variability of the AOT at 500 nm is shown on Fig 6.5. During August 9th the increase of the aerosol optical depth is correlated with an increase of the aerosol absorption. For example, during afternoon the aerosol absorption coefficient was about $30x10^{-6}$ m^{-1}, while the mean aerosol absorption in the MINOS campaign was $12x10^{-6}$ m^{-1}. In addition, Fig 6.5 shows excellent agreement between the AOT obtained from the MICROTOPS (green squares) and the ASD (blue solid line) instruments. The ASD measured the AOT spectra continuously (one spectra every 1 minute). Therefore, the solid line has a lot of the spikes associated with a turbulence effect on the pollution distribution. Notice, that the Finokalia station is localized about 400 meters from the coastline and the circulation is influenced by the local sea breeze and anabatic and katabatic winds.

A column of integrated aerosol properties are described by the Ångstrom exponent, which is defined here as

$$\alpha = -\frac{\ln(\tau_{500}) - \ln(\tau_{1020})}{\ln(\lambda_{500}) - \ln(\lambda_{1020})} \tag{5.1}$$

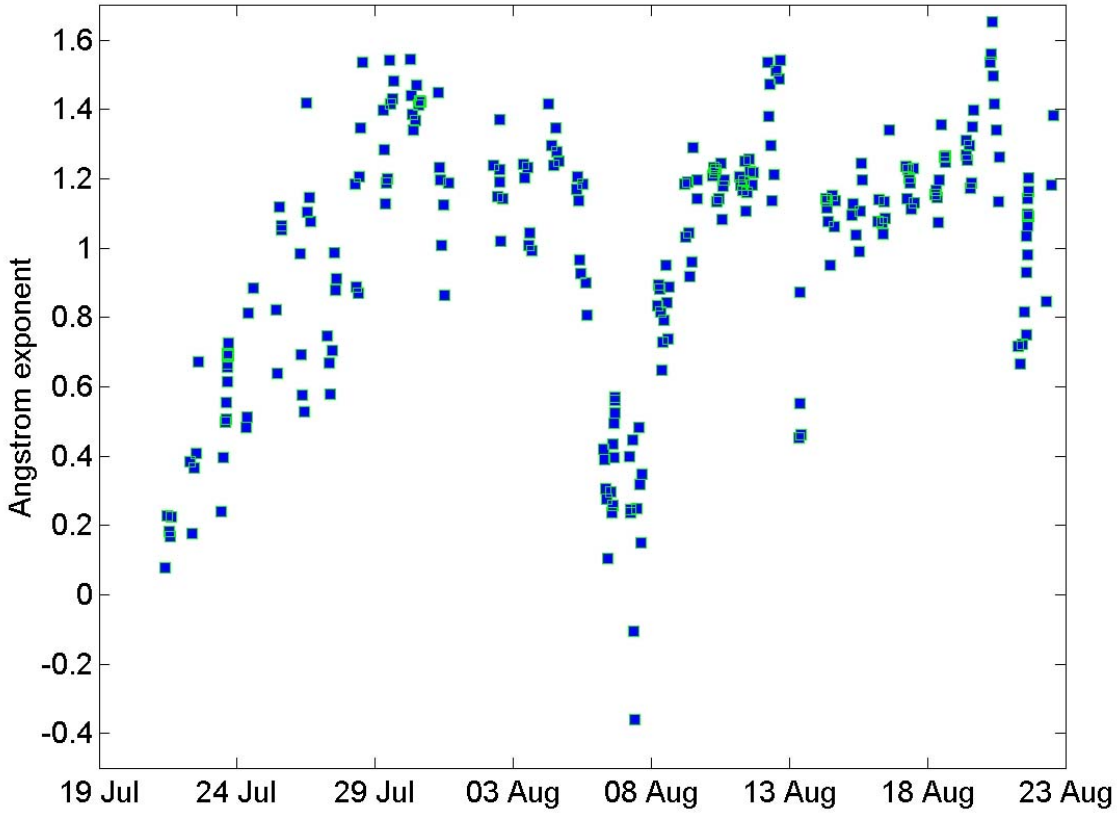

Fig 6.6 Temporal variation of the Ångstrom exponent based on the AOT at 500 and 1020 nm during July and August 2001.

If we assume that the aerosol size spectrum is described by the superposition of two lognormal distributions, the Ångstrom exponent is a function of the ratio of the particles number in accumulation and coarse mode. The Ångstrom exponent for large particles is close to zero, while for small particles it is larger than 1. Fig. 6.6 shows temporal variation of this parameter during the MINOS campaign. The Ångstrom exponent is well correlated with AOT at 500 nm (r^2=0.65) and its smallest values correspond to clear days. Thus, it is implies that the decrease of the AOT is associated with a decrease in the small particles number and is consistent with the fact that accumulation mode has the largest contribution to the total AOT.

The large AOT measured around August 4th cannot by explained by hygroscopic growth of the particles only (see Fig 6.3), but also by an increase in the number of particles in the accumulation mode, which is correlated with high values of the Ångstrom exponent (1.2-1.4).

6.5 Solar aerosol forcing.

Methodology of determination of the aerosol forcing was descried in chapter 3. In this study a hybrid technique [*Conant*, 2000; *Satheesh and Ramanathan*, 2000] is used and the radiative transfer model is used to define clear sky radiative fluxes for a given tropospheric sounding. Additionally, a simple aerosol-optical model was developed, aimed at interpretation of observational results. The aerosol-optical model is based on surface measurements of aerosol optical properties such as scattering and absorption. At first typically polluted marine aerosol

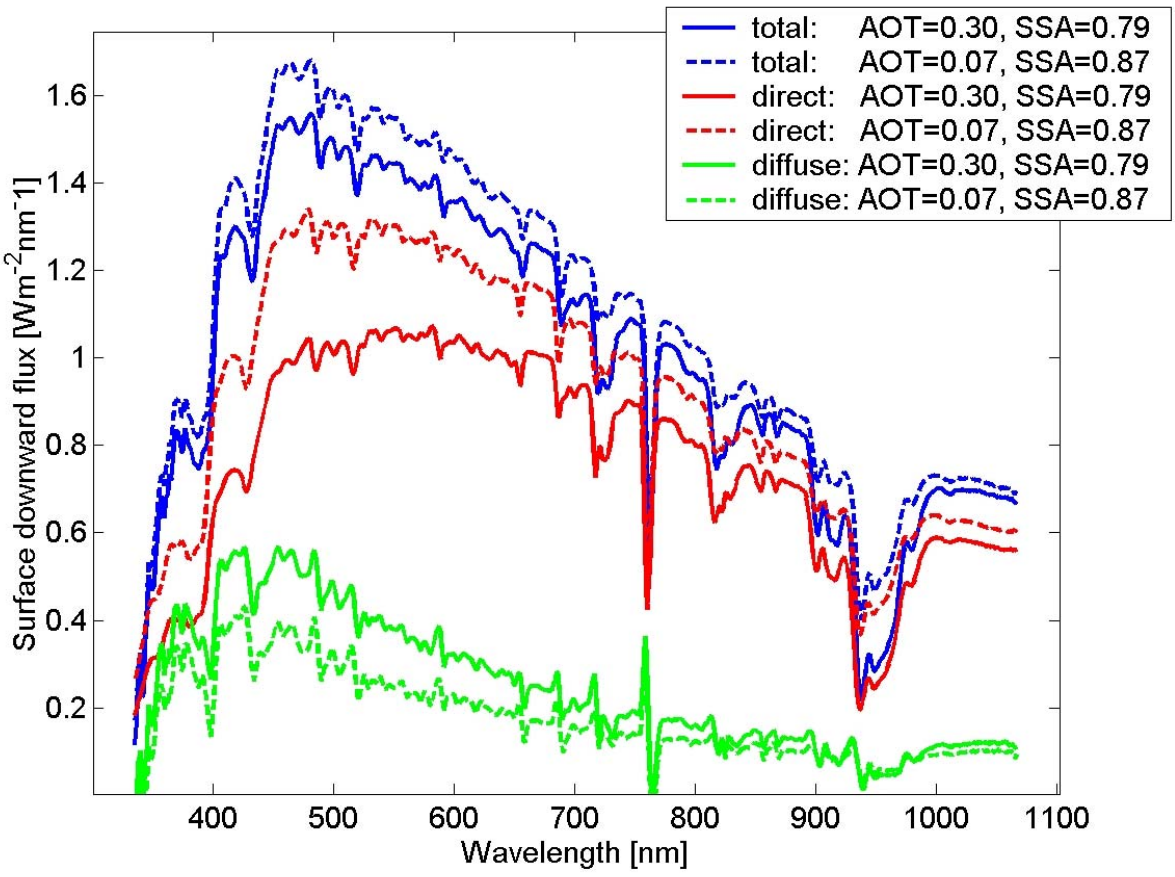

Fig. 6.7 Total (blue line), direct (red line), and diffuse (green line) part of the spectral downward flux during the most pristine day (dotted lines) and polluted day (solid lines). The total and direct spectra are measured for solar zenith angle 20.5° and diffuse irradiance was determined at the difference between total and direct beam.

Type is assumed. Then, soot particles are added until the single scattering albedo and the Ångstrom exponent from observations agree with calculated from aerosol-optical model.

The surface aerosol forcing was determined for 14 clear days. The atmospheric sounding from Heraklion, Crete (00UTC) was used in the radiative transfer model. The vertical profiles of specific humidity was scaled by the total water vapor content from the 0.936 μm channel of MICROTOPS (see Appendix A3).

Significant difference between downward solar flux on August 7th and 11th is shown on Fig. 6.7. Dotted lines correspond to more pristine days (7th of August) with the AOT=0.07 and SSA=0.87. Solid lines mark solar spectra on August 11th while AOT is 0.3 and SSA is 0.79. A reduction of the total flux is about 8% in the visible part of the solar radiation and decrease in UV and infrared. Only at about 940 nm (strong water vapor absorption) the difference between polluted and clear flux is about 40%. A large change of the solar fluxes in this region is due to different total water vapor content. Direct solar flux during the polluted day is about 25% smaller

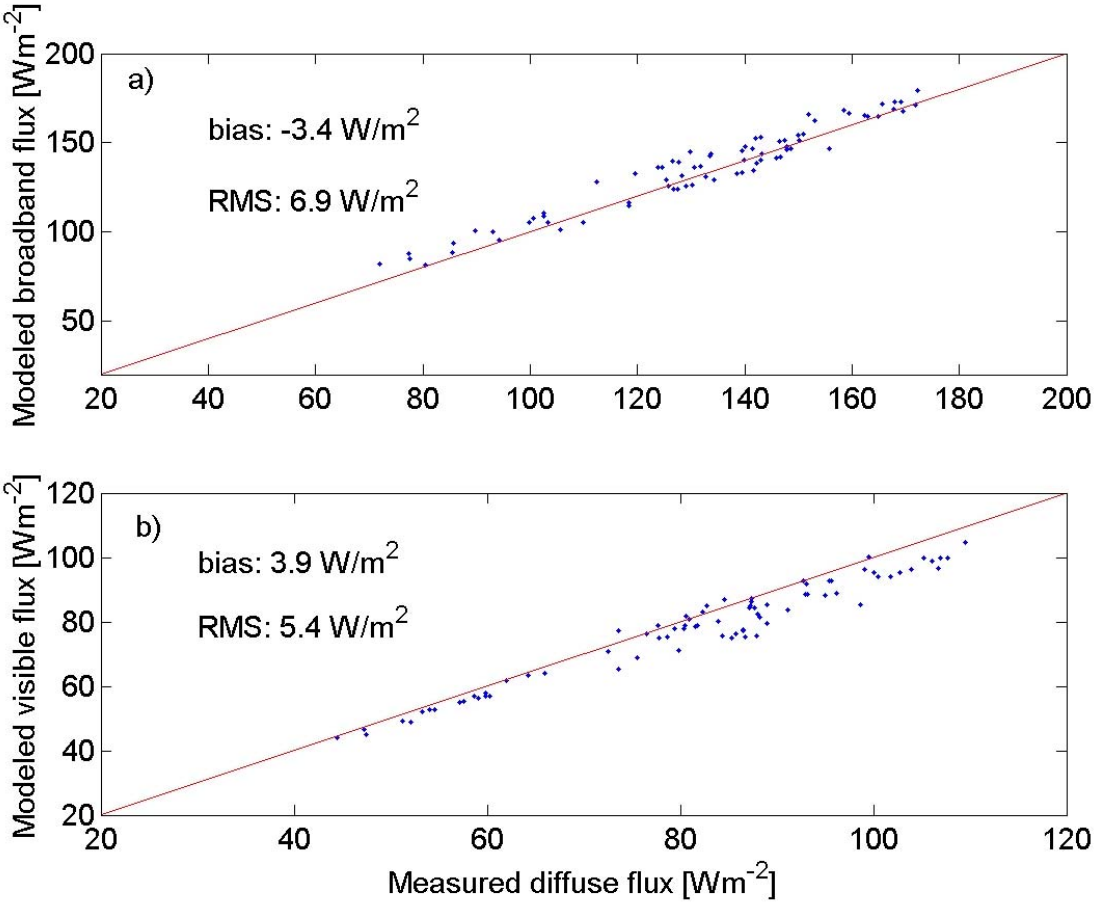

Fig. 6.8. (a) Comparison of measured and estimated surface broadband diffuse fluxes. Solid line corresponds to perfect agreement; (b) The same as (a) but for visible (400-700 nm) range of solar spectrum.

in the visible region. In addition, aerosol leads to change of the direct solar spectrum. The maximum solar irradiance wavelength is at 480 nm for most clean days, whereas the corresponding value for the polluted days shifts to 590 nm. This shift of the maximum towards larger wavelengths is associated with strong wavelength dependence of the AOT.

The major influence of the aerosols is in redistributing radiation from the direct beam into the diffuse skylight by Mie scattering. Therefore the diffuse flux for polluted day exceeds the solar flux for clear day by about 30%. The maximum solar irradiance in both cases is between 430 and 450 nm. A strong decrease of the diffuse fluxes around 480 nm is caused by the Rayleigh scattering.

Fig. 6.8a shows comparison of the broadband diffuse fluxes calculated using radiative transfer model and from the observations. The model results overestimate measured fluxes by 3.4 Wm^{-2} in average. The root mean square (rms) error is 6.7 Wm^{-2} but this difference is within instrumental uncertainty. The comparison of the visible range solar radiation is shown on Fig. 6.8b. In this case the model results underestimates observation by 3.9 Wm^{-2} in average (rms 5.4 Wm^{-2}). Similar differences [*Conant*, 2000] were documented previously.

The top of the atmosphere (TOA) forcing was obtained from CERES on board the TERRA satellite (see chapter 3 for more details). TOA forcing as a function of mean diurnal optical depth at 500 nm is shown in Fig. 6.9a. The flux does not tend to zero for zero optical depth due to offset errors in observations and also due to model errors. However, the slope obtained from the linear fit to the forcing is independent of this bias. The slope, which is the aerosol forcing efficiency, is –31.4 Wm^{-2} with an error of about 10.1 Wm^{-2}. If we ignore two outlier points (the open dots with a forcing of –17 Wm^{-2}) one obtains –39.4 ± 12.8 Wm^{-2}. We do not have a good explanation for the discrepancy, but a possible source of error is cloud contamination and the state of the sea. The forcing efficiency (all days) multiplied by averaged clear sky AOT (0.21) is –6.6±2.1 Wm^{-2} (see Table 6.1) but without the two outlier points it is -8.3±2.7 Wm^{-2} (this is marked by * in front in Table 6.1).

Method	TOA	Surface Broadband	Surface Visible
Observation	-6.6±2.1 *-8.3±2.7	-17.9±2.7	-10.5±1.7
Model, SSA=0.87	-5.9	-18.3	-10.5

Table 6.1 Comparison of mean aerosol direct radiative forcing (Wm^{-2}) between observations and model results. The value indicated by * is without the two outlier points (see text).

The surface aerosol forcing is shown in Fig. 6.9b for broadband flux and in Fig. 6.9c for the visible solar flux (400 to 700 nm). To estimate the total flux we used the sum of the direct and the diffuse components (for details see Appendix A1). Fig. 6.9b shows the daily average

aerosol forcing as a function of aerosol optical depth. Using the same "slope" method we derive

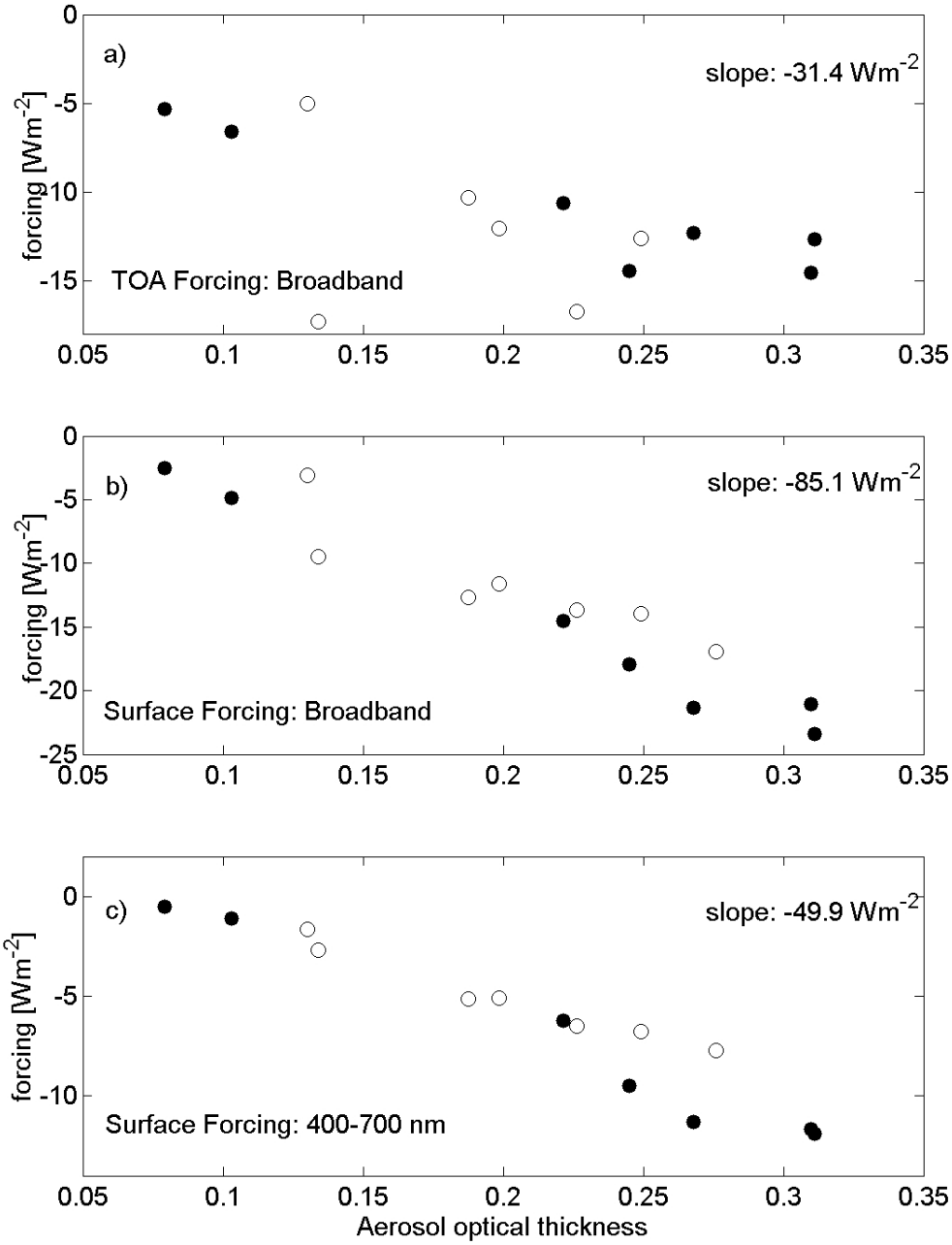

Fig. 6.9. (a) The solar aerosol forcing at the TOA (broadband and diurnally averaged) as a function of aerosol optical depth. The solid circles represent aerosol forcing for days with fires, open circles are for days without fires; (b) the solar aerosol forcing at the Earth's surface (broadband and diurnally averaged); (c) The same as (b) but for visible (400-700 nm) range of solar spectrum.

the mean aerosol forcing for clear sky to be –17.9 ±2.1 Wm^{-2}. The mean aerosol forcing efficiency during MINOS is –85.1 Wm^{-2} (see table 6.1) with 10 Wm^{-2} uncertainty. This forcing is

only about 15% larger than that reported previously [*Satheesh and Ramanathan*, 2000] for the polluted region of the northern Indian Ocean (–75 Wm^{-2}). Figure 6.9c shows aerosol forcing in the visible range of solar spectrum. The mean aerosol forcing efficiency is –49.9 Wm^{-2} and the diurnal reduction of solar radiation is 10.5 Wm^{-2}. An important parameter regulating the aerosol forcing is the vertical distribution of single scattering albedo (SSA), which was not continuously measured during MINOS. The best agreement with the observed forcing and with observed diffuse fluxes at the surface were obtained, when we assumed a column averaged SSA of 0.87. The observations of scattering and absorption (Fig. 6.2) made at the surface are consistent with this value. However, we emphasize that the main thrust of this study is on observed forcing and the model results are only an auxiliary element of this study.

The difference between the cases with and without biomass burning on aerosol forcing is clearly shown in Figs 6.9b and Fig. 6.9c. Solid circles correspond to days with fires (SSA<0.85) and open circles correspond to days without fires (SSA≥0.85); aerosol efficiency is -88 and -71 Wm^{-2} for solar and –52 and –39 Wm^{-2} for visible (see Table 6.2). For days without smoke aerosol forcing efficiency is in good agreement with the INDOEX values [*Satheesh et al.*, 1999] [*Conant*, 2000]. Scaling the visible forcing in Fig. 6.9c to broadband forcing (using the radiative transfer code) one obtains the broadband forcing efficiency –90 Wm^{-2} (fires) and –69 Wm^{-2} (no fires).

An important finding (see Table 6.2) is that during episodes of biomass burning (solid circles on Fig 6.9b and Fig. 6.9c) the forcing efficiency is much larger. The difference between the forcing efficiency for absorbing and less-absorbing aerosols is about -21 Wm^{-2} for broadband and -12 Wm^{-2} for visible solar spectrum range.

Period	Broadband	Visible	Broadband based on BSI
Fires	-88	-52	-90
No-Fires	-71	-39	-69

Table 6.2 Comparison of the mean surface aerosol forcing efficiency (Wm^{-2}) during days with and without fires.

On the basis of this analysis we can derive the ratio of the surface to the TOA aerosol forcing, which is an index for the aerosol absorbing efficiency. For MINOS this ratio is 2.7. For comparison, a model with sulfate or sea salt produces 1.5. When soot is added to the aerosol model the ratio increases to 3.7 for SSA 0.87. Also, the mean atmospheric absorption during MINOS (TOA forcing minus surface forcing) is 11.3 ±3.8 Wm^{-2} (Fig. 6.9). Such absorption leads to a mean diurnal heating rate of about 0.2-0.5 $Kday^{-1}$ in the lower troposphere depending on the vertical distribution of aerosol.

6.6 Summary

The Mediterranean region was subject to pollution from Central and Eastern Europe in the boundary layer and possibly from North Africa and South Asia aloft. The mean value of clear sky aerosol optical thickness at 500 nm and single scattering albedo at 550 nm was 0.21 and 0.87 respectively. Aerosols, mostly of anthropogenic origin, lead to a diurnal average reduction of 17.9 (±2.1) Wm^{-2} in the surface solar radiation, an increase of 11.3 (±3.8) Wm^{-2} (Fig. 6.10) in the atmospheric solar absorption, and an increase of 6.6 (±2.1) Wm^{-2} in the reflected solar radiation at the top-of-the atmosphere. Thus, the present data gives observational proof for the large role of absorbing aerosols (due to industrial pollution from Central Europe and biomass burning from southern Europe) in the Mediterranean. Surprisingly, the negative surface forcing and large positive atmospheric forcing values observed for the Mediterranean aerosols is nearly identical to the highly absorbing south Asian haze observed [*Ramanathan et al.*, 2001b] over the Arabian

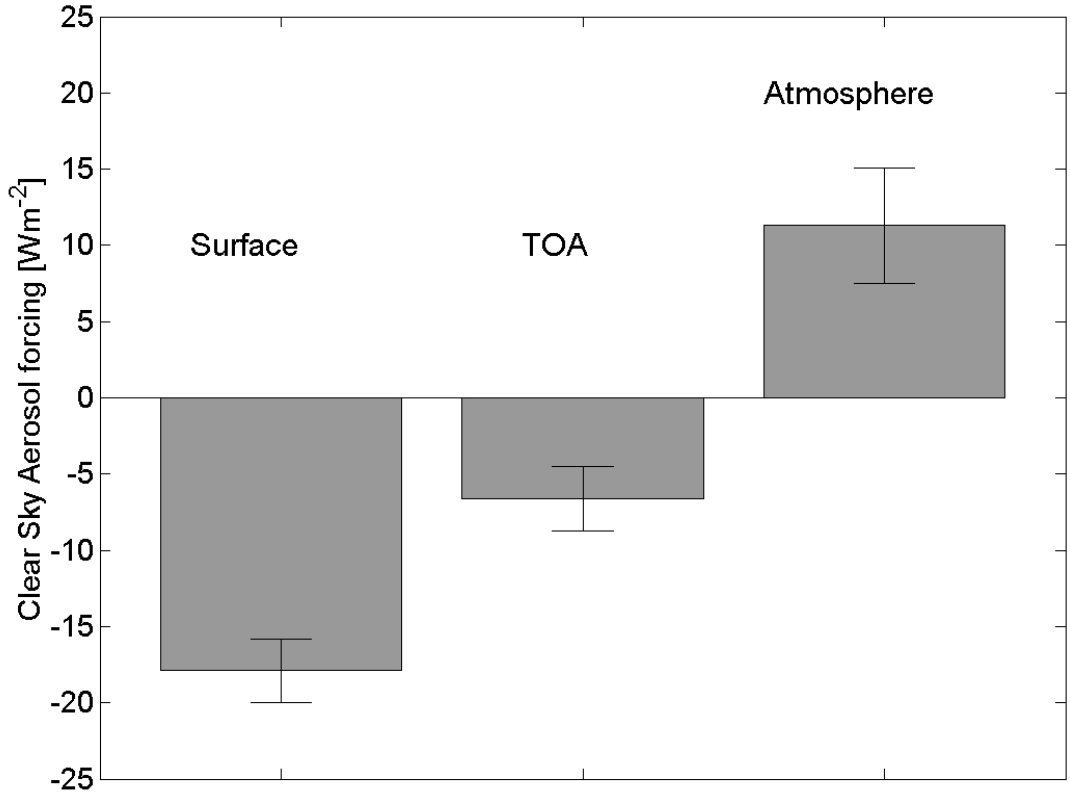

Fig 6.10. The surface, TOA, and atmospheric aerosol forcing.

sea. This similarity raises the urgent need for understanding the absorbing properties and constituents of the aerosols in the Mediterranean region.

The large negative surface aerosol forcing associated with large aerosol absorption (tropospheric heating) may have several important feedbacks. A large reduction of solar radiation absorbed at the surface (diurnal average reduction up to 18 Wm^{-2} and about 65

Wm^{-2} during local noon) may have an impact on the surface evaporation [*Ramanathan et al.*, 2001a], static stability of lower troposphere [*Podgorny et al.*, 2000] [*Vogelmann et al.*, 2001], and suppression of convection by soot heating [*Chung and Ramanathan*, 2002]. It might also lead to a decrease of cloud cover and precipitation which was observed during the last decade [*Long et al.*, 2000].

7 Conclusions

This work contributes to better understanding of the atmospheric aerosols influence on the optical and radiative properties of the Earth's atmosphere bringing a number of new results, which under several respects, change or extend the views present in the literature of this subject. INDOEX, ACE-Asia, and MINOS experiments were carried out in regions affected by different types of aerosol particles of widely varying composition and size. These particles include those emitted by human activities and industrial sources, as well as, wind-blown dust. The experimental results refer to pollution over wide sections of the northern hemisphere. This pollution is being modified while transported. For example, the mineral dust, which can be observed by the satellite transported half way around the globe, is not just dust, it is the dust mixed with other pollutants. Air pollution changes dust aerosols in many ways, adding black carbon, toxic materials, and acidic gases to the mineral particles. Thus atmospheric chemistry and its impact on air quality and climate change are truly global issues.

One of the most important results of this study is estimation of the relative humidity effect on the solar aerosol forcing efficiency. Based on the observations and modeling calculation we found that the mean value of this parameter over the Sea of Japan was only $-60 Wm^{-2}$. Small aerosol forcing efficiency in this region is associated with the effect of high relative humidity on the aerosol optical properties. It was found that decreasing the relative humidity to 55% enhances aerosol forcing efficiency, i.e., decreases its absolute values by as much as 6-10 Wm^{-2} [*Markowicz et al.*, 2003a] as a result of the decrease of the single scattering albedo by hygroscopic particles. Thus, these results point out that there may be important synoptic scale regional differences caused by the relative humidity variations. To the contrary, a recent study [*Kaufman et al., 2002*] suggests that aerosol forcing efficiency is largely invariant in space and time, and is approximately equal to $-80 Wm^{-2}$, and it will be interesting to reconcile this difference in the future. Knowledge of the aerosol forcing efficiency is important and useful for aerosol impact on climate system calculations. The product of this parameter by the aerosol optical thickness (which is relatively easier to measure) provides information about aerosol forcing. Thus, observations of the aerosol optical thickness together with information on concerning the aerosol forcing efficiency, allows estimation of the aerosol forcing at the surface and at the TOA.

Another important result of this work is estimation of the infrared aerosol forcing. Usually, the aerosol impact on the infrared radiative forcing is assumed negligible. However, this

study shows that the infrared forcing can by significant. This follows from the infrared model results which were validated by comparison with detailed Fourier Transform Interferometer, based on infrared aerosol forcing measurements and pyrgeometer infrared downward fluxes. This combined approach attests for the self-consistency of the optical model and allows a derivation of quantities such as the infrared forcing at the top of the atmosphere and the infrared optical thickness. The mean infrared aerosol optical thickness at 10 μm was 0.08 [*Markowicz et al.*, 2003b] and the single scattering albedo was 0.55. The modeled infrared aerosol forcing reaches 10 Wm^{-2} [*Markowicz et al.*, 2003b] during the cruise, which is a significant contribution to the total direct aerosol forcing. The surface infrared aerosol radiative forcing is between 10 to 25% of the shortwave aerosol forcing. The infrared aerosol forcing at the top of the atmosphere can reach 19% of the solar aerosol forcing. Over the Sea of Japan, the average infrared radiative forcing is 4.6 Wm^{-2} in the window region at the surface and it is 1.5 Wm^{-2} [*Markowicz et al.*, 2003b] at top of the atmosphere. The infrared aerosol forcing has opposite sign to the solar aerosol forcing at the TOA and at the surface. Similarly to clouds, aerosols lead to cooling of the atmosphere and the magnitude of this cooling depends strongly on the temperature of the pollution layer. The TOA infrared aerosol forcing efficiency, strongly dependent on the aerosol temperature, changes between 10 to 18 Wm^{-2}, while the surface infrared forcing efficiency varies between 37 and 55 Wm^{-2}. Mineral dust has the largest influence on the infrared forcing, but coarse mode particles (sea salt, sulfate) can also change this quantity.

Although the positive aerosol infrared forcing decreases total (solar plus infrared) aerosol impact on climate, it plays still important role in controlling radiation balance in the atmosphere, at the TOA, and at the surface. Values of the aerosol forcing presented here are significantly greater than the global mean TOA aerosol forcing presented in the IPCC report [*Houghton*, 2001, see also Fig. 1.3]. The mean global solar direct aerosol forcing was estimated there to be from –0.5 to –1.5 Wm^{-2}, but these values are not representative regionally. In polluted regions, the aerosol forcing can be one order of magnitude larger than that given in the IPCC report. Fig 7.2 shows comparison of the mean solar aerosol forcing at the TOA, in the atmosphere, and at the surface during the three campaigns. The largest aerosol impact on the solar radiation budget is observed at the surface. In the Sea of Japan and northern part of the Indian Ocean reduction of the surface solar radiation is about 25 Wm^{-2} [*Markowicz et al.*, 2003a; *Satheesh and Ramanathan*, 2000]. This value corresponds to about 8-10% of total incoming solar radiation. The TOA solar aerosol forcing is about –7 Wm^{-2} over the Indian Ocean and the Mediterranean Sea and –13 Wm^{-2} over the Sea of Japan. Moreover, aerosols significantly change the distribution of sky radiance including the ratio of direct to diffuse irradiance. Increase of the

diffuse flux reaching the surface can be larger than 100% and depends mostly on the aerosol optical thickness and the single scattering albedo.

The next result of this work is an analysis of the aerosol optical properties in different regions and their impact on the radiation balance. Fig. 7.1 and Fig 7.2 show comparisons of the aerosol properties and aerosol forcing over the northern part of the Indian Ocean (INDOEX), the Sea of Japan (ACE-Asia), and the Mediterranean Sea (MINOS). The largest optical depth was measured in the Sea of Japan, where the mean AOT at 500 nm exceeds 0.4 (Fig. 7.1a) [*Markowicz et al.*, 2003a]. However, the aerosol in this region is different from the aerosol observed over the Indian Ocean and the Mediterranean Sea because it does not absorb as much solar radiation (Fig. 7.1b). It was found that high single scattering albedo (SSA=0.95) over the Sea of Japan is connected with

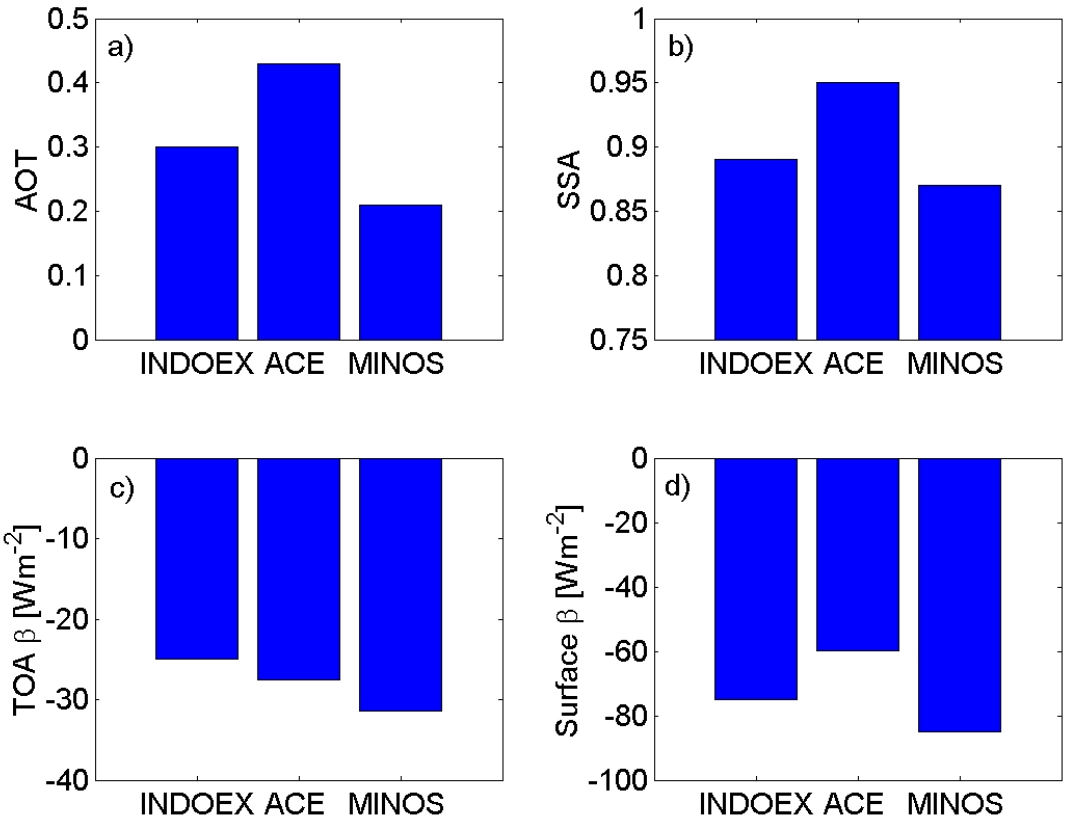

Fig. 7.1 Comparisons of (a) the aerosol optical thickness at 500 nm; (b) single scattering albedo at 550 nm; (c) the TOA aerosol forcing efficiency; (d) the surface aerosol forcing efficiency observed during INDOEX, ACE-Asia, and MINOS experiments.

large relative humidity associated with cold water. Moreover, the dust that is transported from East Asia to the Pacific does not absorb as much light as the dark aerosol from South Asia or some previous measurements of dust from the Sahara Desert [*Diaz at al.,* 2001]. There are

important regional differences in the chemical and optical properties of aerosols. Therefore, we cannot measure dust in one region and assume that dust everywhere around the Earth has the same impact on climate.

Results of the MINOS and the INDOEX experiments show significantly different aerosol properties than pollution observed during the ACE-Asia campaign. Large aerosol absorption in the boundary layer is caused by a high black carbon concentration [*Lelieveld et al.*, 2002; *Ramanathan et al.*, 2001b]. These particles measured during the MINOS experiment were associated with biomass burning in Eastern Europe and with anthropogenic fossil fuel combustion in India during the INDOEX. The mean single scattering albedo observed during the MINOS campaign was 0.87 (Fig. 7.1), while in the "fires" period it decreased to 0.8 what is a relatively small value.

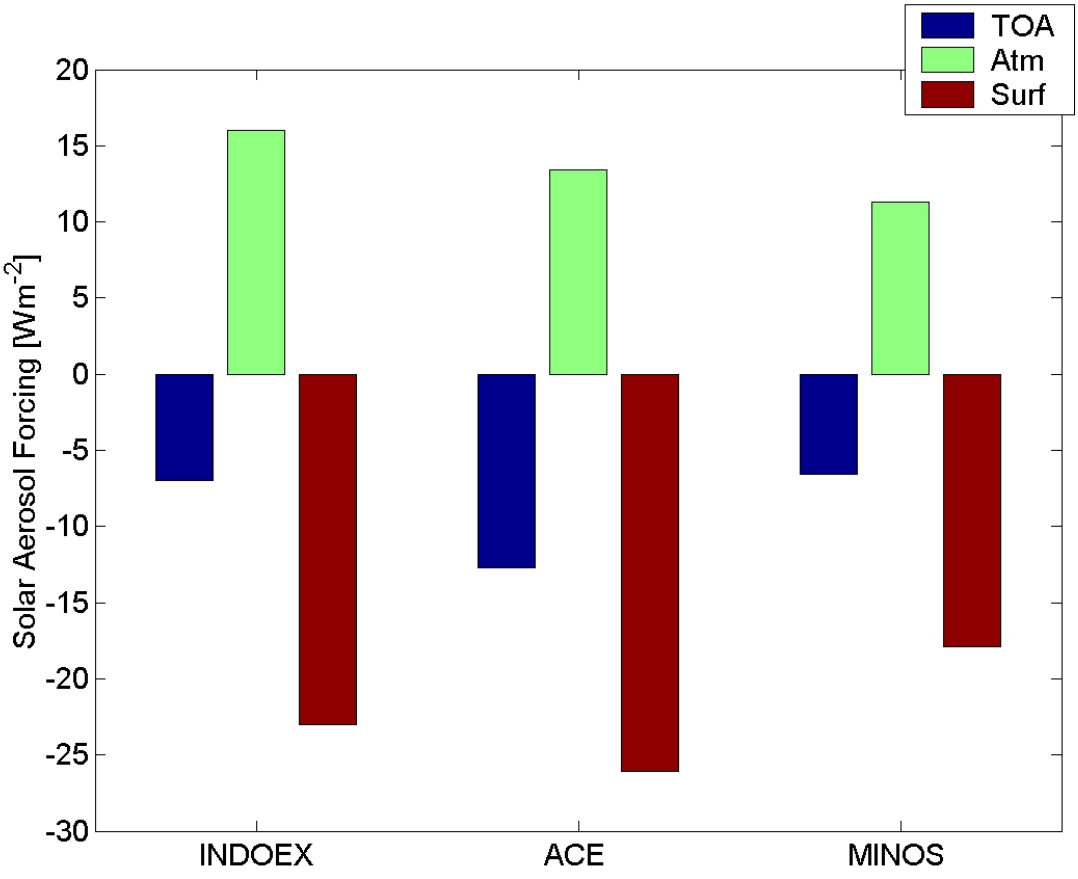

Fig. 7.2 Solar aerosol forcing at the TOA (blue bar), in the atmosphere (green bar), and at the surface (red bar) during INDOEX, ACE-Asia, and MINOS experiments.

Large optical thickness and absorption (small single scattering albedo) of the aerosol leads to significant change in the radiation budget at the TOA, at the surface, and in the atmosphere. Fig. 7.1c and Fig. 7.1d present the TOA and the surface aerosol forcing efficiency

during the INDOEX, ACE-Asia, and MINOS campaigns. The aerosol over the Mediterranean Sea shows the largest impact on the solar radiative balance. Strong reduction of the solar radiation at the surface is caused by large aerosol absorption. Forcing efficiency exceeds –85 Wm^{-2} while observations in the Sea of Japan show lower forcing efficiency of –60 Wm^{-2}.

The solar aerosol forcing in the atmosphere was large and varied from 12 to 16 Wm^{-2} (Fig. 7.2), depending on the aerosol optical thickness and the single scattering albedo. Enhancement of the atmospheric absorption by the aerosol is usually important in the lower troposphere, in the boundary layer. Increase of the solar heating in the lower troposphere can reach up to 50% [*Ramanathan et al. ,* 2001b].

Negative aerosol forcing magnitudes in considered regions is significant, exceeds the green-house gasses forcing and leads to direct cooling of the atmosphere-ocean system. However, the role of aerosol in the climate system is more complicated, because of the aerosol-clouds interaction and large number of possibilities of atmospheric and ocean-atmospheric feedbacks. Large surface cooling and heating in the lower troposphere leads to stabilization the of atmospheric stratification. As the influence of the aerosol occurs mostly in the boundary layer, the largest part of the perturbation of radiation balance is limited to first 2-3 km of the atmosphere. Therefore aerosol forcing affects the surface-atmosphere convective sensible and latent heat fluxes.

Future research along the lines taken in this dissertation can include global effects of the relative humidity on the radiative budget. This is a somewhat neglected topic because most of the climate-sea surface temperature feedback sensitivity studies are performed under the assumption of the constant relative humidity or constant specific humidity. The aerosols have the particular property that their growth depends explicitly on the RH. Another interesting topic is how the hystheresis of the aerosols RH vs single scattering properties can be exploited and parameterized in the Global Circulation Models. It certainly will require a non-local, lagrangian-type, approach. There are efforts underway now to estimate globally the infrared greenhouse effect of dust and pollution based on some of the research proposed and developed in this dissertation. One of the findings here is the large role of the upper level dust on the energy budget over the ACE-Asia region. The research on this topic is being continued. For example, during the recent 2003 ill-fated shuttle flight Columbia the MEIDEX (Mediterranean Israel Dust Experiment) was devoted to investigation of the dust over the Mediterranean Sea.

Appendix A:

In this Appendix we discuss in detail instruments used during campaigns. The first part (A1) contains information about broadband radiometers, their errors, and methods used to reduce uncertainties. In the second part (A2) we present correction techniques which must be performed for lidar. Notice that manufacturer of this instrument does not provide calibrations and corrections needed for interpretation of the lidar signal. In addition we discuss an algorithm which was used to calculate vertical profile of the extinction and backscatter coefficients from the lidar signal. The next part (A3 and A4) contains description of the Langley method used (calibration of the sunphotometers and ASD instruments). Although the sunphotomers (MICROTOPS) were calibrated by the manufacturer we used this technique to check the temporal stability of the instruments. In part A4 of this Appendix we describe one of the most important radiometer corrections used for ASD instruments. This correction deals with deviation from an ideal cosine response of the instrument sensor.

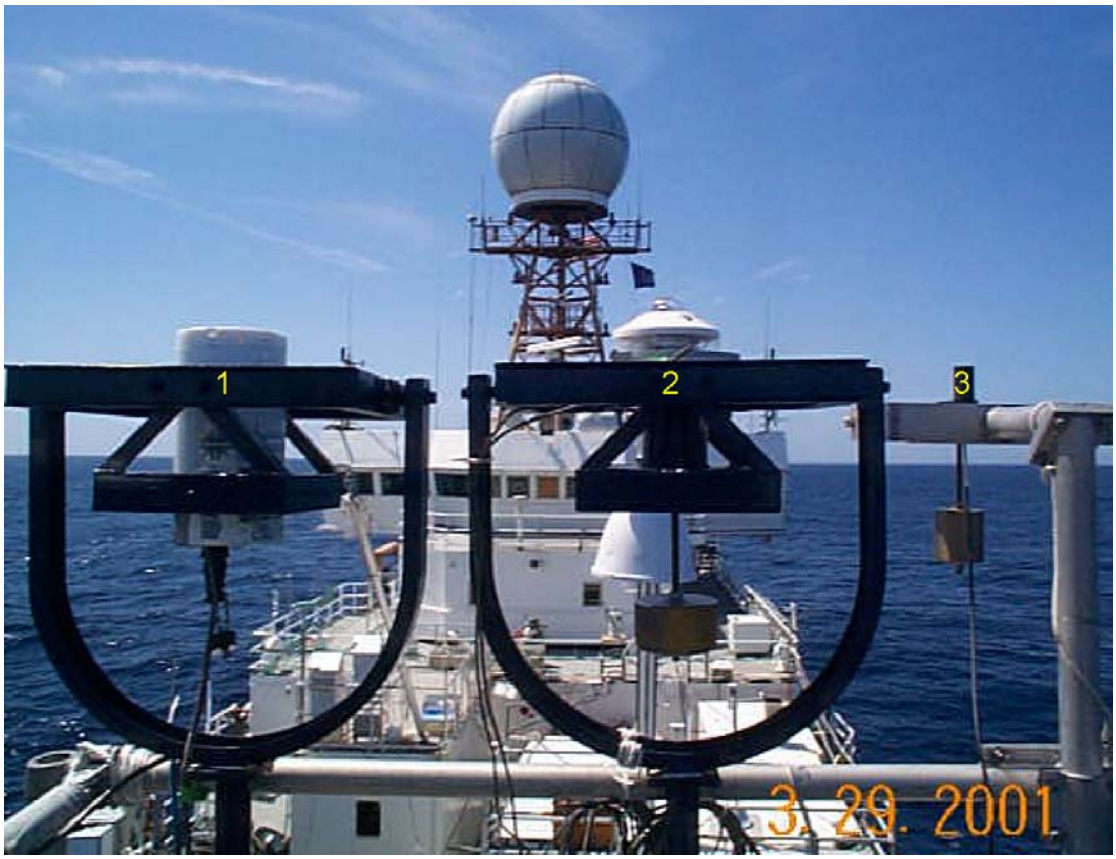

Fig. A1.1: Radiation instruments mounted on gimbaled suspension on NOAA R/V Brown ship during ACE-Asia cruise. (1) GUV-511 Biosherical Instruments, (2) CM21 pyranometer, and (3) total flux analytical spectral device diffuser.

A.1 Broadband instruments

The total broadband radiative (280-2800 nm) fluxes were obtained using CM21 Kipp and Zonen pyranometers. According to the technical specification provided by the manufacturer, this instrument has an absolute accuracy of ±9 Wm^{-2} and the maximum flux error due to incorrect cosine response is ±10 Wm^{-2}. During the ACE-Asia experiment these instruments were mounted on gimbaled suspension (Fig. A1.1) to minimize the ship's pitch and roll. During the MINOS and the ACE-Asia experiments only zero offset correction was performed. This error was measured at nighttime and was as high as –4 Wm^{-2}. Unfortunately zero offset can depend on temperature and may be different during the day [*Bush et al.,* 2000], but this effect is not taken into account in this study. During the MINOS experiment direct broadband (200-4000 nm) and diffuse (280-2800 nm) fluxes were measured by a CH1 pyrheliometer and shadowed CM21 pyranometer. The Kipp and Zonen pyrheliometer and shadowed pyranometer were mounted on the 2AP Kipp & Zonen Sun tracker (Fig A1.2). The manufacturer specified absolute accuracy of

Fig. A1.2 Radiation instruments at the Finokalia station during MINOS experiment 2001. This picture shows sun tracker with (1) CM21 pyranometer, (2) GUV-511 Biospherical Instrumentsradiometers, (3) total flux analytical spectral device (ASD) diffuser, (4) tube with direct flux ASD diffuser, and (5) shading ball.

the pyrheliometer as ±3 Wm^{-2} and that of the shadowed pyranometer ±9 Wm^{-2}. Notice, that the field of view (FOV) of the pyrheliometer is about 5° and the shading ball (affecting the pyranometer) blocks the direct solar beam in the angular radius 3.2° of the solar aureole.

We employed two independent methods for estimating daily average downward total flux. The first one is based on the total fluxes measured by the pyranometer and the second one is based on measurement of a sum of the direct and diffuse fluxes. The second method has better accuracy because a large source of error for a non-shadowed pyranometer is due to the non-cosine angular response of the sensor. Fig. A1.3 shows a comparison of the total fluxes obtained from these two methods. The mean bias of the total fluxes from both methods is –12.4 Wm^{-2} and the rms is 12.9 Wm^{-2}. The total flux obtained directly from the non-shaded pyranometer is significantly larger than determined from the direct and the diffuse fluxes. Although the FOV of the pyrheliometer is a large and direct component, it includes part of diffuse irradiance (see Appendix B) shaded pyranometer blocks sun aureole from FOV=6.4°. Thus, the error of the solar direct and diffuse fluxes due to the FOV of these instruments is small.

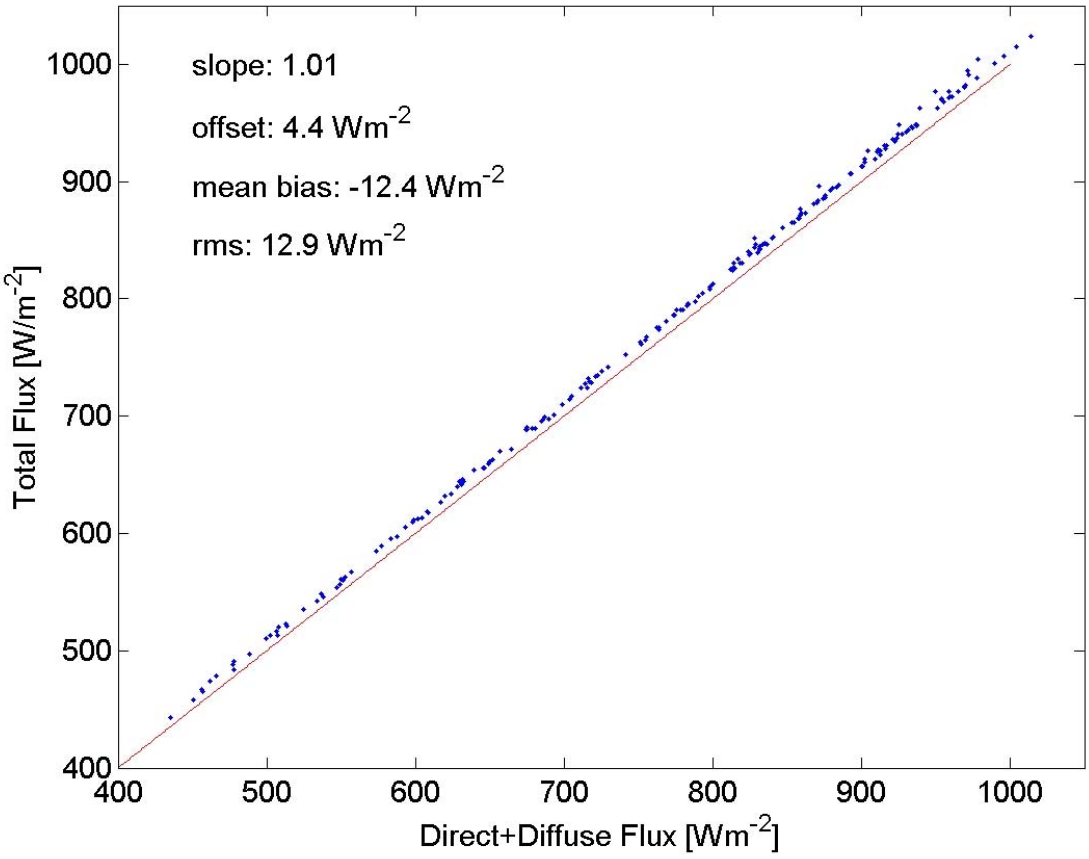

Fig. A1.3: Comparison of the total downward fluxes obtained directly from the pyranometer and the pyrheliometer and shaded pyranometer (direct plus diffuse flux). The solid line corresponds to perfect agreement.

In addition to the solar flux two GUV-511 Biosherical Instruments radiometers (BSI) were used; one of them was shaded and the other was non-shaded. Together, they measure diffuse and total radiation fluxes in the visible region (400-700 nm). The shadowed BSI instrument is shown on Fig. A1.2. GUV-511 and also contains four detectors with filters centered at 305, 320, 340, and 380 nm.

The detector-photodiode in the BSI is temperature stabilized to 50±0.2 °C. The accuracy of the measurement of clear-sky global irradiance is 2.4% and the accuracy of the diffuse irradiance is 1.8%. The BSI instrument has a diffuser with quartz backing, producing a near-isotropic (Lambertian) angular response. The angular response correction of the BSI instruments was measured by *Conant* [2000]. The cosine correction increases with the increase of the solar zenith angle and for 60°, it is about 10% leading to underestimate of the total downward flux.

A.2 Lidar

The Micro Pulse Lidar (MPL) was deployed during the INDOEX [*Welton et al.*, 2002] and ACE-Asia Experiments on R/V Ronald H. Brown ship in order to study the vertical distribution of aerosols. The lidar provides information about the backscatter to extinction ratio and, after additional assumptions, the extinction coefficient. The lidars used during the experiments were operating at 523 nm. The MPL lidar (Fig. A2.1) sends 10 ns light impulses with the frequency of 2500 Hz. The vertical resolution is 75 m. The lidar range is about 20 km during the night and about 6–8 km during the day. Low level and optically thick clouds limit the MPL range. The MPL lidar is a fully eye-safe instrument and allows for full-time, long-term unattended operation.

Fig. A2.1 NASA Langley MPL lidar system

Signal acquisition is performed via photon counting a relatively more accurate and problem free means of handling low level signal than analog detection. For better signal-to-noise ratio the lidar signal was time averaged over one minute.

Let as consider lidar corrections which must be performed to obtain the proper signal. Radiation emitted by lidar laser is gradually dumped in the atmosphere because of molecular scattering, as well as scattering and absorption by aerosols. Backscattered radiation is proportional to backscatter coefficient of molecules and aerosols. In addition, part of the photons is being absorbed or scattered in other directions and is not received by the detector. The signal power returning to detector is

$$\widetilde{S}(z) = \frac{CE}{z^2}\left[\beta_R(z) + \beta_A(z)\right] Tr_R{}^2 Tr_A{}^2, \tag{A2.1}$$

where C is instrument constant, E is initial impulse power, z indicates distance from the detector, β_R , β_A define backscatter coefficients for molecular and aerosols, respectively, Tr_R Tr_A are molecular and aerosol transmission. This transmission includes extinction on the path between a scattering particle and the instrument receiver. Taking into account air transmission we get

$$\widetilde{S}(z) = \frac{CE}{z^2}\left[\beta_R(z) + \beta_A(z)\right] \exp\left(-2\int_0^z \left[\sigma_R(z') + \sigma_A(z')\right] dz' \right), \tag{A2.2}$$

where: σ_R , σ_A define molecular and aerosol extinction. The signal defined by Eq.A2.2 has to be corrected. The corrections include deadtime, background, overlap, and afterpulse corrections.

Deadtime correction compensates for the system photon detectors inability to compile accurate returned photon count rates. Relatively high return rates are simply too fast for the system to count. The detector in the MPL lidar comes with a customized deadtime correction chart and is included in the MPL software. Background correction is associated with a portion of returned photons which comes from ambient light. This correction depends on solar radiation intensity and the precision of the electronic system. The afterpulse correction subtracts a residual signal signature that occurs due to “bleeding” of photoelectronics out of the photon detector with time. The afterpulse correction is determined by blocking the lidar and removing the remaining signal. The last correction (overlap correction) is associated with the signal degradation in the near range caused by the field of view (FOV) conflicts in the transmitter-receiver system. This correction is known as nearfield correction because the part of photons backscattered close to lidar cannot be recorded by detector. The range of the overlap varies from tens of meters to a few kilometers depending on the type of lidar. In the case of the MPL NASA lidar the overlap correction should be done up to the first 2 km.

After all recorrections we introduce the so-called the range corrected lidar signal which can be written as:

$$S(z) = \frac{S_l(z) - S_b - A(z)}{O(z)E} z^2 = \frac{\widetilde{S}(z)}{E} z^2, \tag{A2.3}$$

where S_1 defines the measured signal, S_b is background correction, A(z) is the afterpulse correction, and O(z) is the overlap correction.

The lidar calibration is an important factor determining the final results. The overlap correction is determined with lidar pointing horizontally. The measurement assumes that the atmosphere is horizontally homogeneous. In such a case the backscatter to extinction ratio and extinction itself does not depend on the distance from the lidar. Accounting for the overlap correction, the lidar signal can be written as

$$S(z) = O(z)C\beta \exp(-2\sigma z), \tag{A2.4}$$

where O(z) defines overlap correction, β, and σ are total (molecular plus aerosol) backscatter and total scattering coefficients respectively. The overlap correction varies between 0 and 1, and the signal needs not to be corrected for great distances (i.e. O(z)=1). Thus, for great distances we have

$$S(z) = C\beta \exp(-2\sigma z) \tag{A2.5}$$

and, taking a natural logarithm we obtain

$$\ln S(z) = \ln C\beta - 2\sigma z \tag{A2.6}$$

It can be seen from Eq. A2.6 that there is a linear relationship between the logarithm of lidar signal and distance. Using the linear regression we obtain from Eq. A2.4

$$O(z) = \frac{S(z)}{\beta C \exp(-2\sigma z)} \tag{A2.7}$$

where: $\ln \beta C$ and 2σ are determined from linear regression (Eq. A2.6).

Fig. A2.2 presents overlap calibration results for the "NASA Langley" lidar. The logarithm of the signal is linear function of distance between 2-8 km. The red line on the upper panel (Fig. A2.2) shows the linear fit and extrapolation of the logarithm of the lidar signal for distance less than 2 km. The overlap correction function (Eq. A2.7) is shown at the bottom panel on Fig. A2.2. Because of strong signal dumping on the 2 km pathway omission of this calibration leads to a large error in the boundary layer. This simple method allows use of this lidar for retrieval of the aerosol backscatter and scattering coefficients in the lowest troposphere. However, overlap correction is not easy to determine because the real atmosphere in not ideally homogeneous in horizontal. Additionally the calibration on a ship can be done only during calm sea conditions.

After application of all corrections it is possible to recover information on vertical profiles of backscatter to extinction ratio. For this purpose we need to invert the lidar equation. Molecular properties of the atmosphere are determined from vertical distribution of pressure.

The β_A and σ_A in Eq. A2.2 remain unknown. This equation can be solved only after we assume the relationship between these two quantities. For molecular scattering backscatter and extinction are related by a linear relationship

$$\beta_R = R_R \sigma_R , \tag{A2.8}$$

where R_R in this case is $3/8\pi$.

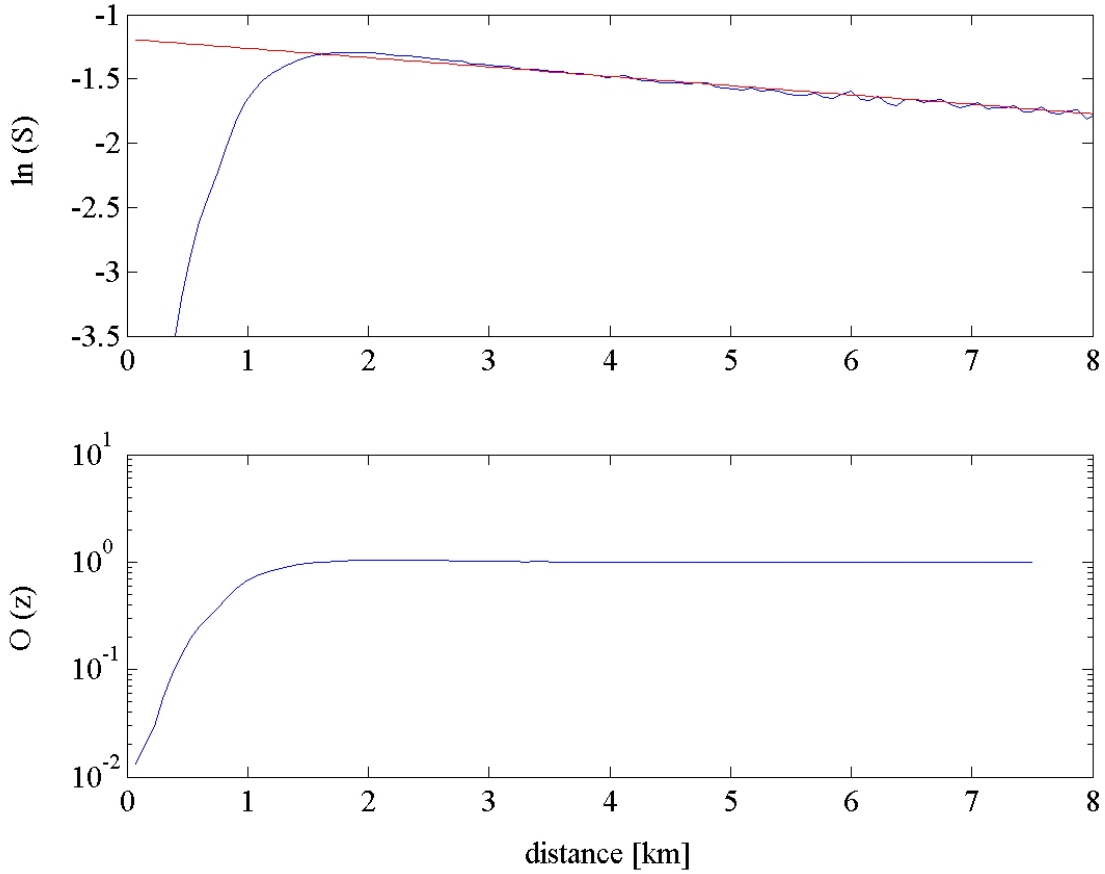

Fig. A2.2: The lidar signal (blue line) during horizontal scan and linear fit (red line). The overlap correction function is shown on bottom panel

In the case of larger particles, the dependence between the backscatter and extinction is more complex. Assuming spherical particles we have

$$\sigma(z) = \pi \int Q_{ext}(x, m + ik) r^2 n(r) dr , \tag{A2.9}$$

$$\beta(z) = \pi \int Q_b(x, m + ik) r^2 n(r) dr , \tag{A2.10}$$

where n(r) is size distribution of aerosol particles, Q_{ext} and Q_b are extinction and backscatter efficiency, respectively. Efficiencies depend on refractive index (real m and imaginary k part) and on size parameter $x=2\pi r/\lambda$. For monochromatic lidar the optical properties depend only on refractive index and non-dimensional size distribution of the aerosol particles. We can write

$$\beta_A(z) = R_A(z)\sigma_A(z), \tag{A2.11}$$

where R_A (z) is the function of distance. In what follows we will assume that $R_A(z)$ z-independent. Thus, Eq. A2.2 becomes

$$S(z) = C[\beta_R(z) + \beta_A(z)]\exp\left(-\frac{2}{R_R}\int_0^z[\beta_R(z')dz'\right)\exp\left(-\frac{2}{R_A}\int_0^z[\beta_A(z')dz'\right) \tag{A2.12}$$

This is an integral equation for $\beta_{A,}$ which contains unknown parameters C and R_A. The solution of this equation has the form

$$\beta_A(z) = \frac{S(z)T_R^{2(\gamma-1)}(z)}{C - \frac{2}{R_A}\int_0^z S(z')T_R^{2(\gamma-1)}(z')dz} - \beta_R(z), \tag{A2.13}$$

where: $\gamma = \frac{R_R}{R_A}$. (A2.14)

Equation A2.13 contains, besides known quantities, parameters R_A and C. R_A determined numerically during the solution of the Eq. A2.13 by minimizing the difference between the aerosol optical thickness calculated numerically and that determined using supplementary measurement (e.g. sunphotometer).

The remaining problem is how to determine constant C, which characterizes the lidar system. One can do it integrating Eq. A2.1 in the upper levels (above aerosol layer) where, the backscatter comes from molecular scattering and the aerosol backscatter ratio is zero. This gives

$$\int_{z_b}^{z_m} S(z)dz = CT_A{}^2\int_{z_b}^{z_m}\beta_R(z)T_R{}^2(z)dz \tag{A2.15}$$

where z_b is the top of the aerosol layer and z_m corresponds to the range of the lidar. From this equation we obtain expression for constant C

$$C = \frac{\int_{z_b}^{z_m} S(z)dz}{T_A{}^2\int_{z_b}^{z_m}\beta_R(z)T_R{}^2(z)dz} \tag{A2.16}$$

To determine C from Eq. A2.16 we need to know the aerosol transmission from sunphotometer observations. Also values of the z_b and the z_m in Eq. A2.16 must be found. Aerosols can be often observed above the top of the boundary layer and thus the top of the aerosol layer is sometimes difficult to determine.

The numerical algorithm based on A2.13 and A2.14 can lead to large uncertainties but in spite of this it is often employed [*Klett*, 1985]. It is based on Eq. A2.13 and an additional strong

assumption that the ratio of the backscatter to scattering coefficient is constant with altitude. The additional algorithm assumes that there is a level in the atmosphere where aerosol backscatter ratio is zero. More realistic assumptions were studied by *King* [1992] and *Kovalev* [1993], but without additional information about aerosol, the vertical profile of backscatter and extinction coefficient includes significant errors. Because backscatter coefficient is defined by:

$$\beta_A = P(\pi)\sigma_{Asca}, \tag{A2.17}$$

where $P(\pi)$ is an aerosol phase function for backscatter and σ_{Asca} is an aerosol scattering coefficient, the ratio of backscatter to extinction coefficient can be written in the form

$$R_A = P(\pi)\omega, \tag{A2.18}$$

where ω is an aerosol single scattering albedo. Thus, deriving R_A from the lidar observations it is possible to estimate changes of the aerosol single scatter albedo.

The algorithm recursively solves the inverse problem from upper to lower atmosphere. A simple rearrangement of the Eq. A2.13 written for two layers: z and z-1 leads to the final result for backscatter coefficient for layer z-1 in form

$$\beta_A(z-1) = \frac{S(z-1)\psi(z-1,z)}{\dfrac{S(z)}{\beta_R(z)+\beta_A(z)} + \dfrac{1}{R_A}\left[S(z)+S(z-1)\psi(z-1,z)\right]} - \beta_R(z-1), \tag{A2.19}$$

where

$$\Psi(z-1,z) = \exp\left[\left(\frac{1}{R_A}-\frac{1}{R_R}\right)\left(\beta_R(z)+\beta_R(z-1)\right)\Delta z\right]. \tag{A2.20}$$

Equation A2.19 describes backscatter ratio for subsequent levels beginning from the upper troposphere. This recurrence depends on the quantity R_A which is unknown. However, it can be determined using the AOT determined from the MICROTOPS instrument. In step zero we assume $R_A = R_R$. Next, we define a new value of R_A such as

$$R_A = \frac{\int \beta_A(z)dz}{\tau_{micr}}, \tag{A2.21}$$

where τ_{micr} is AOT determined from independent measurement. We iterate until R_A determined from A2.21 is close to R_A from the previous step. This satisfies the boundary condition and defines vertical profile of backscatter ratio and extinction. The algorithm defined above is fairly stable and useful for calculations of aerosol optical depth, despite the simplifying assumption that the size distribution of aerosol and its optical properties are constant with height. This leads to a simple relationship between the backscatter and extinction ratio.

A.3 MICROTOPS

Aerosol optical thickness (AOT), total ozone and water vapor were obtained from direct observation of solar radiation by two handheld MICROTOP II instruments (Sunphotometer and Ozonometer) [*Morys et al.*, 2001]. Spectral filters in the MICROTOPS enable the measurement of the solar irradiance in several narrow bands between 300 nm and 1020 nm. The Sunphotometer detects solar irradiance at 380, 440, 500, 675, and 870 nm with filters having a full width - half maximum 10 nm and Ozonemeter at 305, 312, 320, 936, and 1020 nm. The full width - half maxima for the first three UV channels of Ozonometer are 2.4 nm and for the two infrared are 10 nm. The field of view (FOV) of each channel is 2.5º, therefore manual sun tracking is relatively easy. Unfortunately, large FOV in comparison to the sun disk (0.5º) leads to overestimated transmission. This error increases with increase of the aerosol particles size due to a forward pick of the solar scattering. This problem will be discussed in Appendix B.

The GaP photodiodes are used in the MICROTOPS II and are characterized by strong sensitivity in the UV region and low noise level above 500 nm. Because the photodiodes are hermetically packed, the MICROTOPS II has long term stability of about 0.005%/year. The voltage output from instrument is a linear function of the solar irradiance and nonlinearity is less than 0.002%. The temperature of the optical block is monitored and logged during the scan in order to allow temperature compensation. A built-in pressure sensor provides information on the atmospheric pressure needed to calculate the Rayleigh scattering coefficient.

During the MINOS and the ACE-Asia experiments each MICROTOPS observation included 5 independent scans, which were performed to minimize the sun tracking error. The scan with the largest signals, which corresponds to the best sun alignment of the instrument was used. However, each MICROTOPS scan includes 32 fast measurements for each channel (approximate time 10 sec), and only measurements with the largest signal are averaged for the reduction of the error associated with sun targeting and the reduction of the measurement noises. This observation technique is more accurate and additional 5 scans (in particular on a ship) can effectively reduce error associated with the hand-held operations.

The three UV channels in Ozonometer are used to obtain the total column ozone and the ratio of the signal at 936 nm to 1020 nm permits the measurement of the total column water vapor. The signals from channels: 380, 440, 500, 675, 870 and 1020 nm are used to determine AOT.

The absolute accuracy of MICROTOPS instruments is 1-2%, but the error in the derived total optical thickness is the largest for low air-mass factor (near solar noon). Therefore, the accuracy of the AOT is about 0.01 at 500 nm. The MICROTOPS instruments were calibrated at the Mauna Loa Observatory in June of 2001 and calibrated during MINOS and ACE-Asia experiments. The Langley method [*Morys et al.*, 2001] was used to find instrument's extraterrestrial constants. This method is based on measurements of instrument signal for different solar zenith angles. The Langley method is based on the assumption of good temporal stability of the atmospheric condition during measurements, with respect to AOT, water vapor, and total ozone. Additionally, the sun should not be obscured by clouds.

For the Sunphotometer (MICROTOPS II) instrument the voltage output is proportional to incoming irradiance. Thus,

$$V(\lambda) = V_o(\lambda)e^{-m\tau} \tag{A3.1}$$

where: V_o is the signal that the detector should measure at TOA, m is air-mass factor (which is defined as the ratio of the actual and vertical path length of the radiation through the entire atmosphere to the detector), and τ is total optical thickness. The total optical thickness can be determined as:

$$\tau = \tau_R + \tau_A + \tau_{O3} + \tau_g, \tag{A3.2}$$

where, τ_R is the optical thickness due to molecular scattering, τ_A is the aerosol optical thickness (AOT), τ_{O3} is the ozone optical thickness, and τ_g is the optical thickness due to the others gases absorption. Thus, the AOT may be calculated from

$$\tau_A = \frac{1}{m}\ln\frac{V_o(\lambda)}{V(\lambda)} - (\tau_R + \tau_{O3} + \tau_g). \tag{A3.3}$$

Considering Earth and Sun distance we have from Eq. A3.1

$$\ln V(\lambda) = \ln\left[V_o^{st}(\lambda)\left(\frac{d_0}{d}\right)^2\right] - m\tau, \tag{A3.4}$$

where Vo^{st} means TOA signal for certain mean distance, d_0 and d are mean and actual Earth Sun distance. This equation gives a linear relation between the logarithm of air-mass factor and the logarithm of instrument output voltage. Extrapolating relation A3.3 to m=0, one can obtain V_0^{st}. The measurements have to be done during rapid changes of the air-mass factor after the sunrise or before the sunset. The Langley calibration should be done while the solar zenith angle is between 60 and 80º, which corresponds to the changes of the air-mass factor between 2 and 6. In mid-latitudes the period associated with such sun zenith angles is about 1-1.5 hour long and depends on the Year Day and latitude. Relatively short time of the MICROTOPS observation is

important to satisfy the temporal stability of the meteorological conditions. This can be very difficult to satisfy, because before sunset or after sunrise, the atmosphere in the boundary layer changes significantly and relatively fast. Fig A3.1 shows the Langley plot performed for wavelength 500 nm on July 23, 2001. Excellent linear fit to these observations is associated with very stable atmospheric conditions and perfectly clear sky.

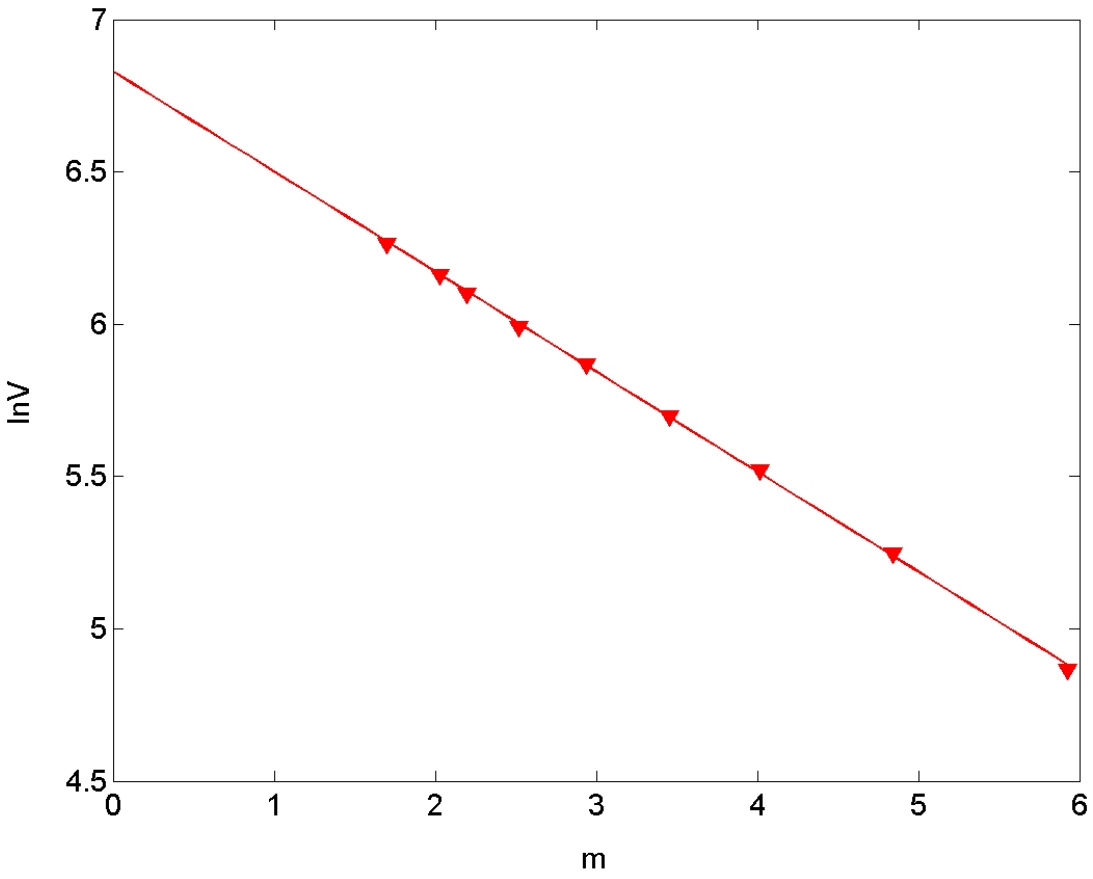

Fig. A3.1: The logarithm of the MICROTOPS signal at 500 nm as a function of the air-mass factor during Langley calibration performed on 204 YD in 2001.

Date	380 nm	440 nm	500 nm	675 nm	870 nm
Mauna Loa	7.531	6.706	6.784	6.919	6.666
204 YD	7.446	6.744	6.811	6.946	6.699
218 YD	7.080	6.639	6.719	6.873	6.662
233 YD	6.882	6.674	6.758	6.915	6.674

Table A3.1: Sunphotometer Langley calibration during the MINOS experiment ($\ln V^{st}_{o}$).

For the 936 nm channel located in the water vapor absorption band calibration needs to be considered separately. In this case we have

$$\ln V(\lambda) = \ln\left[V^{st}{}_0(\lambda)\left(\frac{d_0}{d}\right)^2\right] - m\tau - k(um)^b, \qquad \text{(A3.5)}$$

where k, b are constants which depend on optical characteristics of the filter, u denotes total water vapor content. The calibration method is identical with that for the sunphotometer but the extrapolation technique is different. The assumption of constant water vapor content is often not satisfied during early morning and evening when the boundary layer is evolving fast. To correct this effect we introduce non-linear regression, which takes into account changes in water vapor content

$$\ln V(\lambda) = \ln\left[V^{st}{}_0(\lambda)\left(\frac{d_0}{d}\right)^2\right] - m\tau - k\left[(u_0 + mu_1)m\right]^b, \qquad \text{(A3.6)}$$

where u_0 and u_1 accounts for changes in water vapor content during the calibration. We emphasize that this linear dependence of the water vapor content versus the air-mass factor has weak physical justification, but it seems to be the simplest form qualitatively consistent with typical behavior of diurnal cycle of air humidity in the boundary. Based on this equation and set

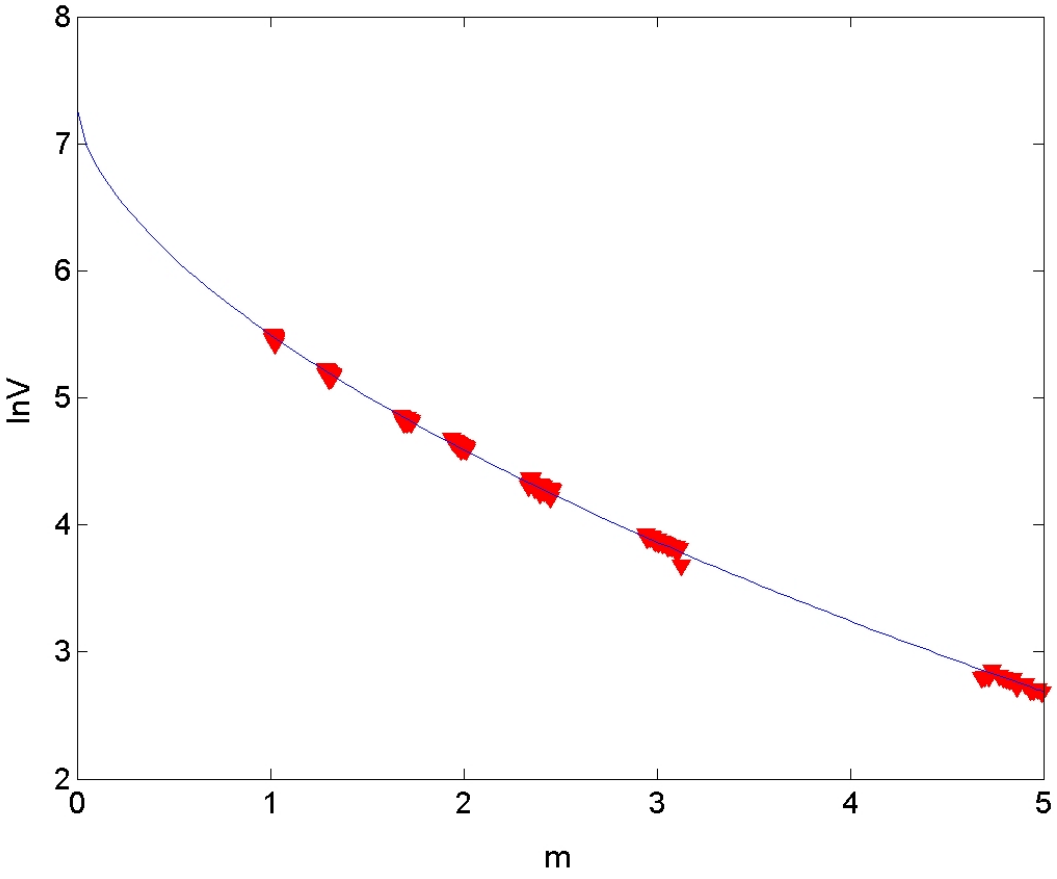

Fig. A3.2: The logarithm of the MICROTOPS signal at 936 nm as a function of the air-mass factor during the Langley calibration performed on 218 YD (July 23, 2001).

of k and b parameters Vo^{st} is fitted. The coefficients b and k must be assumed as equal to those following from properties of the filter but this assumption may be incorrect and is what weakens the accuracy of this method. Because, of these uncertainties, the water vapor content from MICROTOPS was verified with the radio-soundings (see Fig. A3.4). Results of the Langley calibration performed in July 23, 2001 (204 YD) is presented in Fig A3.2.

The vertical water vapor column is calculated as:

$$u = \left(\frac{m(\tau_A^{1020} - \tau_A^{936}) - \ln \frac{V^{936} V_0^{1020}}{V^{1020} V_0^{936}}}{k m^b} \right)^{1/b} . \tag{A3.7}$$

For retrieval of the total water vapor content from channel 936 and 1020 nm data we assume simple relationship between AOT at 936 and 1020 nm:

$$\tau_A^{936} = C\tau_A^{1020}, \tag{A3.8}$$

where C=1.16. This value is recommended by the MICROTOPS factory and was calculated for standard atmosphere from the radiative transfer model. However, the Ångstrom exponent based on this relationship is as high as 1.7. So high value of this exponent is correct only for small particles; usually it varies between 0.5 and 1.5. Thus, parameter C is larger than expected from spectral observation of AOT. The relative error of the total water content due to the change of parameter C follows from the relation:

$$\frac{\Delta u}{u} = -\frac{\tau_A^{1020} m^{1-b}}{bku^b} \Delta C . \tag{A3.9}$$

Fig A3.3 shows the error of the total water vapor content as a function of the air-mass factor. Open circles correspond to the total water column u=1, open squares correspond to u=2 and triangles correspond to u=3. Calculations were performed for constant AOT at 1020 nm (0.2) and ΔC=-0.1. This change of parameter C is associated with the change of Angstrom exponent from 1.7 to 0.67. A typical error of the water vapor retrieval due to the incorrect aerosol optical properties is a few percent. Thus, overestimation of the parameter C (Ångstrom exponent) leads to underestimation of the total water vapor content. This error is a linear function of the 1020 nm AOT and increases with air-mass factor. During days with high AOT associated with large particles, the MICROTOPS measurements of the total water content are underestimated even by 10%.

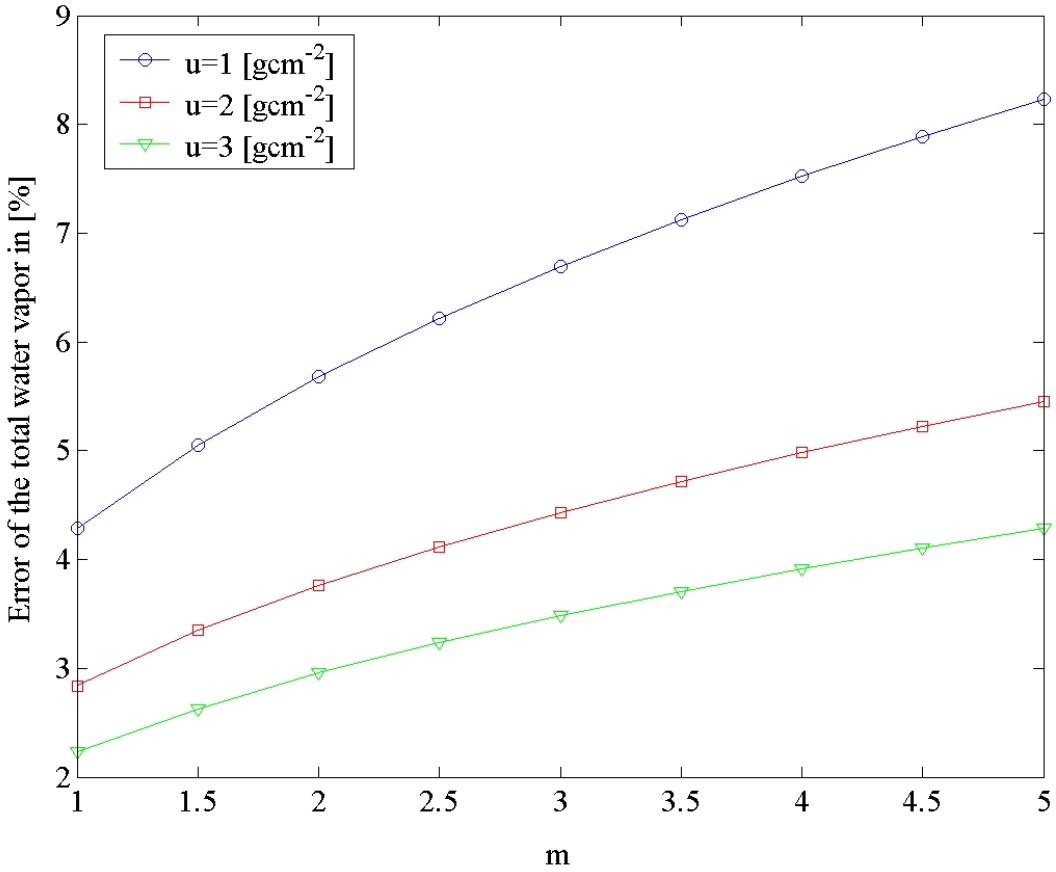

Fig. A3.3: Error of the total water content as function of the air-mass factor. All lines are for 1020 nm AOT=0.2 and parameter C=1.06 (ΔC=-0.1).

The total water content from MICROTOPS observation was verified with the radio-soundings during the ACE-Asia experiments. In this comparison, only observations with a small fraction of clouds and clear sun were chosen. The correlation coefficient between both observations is 0.98 but the MICROTOPS measurements give significantly smaller values (Fig. A3.4). The linear fit of this comparison can by written as:

$$u^{sonde} = 0.28 + 1.37 u^{micr}. \qquad \text{(A3.10)}$$

A large difference between the MICROTOPS and the radio-soundings is not only associated with the incorrect Ångstrom exponent, but also with the physical characteristics of the Sunphotometer's filter. The total water vapor content used in this study was calculated from Eq. A3.10 when the radio soundings weren't available.

Total atmospheric ozone was calculated using a new 3 channel algorithm (305, 312, 320 nm). This method yields smaller errors than the two-channel method [*Morys et al.*, 2001] and extends the applicability of the instrument toward larger air-mass factor. Comparison between

the Ozonometer and the Dobson and Brewer spectrophotometers shows that agreement between both types of these instruments is very good (about 2%) [*Kohler*, 1999].

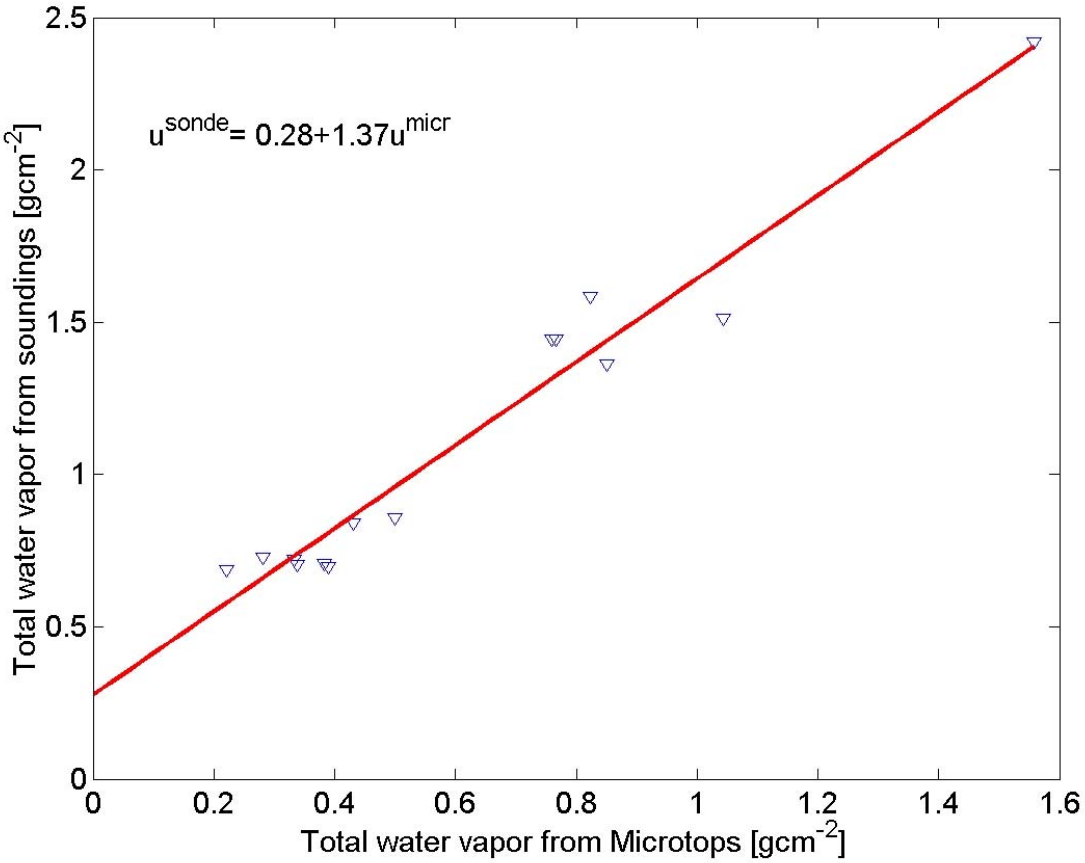

Fig. A3.4: Comparison of the total water content obtained from the MICROTOPS and the radio sounding observations.

A.4 Analytical spectral device

A 512-channel, spectral instrument (FS Dual VNIR) was used to measure the spectral irradiance between 350-1050 nm. Solar radiation is collected by two independent diffusers (RCR) and is projected by fibers optics onto a holographic diffraction grating, where the wavelength components are separated and reflected for independent measurements by silicon photodiodes. Each channel has an individual detector itself and is geometrically positioned to receive light within a narrow (1.4 nm) bandwidth. The analytical spectral device (ASD) instrument has a spectral resolution (the full width - half maximum of single emission line) of approximately 3 nm at 700 nm. The ASD instrument was set up to measure the global and direct irradiance (see Fig. A1.1 and Fig. A1.2). During the MINOS experiment one of the diffusers was covered with narrow pipe (FOV=2°) and located on two-axis SCI-TEC positioner/tracker and measured direct component of the solar radiation. The total and direct continuous spectra measurements (one spectrum every one minute) was interrupted about every hour to measure the direct irradiance manually. The pipe with diffuser was pointed at the sun. During this procedure 15 spectra were measured and the largest irradiance at 500 nm was assumed to represent the true direct irradiance.

The first calibration of this instrument (zero offset) is subtracted automatically. During the dark current calibration, the light entry to the silicon diode array is shut off and the signal is saved. The zero offset is stored in memory and subtracted from subsequent measurement for each channel. The dark current was measured every 1 minute just before the solar spectrum observation. The zero offset signal has temperature dependence and has been minimized by mounting the ASD inside a temperature-controlled enclosure. Signal integration time of ASD was changed automatically and varied from 68 ms close to local noon to 544 ms later afternoon.

The ASD instrument was calibrated using the LICOR optical calibrator. This calibration is basically a wavelength by wavelength comparison of the readings of the spectroradiometer with a secondary National Institute of Standards and Technology standard lamp with known spectral emission at known distance from sources. The manufacturer assumes 3% uncertainty for this kind of calibration. Because of the temperature of the lamp (about 3100 °K), the maximum energy is emitted at about 1000 nm. Therefore, the calibration for shortwave is difficult and leads to significant uncertainties for wavelengths smaller than 400 nm. Table A4.1 shows results of calibrations performed during ACE-Asia and after MINOS experiment. The calibration constant is defined as

$$c(\lambda) = \frac{I_{lamp}(\lambda)}{\Delta t DN}, \qquad \text{(A4.1)}$$

where $I_{lamp}(\lambda)$ is the calibration lamp spectral irradiance, Δt is the integration time, and DN

date	400 nm	500 nm	600 nm	700 nm	800 nm	900 nm	1000 nm
22-03-01	4.769	0.931	0.676	0.507	0.616	1.489	4.875
03-04-01	4.762	0.922	0.677	0.511	0.623	1.541	4.966
06-04-02	4.893	0.944	0.697	0.522	0.636	1.578	5.140
$\sigma_c / < c >$	0.015	0.011	0.017	0.015	0.017	0.029	0.027

Table A4.1 ASD calibrations for diffuser, which measures total solar flux, performed by LICOR optical system during ACE-Asia and after MINOS experiment. The unit of the calibration constants is: [10^{-2} $Wm^{-2}nm^{-1}ms^{-1}DN^{-1}$], where DN is a digital number

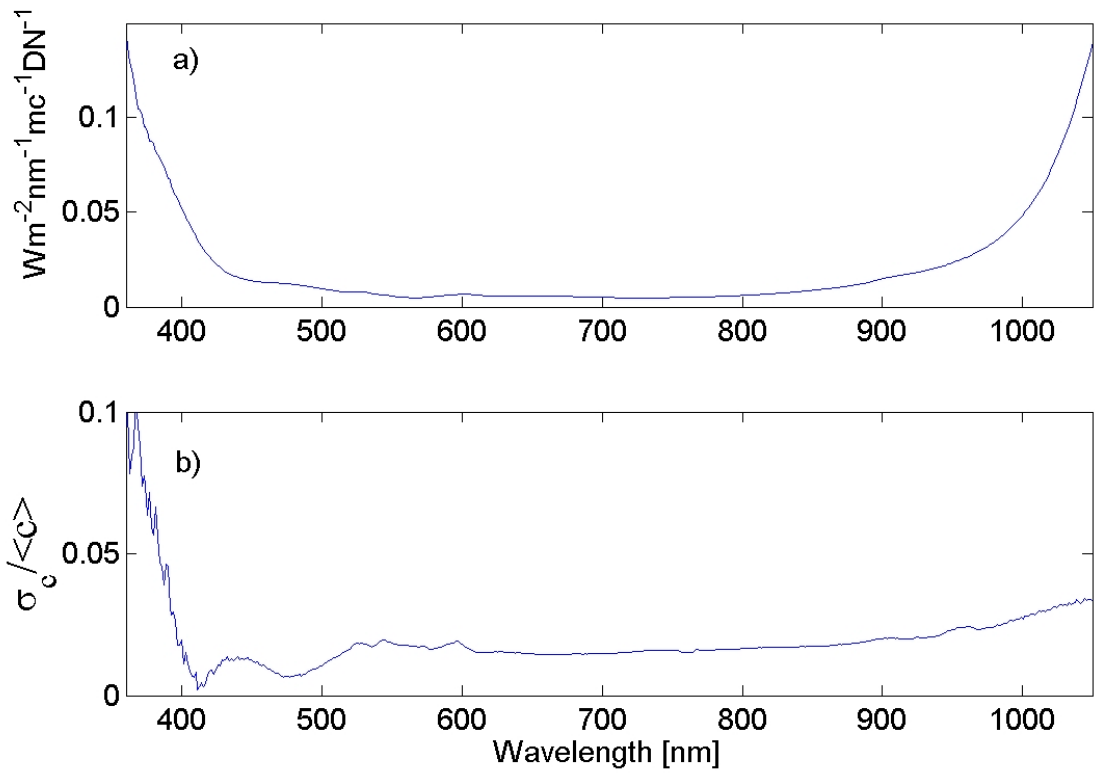

Fig. A4.1: (a) ASD calibration coefficient as a function of wavelength performed by LICOR optical calibrator and (b) relative changes of the calibration coefficient between the ACE-Asia and the MINOS experiment

(digital number) corresponds to instrument output. Spectral dependence of the calibration constant is shown in Fig. A4.1a. Because sensitivity of the ASD detector is much smaller for wavelength larger than 1000 nm and smaller than 400 nm, the instrument applicability is limited

to range 400 to 1000 nm. Temporal variation of the calibration constants is shown in Fig. A4.1b. Relative change of these parameters (σ_c/<c>) is about 0.02 in wide spectral range and only for wavelength smaller than 400 nm the instruments drift is large.

One of the ASD diffusers (which measures the direct flux) was additionally calibrated using the Langley method. This technique was described for the MICROTPS instrument (Appendix A1.3). Calibration of the ASD instrument for all channels is difficult because some of them include strong absorption bands, e.g. water vapor (0.72, 0.82, 0.94 μm) and oxygen (0.63, 0.69, 0.76 μm). This instrument has resolution about 3 nm, thus the structure of absorption lines is important. In this study only the channels without strong gaseous absorption were calibrated using the Langley method because the goal of the ASD direct measurements is AOT retrieval.

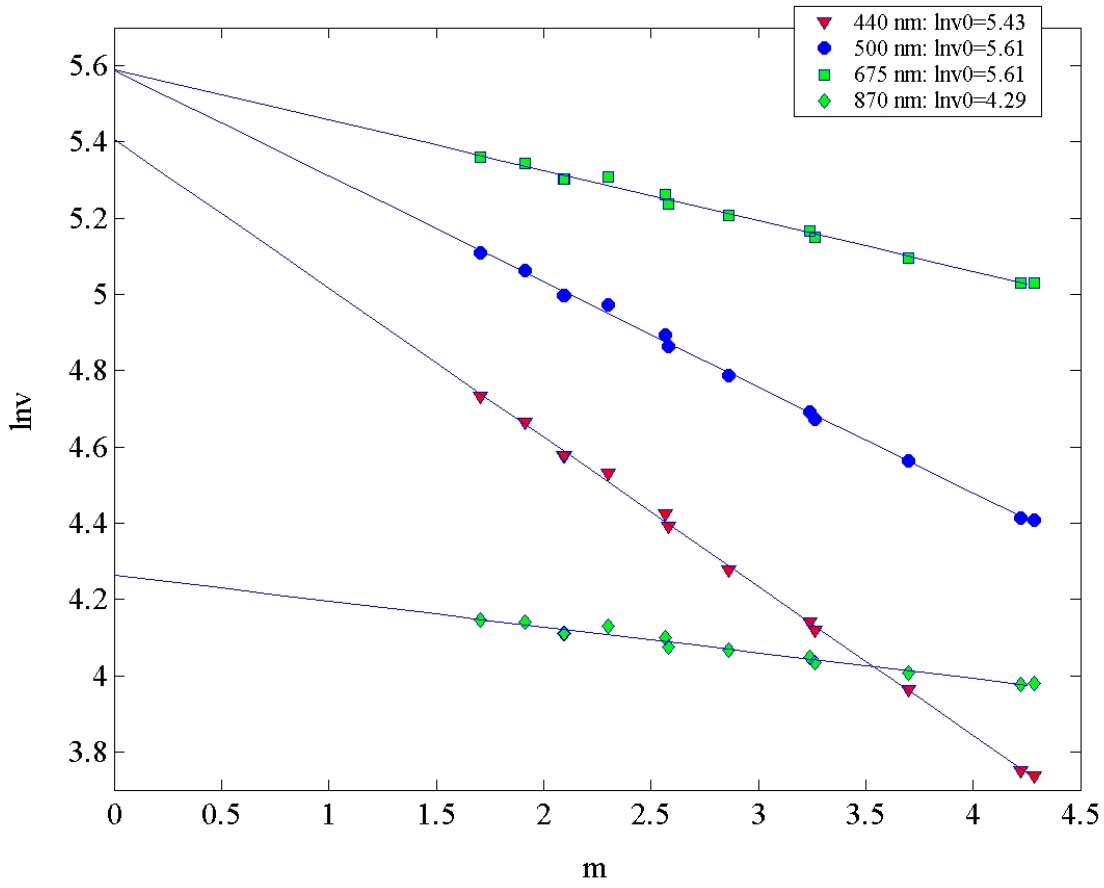

Fig. A4.2 Langley calibration of the ASD instruments during the MINOS experiment (21 Aug 2001). Four solid lines represent linear fit of the logarithm of the signal as a function of the air-mass factor for 440, 500, 675, and 870 nm.

Langley calibration for four wavelengths (440, 500, 675, and 870 nm) is shown in Fig. A4.2. This calibration was performed during the MINOS experiment on August 21, 2001. During this day the afternoon weather conditions were excellent. The logarithm of the instrument

signal is a linear function of the air-mass factor. The values of the logarithm of the signal at the TOA (lnv0) are provided in the legend on Fig A4.2. Notice, that the slope of the linear fit corresponds to the total optical thickness (aerosol plus molecular and gases optical thickness) and decreases with the increasing wavelength.

Total fluxes measured by the ASD instruments include significant error associated with the deviation of the diffuser from an ideal cosine rule. Therefore, angular calibration was performed to reduce this effect. In the ideal case, the solar radiation is scattered through the diffuser (Fig. A4.3) and weighted by the cosine of the angular incidence. However, even a very high quality diffuser does not behave like an ideal one. The cosine response error $\psi(\theta)$ for diffuser can be defined as

$$\psi(\theta) = \frac{I_m(\theta)}{I_o \cos\theta}, \qquad \text{(A4.2)}$$

where $I_m(\theta)$ is the measured irradiance at zenith angle θ of incidence radiance and I_o represents measured radiance at normal incidence (θ=0). In this case the ideal diffuser cosine response error is constant and equals one.

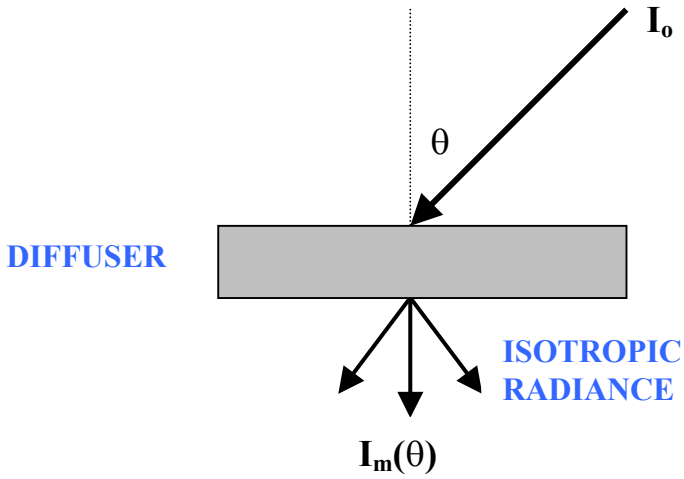

Fig. A4.3 Passes of the solar radiation by the diffuser.

During calibration, a diffuser position was controlled by a stepping motor so that the azimuth angle was changed every 45° and the zenith angle every 5°. Fig. A4.4 displays the azimuthally averaged cosine response error for seven wavelengths. The diffuser overestimates the radiation for zenith angles less than about 70° and rapidly underestimates it for larger zenith angles. The maximum difference between the ASD diffuser and the ideal cosine instrument is about 55° zenith angle. The cosine response error has strong wavelength dependence. For the

near infrared wavelengths the cosine correction is smallest and for zenith angle less than 70° it does not exceed 10%. In the visible range, deviation of the instrument is larger and without the correction the global fluxes are significantly overestimated.

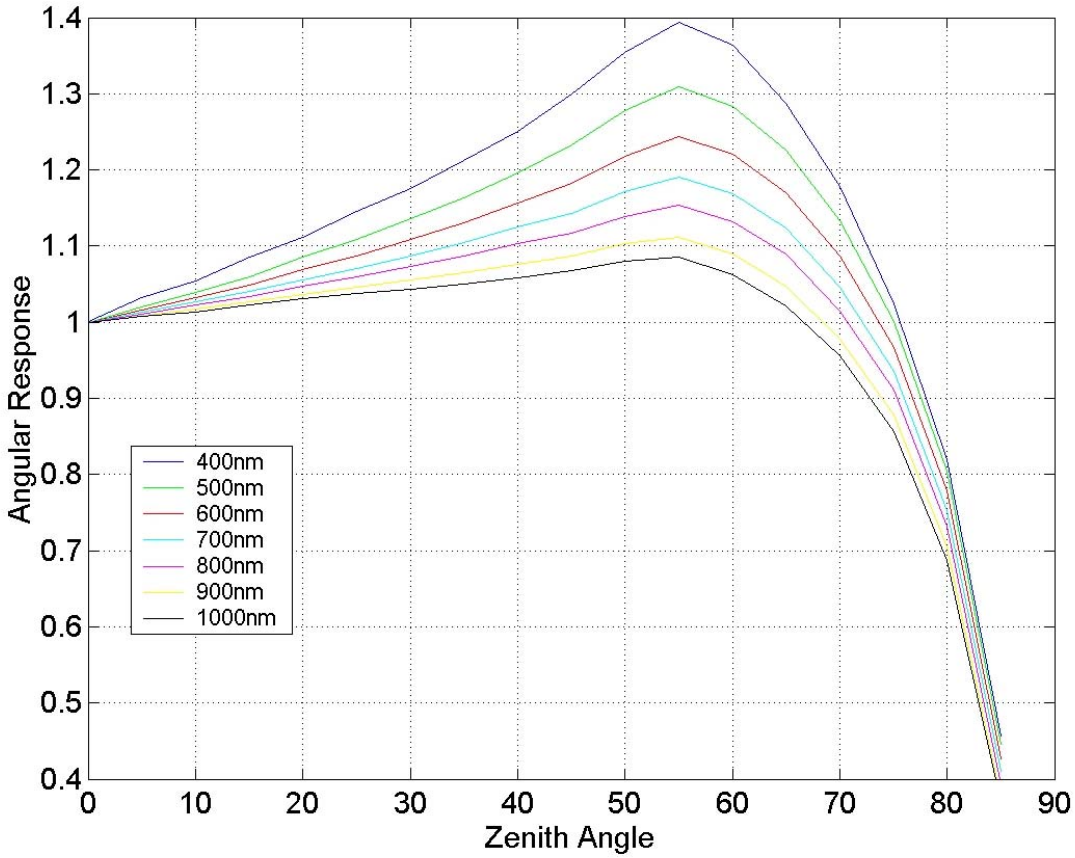

Fig. A4.4: Relative deviation of the diffuser's response from an ideal cosine rule, azimuthally averaged, for seven different wavelengths.

When the direct and total fluxes are measured continuously, the knowledge of the cosine correction allows one to improve the total irradiance observations. Unfortunately, the assumption on the diffuse skylight distribution is required. As a crude approximation, the sky radiance distribution on a clear day can be represented as a collimated direct solar beam plus isotropic diffuse sky radiance. Thus, the total corrected flux can by written as:

$$F_{tot}^{cor} = F_{tot} + \Delta F_{dir} + \Delta F_{dif}\,, \tag{A4.3}$$

where F_{tot} is a measured total flux, ΔF_{dir}, and ΔF_{dif} are a cosine correction for the direct and the diffuse fluxes respectively. The correction introduces significant deviation from the ideal cosine response to the global flux which can be described as

$$\Delta F_{dir} = F_{dir}\left(\frac{1}{\Psi(\lambda,\theta)} - 1\right), \tag{A4.4}$$

where the function $\Psi(\lambda,\theta)$ is a cosine correction shown on Fig. A4.5, θ is a solar zenith angle, and F_{dir} is a directly obtained from second diffuser.

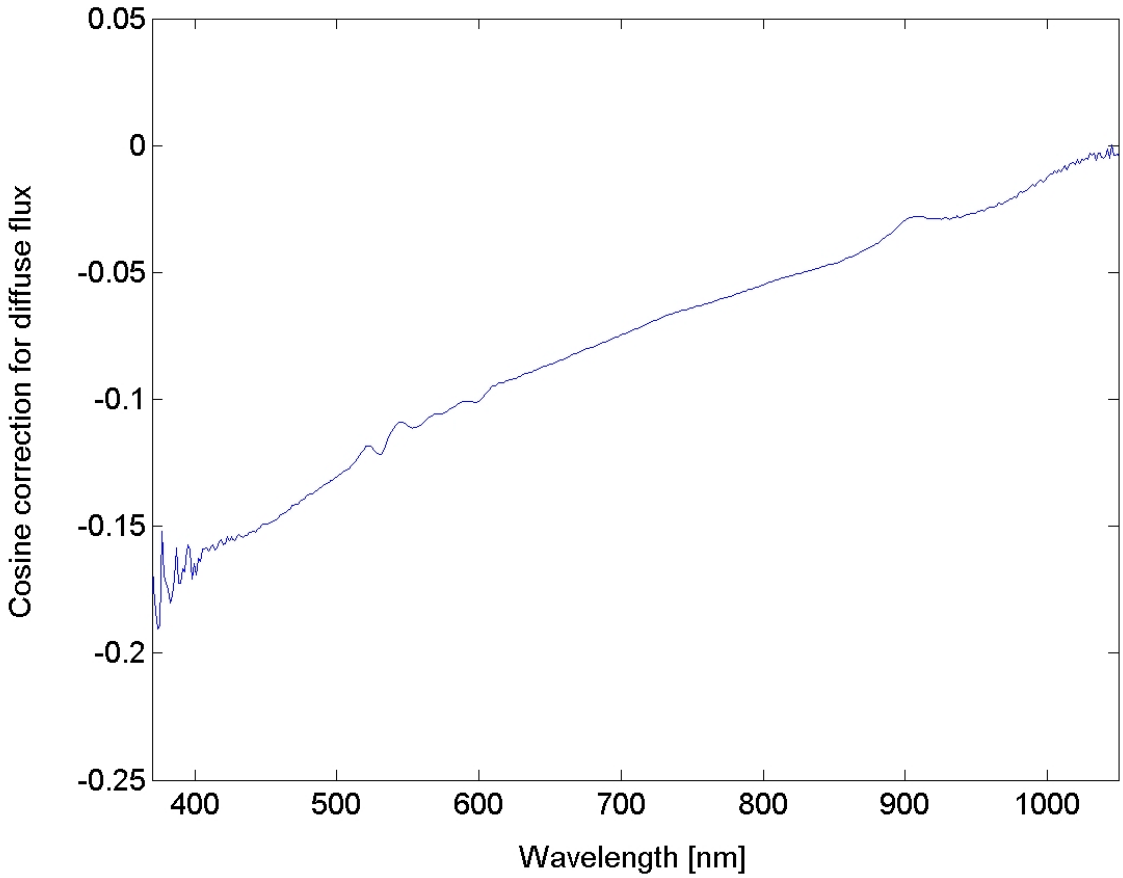

Fig. A4.5: Cosine correction for diffuse fluxes obtained by the means of isotropic sky radiance approximation.

Assuming, that the diffuse sky radiation is isotropic, the correction for the diffuse component can be written as:

$$\Delta F_{dif} = (F_{tot} - F_{dir})\left(2\int_0^1 \frac{\cos\theta}{\Psi(\lambda,\theta)} d\cos\theta - 1\right). \tag{A4.5}$$

The term in the second bracket is shown on Fig. A4.5 as a function of the wavelength. This correction is negative for all wavelengths because the ASD's diffuser on the average overestimates the solar irradiance. However, for wavelengths about 1000 nm the error of the diffuse flux is close to zero. In short, part of the visible range diffuse flux measured by the ASD

is overestimated by about 10 to 15%. Thus, angular calibration shows that for short wave direct and diffuse fluxes obtained from ASD observation are significantly larger than the real values.

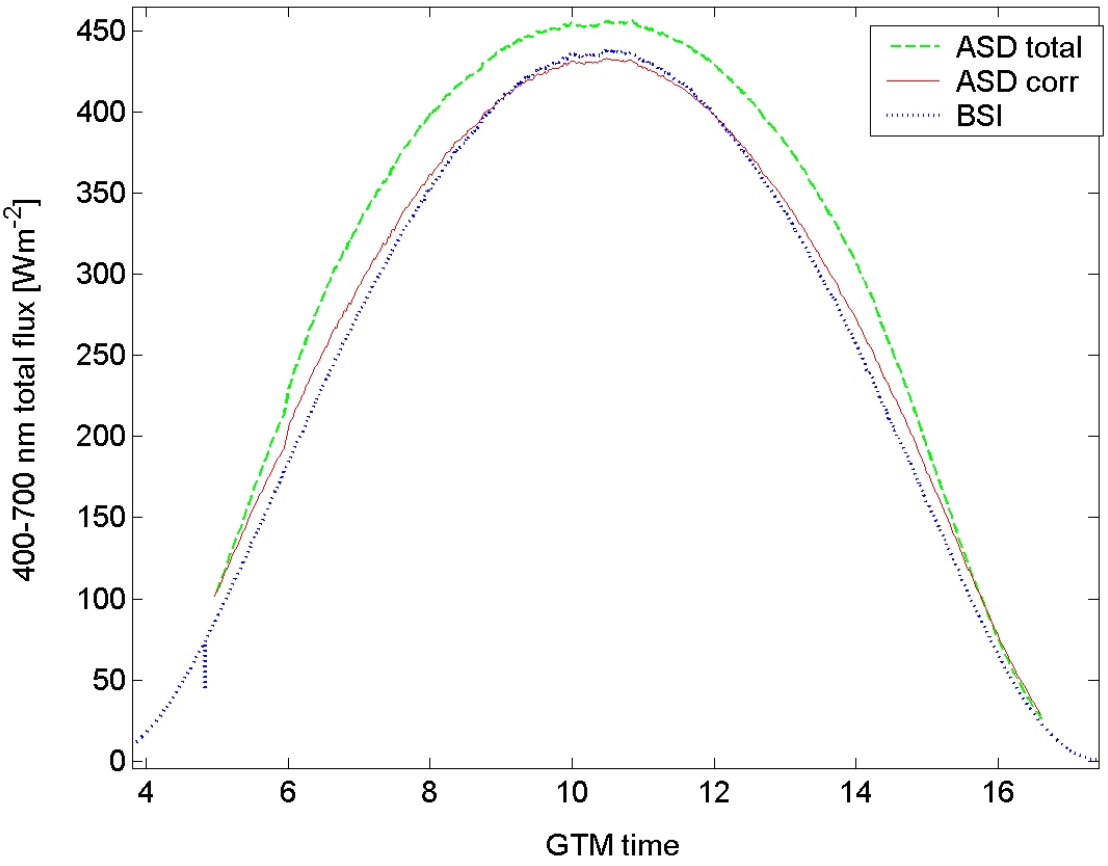

Fig. A4.6 Comparison of the downward total fluxes obtained from ASD and BSI instrument. Green (dashed) line shows the ASD total flux without angular correction, red (solid) line correspond to corrected ASD fluxes, and blue (dotted) line marks the visible flux from BSI.

Fig A4.6 shows a large difference between corrected (red, solid line) and non-corrected (green, dashed line) ASD total flux. Maximum difference is about 40 Wm^{-2} and corresponds to zenith angle between 40 and 50°. Additional dotted line (blue) on Fig. A4.6 shows the total flux from BSI instrument. The agreement between the ASD flux after correction and BSI is very good. However, for zenith angle larger than 60° the difference between these instruments is of the order of 15-20 Wm^{-2}. The possible sources of this error are angular response for the BSI instruments (see Appendix A1) and incorrect model of the diffuse fluxes in the ASD correction method (Eq. A4.5).

Appendix B: The Influence of the Forward Scattering Angles on the Sunphotometer Response Error.

In this appendix we calculate sunphotometers errors associated with the forward scattering (around 0°). The influence of the solar aureole on observed direct and diffuse solar fluxes depends strongly on the forward scattering of the aerosol. A part of the scattered solar radiation is detected by instruments which measure direct solar radiation. For example, the FOV of MICROTOPS is 2.5°, the FOV of the ASD is 2.0° but the FOV of the pyrheliometer is 5.7°. Similarly, the instruments which measure diffuse irradiance (pyranometer and BSI) include error associated with FOV. For example, diffuse pyranometer measures solar irradiance from 3.4°, because for smaller angular radius the solar radiance is blocked by a ball mounted on the sun tracker. A simple approximation to the radiative transfer equation was used to calculate this effect. Assuming that the phase function is altitude independent, radiance at the surface corresponding to in the first-order scattered (diffuse) solar radiance (intensity) can be written as [*Thomas and Stamnes*, 1999]

$$I_d(\theta,\varphi) = \frac{\omega F_o m P(\theta_o,\varphi_o;\theta,\varphi)}{4\pi(m-m_o)}\left[e^{-\tau m_o} - e^{-\tau m}\right], \tag{B.1}$$

where, $I_d(\theta,\varphi)$ is the radiance at zenith angle θ and at azimuth angle φ, m_o is air-mass factor for sun zenith angle θ, m_o is air-mass factor for θ_o zenith angle, τ is the total optical thickness, and $P(\theta_o,\varphi_o;\theta,\varphi)$ is the phase function. This approximation is sufficient to model the intensity field in optically thin medium. However, for large optical thicknesses photons can be multiple-scattered and the intensity limited to small solid angle around the sun can be smaller than that calculated from the single-scattering first-order scattering approximation. Thus, single scattering approximation provides the information about the maximum radiance in a small solid angle around the sun. The total downward flux around the FOV is given by:

$$F_{FOV} = \int_{FOV} I_d(\theta,\varphi)\cos\theta d\Omega . \tag{B.2}$$

Effective optical parameters (ω, P, τ) in (B1) include molecular (subscript m) and aerosol (subscript a) components and are defined by:

$$\tau = \tau_A + \tau_R , \tag{B.3}$$

$$\omega = \frac{\omega_A \tau_A + \tau_R}{\tau}, \tag{B.4}$$

$$P = \frac{P_A \omega_A \tau_A + P_R \tau_R}{\omega_A \tau_A + \tau_R}. \tag{B.5}$$

Aerosol phase function was obtained by two independent methods: (a) from Mie theory [*Bohren and Huffman*, 1983] and (b) from the Henyey-Greenstein approximation [*Henyey and Greenstein*, 1941]

$$P(\Theta) = \frac{1 - g^2}{\left(1 + g^2 - 2g\cos\Theta\right)^{1.5}}, \tag{B.6}$$

where g is asymmetry parameter and Θ is a scattering angle

$$\cos\Theta = \cos\theta_o \cos\theta + \sin\theta_o \sin\theta \cos(\varphi_o - \varphi). \tag{B.7}$$

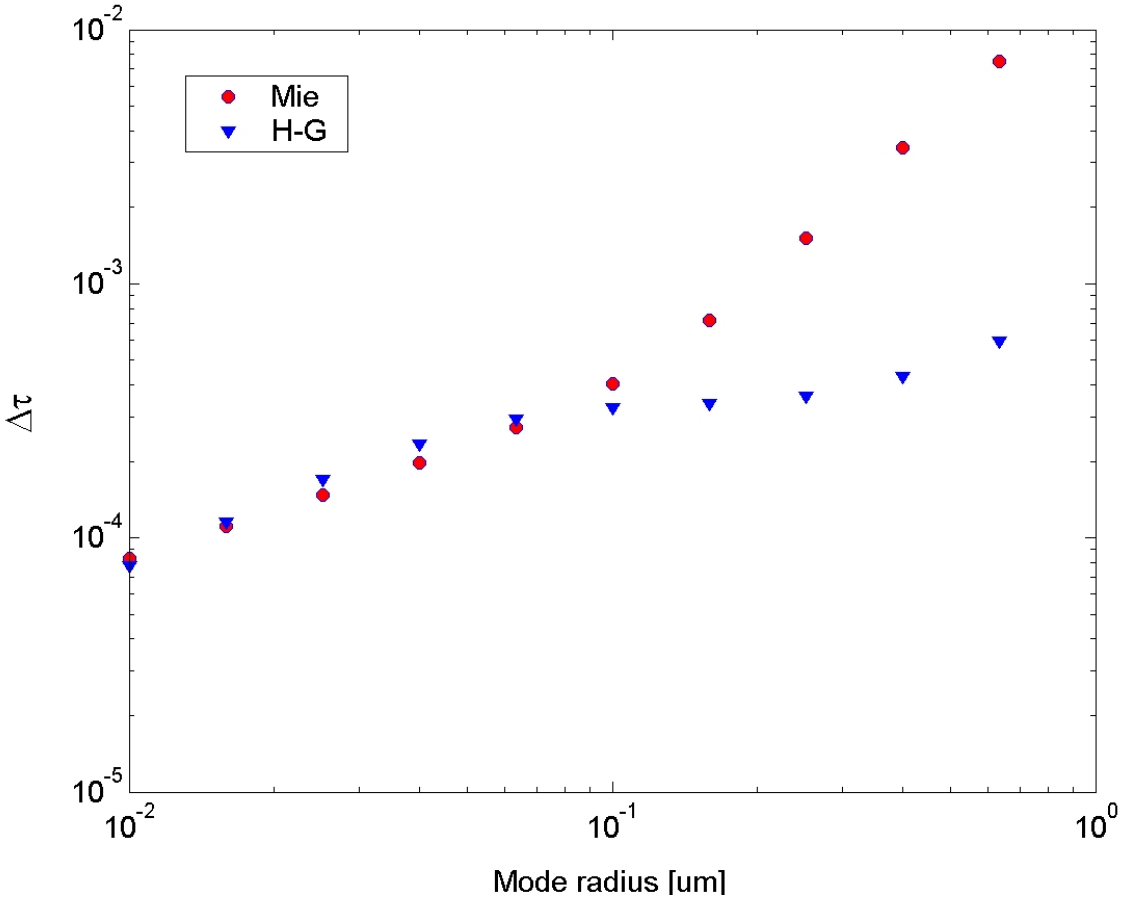

Fig. B.1: Absolute error of the MICROTOPS AOT at 500 nm retrievals due to scattering in the forward cone. Dotted circles correspond to phase function obtained from Mie and the dotted triangles are for phase function based on Henyey-Greenstein approximation.

The calculations of the forward scattering (into FOV of the instruments) were performed for the refractive index of aerosol n=1.5-0.005i and lognormal size distribution. The mode radius was changed between 0.01 μm and 0.75 μm and the width of the size distribution was constant σ=2. Moreover, the aerosol optical thickness at 500 nm was assumed to be small (AOT=0.2) in order to justify the single scattering approximation. For simplicity, only case with the zero solar zenith angle is considered. Fig. B.1 shows the error of the MICROTOPS AOT due to scattering of sun radiation into FOV of the instrument. For small particles (r <0.1μm) the results from both the Mie and the Henyey-Greenstein are in good agreement. The underestimate of the AOT is so small that it can be neglected. Similarly, for larger particles, this error is small and does not exceed the instrument uncertainties (0.01 at 500 nm). However, the Mie and the Henyey-Greenstein phase functions give different results. This problem is associated with the forward pick in phase function which is approximated incorrectly in the Henyey-Greenstein equation. Thus, this simple

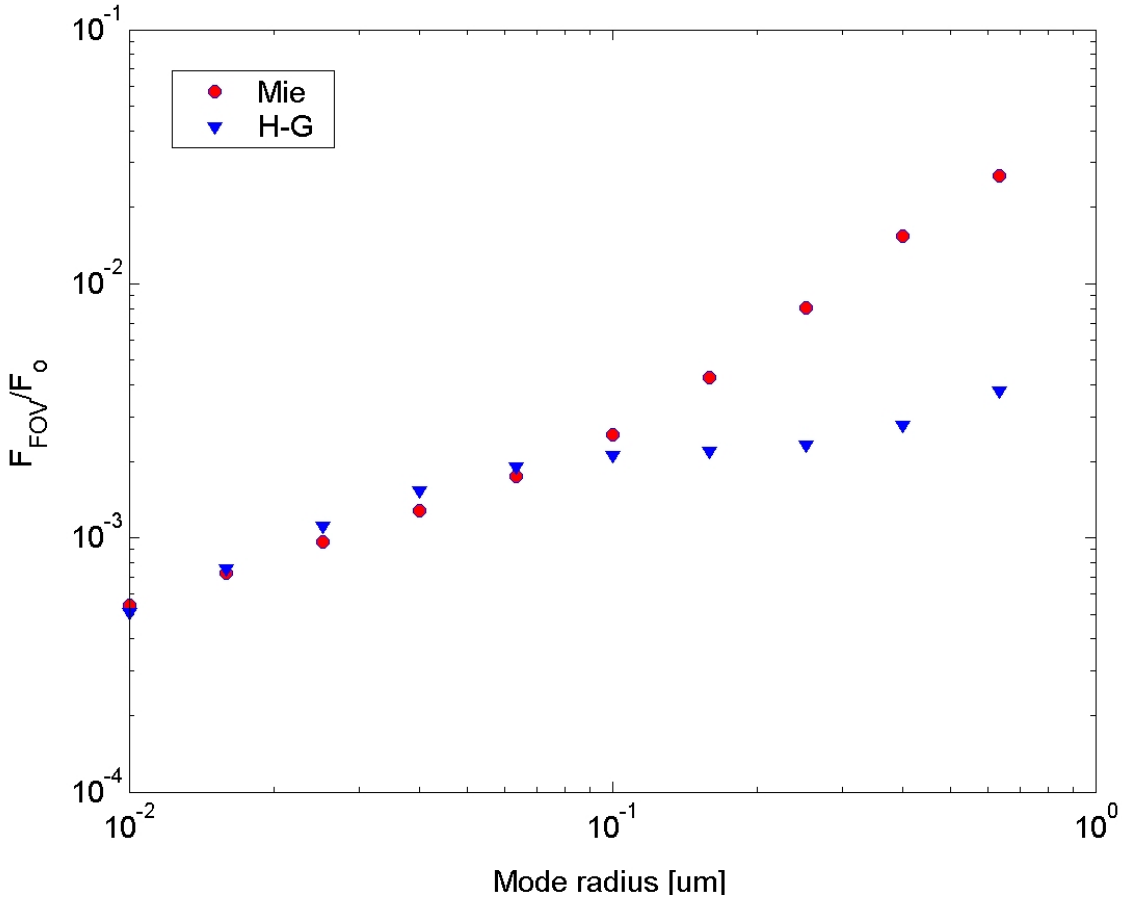

Fig. B.2: Ratio of the scattered flux coming to the forward cone with angular radius 3.2° to the TOA flux as a function of the mode radius. Dotted circles correspond to phase function obtained from Mie and the dotted triangles are for phase function based on Henyey-Greenstein approximation.

model shows that in spite of the relatively large FOV (in comparison to the Sun geometry) the MICROTOPS and the ASD instruments retrieve AOT correctly. Only for large aerosol particles (e.g. dust or sea salt) the AOT is underestimated up to 0.01.

Fig B.2 shows the fraction of the TOA fluxes which is scattered into a forward cone with the angular radius 3.2° (FOV=6.4°). This part of the solar radiation is blocked by the black ball on the sun tracker and isn't detected by shadowed pyranometer and BSI instrument. In this case diffuse flux is significantly larger because of larger solid angle. It changes from less than 0.1% for smaller particles to 3% for dust and sea salt aerosol. For mode radius 0.1μm (fine mode particles) both phase functions provide similar results and neglecting this effect leads to underestimated diffuse flux by 2.7 Wm^{-2} and 1.1 Wm^{-2} for broadband pyranometer and BSI instrument, respectively. These values correspond to about 1% of the downward diffuse flux for the AOT=0.2. In case of the mode radius equal 0.5 μm about 2% (Mie phase function) of the TOA flux is scattered into the forward cone. Thus, diffuse flux for this type of the aerosol is

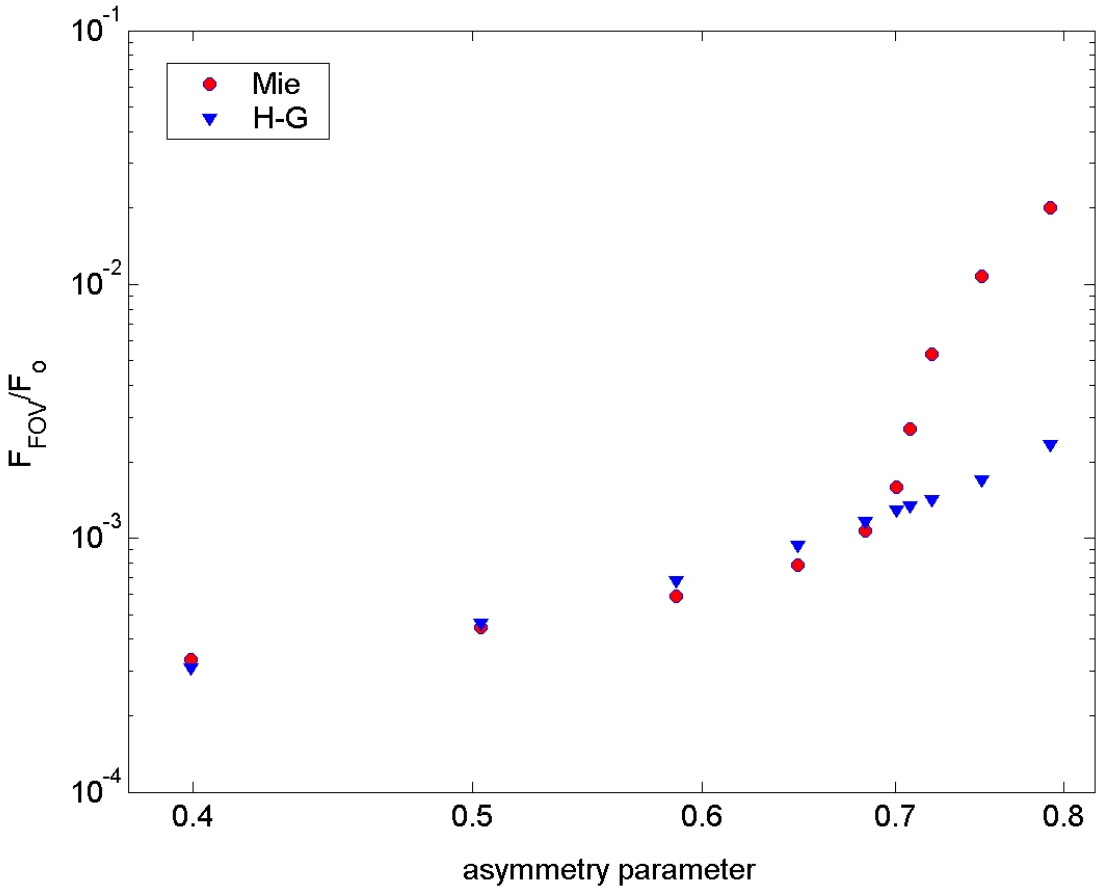

Fig. B.3: Shading effect for the pyrheliometer instruments (FOV=5°) as a function of the asymmetry parameter.

reduced by 10-20%. Fortunately, the number of large particles in comparison with the number of particles in fine mode is usually very low, and, therefore, shading effect on diffuse flux isn't as large. Similar results were obtained by *Podgorny* [2000] who used the Monte Carlo code. For example, he found that shading effect for BSI instrument is between 3 Wm^{-2} and 6 Wm^{-2} when the Mie phase function is used, and only 1-2 Wm^{-2} for the Henyey-Greenstein phase function.

Forward scattering effect on pyrheliometer observation is shown in Fig. B.3. In this case, the fraction of the TOA radiation, which is scattered into FOV=5° is a function of the asymmetry parameter. Likewise, in the MICROTOPS, calculations both Mie and Henyey-Greenstein phase functions provide similar results for small particles (g<0.7). Only for large aerosols, the forward cone scattering part is important and for the asymmetry parameter g=0.75 leads to overestimation of the direct fluxes by 10-14 Wm^{-2}. These results show that the error of the direct flux measured by the pyrheliometer depends strongly on the asymmetry parameter and mode radius.

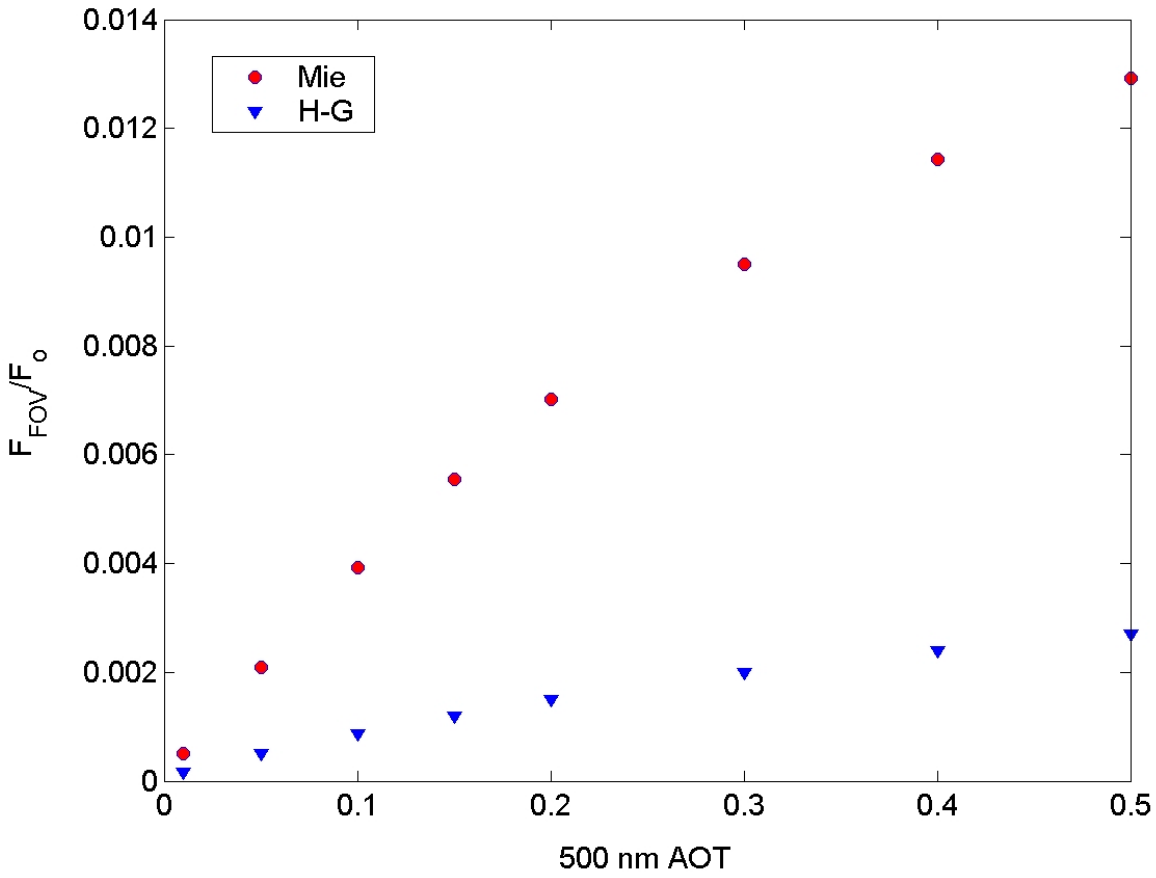

Fig. B.4: The same as Fig. B.3 but the fraction of the forward scattering is a function of the 500 nm AOT.

Fig. B.4 shows the same error of the direct flux based on the pyrheliometer observation but in this case it is a function of the AOT. Calculations were performed for mode radius 0.3 μm. For both phase functions and AOT less than 0.2 the forward scattering is a linear function of the AOT. For larger AOT the single scattering approximation is not valid and the results are uncertain.

In summary, observations of the direct flux by the CH1 pyrheliometer and diffuse flux by the shadowing pyranometer and the BSI instrument include errors. These uncertainties strongly increase with size of the aerosol and for large particles (e.g. dust, sea salt) cannot be neglected. However, if the observations of the direct and diffuse fluxes are used to determine the total flux, this effect is compensated because the FOV of pyrheliometer is 5° and shadowed pyranometer does not detect solar radiation from 6.4°. Thus, only the Sun aureole between 2.5° and 3.2° angular radius is not measured by these instruments.

Appendix C: Aerosol-Optical Database[10]

In this appendix, we discuss aerosol-optical database which was developed during this study. This database is an important part of this dissertation because it makes possible the determination of the aerosol optical properties. Recent databases such as OPAC/GADS [*Hess et al.,* 1998] have several limitations (e.g. fixed aerosol size distribution, and only external mixture of the particles). Our database enables calculating aerosol properties for two types of mixtures (internal and external). Parameters of the aerosol size distribution can be calculated from aerosol mass density or given by user. In addition, optical properties of spherical aerosol coated by different substance can be obtained.

This aerosol-optical database defines optical properties for several predefined aerosol classes. The properties defined are extinction, scattering, absorption coefficient based on the aerosol mass concentration ($\mu g/cm^3$) or the particle number density ($particle/cm^3$). Moreover, a phase function and asymmetry parameter together, with single scattering albedo, are available. The radiative properties are modeled within the following parameter ranges: wavelength, 0.25-40 μm; scattering angle, 0°-180°; and relative humidity, 0%-99%. Optical properties are described for six aerosol components: insoluble, water soluble, soot, sea salt, dust, and sulfate. The insoluble aerosols are soil particles with certain amounts of organic material. Water soluble aerosols includes nitrates and particle organic mater (POM). Soot category contains only elemental carbon. Sea salt particles consist of various kind of salt contained in seawater. Dust aerosol describes mineral particles and includes s mixture of quartz and clay. The sulfate category particles consist of 75% of H_2SO_4. Each component is described by spectral refractive index and size distribution. The spectral refraction index for dry (RH=0%) aerosol was taken from the Optical Properties of Aerosol and Clouds software (OPAC 3.1) [*Hess et al.*, 1998] and HAWKS 2000 [*Rothman et al.*, 1998].

Fig. C.1 shows the procedure by which the spectral optical properties of the aerosol can be obtained from the aerosol mass density and relative humidity.

[10] Available from the author in form of a matlab code.

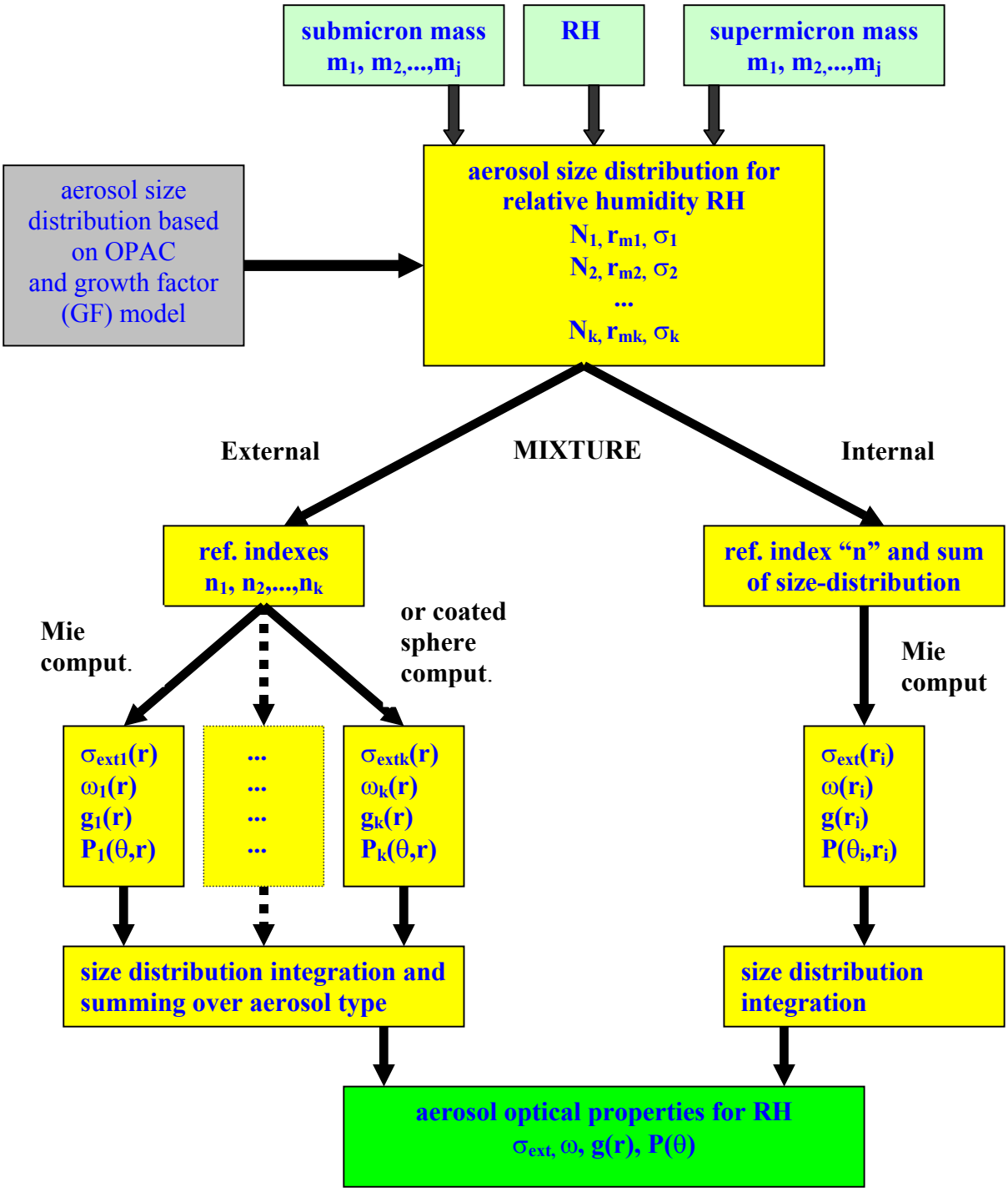

Fig. C.1 Block diagram showing how the aerosol optical properties are determined. The input includes particle mass density in submicron and supermicron regime for the j'th-type of aerosol and relative humidity (RH). Depending on mixture type (internal or external) aerosol optical properties such as extinction coefficient, single scattering albedo, asymmetry parameter, and phase function are computed. Program uses Mie or coated spheres codes to calculate the optical properties of aerosol mixture.

C.1 Internal and external mixtures

In nature aerosol is a mixture of different particles. These particles can be externally or internally mixed. An internal mixture of aerosols is one where two or more species are mixed together into a single particle whose effective index of refraction depends on the type and the amount of each of individual species. The effective refractive index for internal mixture (n_{12}) is approximately obtained from the Maxwell-Garnett mixing rule [*Maxwell Garnett*, 1904]:

$$n_{12} = n_1 \sqrt{1 + \frac{1 + 3f\dfrac{n_2^2 - n_1^2}{n_2^2 + 2n_1^2}}{1 - f\dfrac{n_2^2 - n_1^2}{n_2^2 + 2n_1^2}}}, \tag{C.1}$$

where n_1 and n_2 are the refraction index of the first and second substance, f is volume fraction of second type of the aerosol. The Maxwell-Garnett rule is one of several ways to calculate refractive index of mixture proposed in the literature other works include *Bruggeman* [1935] or *Chylek* [1988].

In external mixture particles of various chemical composition do not coalesce. Single scattering properties are calculated separately for each aerosol component. For an external mixture the volume extinction, scattering, and absorption coefficients of each species are added together to give the overall aerosol volume extinction coefficient

$$\sigma_{ext} = \sum_i \sigma_{ext,i} N_i , \tag{C.2}$$

$$\omega = \frac{\sum_i \omega_i \sigma_{ext,i} N_i}{\sum_i \sigma_{ext,i} N}, \tag{C.3}$$

$$g = \frac{\sum_i \sigma_{ext,i} g_i \omega_i N_i}{\sum_i \sigma_{ext,i} \omega_i N_i}, \tag{C.4}$$

$$P(\theta) = \frac{\sum_i P_i(\theta) \sigma_{ext,i} \omega_i N_i}{\sum_i \sigma_{ext,i} \omega_i N_i}, \tag{C.5}$$

where σ_{ext}, ω, g, $P(\theta)$ are extinction coefficient, single scattering albedo, asymmetry parameter, and phase function respectively. Subscript “ith” is used to define the aerosol properties for “ith” component.

C.2 Aerosol size distribution

Of the various mathematical function that have been proposed, the log-normal distribution [*Aitchison and Brown*, 1957] matches well observed shapes of observed distributions and is regularly used in atmospheric applications. The log-normal distribution for each aerosol component "ith" can by written as:

$$n(r) = \frac{N_i}{r\sqrt{2\pi}\ln\sigma_i}\exp\left[-\frac{1}{2}\left(\frac{\ln r - \ln r_{mod,i}}{\ln\sigma_i}\right)^2\right], \tag{C.6}$$

where $r_{mod,i}$ is the mode radius, σ_i is geometric standard deviation of the distribution, and N_i is the total particle number density of the component "ith" (particles per cubic centimeter). Parameters of the aerosol size distribution can be fitted from measurements of the size distribution or calculated basing on the aerosol mass density. In our applications the mass density was available for accumulation (D<1 μm) and coarse mode (1 μm<D<10 μm) at zero relative humidity. The soluble, soot, and sulfate types of aerosols (which are generally small) are defined by a single lognormal size distribution. The sea salt and dust particles are described by two lognormal size distributions (accumulation and coarse mode).

The radiative properties for each aerosol type are defined by:

$$\sigma_{ext,i}(z) = \pi\int Q_{ext,i}(n,kr)r^2 n_i(r)dr, \tag{C.7}$$

$$g = \frac{\pi\int Q_{sca,i}(n,kr)gr^2 n_i(r)dr}{\pi\int Q_{sca,i}(n,kr)r^2 n_i(r)dr}, \tag{C.8}$$

$$P(\theta) = \frac{\pi\int P_i(\theta)Q_{sca,i}r^2 n_i(r)dr}{\pi\int Q_{sca,i}r^2 n_i(r)dr}, \tag{C.9}$$

where $Q_{ext,i}$ is extinction ($Q_{sca,i}$ scattering and $Q_{abs,i}$ absorption) efficiency and $k=2\pi/\lambda$.

C.3 The growth factor

We assume that only soluble, sea salt, and sulfate particles are hygroscopic. The usual relationship between the radius of dry and wet particles can by written as [*Fitzgerald*, 1975]

$$r_{wet} = \alpha r_{dry}^{\ \beta}, \tag{C.10}$$

where parameters α and β are functions of relative humidity. Wet particles are distributed accordingly to the same size distribution as dry particles, but modified mode radius and size geometric standard deviation are

$$\tilde{r}_{mod} = \alpha r^{\beta}{}_{mod}, \quad \text{(C.11)}$$

$$\tilde{\sigma} = \sigma^{\beta}. \quad \text{(C.12)}$$

We assume that $\beta = 1$ and, therefore, σ is constant with relative humidity and the growth factor is independent of particle radius. The growth factor, which is defined as a ratio of the wet particle radius to dry particle radius (RH=0) was obtained from the OPAC database [*Hess et al.*, 1998]. Table C.1 shows soluble, sea salt and sulfate aerosols growth factors for nine different relative humidities. The sea salt is the most hygroscopic aerosol type and below the deliquescent point the growth factor is significantly different from 1. For example, sea salt particles have deliquescent point at about 75% of relative humidity.

	0%	**50%**	**70%**	**80%**	**90%**	**95%**	**98%**	**99%**
soluble	1.00	1.24	1.34	1.44	1.64	1.88	2.25	2.52
Sea salt	1.00	1.61	1.81	1.99	2.39	2.92	3.91	4.91
sulfate	1.00	1.41	1.57	1.70	1.94	2.27	2.81	3.32

Table C.1: Growth factor for hygroscopic type of aerosols for several values of relative humidity

C.4 Aerosol mass density to particle number density conversion

For typical aerosol particles the accumulation and the coarse modes overlay, and parameters of the log-normal size distribution are difficult to determine. Knowledge of the mass density for submicron and supermicron particles in not sufficient to obtain parameters defining the log-normal distributions. Thus, some of them must be assumed.

In the case of (assumed) single mode distribution the equivalent mode radius (Table C.2)

parameters	**soluble**	**soot**	**Sea salt**		**dust**		**sulfate**
			fine	**Coarse**	**fine**	**coarse**	
$\mathbf{r_m}$	0.03-0.075	0.011	0.10	1.75	0.15	1.9	0.02-0.1
σ	2.24	2.00	2.03	2.03	1.95	2.15	2.03

Table C.2 Mode radius (r_m) and geometric standard deviation (σ) of the lognormal size distribution

and number of particles are calculated. Those parameters are obtained based on submicron and supermicron measured masses assuming the geometric standard deviation of the size distribution (σ) based on the OPAC/GADS data base (Table C.2). For the sea salt and dust, two lognormal distributions are used and mode radius and geometric standard deviation of the size distribution for the fine and coarse mode is assumed (see Table C.2).

The measured dry (RH=0%) mass density of submicron (m_1) and supermicron (m_{10}) fraction can by written as

$$m_1 = N_1 F_1 + N_2 C_1, \tag{C.13}$$

$$m_{10} = N_1 F_{10} + N_2 C_{10}, \tag{C.14}$$

where N_1, N_2 are the number of particles in accumulation and coarse mode respectively, F_1, F_{10}, C_1, and C_{10} are defined below

$$F_1 = \frac{3}{4}\pi\rho_{dry}\int_0^{R_1} dr n_f(r) r^3, \tag{C.15}$$

$$F_{10} = \frac{3}{4}\pi\rho_{dry}\int_{R_1}^{R_2} dr n_f(r) r^3, \tag{C.16}$$

$$C_1 = \frac{3}{4}\pi\rho_{dry}\int_0^{R_1} dr n_c(r) r^3, \tag{C.17}$$

$$C_{10} = \frac{3}{4}\pi\rho_{dry}\int_{R_1}^{R_2} dr n_c(r) r^3, \tag{C.18}$$

where, $n_f(r)$ and $n_c(r)$ are aerosol size distribution for accumulation and coarse mode respectively and ρ_{dry} is density of the dry aerosol particles. Because chemical measurements used in this dissertation provide dry mass density of particles divided at 55% of RH into submicron and supermicron classes, the growth factor at RH 55% is necessary to calculate integrals in (C.15) - (C.18). For this purpose we define R_1 and R_2 as

$$R_1 = 0.5\mu m / GF(55\%), \tag{C.19}$$

$$R_2 = 5\mu m / GF(55\%). \tag{C.20}$$

Growth factor at 55% was calculated from a logarithmic interpolation of the data available from Table C.1. Notice that we have complication when growth factor depends on the aerosol radius but this problem was skipped here. In case of two lognormal size distribution (sea salt and dust) using equations C.13 and C.14 we can obtain the number of particles in accumulation and coarse mode as:

$$N_1 = \frac{m_1 - C_1 / C_{10} m_{10}}{F_1 - F_{10} C_1 / C_{10}}, \tag{C.21}$$

$$N_2 = \frac{m_{10} - N_1 F_{10}}{C_{10}} . \qquad (C.22)$$

In case of the single log size distribution (accumulation mode) ratio of the supermicron to submicron mass density can be written as

$$\frac{m_{10}}{m_1} = \frac{F_{10}}{F_1} . \qquad (C.23)$$

Thus, if σ is constant, the ratio of the supermicron to submicron mass is only a function of the mode radius r_m. Using the inversion method applied to Eq. C.23 the mode radius was obtained and the number of particles is determined from $N=m_1/F_1$.

C.5 Calculations of the optical properties of the individual particle.

The extinction, scattering, and absorption efficiency (Eq. C.7-C.9), phase function, and asymmetry parameter were calculated from Mie theory [*Bohren and Huffman*, 1983]. For the internal mixture we also used the solution based on the homogeneous sphere coated by the homogenous layer of uniform thickness. *Bohren* and *Huffman* [1983] code makes possible to compute the scattering of particles which core has different refractive index than coating medium. This model of aerosol is a good approximation of hygroscopic particles. For relative humidity smaller than the deliquesce point water vapor condenses on the core and mixes with the particle. When relative humidity is larger hygroscopic particles dissolve in water and this aerosol can be modeled as homogeneous internal mixture.

Moreover, soot and dust particles can coagulate to a form of complex cluster (and still be considered as an internal mixture in the nomenclature used here). In first approximation, a coated sphere with dust as central core can be used in this case. This database makes possible the determination of the optical properties of particles which consist of two different, but spherically shaped substances. However, the structure of dust particle covered by soot is more complicated and can enhance radiation absorption (the Mie theory predicts a large resonance for spherical particles). Therefore more specific scattering calculations are needed in this case.

C.6 Uncertainties

Aerosol optical properties computed from this database are subject to a number of errors. One of them is characterization of the refractive index of particles, which depends on the aerosol composition. For example, absorption of the dust particles (imaginary part of refractive index) depends on contribution of the hematite which wasn't known; also the measurements and characterization of the refractive index of soot are uncertain. Moreover, if the size distribution is not measured, the method of obtaining the size parameters from aerosol mass observations includes errors associated with assumptions of modes radiuses and geometric standard deviation of size distribution.

Assumption concerning the mixture type leads to incorrect aerosol optical properties if the refractive indexes of individual components are not specified properly. Internal or external mixture models can also affect single scattering properties. Another uncertainty results from the fact that particles are often non-spherical. A significant part of uncertainties is associated with hygroscopic growth dependence f(RH), and aerosol types such as solubles, sea salt, and sulfates. The growth factor for each separate particle species is difficult to measure, and during the ACE-Asia experiment only total hygroscopic effect for mixture of aerosols has been determined.

Appendix D: Acronyms

ACE-Asia - Aerosol Characterization Experiment
AERONET - Aerosol Robotic Network
AOT - Aerosol Optical Thickness
ASD - Analytical Spectral Devices
AVHRR - Advanced Very High Resolution Radiometer
BRDF - Bi-Directional Diffuse Reflectivity
BSI - Biospherical Instruments
CERES - Clouds and the Earth's Radiant Energy System
COAMPS - Coupled Ocean Atmosphere Mesoscale Prediction System
DISORT - Discrete-Ordinate-Method Radiative Transfer
EARLINET - European Aerosol Research Lidar Network
ERBE - Earth Radiation Budget Experiment
FTIR - Fourier Transform Interferometer
FOV - Field of View
FSS - Finokalia Sampling Station
IPCC - Intergovernmental Panel of Climate Change
INDOEX - Indian Ocean Experiment
INSAT - India and Earth Observation Systems
ITCZ - Inter-Tropical Convergence Zone.
IR - Infrared Radiation (wavelengths larger than 4 μm)
GADS - Global Aerosol Data Set
GF - Growth Factor
GOCART - The GeorgiaTech/Goddard Global Ozone Chemistry Aerosol Radiation Transport
GUV-511 - Ground-based Ultraviolet Radiometer
HAWKS - Hitran Atmospheric Workstation
HITRAN - High-Resolution Transmission Molecular Absorption
LBLRTM - Line-By-Line Radiative Transfer Model
M-AERI - Marine-Atmosphere Emitted Radiance Interferometer
MEIDEX - Mediterranean Israel Dust Experiment

METEOSAT- Meteorological Satellite
MINOS - Mediterranean Intensive Oxidant Study
MPL - Micro Pulse Lidar
MPLNET - The Micro-Pulse Lidar Network
NCEP - National Center for Environmental Prediction
NOAA - National Oceanic and Atmospheric Administration
OC - Organic Carbon
OLR - Outgoing Longwave Radiation
OPAC - Optical Properties of Aerosol and Clouds
PMEL - Pacific Marine Environmental Laboratory
POM - Particle Organic Matter
PSAP - Particle Soot Absorption Photometer
RH - Relative Humidity
SeaWIFS - Sea-Viewing Wide Filed-of-View Sensor
SIMBAD - Sun Photometer/Above Water Radiometer
SSF - Single Scanner Footprint
SSA - Single Scattering Albedo
TERRA - NASA Satellite
TOA - Top of the Atmosphere
TRMM - Tropical Rainfall Measuring Mission
TSI - Nephelometer
YD - Day of Year

A few other acronyms are explained directly in the accompanying text

Appendix E: Symbols

$< >$ - vertical average operator

$(...)_{clear}$ - value of ... for atmosphere without aerosols

$(...)_{aerosol}$-value of ... for atmosphere with aerosol

α - climate sensitivity, Ångstrom exponent, parameter describing hygroscopic growth of the aerosol particle

α_i - Ångstrom exponent of i size distribution component

β - backscatter ratio, exponent describing hygroscopic growth of the aerosol particle

β_A - aerosol backscatter coefficient

β_R - molecular (Rayleigh) backscatter coefficient

γ - shaping parameter of the Junge size distribution, molecular backscatter to extinction ratio divided by aerosol backscatter to extinction ratio.

Δg_i - weights

ΔF_{dif} - cosine correction for diffuse flux

ΔF_{dir} - cosine correction for the direct flux

ΔT_s - change of the surface temperature

Δt - integration time

θ - zenith angle

θ_o - solar zenith angle

Θ - scattering angle

λ - wavelength

λ_{500} - 500 nm wavelength

λ_{1020} - 1020 nm wavelength

μ - cosine of the zenith angle

μ_o - cosine of the solar zenith angle

ρ - density of the matter

ρ_{dry} - density of the dry aerosol particles

σ - Stefan-Boltzmann constant, total (aerosol plus molecular) extinction coefficient

$\tilde{\sigma}$ - geometric standard deviation of lognormal size distribution of the wet particles

σ_c - variance of the calibration constant

σ_i - geometric standard deviation of the ith component lognormal size distribution

σ_{abs} - absorption coefficient

σ_{ext} - extinction coefficient

σ_{sca} - scattering coefficient

σ_A - aerosol extinction coefficient

σ_{Asca} - aerosol scattering coefficient

σ_R - molecular extinction coefficient

σ_{abs}^{550} - absorption coefficient at 550 nm wavelength

σ_{ext}^{550} - extinction coefficient at 550 nm wavelength

$\tilde{\sigma}_{abs}$ - absorption coefficient normalized to extinction at 550 nm wavelength

$\tilde{\sigma}_{ext}$ - extinction coefficient normalized to extinction at 550 nm wavelength

τ - aerosol optical thickness

τ_g - optical thickness due to gases absorption

τ_i - aerosol optical thickness of the ith component of the aerosol size distribution

τ_{500} - aerosol optical thickness at 500 nm.

τ_R - molecular optical thickness

τ_A - aerosol optical thickness

τ_{O3} - ozone optical thickness

τ_A^{936} - aerosol optical thickness at 936 nm

τ_A^{1020} - aerosol optical thickness at 1020 nm

φ - azimuth angle

φ_o - solar azimuth angle

Ψ - function defined in the Eq. A2.20, relative cosine error

ω - single scattering albedo

ω_c - critical single scattering albedo

ω_A - aerosol single scattering albedo

Ω - solid angle

a - part of radiation absorbed by the aerosol

b - MICROTOPS filter constant

c - parameter of the Junge size distribution, ASD calibration constant

d - actual Earth-Sun distance

d_o - mean Earth-Sun distance

g - asymmetry parameter

k - wavenumber, MICROTOPS filter constant, imaginary part of refractive index

m - real part of refractive index, air-mass factor for zenith angle θ

m_o - air-mass factor for zenith angle θ_o

m_1 - aerosol mass density of the submicron particles

m_{10} - aerosol mass density of the supermicron particles

n - refractive index

n_1 - refractive index of the first substance

n_2 - refractive index of the second substance

n_{12} - refractive index of the internal mixture

$n(r)$ - aerosol size distribution

n_c - aerosol size distribution of the coarse mode

n_f - aerosol size distribution of the accumulation mode

q_1, q_2... - parameters depend on the surface temperature

r - particle radius, aerosol reflection, total (aerosol plus molecular) reflection

r_m - molecular reflection

$\tilde{r}_{mod}$ - mode radius for wet particle

$r_{mod,i}$ - mode radius of the component ith

r_{wet} - wet particle radius

r_{dry} - dry particle radius

$r^{\uparrow}$ - part of radiation scattered upward

$r^{\downarrow}$ - part of radiation scattered downward

s - distance

t - aerosol transmission, total (aerosol plus molecular) transmission

t_m - molecular transmission

u - optical path length

u_o - first coefficient of polynomial fit to the total water vapor variability

u_1 - second coefficient of polynomial fit to the total water vapor variability

u^{micr} - total water vapor content obtained from the MICROTOPS

u^{sonde} - total water vapor content obtained from radio soundings

z - altitude

z_b - the top of the aerosol layer

z_m - range of the lidar

A - aerosol radiative forcing, afterpulse lidar correction

A_s - surface aerosol radiative forcing

A_{TOA} - top of the atmosphere aerosol radiative forcing

B - Planck function

B_a - black body irradiance at the temperature of the aerosol layer

B_s - black body irradiance at the temperature of the Earth's surface

C - Lidar calibration constant, ASD calibration constant, MICROTOPS constant

C_1 - integrated coarse size distribution for particles with radius less than 0.5 μm see Eq. C.17

C_{10} - integrated coarse size distribution for particles with radius between 0.5 μm and 5 μm see Eq. C.18

DN - ASD output (digital number)

E - lidar signal energy

F_o - solar radiation at the top of the atmosphere

F_1 - integrated accumulation size distribution for particles with radius less than 0.5 μm see Eq. C.15

F_{10} - integrated accumulation size distribution for particles with radius between 0.5 μm and 5 μm see Eq. C16

F_{TOA} - infrared outgoing radiation at the top of the atmosphere

F_a^{TOA} - upward flux at the top of the atmosphere with aerosols in the atmosphere

F_c^{TOA} - upward flux at the top of the atmosphere without aerosols in the atmosphere

F_c^s - downward flux at the surface for atmosphere without aerosols

F_a^s - downward flux at the surface for atmosphere with aerosols

F_{eff} - aerosol forcing efficiency

$F^{\downarrow}$ - downward irradiance (flux)

$F_s^{\downarrow}$ - downward flux at the surface

$F_s^{\uparrow}$ - upward flux at the surface

$F_t^{\downarrow}$ - downward flux at the top of the atmosphere

$F_t^{\uparrow}$ - upward flux at the top of the atmosphere

F_{dif} - diffuse flux

F_{dir} - direct flux

F_{tot} - measured (non corrected) total flux

F_{tot}^{cor} - total (direct plus diffuse) corrected flux

F_{FOV} - total downward flux around the field of view

GF - growth factor

I - intensity (radiance)

I_d - diffuse irradiance

I_o - incoming radiance measures at normal incidence

I_{lamp} - calibration lamp spectral intensity

I_m - measured irradiance transmitted through the diffuser

J - source function

K_i - monochromatic absorption coefficient

N - net flux at the top of the atmosphere, particle number density

N_1 - accumulation mode particle number density

N_{10} - coarse mode particle number density

Net_a - net radiative flux (down minus up) for atmosphere with aerosols

Net_c - net radiative flux (down minus up) for atmosphere without aerosols

O - overlap lidar correction

P - phase function

P_A - aerosol phase function

P_R - molecular phase function

Q_{abs} - absorption efficiency

Q_b - backscatter efficiency

Q_{sca} - scattering efficiency

R - planetary albedo

R_1 - particle radius at 55% of the relative humidity which at 0% of the relative humidity has radius of 0.5 μm

R_{10} - particle radius at 55% of the relative humidity which at 0% of the relative humidity has radius of 5 μm

R_A - aerosol backscatter to extinction ratio

R_R - molecular backscatter to extinction ratio

R_s - surface albedo

RH - relative humidity

S - lidar range corrected signal

$\widetilde{S}$ - lidar corrected signal

S_1 - lidar raw data

S_b - lidar background signal

Tr_A - direct aerosol transmission

Tr_R - direct molecular transmission

T - atmosphere temperature

T_a - aerosol temperature

T_s - surface temperature

τ_{eff} - effective infrared transmittance

V - MICROTOPS output signal

V^{936} - the same as V but at 936 nm wavelength

V^{1020} - the same as V but at 1020 nm wavelength

V_o - MICROTOPS output signal at the top of the atmosphere

V_o^{st} - the same as V_o but for mean Earth-Sun distance

V_o^{936} - the same as V_o but at 936 nm wavelength

V_o^{1020} - the same as V_o but at 1020 nm wavelength

A few other symbols are defined directly in the accompanying text

References

Ackerman, S. A., and H. Chung: Radiative effects of airborne dust on regional energy budgets at the top of the atmosphere. *J. Appl. Meteor.*, *31*, 223-233, 1992.

Ackerman, A.S., O.B. Toon, D.E. Stevens, A.J. Heymsfield, V. Ramanathan, and E.J. Welton, Reduction of tropical cloudiness by soot, *Science*, *288*, 1042-1047, 2000.

Aitchison, J., and Brown. J.A., *The lognormal distribution*, Cambridge University Press, 1957

Aitken, J., *Colleted Scientific Papers*, Cambridge University Press, 1923.

Albrecht, B.A., Aerosols, cloud microphysics, and fractional cloudiness, *Science*, *245*, 1227-1230, 1989.

Anderson, T.L., and J.A. Ogren, Determining aerosol radiative properties using the TSI 3563 integrating nephelometer, *Aerosol Sci Tech*, *29*, 57-69, 1998.

Bates, T.S., V.N. Kapustin, P.K. Quinn, D.S. Covert, D.J. Coffman, C. Mari, P.A. Durkee, W.J. DeBruyn, and E.S. Saltzman, Processes controlling the distribution of aerosol particles in the lower marine boundary layer during the First Aerosol Characterization Experiment (ACE 1), *J. Geophys. Res.*, *103*, 16369-16383, 1998.

Berk, A., L.S. Bernstein, G.P. Anderson, P.K. Acharya, D.C. Robertson, J.H. Chetwynd, and S.M. Adler-Golden, MODTRAN cloud and multiple scattering upgrades with application to AVIRIS, *Remote Sens. Environ.*, *65*, 367-375, 1998.

Bernstein, L.S., A. Berk, D.C. Robertson, P.K. Acharya, G.P. Anderson, and J.H. Chetwynd, Addition of a correlated-k capability to MODTRAN., in *Meeting of the IRIS Specialty Group on Targets, Backgrounds, and Discrimination*, pp. 248-249, 1996.

Bohren, C.F., and D.R. Huffman, *Absorption and scattering of light by small particles*, xiv, 530 pp., Wiley, New York, 1983.

Bond, T.C., T.L. Anderson, and D. Campbell, Calibration and intercomparison of filter-based measurements of visible light absorption by aerosols, *Aerosol Sci Tech*, *30*, 582-600, 1999.

Bruggeman, C.A.G., Berechnung verschiedener physikalischer Konstanten von heterogenen Subsganzen, *Ann. Phys. Leipzig*, *24*, 636, 1935.

Bush, B.C., F.P.J. Valero, A.S. Simpson, and L. Bignone, Characterization of thermal effects in pyranometers: A data correction algorithm for improved measurement of surface insolation, *J Atmos. Ocean Technol.*, *17*, 165-175, 2000.

Carrico, C.M., M.J. Rood, and J.A. Ogren, Aerosol light scattering properties at Cape Grim, Tasmania, during the First Aerosol Characterization Experiment (ACE 1), *J. Geophys. Res.*, *103*, 16565-16574, 1998.

Carrico, C.M., M.J. Rood, J.A. Ogren, C. Neususs, A. Wiedensohler, and J. Heintzenberg, Aerosol optical properties at Sagres, Portugal during ACE-2, *Tellus B*, *52*, 694-715, 2000.

Chandrasekhar, S., *Radiative Transfer*, Dover, New York, 1950.

Charlson, R.J., J.E. Lovelock, M.O. Andrea, and S.G. Warren, Ocean, phytoplankton, atmospheric sulfur, cloud albedo and climate, *Nature*, *326*, 655-661, 1987.

Charlson, R.J., J. Langner, H. Rodhe, C.B. Leovy, and S.G. Warren, Perturbation of the northern hemisphere radiative balance by backscattering from anthropogenic sulfate aerosols, *Tellus*, *43AB*, 152-163, 1991.

Chung, C.E., and V. Ramanathan, South Asian Haze Forcing: Remote Impacts with Implications to ENSO and AO, *Submitted to J. Climate, 2002*.

Chylek, P., and J.A. Coakley, Aerosol and Climate, *Science*, *183*, 75-77, 1974.

Chylek, P., V. Srivastava, R.G. Pinnick, and R.T. Wang, Scattering of electromagnetic waves by composite spherical particles: experiment and effective medium approximations, *Appl. Opt.*, *27*, 2396-404, 1988.

Coakley, J.A., and R.D. Cess, Response of the NCAR Community Climate Model to the radiative forcing by the naturally-occuring tropospheric aerosol, *J. Atmos. Sci.*, *42*, 1677-1692, 1985.

Conant, W.C., An observational approach for determining aerosol surface radiative forcing: results from the first field phase of INDOEX, *J. Geophys. Res.*, *105*, 15347-60, 2000.

Conant, W. C., J. H. Seinfeld, and J. Wang, G. R. Carmichael, Y. Tang, I. Uno, P. J. Flatau, K. M. Markowicz, P. K. Quinn, A model for the radiative forcing during ACE-Asia derived from CIRPAS Twin Otter and R/V Ronald H. Brown data and comparison with observations, *J. Geophys. Res*., *108, D23, 8661*, 10.1029/2002JD003260, 2003.

Coulier, M., *J. Pharm. Chim.*, *22*, 165-167, 1875.

Crutzen, P.J., and V. Ramanathan, Special section: Indian Ocean Experiment (INDOEX), Part 1 - Foreword, *J. Geophys. Res.*, *106*, 28369-28370, 2001.

Diaz, J.P., F.J. Exposito, C.J. Torres, and F. Herrera, Radiative properties of aerosols in Saharan dust outbreaks using ground-based and satellite data: Applications to radiative forcing, *J. Geophys. Res.*, *106*, 18403-18416, 2001.

Dufresne, J.L., C. Gautier, P. Ricchiazzi, and Y. Fouquart, Longwave scattering effects of mineral aerosols, *J. Atmos. Sci.*, *59*, 1959-1966, 2002.

Eck, T.F., B.N. Holben, O. Dubovik, A. Smirnov, I. Slutsker, J.M. Lobert, and V. Ramanathan, Column-integrated aerosol optical properties over the Maldives during the northeast monsoon for 1998-2000, *J. Geophys. Res.*, *106*, 28555-28566, 2001.

Fitzgerald, J.W., Approximation Formulas for the Equilibrium Size of an Aerosol Particle as a Function of Its Dry Size and Composition and the Ambient Relative Humidity., *J Appl Meteorol*, *14*, 1044-1049, 1975.

Haywood, J.M., and K.P. Shine, The effect of anthropogenic sulfate and soot aerosol on the clear sky planetary radiation budget, *J. Geophys. Res.*, *22*, 603-606, 1995.

Hansen, J., M. Sato, and R. Ruedy, Radiative forcing and climate response, *J. Geophys. Res. (USA)*, *102*, 6831-6864, 1997.

Henyey, L.C., and J.L. Greenstein, Diffuse radiation in the galaxy, *Astrophys. J.*, *93*, 70-83, 1941.

Hess, M., P. Koepke, and I. Schult, Optical properties of aerosols and clouds: The software package OPAC, *Bull. Amer. Meteorol. Soc.*, *79*, 831-844, 1998.

Highwood, E. J., M., H. J., Silverstone, M. D., Newman, S. M., and Taylor, J. P. (2002). Ratiative properties and direct effect of Saharan dust measured by the C-130 aircraft during SHADE.2: Terrestrial spectrum. *J. Geophys. R. (in press)*

Hobbs, P.V., G. Bluhm, and T. Ohtake, *Tellus*, *23*, 28-39, 1971.

Houghton, J.T., *Climate change 2001 : the scientific basis : contribution of Working Group I to the third assessment report of the Intergovernmental Panel on Climate Change*, x, 881 pp., Cambridge University Press, Cambridge, U.K. ; New York, 2001.

Houghton, J.T., Intergovernmental Panel on Climate Change. Working Group I., and Intergovernmental Panel on Climate Change. Working Group III., *Climate change, 1994 : radiative forcing of climate change and an evaluation of the IPCC IS92 emission scenarios*, 339 pp., Cambridge University Press, Cambridge [England] ; New York, 1995.

Hsu, N. C., J. R. Herman, and C. J. Weaver: Determination of radiative forcing of Saharan dust using combined TOMS and ERBE data. *J. Geophys. Res.*, *105*, 20,649-20,661, 2000.

Van de Hulst, H.C., *Light Scattering by Small Particles*, John Wiley & Sons, New York, 1957.

Im, J.S., V.K. Saxena, and B.N. Wenny, An assessment of hygroscopic growth factors for aerosols in the surface boundary layer for computing direct radiative forcing, *J. Geophys. Res.*, *106*, 20213-20224, 2001.

Jacob, D.J., J.A. Logan, and P.P. Murti, Effect of rising Asian emissions on surface ozone in the United States, *Geophys. Res. Lett.*, *26*, 2175-2178, 1999.

Jacobson, M.Z., Global direct radiative forcing due to multicomponent anthropogenic and natural aerosols, *J. Geophys. Res.*, *106*, 1551-1568, 2001.

Kaufman, Y.J., P.V. Hobbs, V. Kirchhoff, P. Artaxo, L.A. Remer, B.N. Holben, M.D. King, D.E. Ward, E.M. Prins, K.M. Longo, L.F. Mattos, C.A. Nobre, J.D. Spinhirne, Q. Ji, A.M. Thompson, J.F. Gleason, S.A. Christopher, and S.C. Tsay, Smoke, Clouds, and Radiation - Brazil (SCAR-B) experiment, *J. Geophys. Res.*, *103*, 31783-31808, 1998.

Kaufman, Y.J., D. Tanre, B.N. Holben, S. Mattoo, L.A. Remer, T.F. Eck, J. Vaughan, and B. Chatenet, Aerosol radiative impact on spectral solar flux at the surface, derived from principal-plane sky measurements, *J. Atmos. Sci.*, *59*, 635-646, 2002.

Kiehl, J.T., V. Ramanathan, J.J. Hack, A. Huffman, and K. Swett, The role of aerosol absorption in determining the atmospheric thermodynamic state during INDOEX (abstract), edited by Eos Trans. AGU, Fall Meet. Suppl., 184, 1999.

King, M.D., Sensitivity of Constrained Linear Inversion to the Selection of the Lagrange Multiplier, *J. Atmos. Sci.*, *39*, 1359-1369, 1992.

Klett, J.D., Lidar inversion with variable backscatter/extinction ratios, *Appl. Opt.*, *24*, 1638-1643, 1985.

Kohler, U., A comparison of the new filter ozonometer MICROTOPS II with Dobson and Brewer spectrometers at Hohenpcissenberg, *Geophys. Res. Lett.*, *26*, 1385-1388, 1999.

Kotchenruther, R.A., P.V. Hobbs, and D.A. Hegg, Humidification factors for atmospheric aerosols off the mid-Atlantic coast of the United States, *J. Geophys. Res.*, *104*, 2239-2251, 1999.

Kovalev, V.A., Lidar measurement of the vertical aerosol extinction profiles with range-dependent backscatter-to-extinction ratios., *Appl. Opt.*, *32*, 6053-6065, 1993.

Lelieveld, J., H. Berresheim, S. Borrmann, P.J. Crutzen, F.J. Dentener, H. Fischer, J. de Gouw, J. Feichter, P. Flatau, J. Heland, R. Holzinger, R. Korrmann, M. Lawrence, Z. Levin, K. Markowicz, N. Mihalopoulos, A. Minikin, V. Ramanathan, M. de Reus, G.J. Roelofs, H.A. Scheeren, J. Sciare, H. Schlager, M. Schultz, P. Siegmund, B. Steil, P. Stier, M. Traub, J. Williams, and H. Ziereis, Global air pollution crossroads over the Mediterranean, *Science*, *298*, 794-799, 2002.

Loeb, N.G., and S. Kato, Top-of-atmosphere direct radiative effect of aerosols over the tropical oceans from the Clouds and the Earth's Radiant Energy System (CERES) satellite instrument, *J. Climate*, *15*, 1474-1484, 2002.

Loeb, N.G., F. Parol, J.C. Buriez, and C. Vanbauce, Top-of-atmosphere albedo estimation from angular distribution models using scene identification from satellite cloud property retrievals, *J. Climate*, *13*, 1269-1285, 2000.

Long, M., D. Entekhabi, and S.E. Nicholson, Interannual variability in rainfall, water vapor flux, and vertical motion over West Africa, *J. Climate*, *13*, 3827-3841, 2000.

Lubin, D., and A. S. Simpson: The longwave emission signature of urban pollution: radiometric FTIR measurement. *Geophys. Res. Lett., 21,* 37-40, 1994.

Lubin, D., J.P. Chen, P. Pilewskie, V. Ramanathan, and F.P.J. Valero, Microphysical Examination of Excess Cloud Absorption in the Tropical Atmosphere, *J. Geophys. Res.*, *101*, 16961-16972, 1996.

Lubin, D., S.K. Satheesh, G. McFarquhar, and A.J. Heymsfield, The longwave radiative forcing of Indian Ocean tropospheric aerosol, *J. Geophys. Res.,* in press, 2002

Malm, W.C., J.F. Sisler, D. Huffman, R.A. Eldred, and T.A. Cahill, Spatial and Seasonal Trends in Particle Concentration and Optical Extinction in the United States, *J. Geophys. Res.*, *99*, 1347-1370, 1994.

Markowicz, K.M., P.J. Flatau, M.V. Ramana, P.J. Crutzen, and V. Ramanathan, Absorbing Mediterranean Aerosols Lead to a Large Reduction in the Solar Radiation at the Surface., *Geophys. Res. Lett.*, 29(DX), 10.1029/2002GL015767, 2002.

Markowicz, K.M., P.J. Flatau, P.K. Quinn, C.M. Carrico, M.K. Flatau, A.M. Vogelmann, D. Bates, M. Liu, and M.J. Rood, Influence of Relative Humidity on Aerosol Radiative Forcing: An ACE-Asia Experiment Perspective, *J. Geophys. Res.*, *108, D23, 8662*, 10.1029/2002JD003066, 2003a .

Markowicz, K.M., P.J. Flatau, A.M. Vogelmann, P.K. Quinn, and E.J. Welton, Infrared aerosol radiative forcing at the surface and the top of the atmosphere., *Quarterly Journal of the Royal Meteorological Society*, in press, 2003b.

Maxwell Garnett, J.C., Colours in Metal Glasses and in Metallic Films, *Philsol. Trans. R. Soc. London*, *203*, 385, 1904.

Mihalopoulos, N., E. Stephanou, M. Kanakidou, S. Pilitsidis, and P. Bousquet, Tropospheric aerosol ionic composition in the Eastern Mediterranean region, *Tellus B*, *49*, 314-326, 1997.

Morys, M., F.M. Mims, S. Hagerup, S.E. Anderson, A. Baker, J. Kia, and T. Walkup, Design, calibration, and performance of MICROTOPS II handheld ozone monitor and Sun photometer, *J. Geophys. Res.*, *106*, 14573-14582, 2001.

Myhre, G., and F. Stordal, Global sensitivity experiments of the radiative forcing due to mineral aerosols, *J. Geophys. Res.*, *106*, 18193-18204, 2001

Podgorny, I.A., W. Conant, V. Ramanathan, and S.K. Satheesh, Aerosol modulation of atmospheric and surface solar heating over the tropical Indian Ocean, *Tellus B*, *52*, 947-958, 2000.

Quinn, P.K., D.J. Coffman, T.S. Bates, T.L. Miller, J.E. Johnson, K. Voss, E.J. Welton, and C. Neususs, Dominant aerosol chemical components and their contribution to extinction during the Aerosols99 cruise across the Atlantic, *J. Geophys. Res.*, *106*, 20783-20809, 2001.

Quinn, P.K., T. Bates, D.J. Coffman, T.L. Miller, D.S. Covert, and E.J. Welton, Marine boundary layer aerosol optical properties during ACE Asia as a function of aerosol source region., *submitted to Journal of Geophysical Research-Atmospheres*, 2002a.

Quinn, P.K., D.J. Coffman, T.S. Bates, T.L. Miller, J.E. Johnson, E.J. Welton, C. Neususs, M. Miller, and P.J. Sheridan, Aerosol Optical Properties during INDOEX 1999: Means, Variability, and Controlling Factors, *J. Geophys. Res.*, *107(DX),10.1029/2000JD000037*, 2002b.

Raes, F., T. Bates, F. McGovern, and M. Van Liedekerke, The 2nd Aerosol Characterization Experiment (ACE-2): general overview and main results, *Tellus B*, *52*, 111-125, 2000.

Ramanathan, V., P.J. Crutzen, J.T. Kiehl, and D. Rosenfeld, Atmosphere - Aerosols, climate, and the hydrological cycle, *Science*, *294*, 2119-2124, 2001a.

Ramanathan, V., P.J. Crutzen, J. Lelieveld, A.P. Mitra, D. Althausen, J. Anderson, M.O. Andreae, W. Cantrell, G.R. Cass, C.E. Chung, A.D. Clarke, J.A. Coakley, W.D. Collins, W.C. Conant, F. Dulac, J. Heintzenberg, A.J. Heymsfield, B. Holben, S. Howell, J. Hudson, A. Jayaraman, J.T. Kiehl, T.N. Krishnamurti, D. Lubin, G. McFarquhar, T. Novakov, J.A. Ogren, I.A. Podgorny, K. Prather, K. Priestley, J.M. Prospero, P.K. Quinn, K. Rajeev, P. Rasch, S. Rupert, R. Sadourny, S.K. Satheesh, G.E. Shaw, P. Sheridan, and F.P.J. Valero, Indian Ocean Experiment: An integrated analysis of the climate forcing and effects of the great Indo-Asian haze, *J. Geophys. Res.*, *106*, 28371-28398, 2001b.

Revercomb, H.E., H. Buijs, H.B. Howell, D.D. LaPorte, W.L. Smith, and L.A. Sromovsky, Radiometric calibration of IR Fourier transform spectrometers: solution to a problem with the High Resolution Interferometer Sounder, *Appl. Opt.*, *27*, 3210-18, 1988.

Rosenfeld, D., Suppression of rain and snow by urban and industrial air pollution, *Science*, *287*, 1793-1796, 2000.

Rothman, L.S., C.P. Rinsland, A. Goldman, S.T. Massie, D.P. Edwards, J.M. Flaud, A. Perrin, C. CamyPeyret, V. Dana, J.Y. Mandin, J. Schroeder, A. McCann, R.R. Gamache, R.B. Wattson, K. Yoshino, K.V. Chance, K.W. Jucks, L.R. Brown, V. Nemtchinov, and P. Varanasi, The HITRAN molecular spectroscopic database and HAWKS (HITRAN Atmospheric Workstation): 1996 edition, *J Quant Spectrosc Radiat*, *60*, 665-710, 1998.

Russell, P.B., P.V. Hobbs, and L.L. Stowe, Aerosol properties and radiative effects in the United States East Coast haze plume: An overview of the Tropospheric Aerosol Radiative Forcing Observational Experiment (TARFOX), *J. Geophys. Res.*, *104*, 2213-2222, 1999.

Satheesh, S.K., and V. Ramanathan, Large differences in tropical aerosol forcing at the top of the atmosphere and Earth's surface, *Nature*, *405*, 60-63, 2000.

Satheesh, S.K., V. Ramanathan, L.J. Xu, J.M. Lobert, I.A. Podgorny, J.M. Prospero, B.N. Holben, and N.G. Loeb, A model for the natural and anthropogenic aerosols over the tropical Indian Ocean derived from Indian Ocean Experiment data, *J. Geophys. Res.*, *104*, 27421-27440, 1999.

Schwarzschild, K., *Diffusion and absorption in the Sun's atmosphere.*, 1183-1200 pp. In "Selected Papers on the Transfer of Radiation" (D.H. Menzel, ed.), Dover, New York, 1914.

Seinfeld, J.H., and S.N. Pandis, Atmospheric chemistry and physics. From air pollution to climate change., John Wiley & Sons, Inc., 1998

Shifrin, K.S., Simple Relationships for the Angstrom Parameter of Disperse Systems, *Appl. Opt.*, *34*, 4480-4485, 1995.

Sokolik, I.N., O.B. Toon, and R.W. Bergstrom, Modeling the radiative characteristics of airborne mineral aerosols at infrared wavelengths, *J. Geophys. Res.*, *103*, 8813-8826, 1998.

Spänkuch, D., W. Dohler, and J. Guldner. (2000). Effect of coarse biogenic aerosol on downwelling infrared flux at the surface. *J. Geophys. Res.,* 105, 17341-17350.

Stamnes, K., S.C. Tsay, W. Wiscombe, and K. Jayaweera, Numerically stable algorithm for discrete-ordinate-method radiative transfer in multiple scattering and emitting layered media, *Appl. Opt.*, *27*, 2502-9, 1988.

Swap, et al., The Southern African Regional Science Initiative (SAFARI 2000): Dry-Season Field Campaign: An Overview, South African Journal of Science, 98, 125-130, 2002

Takemura, T., T. Nakajima, O. Dubovik, B.N. Holben, and S. Kinne, Single-scattering albedo and radiative forcing of various aerosol species with a global three-dimensional model, *J. Climate*, *15*, 333-352, 2002.

Tanre, D., et al., 2003. Measurement and modeling of the Saharan dust radiative impact: overview of the Saharan Dust Experiment (SHADE), Journal of Geophysical Research, submitted to SHADE Special Issue.

Tegen, I., A.A. Lacis, and I. Fung, The Influence on Climate Forcing of Mineral Aerosols from Disturbed Soils, *Nature*, *380*, 419-422, 1996

Thomas, G.E., and K. Stamnes, *Radiative Transfer in the Atmosphere and Ocean*, Cambridge University Press, 1999.

Turpin, B.J., and H.J. Lim, Species contributions to PM2.5 mass concentrations: Revisiting common assumptions for estimating organic mass, *Aerosol Sci Tech*, *35*, 602-610, 2001.

Twomey, S., *Geofis. Pur. Appl.*, *43*, 227-250, 1959.

Twomey, S., *Atmospheric Aerosols*, Elsevier Sci., New York, 1977.

Vogelmann, A.M., P.J. Flatau, M. Szczodrak, K.M. Markowicz, and P.J. Minnett, Observations of large greenhouse effects for anthropogenic aerosols, *Geophys. Res. Lett, 30, No. 12, 1654,* 10.1029/2003GL017229, 2003

Vogelmann, A.M., V. Ramanathan, and I.A. Podgorny, Scale dependence of solar heating rates in convective cloud systems with implications to general circulation models, *J. Climate*, *14*, 1738-1752, 2001.

Warneck, P., *Chemistry of the Natural Atmosphere*, Academic Press., 1988.

Welton, E.J., K.J. Voss, H.R. Gordon, H. Maring, A. Smirnov, B. Holben, B. Schmid, J.M. Livingston, P.B. Russell, P.A. Durkee, P. Formenti, and M.O. Andreae, Ground-based lidar measurements of aerosols during ACE-2: instrument description, results, and comparisons with other ground-based and airborne measurements, *Tellus B*, *52*, 636-651, 2000.

Welton, E.J., P.K. Voss, P.K. Quinn, P. Flatau, K. Markowicz, J. Campbell, J.D. Spinhirne, H.R. Gordon, and J. Johnson, Measurements of aerosol vertical profiles and optical properties during INDOEX 1999 using micropulse lidars, *J. Geophys. Res.*, *107(DX), 10.1029/2000JD000038*, 2002.

Wielicki, B.A., Clouds and the Earths Radiant Energy System (CERES) - an Earth Observing System Experiment, *Bull. Amer. Meteorol. Soc.*, *77*, 1590-1590, 1996.

Winter, B., and P. Chylek, Contribution of sea salt aerosol to the planetary clear-sky albedo, *Tellus B*, *49*, 72-79, 1997.

Wiscombe, W.J., and G.W. Grams, The backscattered fraction in two-stream approximations, *J. Atmos. Sci.*, *33*, 2440-51, 1976.

Acknowledgements

I would like to express thanks to all those who have assisted me during preparing and writing this thesis in particular d*r Piotr Flat*au (consultant) for his constant and enthusiastic support, for suggesting the line of work, interesting discussions and his patient guidance throughout this work and *prof. dr hab. Krzysztof Haman* (supervisor) for constructive suggestions and comments.

All radiation instruments which I used during INDOEX, ACE-Asia, and MINOS projects are the property of Center for Atmospheric Science Scripps Institution of Oceanography UCSD. That is the reason why I would like to thank *prof. V. Ramanathan* rendering the equipment accessible and for financial support. Additionally I would like to thank him and *prof. P. Crutzen* for important comments and constructive suggestions during my work at Scripps.

I must also acknowledge a number of friends, colleagues, students, teachers who assisted, advised, and supported my research and writing efforts over the last years. I am also grateful to many persons who shared their memories and experiences. Especially, I need to express my gratitude and deep appreciation to:

Andy Vogelmann for close collaboration and constructive discussions which we had;

Patricia Quinn for chemical data and interesting discussions;

Christian Carrico for aerosol optical data from ACE-Asia cruise;

Nikos Mihalopoulos for assistance during MINOS experiment and possibility of using Finakalia station;

Muvva VenKata Ramana for helping with experimental stuff on Crete and his assistance;

Jos Lelieveld for interesting disscusions during MINOS experiment and his support

Weyning Su for close cooperation during ACE-Asia cruise.

John Porter who helped me with the lidar system.

David Bates who provided me MPL lidar data from ACE-Asia cruise

Gabrielle Ayres for language correction

This research was supported by Fulbright commission, who funded my 9-months stay at Scripps and NRL in 2002.

Krzysztof Markowicz

Wpływ aerozolu na zmiany promieniowania krótko- i długofalowego w atmosferze- badania eksperymentalne.

Streszczenie

Aerozole atmosferyczne to małe cząstki stałe lub ciekłe stanowiące zanieczyszczenie powietrza. Powstają one zarówno w czasie procesów naturalnych jak i w wyniku działalności przemysłowej człowieka. Obecność aerozoli w atmosferze przyczynia się do zmian w bilansie promieniowania elektromagnetycznego Ziemi, gdyż aerozole pochłaniają i rozpraszają promieniowanie krótko- i długofalowe. Ponadto cząstki zanieczyszczeń atmosfery spełniają rolę tzw. jąder kondensacji przez co przyczyniają się do powstawania chmur i opadów.

Aerozole są obecnie przedmiotem intensywnych badań w fizyce atmosfery, ponieważ wpływają istotnie na klimat Ziemi. W przeciwieństwie do gazów cieplarnianych drobne cząstki atmosferyczne prowadzą do ochładzania klimatu zarówno przez tzw. efekt bezpośredni jak i pośredni. Pierwszy z nich związany jest z wpływem aerozolu na zmiany promieniowania w przypadku braku chmur, zaś drugi dotyczy modyfikacji własności mikrofizycznych chmur i w konsekwencji albeda układu Ziemia-atmosfera.

Niniejsza praca zawiera obserwacyjne oraz modelowe studia nad bezpośrednim wpływem aerozolu na zmiany promieniowania na powierzchni ziemi, w atmosferze oraz na górnej granicy atmosfery. Prezentowane wyniki badań pochodzą z pomiarów prowadzonych na stacji Finokalia na Krecie w czasie eksperymentu MINOS oraz na statku badawczym *R/V Ronald H. Brown* podczas eksperymentów: INDOEX i ACE-Asia.

Wyniki tych badań dowodzą, że aerozole w pobliżu uprzemysłowionych obszarów świata wykazują silne właściwości absorpcyjne. Prowadzi to do znacznej redukcji promieniowania słonecznego dochodzącego do powierzchni Ziemi (około 5-8%). Silna absorpcja przez aerozole atmosferyczne była obserwowana zarówno nad wschodnią częścią Morza Śródziemnego jak i w północnej części Oceanu Indyjskiego. Dodatkowo nad Morzem Śródziemnym właściwości optyczne aerozolu antropogenicznego były zmodyfikowane przez silnie absorbujące cząstki sadzy produkowane podczas intensywnych pożarów w Europie wschodniej oraz południowo-wschodniej. Zauważano, że podczas pożarów wydajność wymuszania radiacyjnego aerozolu na powierzchni ziemi rośnie, co do wartości bezwzględnej i osiąga około -90 Wm^{-2} na jednostkę grubości optycznej. W okresie poprzedzającym je wydajność ta wynosiła jedynie około

-70 Wm^{-2} na jednostkę grubości optycznej a więc tyle co w pobliżu silnie zanieczyszczonego półwyspu Indyjskiego.

Kolejnym ważnym celem tej pracy były studia nad wpływem wilgotności powietrza na właściwości optyczne aerozolu oraz na wymuszanie radiacyjne. Analiza danych z omawianych eksperymentów pokazała istnienie silnej zależności pomiędzy wilgotnością względna (a także opadem potencjalnym) a grubością optyczną aerozolu. Ponadto bazując na obserwacjach prowadzonych na Morzu Japońskim podczas eksperymentu ACE-Asia pokazano istnienie silnej korelacji pomiędzy albedem pojedynczego rozpraszania a wilgotnością względną, co z kolei wskazuje na istnienie zależności pomiędzy wilgotnością względną a wydajnością wymuszenia radiacyjnego aerozolu. W szczególności wysoka wilgotność powietrza obserwowana w czasie ACE-Asia wyjaśnia stosunkowo słabą absorpcję promieniowania słonecznego przez aerozol w tym rejonie w porównaniu do absorpcji obserwowanej w południowej Azji i Europie.

Dyskutowane różnice i podobieństwa właściwości optycznych aerozolu oraz jego wpływu na bilans promieniowania w różnych rejonach świata pokazują, że kluczową rolę w kształtowaniu tego bilansu mogą odgrywać takie czynniki meteorologiczne jak cyrkulacja powietrza, stratyfikacja warstwy granicznej atmosfery oraz wilgotność powietrza. Ponadto wymuszanie radiacyjne w badanych rejonach znacznie przewyższa średnią wartość globalną oraz wymuszanie radiacyjne związane ze wzrostem koncentracji tzw. gazów cieplarniach.

Praca zawiera unikalne studia nad wpływem aerozolu na zmiany promieniowania długofalowego na powierzchni ziemi i górnej granicy atmosfery. Analizowane są wyniki modelowania opartego na danych obserwacyjnych dotyczących składu chemicznego oraz właściwości optycznych aerozolu. Dodatkowo wyniki z modelu były weryfikowane pomiarami spektralnej radiancji w dalekiej podczerwieni prowadzonymi podczas eksperymentu ACE-Asia. W wyniku tych analiz pokazano, że wbrew dotychczasowym poglądom, wpływ aerozolu na bilans promieniowania długofalowego nie może być zaniedbywany - zarówno aerozol naturalny (a w szczególności piasek pustynny) jak i antropogeniczny mogą istotnie wpływać na wartość tego bilansu. Wykazano, że wymuszanie radiacyjne aerozolu w dalekiej podczerwieni, w przeciwieństwie do wymuszenia w zakresie krótkofalowym, jest dodatnie zarówno na powierzchni ziemi jak i na górnej granicy atmosfery i co do wartości bezwzględnej może przyjmować wartość dochodzącą do 20% wartości tego ostatniego.